



UNIVERSITY OF
CAMBRIDGE

Cavendish Laboratory

Superfluidity in a uniform two-dimensional Bose gas

Panagiotis Christodoulou

Hughes Hall College, June 2021

This dissertation is submitted for the degree of
Doctor of Philosophy

*To my parents, Spyros and Constantina,
to my sister, Demetra.*

DECLARATION

I declare that this thesis is my own work and is not substantially the same as any that I have submitted or am currently submitting for a degree, diploma or any other qualification at any other university. No part of this thesis has already been or is being concurrently submitted for any such degree, diploma or any other qualification. This thesis does not exceed the word limit of sixty thousand words, including tables, footnotes, bibliography and appendices, set out by the Faculty of Physics and Chemistry.

Panagiotis Christodoulou
June 2021

Cavendish Laboratory
University of Cambridge
JJ Thomson Avenue
Cambridge CB3 0HE
United Kingdom

ABSTRACT

Superfluidity in a uniform two-dimensional Bose gas

Panagiotis Christodoulou

This thesis describes experimental studies regarding superfluidity in a two-dimensional gas of ultracold atoms trapped in a uniform potential. It is conceptually divided into three parts.

In the first part we offer a theoretical discussion of a superfluid, first from a general perspective and then concentrating on its distinct features when restricted to two-dimensions. One of the hallmarks of superfluidity in all dimensions, predicted by the highly successful hydrodynamic two-fluid model and observed in both liquid helium and ultracold atomic gases, is the existence of two kinds of sound excitations, the first and second sound. Unlike its three dimensional counter-part, however, superfluidity in two dimensions is associated with the pairing of vortices of opposite circulation as described by the Berezinskii-Kosterlitz-Thouless (BKT) theory, rather than the emergence of true long-range order. One of the most well-known features of BKT superfluidity is the universal jump in its superfluid density at a critical temperature without any discontinuities in the fluid's thermodynamic properties.

In the second part we describe the experimental realisation and the characterisation of a versatile two-dimensional box trap for the confinement of a ^{39}K atomic gas. Our apparatus is the outcome of merging a previously existing experimental setup with a series of modifications and extensive additions. Importantly for this thesis, we are able to tune the interactions of the gas with the aid of a magnetic Feshbach resonance, reaching the hydrodynamic regime where the predictions of the two-fluid model for a two-dimensional superfluid are expected to be valid.

With a homogeneous and tunable two-dimensional gas at hand, in the third part of this thesis we describe our experimental method to observe both first and second sound; the latter is seen for the first time in any two-dimensional fluid. From the two temperature-dependent measured sound speeds we deduce its superfluid density, a central quantity for a superfluid that had so far remained elusive in ultracold gases. Our results agree with BKT theory, including the prediction for the universal superfluid-density jump.

Acknowledgements

Vividly recalling traveling through those vast plains to Cambridge and discovering N. Cave's 'Wonderful life' during my first day in this old country. I won't forget that song. I won't forget that feeling.

I am nothing but my limitations; an inability to express my thoughts on paper for the intangible reader led me to keep it personal throughout. This dissertation is thus a constant talk with you.

I am nothing but my limitations; to be honest, I never got it how one can write pages after pages, keeping it meaningful. I highly admire the condensation of words into a single phrase, if possible, that recaptures the truth; the excess of words only befogs the essence. This lengthy report may thus contain unworthy words, awkward expressions, unnecessary commas, prosaic phrases, 'fallen robins' that you could have kept track of.

I am nothing but my limitations; I feel the need to express my gratitude to a number of people who lifted part of these limitations with their advice, passion, guidance and assistance, even during periods that 'nothing seemed to work' and, believe me, there were quite a few. I tried my best to avoid kitsch expressions and fake kindness that would only belittle the honesty of my intentions.

To start, I am indebted to my supervisor, Zoran Hadzibabic, for initially giving me the opportunity to work in this field and to join a group of charismatic people with a genuine interest in physics and subsequently for the overall attitude towards me. The latter contains, but is not limited by, the freedom you gave me to experiment with the machine, your guidance that often prevented me from straying away, and your time-investment that allowed me to finish this thesis as fast as possible. I especially enjoyed our numerous Skype meetings during the lockdown, most of which started with a despair on the air and ended up with renewed confidence of our ideas, even if we often had to talk until 3 am; the angry reaction of my neighbor Valeria, whom we often kept awake, was just a collateral damage.

I would like to give a very special thanks to Julian Schmitt and Maciej Galka; they both appeared in the life of the lab around the same period, one year after my coming here, as the new post-doc and PhD student of our 'BEC2' experiment, respectively, and together we passed through all the important phases of this experience since: we reinvented the wheel of how this capricious machine was previously built, we installed the new experimental bits, and we got into the details of a two-dimensional world that in the end was not restricting at all. Julian, I have always been impressed, among others, by your experimental skills, especially in optics and in coding, which greatly enhanced our work and saved us a great deal of time. I will specifically remember with gratitude your willingness

to discuss any related or unrelated question I may have until we find the solution; Maciej, the provider of vodka that destroys (some of) your colleagues, you have many times surprised me with your ability to combine knowledge from different fields in such a fast way. Also, I have to admit that it has been always a relief for me to know that my easy-to-forget mind could depend on someone who would definitely remember even the smallest detail of our experiment. Maciej and Julian, I already miss our 4pm-canteen-break and the weird discussions that came together, and our walks to get the best kebab in the town (although the exact spot changed throughout the years). I am very glad that it was you two who I had to collaborate with during these years and I hope to keep you both as good friends in the future.

I also want to thank Raphael Lopes, Jay Man, Nishant Dogra, and Rob Smith. Rapha, you proved to be a central figure during my first year in Cambridge, introducing me to the lab and guiding me during that adjusting period. You have undoubtedly been a strong influence on my working habits. I still recall our common love for the Beatles and football; it is however a bit annoying that Porto always beats Olympiacos. Jay, as the main PhD student at the time, you showed me the whereabouts and answered patiently all my ignorant questions. Nishant, a relatively recent addition to BEC2 (started also a new 'BEC4' experiment), you kept 'annoying' me with questions that I found hard to answer. I am thankful for your immediate integration to the team and your constant offer to help and convey your knowledge. Together with Julian and Maciej I want to thank you for taking the time to read and comment various parts of this report. Rob, although we never worked together, your suggestions and your knowledge of all the details of the BEC2 machine, from which you had recently retired, were always invaluable.

I am very confident that with the addition of the new PhD students, Andrey Karailiev and Martin Gažo in BEC2, we put the machine into good hands. I leave knowing that, together with the new 'BEC3' students, Jiří Etrych and Gevorg Martirosyan and BEC4 student, Konstantinos Konstantinou, the group has a bright future ahead.

Speaking of the complementary BEC1/BEC3 sub-group, I want to thank Chris Eigen, Jake Glidden, Timon Hilker, Lena Dogra and Jinyi Zhang for various interesting discussions and for the occasional technical support they provided. I have enjoyed your company throughout, as well as social activities from football games to pub nights.

Apart from those above, constantly moving around the lab, there was a number of other people who passed by and with whom we shared discussions, knowledge, opinions and generally our time. Among them I want to single out our neighbors, Matteo Sbroscia, Konrad Viebahn and the rest of the Schneider team; at the same time various Master and summer students appeared, Milan (who 'unfortunately' moved to Oxford), Nathaniel, Sri, Marine, and Andreas, adding weight to this experience.

Outside of the Cavendish, I first want to thank my family, to whom I devote this dissertation, for their unlimited support and trust in me throughout the years and especially the difficult ones that

we have been living apart. I also feel gratitude for the support of my old friends in Greece, with whom we never lost this connection of familiarity despite distance, but also the new ones made here.

Finally, I would like to thank Caterina for your constant and passionate support, for your unselfish patience despite my crazy and unreasonable working schedule and for teaching me proper English with this silly Italian accent since our first common day in Cambridge and since accidentally - I have to admit it eventually - stealing your seat.

Contents

1	Introduction	1
2	Superfluidity in a Bose gas	5
2.1	A phenomenological treatment	6
2.1.1	One-fluid hydrodynamics	7
2.1.2	Two-fluid hydrodynamics	8
2.1.3	Density response to an external probe	11
2.2	A semi-phenomenological treatment	16
2.3	A microscopic treatment	18
2.3.1	Interactions in a dilute Bose gas	18
2.3.2	Elementary excitations vs density fluctuations	23
2.3.3	Bose-Einstein condensate and superfluidity	25
3	The two-dimensional atomic Bose gas	31
3.1	The quasi-two-dimensional Bose gas	32
3.2	Low-temperature behaviour	33
3.2.1	Implications of the Bogoliubov analysis	35
3.2.2	The Berezinskii-Kosterlitz-Thouless phase transition	36
3.2.3	The equation of state for the atomic two-dimensional Bose gas	42
3.3	Real gases: finite-size-system modifications	47
4	The realisation of a two-dimensional box trap	51
4.1	Setting the stage and initial steps	51
4.2	Production of a Bose-Einstein condensate	57
4.3	The two-dimensional confinement	61
4.4	The uniform in-plane confinement	74
4.5	Integration of the DMDs into the experimental setup	81
4.6	Compensation of magnetic fields	84
4.7	The procedure for producing a degenerate 2D uniform gas	87
4.8	Imaging and calibration of density and temperature	92

4.8.1	High-field imaging of the 2D plane	93
4.8.2	Calibration of density and temperature	94
5	First and second sound in a BKT superfluid	103
5.1	Setting the stage	103
5.2	Probing first and second sound excitations	106
5.2.1	Density probes and the ability to observe first and second sound	106
5.2.2	Our experimental protocol for exciting first and second sound	109
5.3	Data analysis and experimental results	112
5.3.1	Excitation spectra	112
5.3.2	f sum rule and the critical temperature	114
5.3.3	First and second sound speeds	116
5.3.4	Dissipation of first and second sound	118
5.3.5	Superfluid fraction and superfluid density	120
5.3.6	Further remarks	121
6	Conclusions and outlook	127

1

Introduction

“In the beginning was the Word.”

— John 1:1

The general framework

The theoretical prediction of a Bose-Einstein condensate (BEC) [1] in 1925 and the observation of dissipationless flow of liquid ^4He [2, 3] in 1938 are considered two milestones in shaping the field of *Quantum Fluids*, a field that has been providing great insights into the quantum many-body problem for almost a century. A quantum fluid is any many-particle system that exhibits both quantum mechanical and quantum statistical behaviour. The former emerges when the de Broglie wavelength of individual particles becomes comparable to their inter-particle distances at low temperatures, at which the statistics of the indistinguishable particles has an effect.

It is then not a surprise that Bose and Fermi quantum fluids, obeying Bose-Einstein and Fermi-Dirac statistics respectively, require a different theoretical treatment on a microscopic level. However, on the macroscopic scale, the single most spectacular feature of the various quantum fluids is their ability to become superfluids, i.e. to show exotic manifestations not expected for classical fluids. Flow without friction in capillaries [2, 3] is probably the most striking behaviour of a superfluid. Other hallmarks include the emergence of irrotational flow [4–6], the existence of metastable persistent currents [7, 8] and a macroscopic tunneling in Josephson junctions [9, 10]. Conceptually, superfluidity is now linked with the existence of an ordered phase, most commonly a BEC, either directly as in the case of Bose fluids, or through a pair formation (Cooper pairs or Bosonic dimers) as in the case of Fermi fluids.

Concentrating on neutral quantum fluids, the first one¹ studied experimentally for its superfluid properties was the Bosonic liquid ^4He . At 2.19K it undergoes a second order phase transition to

¹Other quantum fluids, such as stellar objects (neutron and quark stars) seem to appear in nature, although difficult to be tested in the laboratory. The conduction electron gas in metals can be considered also a quantum fluid, which in this case is charged.

a superfluid state. The other stable helium isotope, the Fermionic ^3He , was found also to support superfluidity [11] with a critical temperature of about 2.6mK, three orders of magnitude lower than ^4He . Helium, in both its stable isotopes, is the only element that remains liquid down to the lowest attainable temperatures, as a consequence of the large zero-point kinetic energy of the atoms. This renders liquid helium a unique system for studying quantum behaviour on a macroscopic scale. Nevertheless, for this strongly-correlated fluid a quantitative microscopic theory, especially for finite temperatures, is not yet satisfying; liquid helium cannot be treated as a perturbation to the non-interacting case where the behaviour is well-understood.

This is not the case for a dilute weakly-interacting quantum gas. Nowadays, gases of ultracold atoms, but also of photons [12] and quasi-particles, like exciton-polaritons [13] and magnons [14], have reached quantum degeneracy in a metastable state². Among the systems above, ultracold gases have gained exceptional attention after the first realisation of a gaseous BEC in ^{87}Rb [15] and ^{23}Na [16] vapour. Since then, gases of various Fermionic and Bosonic isotopes have been cooled to degeneracy: spin-polarised atomic hydrogen [17], alkali atoms [18–25], alkaline earths [26–29], rare earth elements [30–32], and ^{52}Cr [33]. Beyond mono-atomic particles, non-polar [34–36] and recently polar [37] molecules have also been observed in the degenerate regime.

This plethora of available systems is a direct consequence of the way ultracold atomic gases are prepared and manipulated. Their wall-free magnetic or optical confinement provides isolation from the surroundings and a clean environment, free of the ubiquitous impurities of a solid-state system; disorder can, additionally, be introduced in a controlled way for studies of impurity effects. Their diluteness offers, in general, an *ab initio* description of interactions, giving the possibility of quantitative theoretical predictions. The extreme control over nearly all experimental parameters (atomic internal states, interaction strength, trapping geometry, dimensionality) and the intrinsic long time- and length-scales of their dynamics make ultracold gases an ideal platform for numerous studies in the modern fields of phase transitions, strongly-correlated many-body systems, and out-of-equilibrium behaviour.

Indeed, now, around 25 years after the ignition of the field, there is a vast amount of studies on ultracold gases. The thermodynamics of the Bose [38, 39] and Fermi [40, 41] gas in the form of an equation of state is currently, in many cases, well understood. The gas dynamics [6, 42–45] close to equilibrium has also been investigated and many superfluid features [46–49] have been identified. More complex situations, like far-from-equilibrium behaviour and open systems have started to make

²For ultracold gases, one must preserve them in a metastable gaseous phase for sufficient time before the formation of a solid. This is possible at extremely low densities, where the two-body interactions between the particles, responsible for reaching thermal equilibrium, dominate molecular recombination. This low density, though, implies also the need for very low critical temperatures in the ultracold regime. Systems of quasiparticles, on the other hand, cannot reach thermal equilibrium with a non-zero chemical potential, i.e. with a conserved particle number. To overcome this, one should add an external pumping mechanism to compensate relaxation, such that a stationary metastable state emerges with a quasi-conserved number of particles. However, this combination of injection and damping leads to a system that is intrinsically out-of-equilibrium. It is worth mentioning, though, that because of the small mass of the quasi-particles, degeneracy can be reached even at room temperatures, a property that could be exploited for potential applications.

their infant steps in the field. Various phase transitions, quantum and thermal, have been observed and extensively investigated, especially after achieving a precise control of the atomic interactions, by exploiting Feshbach resonances [50]. Among other quantum transitions and crossovers [51–59], the observation of the Mott-to-superfluid transition [60] and the BCS-BEC crossover [61–63] had been long-standing goals that were finally met. In addition, various thermal transitions were identified, like the aforementioned BEC transition in three dimensions and the Berezinskii-Kosterlitz-Thouless (BKT) transition [64] in two dimensions.

This thesis

The case of two-dimensional (2D) systems is of particular interest for understanding superfluidity because of its distinct origin. Unlike their 3D counter-part, 2D superfluids are not associated with a BEC with true long-range order [65, 66], but they rather emerge from the behaviour of existing topological defects, known as vortices. The mechanism behind 2D superfluidity was theoretically explained within the work of Kosterlitz and Thouless [67] and Berezinskii [68], first derived to explain the melting of 2D crystals, but later also applied to other 2D systems (superconductors, magnets, Coulomb plasma etc). The topological transition to BKT superfluidity is characterised as of infinite order, followed by the emergence of quasi-long-range order and it does not involve any spontaneous symmetry breaking or any discontinuity in the thermodynamic quantities; however, a universal jump of the superfluid density at the critical point [69] constitutes one of the main signatures of BKT superfluidity.

This jump has been long observed in thin films of the dense liquid ^4He [70–72] verifying the BKT predictions. In ultracold gases many complementary studies on BKT superfluidity have been conducted [64, 73–82], going even beyond those in liquid helium³ [64, 73, 78], all of which provide good evidence for the applicability of the BKT theory. However, in 2D ultracold gases a direct measurement of the superfluid density is still missing. This can be attributed (partially at least) to the existence of an additional inhomogeneous confinement used for the trapping of the atoms. Unlike helium, customary traps for ultracold gases have been harmonic in space, inducing a position-dependent atomic density and obscuring many phenomena around a phase transition. With the advent of textbook-like box potentials for confining the atoms [83], and also in two dimensions [84–87], there is a renewed interest in measuring the superfluid density in such systems, one of the last standing questions for understanding the (close to) equilibrium behaviour of a 2D Bose gas.

The extraction of the 2D superfluid density is the main topic of this thesis. Various ideas have been proposed for a quantitative measurement of it in a system of ultracold gases [88–91], most of which being an adaptation of the techniques used in liquid helium films. However, new opportunities

³Apart from a direct observation of the underlying mechanisms, the close connection with the theory, and their aptness for control, ultracold gases provide a strong tool for studying superfluidity compared to helium as with the former one can distinguish effects coming from various sources like the substrate, the dynamic nature of the measurements and the finite size of the system. One can also vary at will the various parameters of the gas, a difficult task in helium films. These capabilities can lead to a deeper understanding and maybe even to new physics.

but also new difficulties arise because of the different nature of these experiments compared to those in liquid helium. The remainder of this thesis is devoted to the theoretical understanding of BKT superfluidity and the experimental description of the challenges we faced to extract superfluid density and observe its discontinuity at the critical point.

In the next two chapters, we attempt to clarify the various notions, silently introduced already here, that are related with a superfluid. In Chapter 2, we approach the general concept of superfluidity from various theoretical points of view, ranging from a phenomenological to a fully microscopic treatment. In Chapter 3, we concentrate on a two dimensional system and describe the unique behaviour of BKT superfluidity. Throughout these two chapters, we always keep in mind that we experimentally work with a dilute ultracold gas which allows many conceptual simplifications.

Chapter 4 describes the construction and the characterisation of a newly-built 2D uniform trap of ^{39}K atoms on the ‘ashes’ of a previous experimental setup [92], which serves as the platform for our measurements. ^{39}K is a relatively difficult alkali species to cool down towards degeneracy, mainly due to the lack of separation of its hyperfine states, but it provides us with some broad magnetic Feshbach resonances to finely tune the atomic interaction strength. This opportunity will be proven crucial for the experimental success of this project.

In Chapter 5, we present our experimental studies and show our final results. In short, we realise a proposal [91] that makes use of the existence of two discernible sound perturbations (of the same wavelength) when a superfluid is formed. The first and second sound, as these two modes are widely known, serve as the means for the extraction of the superfluid density. It is worth noticing that second sound has never been observed before in any 2D system, and thus such a measurement has its own weight. The main results discussed in this chapter have been published in: P. Christodoulou, M. Gałka, N. Dogra, R. Lopes, J. Schmitt, and Z. Hadzibabic, Observation of first and second sound in a BKT superfluid, *Nature* 594, 191 (2021).

Finally, in chapter 6 we shortly discuss the various further opportunities that are offered by this newly-built experimental platform.

2

Superfluidity in a Bose gas

“I fear those big words, Stephen said, which make us so unhappy.”

— James Joyce, *Ulysses*

Superfluidity, a term coined [2] in 1938 to accentuate the then-novel observation of frictionless flow of liquid helium in narrow channels, now rather refers collectively to a number of non-classical manifestations of low-temperature matter; the creeping effect [93], the fountain effect [94], the extremely good heat conduction [95], and the preservation of dissipationless currents [7] are examples of such manifestations. Since that first observation in helium, the various phenomena of superfluidity have been extensively studied both theoretically and experimentally.

From a theoretical perspective, primal studies attempted to understand superfluidity on a phenomenological level by exploiting the general tools of hydrodynamics. On a next, semi - phenomenological level, the macroscopic behaviour of superfluidity has been connected with certain microscopic properties, like the notion of elementary excitations¹. On a third level, attempts are made to explain the superfluid properties from a purely microscopic point of view, a task that still remains far from being complete.

In this chapter, we present a theoretical overview of superfluidity. We discuss all three aforementioned levels of description, each of them providing a complementary picture in understanding superfluid behaviour. Preparing for next chapters, we focus our attention on the sound perturbations that may be excited within a superfluid. To set the framework, sound propagation can be classified into two categories in a quantum fluid: collisionless sounds, like the zero sound, emerging from dynamic self-consistent mean fields², and hydrodynamic sounds, like the first and second sounds, where

¹In realistic systems the elementary excitations have not been deduced ab initio but rather extracted from experimental processes; this renders this level of treatment semi-phenomenological.

²We should note that the terminology of zero sound exists also in the collisionless regime of the strongly-interacting liquid helium, but in that case it is more related with mean-field effects arising from the excited atoms rather than a coherent ground state.

collisions between the constituent particles suffice to sustain local equilibrium. Finally, we point out that our discussion remains restricted to a uniform and isotropic fluid.

2.1 A phenomenological treatment

Among its manifestations, the conceptually simplest behaviour that often serves as a definition for a superfluid on a macroscopic level is its unique response to slow rotations. Consider³ a quantum fluid of mass density $\rho = mn$ (m the mass of the particles and n the number density of the fluid) inside a thin annular ring of volume V with a very similar inner and outer radius of its walls ($\approx R$) both of which rotate with extremely small angular velocity Ω . The fluid then, being essentially in equilibrium with the moving walls, is a superfluid at low temperatures T if its total angular momentum $L(T) = f(T)\rho VR^2\Omega$ deviates by a factor $f(T) < 1$ from the classically expected case in which all the constituent particles travel approximately with a velocity ΩR .

To explain this deviation, one may postulate a split of the fluid into two parts, one with a density $\rho_n = \rho f(T)$ that behaves normally with its constituent particles moving with velocity $v_n = \Omega R$, and a second (superfluid) component with a density $\rho_s = \rho[1 - f(T)]$ and velocity $v_s = 0$. For high enough temperatures $f(T) = 1$ and the normal behaviour is restored. In the other limit, for $T \rightarrow 0$ the normal component diminishes ($f \rightarrow 0$) and the whole fluid becomes a superfluid with no rotation at all. Although the fact that $v_s = 0$ is a result for the specific configuration, the description of a superfluid as two interpenetrating components [97, 98], each with its own density and velocity fields, was found to be more general and successful in describing both thermodynamic equilibrium, as above, or small deviations from it.

Such small deviations from equilibrium are typically described within the theory of hydrodynamics. For a distortion of a frequency ω to be close to equilibrium, $1/\omega$ should remain large compared to any relevant timescales in the system; in this case, equilibrium can be at least locally established. Equilibrium is maintained by elastic collisions between the particles in the fluid with a characteristic relaxation time τ . The condition, then, for reaching local equilibrium can be quantified as

$$\omega\tau \ll 1. \tag{2.1}$$

Before discussing the hydrodynamic two-fluid model for a superfluid, we present a short (but essential in the framework of this thesis) reminder of single-fluid hydrodynamics. For both models we omit an extensive derivation and keep only the necessary steps for grasping the physics behind the results. Details of such derivations can be found, for example, in the classical textbooks for the single-fluid [99] and the two-fluid [100] models.

³This hypothetical experiment is very similar to the first experiment conducted by Andronikashvili [96] for the measurement of the normal and superfluid densities in three-dimensional liquid helium.

2.1.1 One-fluid hydrodynamics

When the hydrodynamic condition of Eq. (2.1) is met, one can treat the behaviour of a fluid as a perturbation in its thermodynamic state, and simplify its description with the use of only a small number of (hydrodynamic) variables. These are the densities of quantities that satisfy a conservation law⁴. We then expect for the system to show one low-frequency excitation mode for each hydrodynamic variable.

A single isotropic fluid in d dimensions obeys the following conservation laws:

$$\frac{\partial \rho}{\partial t} + \nabla \mathbf{g} = 0 \quad (2.2)$$

$$\frac{\partial \mathbf{g}}{\partial t} + \nabla p - \frac{\eta}{\rho} \nabla^2 \mathbf{g} - \frac{1}{\rho} \left(\zeta + \frac{1}{d} \eta \right) \nabla (\nabla \mathbf{g}) = 0 \quad (2.3)$$

$$\frac{\partial \epsilon}{\partial t} + \nabla [(\epsilon + p) \mathbf{v} - \kappa \nabla T] = 0 \quad (2.4)$$

The first equation expresses the conservation of particles and connects the mass density ρ with the mass current which is nothing but the momentum density $\mathbf{g} = \rho \mathbf{v}$, with \mathbf{v} the velocity field of the fluid. The second equation, a generalised Euler's equation, is an expression of Newton's second law with the net force arising from both spatial (longitudinal) variations in pressure p and viscous stresses which act as sources of momentum. There are two coefficients of viscosity in a single fluid: shear viscosity η arising from momentum exchange due to atomic motion, and bulk viscosity ζ that connects the colliding atoms with internal degrees of freedom. Finally, the third equation represents the energy conservation in the presence of dissipation. Here ϵ is the energy density, κ the thermal conductivity and T the temperature of the fluid. The term $\epsilon \mathbf{v}$ corresponds to the internal energy, while the term $p \mathbf{v}$ to the work done on the fluid.

The energy and mass conservation together with conservation of the three components of the momentum lead to five hydrodynamic modes. We restrict ourselves to the case of small deviations $\delta X(r, t)$ from the equilibrium value $X_0(r)$, i.e. $X(r, t) = X_0(r) + \delta X(r, t)$, for the relevant quantities entering the above equations, $X = \{\rho, p, \mathbf{g}, \epsilon, \dots\}$. In the absence of any coupling, all five modes would be expected to satisfy a diffusion equation. This is, indeed, the case for the two transverse components of momentum g_t , where from Eq. (2.3) one gets $\frac{\partial \delta g_t}{\partial t} = \frac{\eta}{\rho} \nabla^2 \delta g_t$.

However, the coupling of Eqs. (2.2) and (2.3) through the longitudinal momentum density, and of Eq. (2.4) through the velocity field results in the following set of closed equations for the small

⁴Such quantities, unlike other degrees of freedom that decay to zero on timescales of the order of τ , are characterised by slow temporal variations at long wavelengths; this can be easily seen by Fourier-transforming a conservation law, for example Eq. (2.2), in time and space and identify that time diverges ($\omega \rightarrow 0$) when the system approaches equilibrium ($q \rightarrow 0$).

fluctuations $\delta X = \{\delta\rho, \delta s\}$

$$\frac{\partial^2 \delta\rho}{\partial t^2} = \frac{1}{\rho} \left(\frac{d+1}{d} \eta + \zeta \right) \frac{\partial}{\partial t} \nabla^2 \delta\rho + \left(\frac{\partial p}{\partial \rho} \right)_s \nabla^2 \delta\rho + \left(\frac{\partial p}{\partial s} \right)_\rho \nabla^2 \delta s \quad (2.5)$$

$$\frac{\partial \delta s}{\partial t} = \frac{\kappa}{T\rho} \left(\frac{\partial T}{\partial \rho} \right)_s \nabla^2 \delta\rho - \frac{\kappa}{T\rho} \left(\frac{\partial T}{\partial s} \right)_\rho \nabla^2 \delta s. \quad (2.6)$$

Here we replaced, as commonly practiced, the energy density with the entropy per unit mass s through the thermodynamic relation $T\rho ds = d\epsilon - \frac{(\epsilon+p)}{\rho} d\rho$. By simply inspecting Eqs. (2.5) - (2.6), one anticipates the existence of a diffusive mode for the entropy (heat mode) and a sound propagation for the density. The latter becomes obvious in the absence of dissipation (η , ζ and κ being zero) where the above equations reduce to

$$\frac{\partial^2 \delta\rho}{\partial t^2} = \left(\frac{\partial p}{\partial \rho} \right)_s \nabla^2 \delta\rho \quad (2.7)$$

$$\frac{\partial \delta s}{\partial t} = 0 \quad (2.8)$$

with the density sound mode propagating at a speed $c_{10} = \sqrt{\left(\frac{\partial p}{\partial \rho} \right)_s}$. This mode is usually called first sound in the literature.

When dissipation is considered, the diffusive heat mode that appears is characterised by the diffusivity

$$D_T = \frac{\kappa}{\rho c_p}. \quad (2.9)$$

Additionally, first sound gets also attenuated with a damping rate $\Gamma_{10} = D_{10}q^2$, where [99, 101]

$$D_{10} = \frac{1}{\rho} \left(\frac{d+1}{d} \eta + \zeta \right) + \frac{\kappa}{\rho c_p} (\gamma - 1) \quad (2.10)$$

is the so-called sound diffusivity and q the sound's wavenumber. The second term in D_{10} depends directly on $\gamma = c_p/c_v$, the ratio of the heat capacities per unit mass, $c_{p,v} = T(ds/dT)_{p,V}$, under constant pressure and under constant volume V , respectively. By using simple and general thermodynamic arguments, we can also write $\gamma = \kappa_T/\kappa_s$, with $\kappa_{T,s} = -\frac{1}{\rho} \left(\frac{\partial \rho}{\partial p} \right)_{T,s}$ the isothermal (subscript T) and isentropic (subscript s) compressibility of the fluid. The quantity γ will play an important role throughout this thesis and we discuss it more in the next section.

2.1.2 Two-fluid hydrodynamics

We now turn our attention to the case of a superfluid. As already discussed, a good model to catch the basic physics of a superfluid is its separation into two components, the normal and the

superfluid, with their densities, $\rho_n = mn_n$ and $\rho_s = mn_s$ respectively, satisfying

$$\rho = \rho_s + \rho_n. \quad (2.11)$$

for the total mass density $\rho = mn$. It is important to note that neither of these components satisfies a continuity equation alone and particles can interchange between the two fluids. Similar to the one-fluid case, our starting point is the proper extraction of the underlying conservation laws. In order to keep a clear intuition for the modifications from the one-fluid case, we first restrict ourselves to a dissipationless situation. Later on, we discuss about those physical effects that appear when dissipation is included.

The conservation relations characterising a two-fluid system are:

$$\frac{\partial \rho}{\partial t} + \nabla g = 0, \quad (2.12)$$

$$\frac{\partial g}{\partial t} + \nabla p = 0, \quad (2.13)$$

$$\frac{\partial s}{\partial t} + \nabla(sv_n) = 0. \quad (2.14)$$

Eqs. (2.12) and (2.13) for the mass and the momentum conservation have the same form as the corresponding Eqs. (2.2) and (2.3) for a single fluid; here the total current density is $g = \rho_n v_n + \rho_s v_s$. Unlike the first two equations, where both components contribute to the corresponding currents, Eq. (2.14) states that only the normal component carries entropy. For the complete description of the two-fluid model, in the above set of equations one needs to add the irrotational character of the superfluid motion

$$\nabla \times v_s = 0. \quad (2.15)$$

We next determine the small amplitude modes of the model described by Eq. (2.12) - Eq. (2.15), in the same spirit as in Sec. 2.1.1. Following Khalatnikov's treatment [100], the linearised version of the two-fluid system gives:

$$\frac{\partial^2 \delta \rho}{\partial t^2} = \left(\frac{\partial p}{\partial \rho} \right)_s \nabla^2 \delta \rho + \left(\frac{\partial p}{\partial s} \right)_\rho \nabla^2 \delta s, \quad (2.16)$$

$$\frac{\partial^2 \delta s}{\partial t^2} = \frac{s^2 \rho_s}{\rho_n} \left(\frac{\partial T}{\partial \rho} \right)_s \nabla^2 \delta \rho + \frac{s^2 \rho_s}{\rho_n} \left(\frac{\partial T}{\partial s} \right)_\rho \nabla^2 \delta s. \quad (2.17)$$

Comparing this set of equations with the corresponding set of Eqs. (2.7) - (2.8) for the one-fluid case, we now observe the existence of an additional sound mode, known as second sound. Even from Eq. (2.17) it becomes apparent that it is the coupling of the heat to the superfluid density ρ_s that converts energy diffusion into a sound mode. With an assumption of harmonic fluctuations in time

t and space⁵ y ($\delta\rho, \delta s \propto e^{-j(\omega t - qy)}$), the velocities of first and second sound $c = \omega/q$ are eventually found to satisfy the following Landau's quartic equation

$$c^4 - (c_{10}^2 + c_{20}^2)c^2 + c_{10}^2 c_{20}^2 / \gamma = 0 \quad (2.18)$$

where $c_{10}^2 = \left(\frac{\partial p}{\partial \rho}\right)_s = \frac{1}{\rho \kappa_s}$ and $c_{20}^2 = \frac{\rho_s T s^2}{\rho_n c_v}$ are quantities determined from thermodynamics. The solution of the previous equation gives the speeds for first (c_1) and second (c_2) sound

$$c_{1,2}^2 = \frac{c_{10}^2 + c_{20}^2 \pm \sqrt{(c_{10}^2 - c_{20}^2)^2 + \Delta}}{2}, \quad (2.19)$$

with $\Delta = 4c_{10}^2 c_{20}^2 (\gamma - 1) / \gamma$. In the above, following literature, first sound is defined as the mode with the higher velocity.

The nature of first and second sound

We first inspect the terms $\left(\frac{\partial p}{\partial s}\right)_\rho$ and $\left(\frac{\partial T}{\partial \rho}\right)_s$ that couple $\delta\rho$ and δs in the two-fluid model (Eqs. (2.16) - (2.17)), and also in the dissipational single fluid (Eqs. (2.5) - (2.6)). Using Maxwell relations and the general thermodynamic identity [102]

$$c_p - c_v = \frac{T a_T^2}{\rho \kappa_T}, \quad (2.20)$$

one can find that $\left(\frac{\partial p}{\partial s}\right)_\rho$ and $\left(\frac{\partial T}{\partial \rho}\right)_s$ are equal and proportional to $\gamma - 1$. In the above, $a_T = -\frac{1}{\rho} \left(\frac{\partial \rho}{\partial T}\right)_p$ is the thermal expansion coefficient of the fluid. It is then not a surprise (actually part of the derivation process) that both sound speeds in a superfluid, and also the damping rate of the sound in a normal gas depend on this mixing quantity⁶ $\gamma - 1$.

In order to investigate the nature of first and second sound, we first notice that for a perfectly incompressible fluid ($\kappa_T = 0$), the quantity $c_p - c_v$ in Eq. (2.20) unphysically diverges unless a_T becomes zero. Since $a_T / \kappa_T = (\partial p / \partial T)_\rho$ has to remain finite, it turns out that $c_p = c_v$ or equivalently an incompressible fluid is characterised by $\gamma - 1 = 0$. In this case, no coupling is present and first and second sound are pure density and entropy waves, respectively, with $c_1 = c_{10}$ and $c_2 = c_{20}$, as found from Eq. (2.19). Any local excess of superfluid density would result in local excess of the normal component at another point of space and thus to temperature differences. Since first sound does not contain any such temperature differences, the two components of the superfluid have to fluctuate in-phase with the same velocity, $v_s = v_n$. Similarly, for second sound there is no density change, so the total density current $g = v_s \rho_s + v_n \rho_n$ should be zero; second sound is an out-of-phase propagation of the normal and the superfluid components with $v_s / v_n = -\rho_n / \rho_s$. In practice, liquid helium and also unitary Fermi gases are well-considered to be incompressible fluids.

⁵Here and in the rest of this thesis j denotes the imaginary unit.

⁶In studies of Fermi gases this parameter is often referred to as the Landau - Placzek ratio.

The situation is very different for a non-zero a_T (and κ_T), where one finds⁷ $\gamma > 1$. Although not obvious from the results presented until now, in the case of a large a_T , the first sound becomes mainly an oscillation of the normal component and second sound an oscillation of the superfluid component [103]. The weak oscillations of the complementary components in each sound mode follow the previous prescription to keep first sound an in-phase and second sound an out-of-phase oscillation [103]. The non-zero $\gamma - 1$ has important consequences also for a single fluid (like a degenerate gas above the critical superfluid temperature), since it allows the coupling of the damped heat mode with density. In reality, weakly-interacting dilute Bose gases are a good example of such compressible fluids with an important mixing of density and entropy fluctuations in both first and second sound.

Finally, we note that from Eq. (2.20), even if $a_T, \kappa_T \neq 0$, at $T = 0$ all fluids behave like incompressible ($\gamma = 1$). In the other limit, at high temperatures, a classical treatment for a monoatomic ideal gas gives $\gamma = (d + 2)/d$, which for our relevant 2D case in the next chapters becomes $\gamma = 2$.

2.1.3 Density response to an external probe

In experiments with ultracold gases, where entropy oscillations are difficult to observe⁸, the most efficient way of studying the dynamics of the gas is through density fluctuations. The coupling of second sound with density fluctuations in compressible fluids offers a great opportunity for its detection and further investigation. Here, we focus on the density response of a superfluid to some external perturbation. Generally, there are two different approaches for characterising such a response. On a purely experimental level, the emerging quantity of interest is the dynamic structure factor, whereas starting from a more theoretical perspective it is the density response function that contains all the information we need. These two quantities, connected through the dissipation - fluctuation theorem, will be discussed here, first from a more general point of view and afterwards in the framework of the one- and two-fluid models. They will play a crucial role in our experimental work as described in the next chapters.

Density response function

A straightforward way to study density fluctuations is to observe the effects of applying some external-potential perturbation $\delta U(r, t)$. When this perturbation is small, within the linear response theory, the density fluctuation $\delta n(r, t)$ becomes

$$\delta n(r, t) = \int \frac{dq}{(2\pi)^d} \int \frac{d\omega}{2\pi} \chi(q, \omega) \delta U(q, \omega) e^{j(qr - \omega t)} \quad (2.21)$$

⁷Physically, this inequality expresses the fact that one needs to put more energy into a system that is able to expand ($c_p = (dW + pdV)/dT$ with dW the added energy to the fluid) compared to an isochoric process ($c_v = dW/dT$) for the same increase in temperature.

⁸A recent attempt has been publicly reported from the group of M. Zwierlein.

or equivalently $\delta n(q, \omega) = \chi(q, \omega)\delta U(q, \omega)$ for the Fourier components $\delta n(q, \omega)$ and $\delta U(q, \omega)$ of the density and the perturbing potential, respectively. The function $\chi(q, \omega)$ that connects δn and δU is known as the density response function. It does not depend on the external perturbation but only on the intrinsic properties of the system and can be used for its characterisation.

The response function is in general a complex function, i.e. $\chi(q, \omega) = \text{Re}\chi(q, \omega) + j\text{Im}\chi(q, \omega)$. Its imaginary part can be expressed as

$$\text{Im}\chi(\omega) = -\frac{j}{2}[\chi(\omega) - \chi^*(\omega)] = -\frac{j}{2} \int_{-\infty}^{+\infty} dt \chi(t) [e^{j\omega t} - e^{-j\omega t}] \quad (2.22)$$

for any q , with $\chi(t)$ the Fourier transform of $\chi(\omega)$, from which one observes that $\text{Im}\chi(\omega)$ is an odd function of ω . Re-expressing Eq. (2.22) as $\text{Im}\chi(\omega) = -\frac{j}{2} \int_{-\infty}^{+\infty} dt e^{j\omega t} [\chi(t) - \chi(-t)]$, it reveals that $\text{Im}\chi(\omega)$ is not invariant under time reversal $t \rightarrow -t$; $\text{Im}\chi$ is related to dissipation. The energy absorbed by the system during the perturbation is [104]

$$\Delta E = \int_{-\infty}^{\infty} d\omega \omega \text{Im}\chi(\omega) |F(\omega)|^2, \quad (2.23)$$

with $F(\omega)$ the Fourier transform of the force $F(t) = -\nabla_r \delta U(t)$. For spectroscopic measurements with a monochromatic $F(\omega) = F_0 \delta(\omega - \omega_0)$, the absorbed energy is $\Delta E \propto \omega_0 \text{Im}\chi(\omega_0)$.

Dynamic Structure factor

Experimentally, a widely-spread method to extract the density response of a system consists of using inelastically-scattered external particles⁹ which transfer momentum q and energy ω to the system. It has long been found [105] that the differential cross-section per unit solid angle Ω and unit energy E of such a scattering process

$$\frac{d\sigma}{d\Omega dE} = W_{\text{sc}} \cdot S(q, \omega) \quad (2.24)$$

can be separated into two parts. The first part, W_{sc} , depends on the actual interaction details between the probed and the probing particles. The second part, $S(q, \omega)$, known as the dynamic structure factor, is the Fourier transform in space and time of the time-dependent pair correlation function

$$C_{nn}(r, t) = \langle n(r, t)n(0, 0) \rangle \quad (2.25)$$

where $\langle \dots \rangle$ signifies an average with respect to an equilibrium ensemble. $C_{nn}(r, t)$ describes the probability of finding a particle of the system in position r at time t if another lies at $r = 0$ at $t = 0$; $S(q, \omega)$ then depends only on the intrinsic spatial and temporal properties of the system, and thus

⁹The appropriate particles for each system depend on the inter-particle distance in the system and the wavelength of the particles. In this way, neutron scattering for liquid helium and light scattering for dilute ultracold gases are the most common techniques.

it becomes a valuable tool for characterising the system's fluctuations.

The integration of $S(q, \omega)$ over all energy transfers

$$S(q) = \int_{-\infty}^{+\infty} S(q, \omega) d\omega \quad (2.26)$$

corresponds to the static correlation function $C_{nn}(r, t = 0)$ which gives information about the instant spatial distribution of the particles, rather than dynamic properties of the system. The dimensionless quantity $S(q)$ thus is called the static structure factor and has historically played an important role in studying excitations¹⁰.

In a more technical language, $S(q)$ is the zeroth moment of the dynamic structure factor. Its first-order moment has also been proven to be an important test for the credibility of experimental results, since it is found to be

$$\int_{-\infty}^{+\infty} \omega S(q, \omega) d\omega = \frac{\hbar q^2}{2m}. \quad (2.27)$$

Eq. 2.27 is often also called the f sum rule or the energy-weighted sum rule. The validity of Eq. (2.27) is quite general as long as the forces between the particles are not velocity-dependent. The derivation and the physical meaning of the above relation will become straightforward with the introduction of the notion of elementary excitations, so we postpone this discussion for the next section.

Fluctuation - Dissipation theorem

On one hand, $\text{Im}\chi(q, \omega)$ is linked to the absorption of energy by the system when perturbed by an external potential. On the other hand, $S(q, \omega)$ is a measure of the density fluctuations of the same system as it scatters incoming particles. Since they both characterise the intrinsic properties of the fluid, one expects to find a connection between these two quantities. Indeed, such a connection exists, as first discussed in Ref. [107] and has taken the figurative name of the fluctuation-dissipation relation

$$S(q, \omega) = -\frac{1}{\pi n} [N^0(\omega) + 1] \text{Im}\chi(q, \omega), \quad (2.28)$$

where $N^0(\omega) = (e^{\hbar\omega/k_B T} + 1)^{-1}$ is the Bose distribution function and k_B the Boltzmann's constant. The factor $[N^0(\omega) + 1]$ represents both thermal (through the first term) and quantum (through the second term) fluctuations.

For low energies compared to the thermal energy ($\hbar\omega \ll k_B T$), one can approximate $[N^0(\omega) + 1] \approx \frac{k_B T}{\hbar\omega} + \frac{1}{2}$. The first term is much larger than the second, and therefore the dynamic structure factor can be practically approximated by

$$S(q, \omega) \approx -\frac{k_B T}{\pi n} \frac{\text{Im}\chi(q, \omega)}{\omega} \quad (2.29)$$

¹⁰ $S(q)$ remains the only available experimental quantity when the energy transfer from scattering is much larger than the typical energies of the excited modes, as with x-ray scattering in liquid helium [106].

The second term of $1/2$, though, becomes necessary to satisfy the resultant f sum rule of Eq. (2.27) when expressed via $\text{Im}\chi$, since the latter is an odd-function of ω so its even moments are zero. With the use of the fluctuation-dissipation relation, the f sum rule is expressed in terms of the response function as

$$\int_{-\infty}^{\infty} d\omega \omega \text{Im}\chi(q, \omega) = -\frac{\pi n q^2}{m}. \quad (2.30)$$

Response within the hydrodynamic one- and two-fluid models

Having discussed about the general properties of $\chi(q, \omega)$ and $S(q, \omega)$, we now concentrate on their specific forms within the one- and two-fluid models. We note that these quantities do not provide any new information that is not contained in the linearised results of Sec. 2.1.1 and 2.1.2. Their advantage is their simplicity and the direct access to experimental observations.

One-fluid response. The methodology for obtaining the density response from hydrodynamic equations can be conveniently sketched for the simplest case of a single dissipationless fluid. The addition of the effect of an external perturbing potential in the relevant equation Eq. (2.7) yields [108]

$$\frac{\partial^2 \delta\rho(r, t)}{\partial t^2} = c_{10}^2 \nabla^2 \delta\rho(r, t) + n \nabla^2 \delta U(r, t) \quad (2.31)$$

By Fourier-transforming Eq. (2.31) in both space and time one directly gets the response function

$$\chi_1(q, \omega) = \frac{\delta\rho(q, \omega)/m}{\delta U(q, \omega)} = \frac{nq^2/m}{\omega^2 - c_{10}^2 q^2}. \quad (2.32)$$

Its imaginary part is extracted after the replacement $\omega^2 - c_{10}^2 q^2 \rightarrow \omega^2 - c_{10}^2 q^2 + j\eta$ in χ_1 , where the small parameter η is set in the end to zero to find $\text{Im}\chi_1(q, \omega) = \frac{\pi n q}{2m c_{10}} [\delta(\omega + c_{10}q) - \delta(\omega - c_{10}q)]$, two Dirac δ -peaks at $\omega = \pm c_{10}q$.

Following the same strategy, one deduces the density response for the single fluid when dissipation is present [99, 109]. Its experimentally relevant imaginary part can be well approximated by [101]

$$\text{Im}\chi_1(q, \omega) \approx \frac{(nq^2/m)\Gamma_{10}\omega}{(\omega^2 - c_{10}^2 q^2)^2 + (\Gamma_{10}\omega)^2} - (\gamma - 1) \frac{1}{m c_{10}^2} \frac{\omega D_T q^2}{\omega^2 + (D_T q^2)^2} \quad (2.33)$$

in which two additional features emerge compared to the dissipationless case. First, the sound δ -peaks are broadened by Γ_{10} as given by Eq. (2.10) and second, a diffusive component from the coupling with the heat makes its appearance; by reconstructing the dynamic structure factor $S_1(q, \omega) \propto \text{Im}\chi_1(q, \omega)/\omega$ from Eq. (2.29), this diffusive part becomes clear as an additional peak, centered at $\omega = 0$. It is worth noting that starting from this dissipational $S_1(q, \omega)$ and taking the limits Γ_{10} and

$D_T \rightarrow 0$, one finds [110]

$$S_1(q, \omega) = \frac{k_B T}{2mc^2} [\delta(\omega + cq) + \delta(\omega - cq) + (\gamma - 1)\delta(\omega)] \quad (2.34)$$

which allows for a heuristical study of the effects of heat diffusion even within a dissipationless model. With or without dissipation, the relative importance of this diffusive mode in $S_1(q, \omega)$ is approximated by the coupling parameter $\gamma - 1$.

Two-fluid response. In essence, there is nothing new in the treatment of extracting the two-fluid response compared to the single-fluid case. The dissipational two-fluid response was first calculated by Hohenberg and Martin [109] with the final result being

$$\chi_2(q, \omega) = \frac{(nq^2/m)(\omega^2 - c_{20}^2 q^2 + j\Gamma_s \omega)}{(\omega^2 - c_1^2 q^2 + j\Gamma_1 \omega)(\omega^2 - c_2^2 q^2 + j\Gamma_2 \omega)} \quad (2.35)$$

In this case, two distinct poles appear corresponding to first and second sound, with speeds c_1 and c_2 , respectively, as given by Eq. (2.19). The additional information compared to our previous discussion about the two-fluid model is the presence of the sound dissipations $\Gamma_{1,2} = D_{1,2} q^2$ together with the parameter $q^2 \Gamma_s = \frac{1}{\rho} \left(\frac{d+1}{d} \frac{\rho_s}{\rho_n} \eta + \frac{\kappa}{c_v} \right)$. The first and second sound damping rates satisfy¹¹

$$D_1 + D_2 = \frac{1}{\rho} \left(\frac{d+1}{d} \eta + \frac{\kappa}{c_v} \right) \quad \text{and} \quad c_1^2 D_2 + c_2^2 D_1 = \frac{c_{10}^2}{\rho} \left[\frac{d+1}{d} \eta \left(\frac{c_{20}^2}{c_{10}^2} - \frac{2c_{20}^2 (\partial p / \partial T)_\rho}{\rho s c_{20}^2} \right) + \frac{\kappa}{c_p} \right]. \quad (2.36)$$

By setting all the damping terms to zero in Eq. (2.35), we deduce the dissipationless version of the two-fluid model, yielding

$$\begin{aligned} \chi_2(q, \omega) &= \frac{(nq^2/m)(\omega^2 - c_{20}^2 q^2)}{(\omega^2 - c_1^2 q^2)(\omega^2 - c_2^2 q^2)} \\ &= \frac{nq^2}{m} \left[\frac{Z_1}{\omega^2 - c_1^2 q^2} + \frac{Z_2}{\omega^2 - c_2^2 q^2} \right], \end{aligned} \quad (2.37)$$

with $Z_1 = (c_1^2 - c_{20}^2)/(c_1^2 - c_2^2)$ and $Z_2 = (c_{20}^2 - c_2^2)/(c_1^2 - c_2^2)$. The absorptive part of the response comprises two pairs of δ -peaks

$$\text{Im} \chi_2(q, \omega) = \frac{\pi n q^2}{m} \left[\frac{Z_1}{c_1 q} \{ \delta(\omega + c_1 q) - \delta(\omega - c_1 q) \} + \frac{Z_2}{c_2 q} \{ \delta(\omega + c_2 q) - \delta(\omega - c_2 q) \} \right]. \quad (2.38)$$

The comparison with Eq. (2.34), relevant in the absence of superfluidity, allows a description in which second sound is converted into a heat diffusive mode at the critical point for the superfluid

¹¹These formulas neglect the effects from the four different bulk viscosities present in superfluid, as first introduced by Landau [111], which are expected to be either zero or small for a scale invariant system [112], as the one we study in next chapters. The more general formulas including the bulk viscosities are given in [109].

transition. Also, from the fact that $Z_1 + Z_2 = 1$, the f sum rule (Eq. (2.30)) is satisfied. Finally, we verify using Eq. (2.37) (in its top version) that for an incompressible fluid with $\gamma = 1$ where $c_2 = c_{20}$, only the first mode couples to density perturbations.

2.2 A semi-phenomenological treatment

Superfluidity and elementary excitations

The two-fluid model, as described in the previous section, makes no connection with a more fundamental understanding of superfluidity; it simply associates the macroscopic densities ρ_s and ρ_n with the various thermodynamic and transport quantities. A quantitative connection with more microscopic properties of the superfluid was initiated with the work of Landau and the introduction of the concept of elementary excitations with a well-defined momentum q and energy $\omega_q = \omega(q)$. A superfluid then can be conceived as the combination of its ground state and a weakly-interacting gas of elementary excitations characterised by a dispersion relation ω_q .

The form of the excitation spectrum helps to check if a system can manifest superfluidity¹². To understand that, we consider for simplicity a fluid at $T = 0$ in its ground state moving with velocity \mathbf{v}_s with respect to the lab frame. Superfluidity is connected with the absence of viscosity and thus with the inability to generate elementary excitations. If such an excitation occurs, the total energy of the fluid changes by $\Delta E = \hbar(\omega_q + \mathbf{q} \cdot \mathbf{v}_s)$, with \mathbf{q} its momentum vector of magnitude q . Due to dissipation this excitation should lead to $\Delta E < 0$, feasible only if $\omega_q - qv_s$ is negative; such an excitation cannot then occur for velocities lower than a critical value¹³

$$v_c = \min_q \frac{\omega_q}{q} = \min_q \frac{d\omega_q}{dq}. \quad (2.39)$$

In other words, if $v_c > 0$ the system is a superfluid.

In Fig. 2.1 we show qualitatively three different cases of excitation spectra together with the extracted critical velocities. In (a) the spectrum of a normal fluid characterised by $\omega_q \propto q^2$ leads to a zero v_c and the absence of superfluid behaviour. Since such a dispersion describes also an ideal gas at any temperature, one concludes that the latter is not a superfluid at any non-zero temperature. Contrary, for a superfluid, as in (b) and (c), the spectrum is modified from the ideal gas case to a phononic dispersion $\omega_q = cq$ for long wavelengths, with c the phonon speed, which leads to a finite critical velocity with an upper bound $v_c \leq c$.

The picture of elementary excitations on top of the ground state becomes extremely fruitful when collisions between these excitations are frequent enough to establish equilibrium. This regime corre-

¹²The discussion here pertains mainly to the effects rather than the cause of superfluidity, since we neglect looking into the ground state, which is in the end responsible for the spectrum of excitations. Such an investigation is feasible only within the microscopic treatment of next section.

¹³The initial assumption of $T = 0$ is not restrictive. For a finite temperature there will be already some excitations in the system, but new excitations from the ground state will be forbidden under the same conditions.

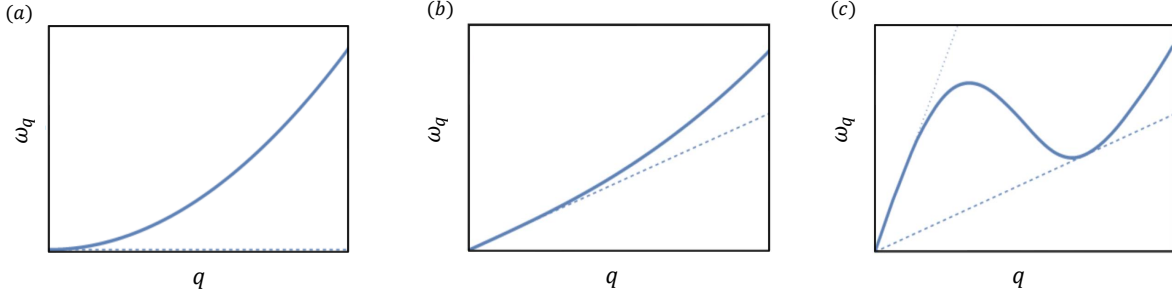


Figure 2.1: A qualitative dispersion relation of the elementary excitations in three different cases: (a) of an ideal gas or a normal fluid above the superfluid critical temperature, (b) of a superfluid gas and (c) of superfluid liquid. For the case (a) the typical dispersion is $\omega_q \propto q^2$ whereas the long-wavelength limit of a superfluid, whether a gas or a liquid, is characterised by a phononic dispersion $\omega_q \propto q$. The dashed lines indicate the minimum slope of the spectrum giving access to the critical velocity for superfluidity. The spectrum in a quantum gas, as in case (b), was first measured in Ref. [113], whereas an overview of the corresponding measurements in liquid helium, as in case (c), can be found in Ref. [106].

sponds to the hydrodynamic behaviour discussed in the previous section, where now the condition $\omega_q \tau \ll 1$ pertains to the relation between the excitations' energy ω_q and lifetime τ due to collisions. Connecting with the two-fluid model, the background gas is identified as the superfluid component ρ_s and the gas of thermally-excited elementary excitations as the normal component ρ_n . The normal density can then be calculated with the use of the equilibrium distribution of the Bose excitations with the final result (see for example Ref. [114] for the 3D and Ref. [115] for the 2D case)

$$\rho_n = \frac{1}{d} \frac{1}{k_B T} \int \frac{d^d q}{(2\pi)^d} \frac{(\hbar q)^2 e^{\hbar \omega_q / k_B T}}{(e^{\hbar \omega_q / k_B T} - 1)^2}. \quad (2.40)$$

It becomes then clear that with the knowledge of the dispersion relation of a superfluid, one can predict the normal and superfluid ($\rho_s = \rho - \rho_n$) densities. In addition, as the ground state does not carry any entropy, it is also clear that it is the distribution of the excitations that determines the thermodynamics of the fluid.

A theoretical deduction of ω_q is, in most cases, a difficult task and experimental results have been used throughout the years to extract approximations of this spectrum. A situation where a theoretical treatment should be applicable is for studying the limit $T \rightarrow 0$. In this case, the only occupied excitations are the long-wavelength ones and the adoption of a phononic spectrum $\omega_q = cq$ is quite precise. By calculating the normal density from Eq. (2.40) and the thermodynamic quantities that enter Eq. (2.19) using this phononic dispersion, one finally finds [114] that first and second sounds satisfy $c_1 = c$ and $c_2 = c/\sqrt{d}$. However, this result has to be treated with care and two notes are worth being mentioned. First, since the existence of two sounds is the consequence of two different components, one has to think of the above result as the limit of very low temperatures and not at the absolute $T = 0$. Second, the excitation of first and second sound relies on hydrodynamic conditions secured by collisions between the excitations. As temperature is decreased, the number

of excitations vanishes, hinting at a departure from the hydrodynamic regime.

Although extremely helpful for a quantitative description of various experimental results, elementary excitations in the spirit introduced by Landau, do not provide a deeper connection with the microscopic mechanisms which lead to superfluid behavior.

2.3 A microscopic treatment

In 1938, F. London linked superfluidity with a BEC of an ideal gas. Together with L. Tisza, they attempted to identify the superfluid fraction ρ_s/ρ with a theoretically deduced condensed fraction n_0/n . We now know that this is not generally true. As already discussed, the archetype ideal Bose gas does not manifest superfluidity at $T \neq 0$. In the other limit of the strongly-interacting liquid helium, the condensed fraction is calculated [116] and measured [117–119] not to exceed a value of 10% even at extremely low temperatures where the whole fluid becomes a superfluid. This distinction is more dramatic in two-dimensions where BEC is forbidden in the thermodynamic limit, and yet a Bose fluid behaves as a superfluid at low temperatures. Before we concentrate on this 2D-exception, here we discuss the basic aspects of a connection between superfluidity and BEC having as a goal the introduction of various useful concepts.

The starting point for a microscopic investigation of superfluidity is the Hamiltonian of a cold Bose fluid of N interacting particles being in the same internal state

$$\begin{aligned} \hat{H} = & \int d^3r \hat{\psi}^\dagger(r) \left(-\frac{\hbar^2 \nabla^2}{2m} - \mu \right) \hat{\psi}(r) + \frac{1}{2!} \int d^3r d^3r' \hat{\psi}^\dagger(r) \hat{\psi}^\dagger(r') V_2(r, r') \hat{\psi}(r') \hat{\psi}(r) \\ & + \frac{1}{3!} \int d^3r d^3r' d^3r'' \hat{\psi}^\dagger(r) \hat{\psi}^\dagger(r') \hat{\psi}^\dagger(r'') V_3(r, r', r'') \hat{\psi}(r) \hat{\psi}(r') \hat{\psi}(r'') + \dots \end{aligned} \quad (2.41)$$

Here the field operators $\hat{\psi}^\dagger(r)$ and $\hat{\psi}(r)$ create and annihilate respectively a particle at position r obeying the typical Bose commutative relations¹⁴ $[\hat{\psi}(r), \hat{\psi}^\dagger(r')] = \delta(r - r')$ and $[\hat{\psi}(r), \hat{\psi}(r')] = 0$, and μ is the chemical potential. The first term in the Hamiltonian represents the kinetic energy of the gas, the second term describes two-body interactions through the pair-potential V_2 , the third describes three-body interactions through V_3 . Terms of higher order are not common in the literature, and for a dilute gas their absence is fully justified.

A simplification of the above Hamiltonian, appropriate for the dilute and weakly interacting ultracold gases, will facilitate the direct connection between a BEC and superfluidity.

2.3.1 Interactions in a dilute Bose gas

Two-body interactions. In the absence of long-range dipole-dipole interactions, a typical two-body potential is of a Lennard-Jones type, $V_2(r) = C_{12}/r^{12} - C_6/r^6$, which captures quite well both

¹⁴ $[A, B] = AB - BA$

the longer-range van der Waals attraction ($\sim r^{-6}$) and the short-range repulsion at an inter-atomic distance r . For degenerate ultracold gases, the effective range¹⁵ of V_2 ($\sim 10^2 a_0$, with a_0 the Bohr radius) is about two orders of magnitude shorter than typical inter-atomic separations, and thus we are permitted to treat two-body interactions like point-like collisions within scattering theory. Scattering may alter the external and/or the internal degrees of freedom of the two participating atoms. The internal degrees (e.g. hyperfine states) of the two colliding atoms are labeled as a scattering ‘channel’. A collision is elastic when the atoms remain in the same channel before and after the event. For atoms prepared in their lowest internal state, the colliding atoms have no chance to change channel unless a third atom is involved. We thus start our discussion with the two-body single-channel problem. For reasons that will become obvious later, we restrict ourselves to the specific case of collisions in three dimensions.

The single-channel problem is equivalent to that of a moving particle of mass $m^* = m/2$ in a static potential $V_2(\mathbf{r})$. In general, scattering states with a positive energy and bound states with a negative energy exist. A scattering state with an energy $E = \hbar^2 k^2 / 2m^*$, (\mathbf{k} being the relative momentum of the two atoms of magnitude k) is characterised by a wavefunction ψ_{rel} , the asymptotic ($r \gg r_0$) behaviour of which becomes within the first Born approximation (see for example [121, 122])

$$\psi_{\text{rel}}(r) = e^{i\mathbf{k}\cdot\mathbf{r}} - \left(\frac{m}{4\pi\hbar^2} \int d^3r' V_2(\mathbf{r}') e^{-i\mathbf{q}\cdot\mathbf{r}'} \right) \frac{e^{ikr}}{r}. \quad (2.42)$$

This result is often interpreted as the sum of the incoming (first term) and a scattered (second term) wave, where the amplitude of the scattering in the parenthesis is proportional to the Fourier transform of the interaction potential. Here \mathbf{q} is the vectorial change of momentum between the incoming to the outgoing wave which in general has an azimuthal dependence.

A further simplification of ψ_{rel} occurs for relevant low energies of $kr_0 \ll 1$; one then approaches $e^{-i\mathbf{q}\cdot\mathbf{r}'} \sim 1$ for those r' at which $V_2(r')$ is appreciable, and taking into account the typical spherical symmetry¹⁶ of V_2 we reach at the final result

$$\psi_{\text{rel}}(\mathbf{r}) = e^{i\mathbf{k}\cdot\mathbf{r}} - \underbrace{\left(\frac{m}{4\pi\hbar^2} \int d^3r' V_2(r') \right)}_a \frac{e^{ikr}}{r}. \quad (2.43)$$

The quantity inside the parenthesis, defined as the s-wave scattering length a , becomes under the aforementioned conditions a constant parameter, independent of \mathbf{k} , which fully characterises two-

¹⁵An effective range r_0 of the potential can be estimated by equating the van der Waals interaction with the kinetic energy, leading to $r_0 \sim (C_6 m / \hbar)^{1/4}$ [120].

¹⁶For a spherically symmetric potential, the scattering eigenstates of the relevant Hamiltonian $H_{\text{sc}} = \frac{\hbar^2 k^2}{2m^*} + V_2(\mathbf{r})$ are waves of definite angular momentum characterised by a quantum number l , so it is a common practice to expand the incident and scattered waves in this basis of these ‘partial waves’. For each independent l one can write a 1D Schrödinger equation with a total potential consisting of V_2 plus an effective centrifugal barrier $\hbar^2 l(l+1)/(2m^* r^2)$. At low temperatures, this barrier is high enough to suppress all $l \neq 0$ partial waves and the $l = 0$ s-wave solution is adequate to characterise scattering. This is what we silently considered with the use of the condition $kr_0 \ll 1$.

body scattering at low energies.

The description of the problem with a single parameter permits to additionally simplify it by replacing the exact potential $V_2(r)$ with a simpler contact pseudo-potential $g_{3D}\delta(r)$; if both potentials are characterised by the same a , the asymptotic behaviour of scattering from these two is identical. By inserting this pseudo-potential in Eq. (2.43) we directly find the expression for the interaction strength of the pseudo-potential

$$g_{3D} = \frac{4\pi\hbar^2 a}{m}. \quad (2.44)$$

Among the various scattering quantities that are now expressed in terms of a , we single out the scattering cross-section¹⁷ $\sigma = 2 \times 4\pi a^2$, the mean-free path between two collisions $l_{\text{mfp}} = 1/(n\sigma)$, and finally the elastic collision rate

$$\gamma_{\text{el}} = n\sigma\bar{v} \quad (2.45)$$

with \bar{v} the mean relative velocity of the two atoms. For a thermal cloud $\bar{v} = \sqrt{6k_{\text{B}}T/m}$.

Three-body interactions. Due to diluteness, we assume the dominance of two-body physics in three-body processes. In other words, we set the intrinsic three-body potential of Eq. (2.41) to zero, i.e. $V_3 = 0$, and focus on the effective three-body interactions induced by V_2 when three atoms are found simultaneously within their interaction range. In this scenario, the s-wave scattering length is sufficient to describe also the effective three-body interactions.

With simple arguments, we can estimate the three-body scattering rate as $\gamma_{3b} = n\sigma\bar{v}w$, where $w \sim (a/n^{-1/3})^3$ is the probability of a third atom to be present during the scattering of the other two and $\bar{v} \sim \hbar/ma$ now is the velocity of that third atom relatively to the center of mass of the other two. Combining the above relations, we find $\gamma_{3b} \sim (\hbar a^4/m)n^2$. In reality, the main three-body inelastic effect is a recombination process in which two atoms form a diatomic molecule while the third atom receives the excess of the molecular binding energy. Typically in an ultracold gas, this additional energy is sufficient to remove all three participating atoms from the gas. With $dn/dt \propto \gamma_{3b}n$, the average atom loss can then be expressed as

$$dN/dt = -L_3 \langle n^2 \rangle N \quad (2.46)$$

with the recombination constant L_3 scaling as $L_3 \propto \frac{\hbar}{m}a^4$ in the absence of additional effects, like Efimov effects¹⁸ [124, 125]. For a uniform system we get the simple relation $dN/dt = -L'_3 N^3$ with $L'_3 = L_3/V^2$. With a known coefficient L_3 , this differential equation gives $N(t) = [2L'_3 t + N(0)^{-2}]^{-1/2}$, with $N(0)$ the initial atom number.

We note here that with the emergence of coherence, as we describe in the next section, relation

¹⁷The additional factor of 2 compared to the classical result for the scattering cross-section, valid only in the absence of coherence, stems from the bosonic character of the atoms.

¹⁸When Efimov states are present, there are additional log-periodic oscillations of L_3 with a , a theoretical prediction of which together with the experimental investigation for the case of ³⁹K atoms can be found in [123].

Eq. (2.46), as well as the formula for the scattering cross-section given above, are deficient; in that case one needs to distinguish between collisions among condensed, non-condensed or mixed atoms, each case characterised by different scattering rates [126]. For a pure condensate, however, Eq. (2.46) is restored with a new recombination constant 3! times smaller than that of a non-condensed cloud [127]. This constant has been experimentally measured for the case of a pure BEC of ^{39}K atoms [123], and the proportionality constant $L_{30} = L_3/(\hbar a^4/m)$ can be extracted from those results giving $L_{30} \approx 180$.

Tuning the interactions: Feshbach resonances. In the previous discussion we considered scattering in a single channel and concluded that the strength of interactions, inferred by a , is an intrinsic property of the gas. This is no longer necessarily true when one takes into account other channels, even if they remain energetically unfavourable (‘closed’). These different channels get coupled to each other through an additional spin-dependent term in the interaction potential. The existence of such a spin-dependent term can be argued based on the fact that two singlet electrons, unlike two triplet ones, can build a covalent bond and deeply decrease their total energy. The coupling occurs since the quantum numbers of the scattering channel (characterised by the hyperfine states of the separate atoms) do not remain good in the presence of the spin-dependent term. This coupling becomes strong when a bound state of a closed channel comes close to the dissociation threshold of the scattering channel. Then a ‘virtual’ transition¹⁹ to the closed channel takes place for a short period of time. The increase of this virtual-transition time results in the modification of the scattering length in the open channel. This phenomenon is widely known as a Feshbach resonance [50].

At large distances, the two potentials with the scattering and the bound states are characterised by different hyperfine states and thus with the application of an external magnetic field they shift differently in energy. This allows the tuning of the relative energy difference and therefore the value of the scattering length. Within a two-channel model [130] (but also experimentally compatible), the field-dependent scattering length takes the form

$$a(B) = a_{\text{bg}} \left(1 - \frac{\Delta_0}{B - B_0} \right). \quad (2.47)$$

The value a_{bg} corresponds to the previously considered intrinsic scattering length in the absence of any resonance, the resonant field B_0 is the magnetic field at which the bound and the open-channel energies are equal (neglecting a small correction [131]) and Δ_0 is to the width of this resonance. To experimentally exploit such a resonant feature, Δ_0 has to be much wider than the typical magnetic field noise in real situations.

¹⁹The characterisation as a virtual transition stems from the fact that the atoms insert and exert in the end the collision from the same initial open channel.

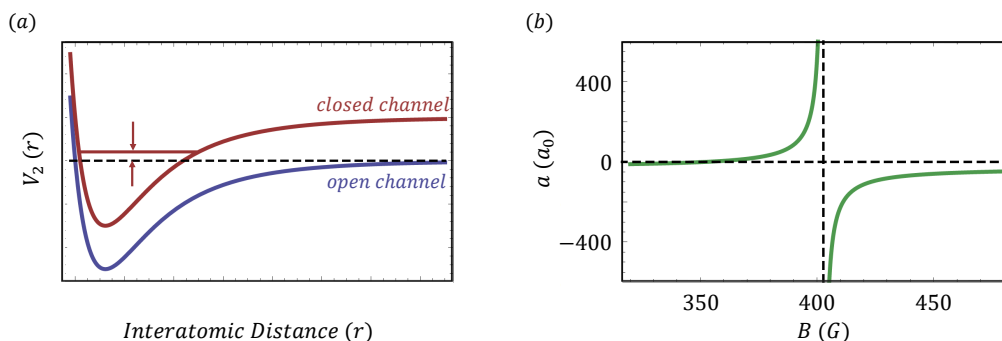


Figure 2.2: (a) The principle of a Feshbach resonance. The coupling between the open channel (blue) and a bound state of the closed channel (red) leads to a virtual transition and an effective change of the scattering length a from its background value a_{bg} . (b) The application of an external magnetic field tunes a since the two channels are associated with different spins. The plot corresponds to the resonance we use throughout this thesis for ^{39}K between atoms trapped in their $F = 1$, $m_F = 1$ ground hyperfine state. In this case, $a_{\text{bg}} = -29a_0$ [128], $\Delta = 50\text{G}$ and $B_0 = 402.7\text{G}$ as measured in [129]. A detailed description of the specific resonance can be found in Ref. [128].

Summary. The bottom line from the discussion above is the approximation of Eq. (2.41) by

$$\hat{H} = \int d^3r \hat{\psi}^\dagger(r) \left(-\frac{\hbar^2 \nabla^2}{2m} - \mu \right) \hat{\psi}(r) + \frac{g_{3D}}{2} \int d^3r d^3r' \hat{\psi}^\dagger(r) \hat{\psi}^\dagger(r') \hat{\psi}(r') \hat{\psi}(r) \quad (2.48)$$

when three-body losses can be neglected. The Heisenberg equation of motion describing the time evolution for the field operator becomes²⁰

$$j\hbar \frac{\partial \hat{\psi}(r, t)}{\partial t} = [\hat{\psi}, \hat{H}] = \left(-\frac{\hbar^2 \nabla^2}{2m} - \mu + g_{3D} \hat{\psi}^\dagger(r, t) \hat{\psi}(r, t) \right) \hat{\psi}(r, t) \quad (2.49)$$

We note here, that the interaction term, in its exact form, contains collisions that leave the atoms in their same initial external states and collisions that redistribute the atoms within the various energy states. The former type of collisions are treated within mean fields and the regime where they dominate is called collisionless, while the latter type of collisions describe the collisional regime of interactions. When such collisions prevail, the behaviour is very well described within macroscopic hydrodynamic models, as the one described in Sec. 2.1.

Next, we briefly discuss the connection between the notions of elementary excitations and density fluctuations from a more microscopic point of view and introduce some fundamental concepts.

²⁰One could heuristically add the effect of three body-losses by adding a term $-j\hbar(L_3/2)|\hat{\psi}(r)|^4\hat{\psi}(r)$ in the equation of motion [132]. To keep the discussion simple, we neglect such effects.

2.3.2 Elementary excitations vs density fluctuations

Landau postulated that the dispersion relation of elementary excitations is experimentally obtainable through measuring the density fluctuations of the superfluid. Indeed, he used the experimental results from neutron scattering to deduce the phonon-roton spectrum in liquid helium as qualitatively depicted in Fig. 2.1(c). This assumption, although valid for a superfluid, is not universally correct. With a goal to show this subtlety, we start with a reminder of the various correlation functions, intuitively entering the discussion about the dynamics of a fluid. To that end, we first introduce the density operator of the fluid as $\hat{n} = \sum_i \delta(r - r_i) = \hat{\psi}^\dagger(r)\hat{\psi}(r)$, where r_i the position operator of the i -th atom inside the fluid, and its Fourier component $\hat{N}_q = \sum_i e^{-jqr_i}$. For a uniform system the latter is also expressed as $\hat{N}_q = \sum_k \hat{a}_{k+q}^\dagger \hat{a}_k$ with $\hat{a}_k = \int dr \hat{\psi}(r) e^{-jkr} / \sqrt{V}$ the operator that annihilates an atom of momentum k .

The one-body density matrix²¹ $G^{(1)}(r) = \langle \hat{\psi}^\dagger(r)\hat{\psi}(0) \rangle$, with $G^{(1)}(0) = n$ (n being the average density of the uniform fluid), expresses the system's long-range order through its off-diagonal terms ($r \neq 0$). In the thermodynamic limit, $G^{(1)}(r)$ is the Fourier transform of the momentum distribution n_q [114]. The normalised first-order correlation function $g_1(r) = G^{(1)}(r)/n$ is a measure of the proximity of the many-body state to a mean-field in which $\langle \hat{\psi}(r)^\dagger \hat{\psi}(r) \rangle = \langle \hat{\psi}^\dagger(r) \rangle \langle \hat{\psi}(r) \rangle$. The above correlations can be generalised to include also time differences t . In that spirit, one also defines an ‘intermediate’ first-order correlation²² $A(q, t) = \langle \hat{a}_q(t) \hat{a}_q^\dagger(0) \rangle$, characterising the propagation of a single atom of momentum q over time in the fluid. The poles of $A(q, \omega)$, the temporal Fourier transform of $A(q, t)$, correspond to the elementary excitations of the fluid.

In a similar way, the two-body density matrix is $G^{(2)}(r) = \langle \hat{\psi}^\dagger(r)\hat{\psi}^\dagger(0)\hat{\psi}(r)\hat{\psi}(0) \rangle$ and its normalised version $g_2(r) = G^{(2)}(r)/n^2$. Another useful and experimentally observable quantity is the density-density correlation function, defined as $C_{nn}(r) = \langle \hat{n}(r)\hat{n}(0) \rangle$, which expresses the probability of simultaneously detecting two particles at a distance r . Using the Bose commutation relations, one finds $C_{nn}(r) = n\delta(r) + n^2 g_2(r)$. The time-generalisation of $C_{nn}(r)$ was already introduced in Sec. 2.1.3, where we described it as the temporal and spatial inverse Fourier transform of the dynamic structure factor $S(q, \omega)$; the poles in $S(q, \omega)$ correspond to the density fluctuations allowed by the fluid. For completeness, we also introduce the ‘intermediate’ density correlator $S(q, t) = \langle \hat{N}_q(t) \hat{N}_q^\dagger(0) \rangle / N$. Finally, one can show [104] that also the density response function $\chi(q, \omega)$ can be expressed as a correlation function; its ‘intermediate’ transform is $\chi(q, t) = -j\theta(t) \langle [\hat{N}_q(t), \hat{N}_q^\dagger(0)] \rangle / V$, with the Heaviside function $\theta(t)$ denoting the causality of the response.

A clear picture for the comparison between elementary excitations and density fluctuations can be extracted if we express the relevant correlation functions in terms of the (unknown) many-body eigenstates $|m\rangle, |n\rangle$ of the effective Hamiltonian H , i.e. $H|m, n\rangle = \hbar\omega_{m,n}|m, n\rangle$. For instance, the

²¹Here, we silently assume a translation invariance, appropriate for uniform systems, in which r is equivalent to the distance between the two points under consideration in space.

²²Here the word ‘intermediate’ has the meaning of being only a spatial Fourier transform of $G^{(1)}$.

first-order correlation function $A(q, \omega)$ can be written as

$$\begin{aligned} A(q, \omega) &= \int_0^\infty dt e^{j\omega t} \langle \hat{a}_q(t) \hat{a}_q^\dagger(0) \rangle \\ &= \frac{1}{Z} \int_0^\infty dt e^{j\omega t} \sum_{m,n} e^{-\hbar\omega_m/k_B T} \langle m | \hat{a}_q(t) | n \rangle \langle n | \hat{a}_q^\dagger(0) | m \rangle \end{aligned} \quad (2.50)$$

where in the second line we averaged with respect to the canonical ensemble characterised by the partition function $Z = \sum_m \exp(-\hbar\omega_m/k_B T)$. By changing from a Heisenberg to a Schrödinger representation, $\hat{a}_q(t) = e^{jHt/\hbar} \hat{a}_q e^{-jHt/\hbar}$, and with the use of the integral $\int_0^\infty dt e^{j(\omega - \omega_0 + j\eta)t} = j/(\omega - \omega_0 + j\eta)$ where again $\eta \rightarrow 0$, one finally finds

$$A(q, \omega) = Z^{-1} \sum_{m,n} e^{-\hbar\omega_m/k_B T} |\langle n | \hat{a}_q^\dagger | m \rangle|^2 \delta[\omega - (\omega_n - \omega_m)] \quad (2.51)$$

In the same way, the dynamic structure factor and the density response function are written as [133]

$$S(q, \omega) = (ZN)^{-1} \sum_{m,n} e^{-\hbar\omega_m/k_B T} |\langle n | \hat{N}_q^\dagger | m \rangle|^2 \delta[\omega - (\omega_n - \omega_m)] \quad (2.52)$$

$$\chi(q, \omega) = (ZV)^{-1} \sum_{m,n} e^{-\hbar\omega_m/k_B T} |\langle n | \hat{N}_q^\dagger | m \rangle|^2 \frac{[1 - e^{-\hbar(\omega_n - \omega_m)/k_B T}]}{\omega - (\omega_n - \omega_m) + j\eta} \quad (2.53)$$

where we deliberately kept the infinitesimal η -dependence in the last formula to point out the complex nature of $\chi(q, \omega)$.

The spectral representations, Eq. (2.51) and (2.52), of $A(q, \omega)$ and $S(q, \omega)$ show clearly that the elementary (single) excitations are described within the former, whereas $S(q, \omega)$ characterises particle-hole (or equivalently density) excitations. Although all transitions $|m\rangle \rightarrow |n\rangle$ are included in both $A(q, \omega)$ and $S(q, \omega)$, their relative weights, $|\langle n | \hat{a}_q^\dagger | m \rangle|^2$ and $|\langle n | \hat{N}_q^\dagger | m \rangle|^2$ respectively, can be in general significantly different; in that case, different states end up contributing to either $A(q, \omega)$ or $S(q, \omega)$. This is expected for a normal fluid; the transition $|m\rangle \rightarrow |n\rangle$ has a significant weight in $A(q, \omega)$ if these states differ by one particle through the operator \hat{a}_q^\dagger , whereas it has a considerable weight in $S(q, \omega)$ if they both have the same number of particles. This difference between the spectra of the elementary excitations and density fluctuations is not the case anymore in a superfluid, where the density fluctuations become the elementary excitations as long as a continuum of multi-particle excitations in $S(q, \omega)$ is ignored.

What is more, the spectral representation of $S(q, \omega)$ and $\chi(q, \omega)$ provides a tool for an almost trivial derivation of the relations introduced in Sec. 2.1.3, like the fluctuation - dissipation theorem and the f sum rule. An example is presented in Box 2.1 where we discuss the f sum rule from a more conceptual perspective.

Box 2.1: The f sum rule and the detailed balance

Here, we sketch the calculation of the integral $I = \int_{-\infty}^{+\infty} \omega S(q, \omega) d\omega$, the left-hand side of the so-called f sum rule introduced in Eq. (2.27) and we attempt to reveal the physical meaning of this relation. To that end, we first note that the integral I is related to the total energy put into the system; this is a direct consequence of expressing the dissipation energy from Eq. (2.23) in terms of $S(q, \omega)$ through the fluctuation - dissipation theorem of Eq. (2.28).

Using the spectral representation of $S(q, \omega)$ from Eq. (2.52), we get

$$I = \int_{-\infty}^{+\infty} \omega S(q, \omega) d\omega = (ZN)^{-1} \sum_{m,n} e^{-\hbar\omega_m/k_B T} (\omega_n - \omega_m) |\langle n | \hat{N}_q^\dagger | m \rangle|^2. \quad (2.54)$$

The right-hand side of the equation above represents a sum of all the energies of the transitions occurring after a density perturbation in the fluid weighted by their oscillator strengths. The f sum rule is then nothing but an effective energy conservation law for the fluid: the energy pumped into the system equates the total excitation energy.

Additionally, if one interchanges the indices m and n in the spectral representation of $S(q, \omega)$, one finds

$$S(q, -\omega) = e^{-\hbar\omega/k_B T} S(q, \omega) \quad (2.55)$$

which is known as the ‘detailed balance’ relation. It expresses the fact that at finite temperatures, transitions to lower energies are also allowed with a relative probability $e^{-\hbar\omega/k_B T}$ and thus the total pumped energy is the difference between the absorbed and the released energy from the fluid.

Continuing from Eq. (2.54), we note that $\hbar(\omega_n - \omega_m) \langle n | \hat{N}_q^\dagger | m \rangle = \langle n | [H, \hat{N}_q^\dagger] | m \rangle$ which eventually leads to the result [114]

$$I = \frac{1}{2N\hbar} \langle \hat{n}_q^\dagger, [H, \hat{N}_q^\dagger] \rangle = \frac{\hbar q^2}{2m} \quad (2.56)$$

the last equality being valid for velocity-independent interactions.

2.3.3 Bose-Einstein condensate and superfluidity

Bose-Einstein condensate. The concept of a BEC was first introduced for an ideal Bose gas as a phase emerging solely due to the statistics obeyed by the gas. It is linked with the saturation of the available single-particle excited states and the subsequent macroscopic population N_0 of the system’s ground state characterised by a zero momentum ($q = 0$). In the presence of a BEC, then, the momentum distribution n_q gets a δ -peak of height $n_0 = N_0/V$ at $q = 0$ in addition to the smooth behaviour at finite momenta. This in turn results in a non-zero value of $G^{(1)}(r)$ (the Fourier transform of n_q) even for large separations r , i.e. $\lim_{r \rightarrow \infty} G^{(1)}(r) = n_0 \neq 0$. The quantity n_0 is defined as the condensate density and the remaining $n_{\text{th}} = n - n_0$ constitutes the thermal part of the ideal gas. At zero temperature all the atoms are in the same state and thus $n_0 = n$.

Penrose and Onsager [134] generalised the concept of a BEC also for an interacting Bose fluid, by applying the same defining condition

$$\lim_{r \rightarrow \infty} G^{(1)}(r) = n_0 \neq 0 \quad (2.57)$$

as for the ideal gas. The condensate can be still considered as the macroscopic occupation of the

$q = 0$ state, but now $n_0 \neq n$ even at $T = 0$. Conceptually one can think of it by considering an adiabatic turning on of the interactions starting from the ideal gas; the modification of the ground state couples different q states and thus some of the atoms seem ‘virtually’ excited to states different than the $q = 0$. The zero-temperature difference $n - n_0$ in the absence of additional real excitations is called the quantum depletion of the condensate.

The *long-range order* or LRO (Eq. (2.57)) that characterises a BEC leads to a non-zero average $\langle \hat{\psi} \rangle$. One then may find it natural to split the field operator

$$\hat{\psi}(r) = \psi_0 + \delta\hat{\psi}(r) \quad (2.58)$$

into a mean-field classical component $\psi_0 = \langle \hat{\psi} \rangle$ and the fluctuations $\delta\hat{\psi}(r)$ containing, in general, the condensate depletion, thermally excited atoms and externally-induced fluctuations. For low temperatures and weak interactions, such that $n_0 \approx n$, the fluctuations can be neglected and one finds $\lim_{r \rightarrow \infty} G^{(1)}(r) = \psi_0^*(r)\psi_0(0)$ which, in turn, provides the required form for the complex classical field $\psi_0(r) = \sqrt{n_0}e^{j\theta}$. The fixing of the condensate phase θ breaks the phase invariance of the initial Hamiltonian and leads to the non-conservation of its canonically conjugate condensed number N_0 . In other words, a BEC with N_0 or $N_0 + 1$ atoms characterise the same state. By neglecting the fluctuations, the Hamiltonian in Eq. (2.48) reduces to its classical version

$$H = \int \left(\frac{\hbar^2}{2m} |\nabla\psi(r)|^2 - \mu|\psi(r)|^2 \right) d^3r + \frac{g_{3D}}{2} \int |\psi(r)|^4 d^3r \quad (2.59)$$

and Eq. (2.49) converts into the Gross-Pitaevskii (GP) equation, $j\hbar\frac{\partial\psi}{\partial t} = \left(-\frac{\hbar^2\nabla^2}{2m} - \mu + g_{3D}n_0 \right) \psi$, that describes the evolution of the classical field ψ_0 . The condensate ground state can be easily obtained by setting $\partial\psi/\partial t = 0$ which gives $n_0 = \mu/g_{3D}$ for an infinite system; in a finite-sized system the condensate density goes to zero at the system’s edges within a healing length $\xi = \sqrt{\hbar^2/(2mg_{3D}n_0)}$.

Bogoliubov excitations. The next step is to estimate the excitations on top of the ground state by considering also the effect of weak fluctuations $\delta\hat{\psi}$. Typically, for weak fluctuations this is achieved with a diagonalisation process (Bogoliubov transformation) of the Hamiltonian in Eq. (2.48) using Eq. (2.58) after discarding all terms higher than quadratic in $\delta\hat{\psi}$ in the interaction term [135]. An equivalent way to formulate the problem consists in considering small classical, plane-wave fluctuations on top of the condensate ground state, i.e.

$$\psi(r, t) = e^{-j\mu t/\hbar} \left[\psi_0 + \sum_q \left(u_q e^{j(qr - \omega_q t)} + v_q^* e^{-j(qr - \omega_q t)} \right) \right] \quad (2.60)$$

which have to satisfy the GP equation under the normalisation condition $u_q^2 = v_q^2 + 1$ for the small amplitudes u_q and v_q . Within a quasi-particle picture, Eq. (2.60) with its normalisation can be

interpreted as u_q^2 atoms to propagate along the q -direction and v_q^2 atoms along the opposite direction, resulting in a net momentum of $\hbar q$. Plugging Eq. (2.60) into the time-dependent GP equation, one extracts the Bogoliubov excitation spectrum

$$\hbar\omega_q = \sqrt{\epsilon_q^0 (\epsilon_q^0 + 2ng_{3D})} \quad (2.61)$$

and the amplitudes

$$u_q^2 = v_q^2 + 1 = \frac{1}{2} \left(\frac{\epsilon_q^0 + ng_{3D}}{\epsilon_q} + 1 \right). \quad (2.62)$$

In the above, $\epsilon_q^0 = \hbar^2 q^2 / 2m$ is the ideal-gas kinetic energy.

The Bogoliubov spectrum ω_q has the typical form as shown in Fig. 2.1(b). At long wavelengths, $\epsilon_q^0 \ll 2ng_{3D}$ and the spectrum becomes phononic with $\omega_q = q\sqrt{ng_{3D}/m}$. The corresponding speed of sound $c_B = \sqrt{ng_{3D}/m}$ is widely known as the Bogoliubov speed and it is a collisionless ‘zero’ sound emerging from the mean-field ng_{3D} among the condensed atoms. By calculating the pressure in the ground state²³, one finds that $c_B = (\partial p / \partial \rho)_s$; this implies, on one hand, that the elementary phononic excitations are equal to the density fluctuations of the gas, and on the other hand that c_B is the collisionless analogue of the first sound c_1 in the $T = 0$ (necessarily) incompressible case. In this phononic regime, Eq. (2.62) yields $u_q^2, v_q^2 \approx 1/2q\xi \gg 1$ and thus, as expected for a phonon, the fluctuation involves a large number of atoms.

On the other hand, for short excitation wavelengths, $\epsilon_q^0 \gg 2ng_{3D}$ and ω_q gives a free-particle spectrum, $\epsilon_q \approx \epsilon_q^0 + ng_{3D}$, shifted by the mean field. The amplitudes in this regime approach $u_q^2 = 1$ and $v_q^2 = 0$ indicating again the single-particle character of these excitations. The crossover regime between the phonons and the free-particle excitations is indicated by a wavelength similar to the healing length at which the kinetic and the interaction energies are equal.

BEC and superfluidity. The presence of a BEC in a gas has served as a microscopic platform for explaining superfluidity. The $T = 0$ Bogoliubov excitation spectrum is the simplest framework for understanding this connection. For example, the phononic Bogoliubov spectrum of a BEC at long wavelengths, different from the usual free particle spectrum, supports a non-zero critical velocity equal to the Bogoliubov speed of sound. The superfluid density, at $T = 0$ (where $\rho_s = \rho$), is equal to the condensate density plus the BEC depletion; in the absence of the latter, one gets $\rho_s = mn_0$. The superfluid velocity, on the other hand, is identified as the velocity of the condensate, $v_s = \hbar\nabla\theta/m$, even in the presence of depletion²⁴.

²³The ground state, characterised by the chemical potential $\mu = \left(\frac{\partial E}{\partial N}\right)_V = ng_{3D}$, has a total energy of $E = \frac{1}{2}g_{3D}N^2/V$. The pressure of the gas is then $p = -\left(\frac{\partial E}{\partial V}\right)_N = \frac{1}{2}g_{3D}n^2$.

²⁴Since superfluidity is a dynamical effect, to see that, we consider a frame of reference that moves at a velocity $-v_s$ with respect to a static BEC; in that frame, there is a macroscopic population of the state with momentum $\hbar q = mv_s$ characterised by the classical field $\psi_0 = \sqrt{n_0}e^{j(\theta_0 + q_0 r)}$; the condensed atoms move coherently at a velocity $\hbar\nabla(\theta_0 + q_0 r)/m = v_s$. The depleted atoms get the same shift $\hbar q_0$ in momentum compared to the static case, and so they are essentially attached with the condensed atoms when the latter are set in motion (see [136]).

Another unique property arising from the presence of a BEC is the hybridisation between the Bogoliubov excitations and the density fluctuations at $T = 0$ in the long-wavelength limit, as we hinted before through the relation $c_B = (\partial p / \partial \rho)_s$. In Section 2.3.1 we discussed about the different oscillator strengths $|\langle n | \hat{a}_q^\dagger | m \rangle|$ and $|\langle n | \hat{N}_q^\dagger | m \rangle|$ for normal states. The presence of the BEC with the breaking of the global phase symmetry and the non-conservation of the condensed atoms modifies these conclusions; indeed, in this case the density operator can be approximated by

$$\hat{N}_q = \sum_k \hat{a}_{k+q}^\dagger \hat{a}_k \approx \sqrt{n_0} (\hat{a}_q + \hat{a}_q^\dagger), \quad (2.63)$$

where we kept only the macroscopic $k = 0$ classical mode in the sum. Eq. (2.63) directly shows that $S(q, \omega)$ is expressed in terms of $A(q, \omega)$. With this hybridisation in mind, the dynamic structure factor can be expressed as $S(q, \omega) = S(q) \delta(\omega - \omega_q)$, with ω_q the Bogoliubov excitation spectrum. Using the f sum rule of Eq. (2.27), one gets

$$\hbar \omega_q = \frac{\epsilon_q^0}{S(q)}, \quad (2.64)$$

which is known as the Feynman relation, an alternative way of linking excitations with density fluctuations.

Going beyond zero temperature, the thermal depletion of the condensate prevails over the quantum depletion and a quantitative understanding of superfluidity through condensation is proven more challenging. Various approximations (see for example the reviews in [137–139]) have been applied which allow numerical investigations of the low temperature behaviour of a Bose gas. The various approaches can be categorised, generally speaking, into two types. In the first type, the so-called classical-field approaches, one generalises the notion of the classical field ψ_0 to include also heavily-populated low-lying excitations on top of the single-particle ground state. Since ψ_0 does not simply model the condensate anymore, it allows the study of the prevailing ‘classical’ aspects of the gas and the extraction of various correlation functions. This methodology will be proven important in the case of 2D systems.

In the second type of approaches, collectively known as two-gas models, the condensate and the thermal cloud are treated from the beginning in a separate way. One such two-gas model is the so-called ZNG theory [140, 141]. Neglecting the quantum depletion, ZNG treatment makes use of a generalised GP equation for the condensed part, coupled with a quantum Boltzmann equation that describes the thermal component. The generalisation in the GP equation consists of including both a mean-field coupling between the two subsystems and also collisional processes beyond a mean field (also in the kinetic equation). Specifically, the theory allows atom-exchange collisions between the condensate and the thermal component and thermalising collisions among the thermal part.

The exact details of this model lie beyond the scope of this thesis. However, we want to mention two significant results of this theory in the spirit of our discussion for the connection between

superfluidity and a BEC. First, when full collisional processes (i.e. collisions between condensate-thermal and thermal-thermal atoms) are taken into account, it was shown [103] that ZNG theory can properly lead to the exact Landau's hydrodynamic two-fluid equations described in Sec. 2.1.1, if the condensate and thermal components play the role of the superfluid and normal components, respectively.

Second, with the theoretical ability to control collisions, ZNG theory was able to test beyond the realm of hydrodynamics, from a purely collisionless to a partially collisional gas. For a purely collisionless gas only mean-field interactions consist a source of (zero-) sound propagation. In this regime, the $T = 0$ Bogoliubov approximation seems to be well-extended to non-zero temperatures, after a proper account for the thermally-depleted condensate density. On the other hand, for a partially collisional gas, characterised by an equilibrium within the thermal part but not an equilibrium between the two components, ZNG theory predicts the existence of first and second sound, with the predictions though being different from the fully hydrodynamic model.

3

The two-dimensional atomic Bose gas

“In order to understand the wor[l]d, one has to turn away from it on occasion.”

— Albert Camus, *The Myth of Sisyphus*

In the previous chapter we looked at superfluidity from a general perspective, presented the hydrodynamic two-fluid model, and finally discussed the microscopic connection between a superfluid and the existence of long-range order in three dimensions. In the current chapter we give a brief overview of the theory of superfluidity in two dimensions where true long-range order does not emerge, with a goal to set the theoretical framework for our experimental work in the next chapters. We concentrate on the predictions for the superfluid density and the thermodynamic quantities that enter the 2D version of the hydrodynamic two-fluid model. In the same spirit as before, and although some of the results are more generally applicable, we will discuss the topic in the context of the atomic 2D Bose gas, which is studied in our experiments.

To that end, we first introduce in Sec. 3.1 the concept of a quasi-2D gas and its characteristic scale invariance as is relevant for experiments with atomic gases. Following that, in Sec. 3.2 we discuss the low-temperature behaviour of an infinite uniform Bose gas where phase fluctuations induced by phonons prevent the appearance of a BEC, but not of a superfluid (Sec. 3.2.1); a quasi-long-range order occurs at $T > 0$. The suppression of density fluctuations and the emergence of the so-called quasi-condensate enable the appearance of another type of phase defects, the quantised vortices. At low enough temperatures, the pairing of such whirls restores quasi-long-range order in the system. At higher temperatures, the proliferation of free vortices destroys both quasi-long-range correlations and superfluidity. The mechanism for this transition from a normal gas to a superfluid is described within the BKT theory (Sec. 3.2.2). We also present the equation of state for the 2D gas (Sec. 3.2.3), which prescribes the thermodynamics of the gas and allows the determination of the BKT transition point. Finally, in Sec. 3.3 we discuss modifications in the above picture that arise when probing a 2D gas in an experiment.

3.1 The quasi-two-dimensional Bose gas

To provide the experimentally relevant theoretical background for this thesis we focus on the ‘quasi-two-dimensional’ regime¹ of an atomic gas: a kinematically two-dimensional but collisionally three-dimensional system. These two aspects are discussed below.

Kinematics

Given that both the thermal and interaction energies of the gas are small compared to the energy difference between the ground and the first excited states allowed in one spatial direction, say z , the atoms populate predominantly this ‘transverse’ ground state and excitations to other energy levels associated with the motion along z are energetically suppressed; the gas is then considered kinematically reduced to 2D.

For the case of ultracold gases, one typically confines the atoms in a tight harmonic potential in one dimension in order to produce a kinematically 2D gas; this is also the approach pursued in this thesis. The gas is then restricted to zero-point oscillations in the ground state of the harmonic trap along z , with a size of about one oscillator length $\ell_z = \sqrt{\hbar/(m\omega_z)}$ and ω_z the corresponding trapping frequency, when

$$\hbar\omega_z \gg \mu_{3D} \quad \text{and} \quad \hbar\omega_z \gg k_B T. \quad (3.1)$$

These strict conditions in Eq. (3.1) define the 2D regime of the gas. It is worth noting, however, that due to bosonic stimulation, a dimensional reduction in the kinematics can take place even for $\hbar\omega_z \lesssim k_B T$, μ_{3D} , as the gas effectively ‘condenses’ into the ground state of the tightly-confined direction while it still occupies many states associated with the motion in the x - y plane, a phenomenon known as transverse condensation [142, 143].

Interactions

When $\ell_z \gg a$, as realised in most ultracold gases, the relative motion of the atoms in the region of the scattering event is not affected by the tight confinement, and the gas behaves collisionally as a three-dimensional system. In this regime, the 3D pseudo-potential g_{3D} , discussed in the previous chapter, remains valid for the description of collisions. An effective 2D Hamiltonian can be constructed starting from the 3D Hamiltonian of Eq. (2.48) by separating the field operator $\hat{\psi}(r) \equiv \hat{\psi}_{3D}(r) \rightarrow \hat{\psi}_{2D}(x, y)\phi_0(z)$, where ϕ_0 is the classical field describing the ground state along z .

¹The notion of a ‘quasi-2D’ gas has been also used in the literature for situations where the defining conditions of Eq. (3.1) for a kinematically 2D gas are not strictly satisfied. In this thesis, these conditions are always well satisfied and we keep the definition of the main text for a ‘quasi-2D gas’.

The interaction term of the Hamiltonian then becomes

$$\hat{V}_{\text{int}} = \frac{1}{2} \underbrace{\left(g_{3\text{D}} \int dz |\phi_0(z)|^4 \right)}_{g_{\text{q2D}}} \int dx dy dx' dy' \hat{\psi}_{2\text{D}}^\dagger(x, y) \hat{\psi}_{2\text{D}}^\dagger(x', y') \hat{\psi}_{2\text{D}}(x', y') \hat{\psi}_{2\text{D}}(x, y). \quad (3.2)$$

The resulting 2D interaction strength g_{q2D} takes the simple form

$$g_{\text{q2D}} = \frac{\hbar^2}{m} \sqrt{8\pi} \frac{a}{\ell_z} \equiv \frac{\hbar^2}{m} \tilde{g} \quad (3.3)$$

for the Gaussian ground state ϕ_0 of a harmonic potential. Here, we define $\tilde{g} = \sqrt{8\pi}a/\ell_z$ as the dimensionless quantity that characterizes the strength of the interactions in this geometry.

The existence of the dimensionless and energy-independent coupling parameter \tilde{g} results in the same $1/L^2$ -scaling² of the kinetic and interaction energy with the in-plane system size L . In other words, the gas shows the same behaviour independently of its size; it is then solely the ratio of the two energy scales, or equivalently the quantity $x = \mu/k_{\text{B}}T$, with μ the chemical potential in 2D, that determines the thermodynamics of the gas for a specific value of \tilde{g} . This property is often referred to as the scale invariance of a quasi-2D gas and will be an important concept for the rest of this thesis.

Scale invariance breaks down when the interaction strength starts showing a dependence on the atomic density. A more careful calculation of the 2D interaction strength yields the low-scattering-energy approximation [144]

$$g_{\text{q2D}}(k) = \frac{\sqrt{8\pi}\hbar^2/m}{\ell_z/a - (1/\sqrt{2\pi}) \ln(\pi k^2 \ell_z^2)}, \quad (3.4)$$

with $\hbar k = \sqrt{2\mu_{3\text{D}}m}$. For $\ell_z \gg a$ (or equivalently $\tilde{g} \ll 1$) the second term in the denominator can be safely neglected and Eq. (3.3) is restored; scale invariance is then well satisfied in this (weakly-interacting) regime, unlike the opposite strong-coupling limit ($\tilde{g} \gg 1$) for the typical densities of interest. The experiments discussed in this thesis use an interaction parameter lying in the intermediate regime near $\tilde{g} \approx 0.5$.

3.2 Low-temperature behaviour

Having introduced the notion of a quasi-2D gas, we now investigate its behaviour at low temperatures. A full description requires to consider two types of excitations: smooth phonons and quantised vortices. In the following, we attempt to introduce each of them in a natural way and

²The interaction energy of the 2D gas is $E_{\text{int}} = \frac{g_{\text{q2D}}}{2} \int \langle n^2(r) \rangle d^2r \approx \frac{\hbar^2}{2m} \tilde{g} \frac{N^2}{L^2}$ and the kinetic energy of a non-interacting gas is approximated by $E_{\text{kin}} = \int_0^{E_N} \epsilon G(\epsilon) d\epsilon \approx \frac{\pi \hbar^2}{m} \frac{N^2}{L^2}$ with $G(\epsilon) = mL^2/(2\pi \hbar^2)$ the 2D density of states, $N = \int_0^{E_N} G(\epsilon) d\epsilon$ the atom number and E_N the highest energy of the free atoms.

clarify their effect on the behaviour of the gas. The starting point for the description of this 2D gas is the Hamiltonian in Eq. (2.41), which we repeat here in its final 2D form:

$$\hat{H} = \int d^2r \hat{\psi}^\dagger(r) \left(-\frac{\hbar^2 \nabla^2}{2m} - \mu \right) \hat{\psi}(r) + \frac{g_{\text{q2D}}}{2} \int d^2r d^2r' \hat{\psi}^\dagger(r) \hat{\psi}^\dagger(r') \hat{\psi}(r') \hat{\psi}(r), \quad (3.5)$$

where now all the involving quantities describe the relevant 2D gas³. By adopting Eq. (3.5), we do not assume a priori a BEC, as in 3D, where we split the field operator into a classical field and an operator for the fluctuations (see Eq. (2.58)). Instead, we express $\hat{\psi}$ in a more general fashion using the density-phase representation

$$\hat{\psi}(r) = e^{j\hat{\theta}(r)} \sqrt{\hat{n}(r)}, \quad (3.6)$$

with the density $\hat{n}(r)$ and phase $\hat{\theta}(r)$ operators satisfying the commutation relation $[\hat{n}(r), \hat{\theta}(r')] = j\delta(r - r')$. Under the assumption that the density operator is split as $\hat{n}(r) = n + \delta\hat{n}(r)$ where

Box 3.1: Bogoliubov spectrum of excitations in 2D

By inserting the density-phase representation of $\hat{\psi}$ (Eq. (3.6)) in the general 2D Hamiltonian (Eq. (3.5)) and the 2D version of the Heisenberg equation of motion (Eq. (2.49)), one obtains two coupled equations of motion for the density and the phase operators:

$$\begin{aligned} -\hbar \partial \hat{n} / \partial t &= (\hbar^2 / m) \nabla (\nabla \hat{\theta} \hat{n}), \\ -\hbar \partial \hat{\theta} / \partial t &= [\hbar^2 / (2m)] (\nabla \hat{\theta})^2 - [\hbar^2 / (2m)] (\nabla^2 \sqrt{\hat{n}}) / \sqrt{\hat{n}} + g_{\text{q2D}} \hat{n}. \end{aligned} \quad (3.7)$$

With the assumption that $\hat{n}(r) = n + \delta\hat{n}(r)$ where $n = \langle \hat{n}(r) \rangle$, one expresses the density and phase fluctuations in terms of the (yet unknown) elementary excitations [145]:

$$\begin{aligned} \delta\hat{n}(r) &= \sqrt{n(r)} \sum_q A_q^- e^{-j\epsilon_q t / \hbar} \hat{a}_q + (A_q^-)^* e^{j\epsilon_q t / \hbar} \hat{a}_q^\dagger, \\ \hat{\theta}(r) &= [4n(r)]^{-1/2} \sum_q A_q^+ e^{-j\epsilon_q t / \hbar} \hat{a}_q + (A_q^+)^* e^{j\epsilon_q t / \hbar} \hat{a}_q^\dagger. \end{aligned} \quad (3.8)$$

Substituting the expanded operators of Eq. (3.8) into Eq. (3.7) and keeping the first-order terms, gives

$$\begin{aligned} (-\hbar^2 \nabla^2 / (2m) + g_{\text{q2D}} n - \mu) A_q^+ &= \epsilon_q A_q^- \\ (-\hbar^2 \nabla^2 / (2m) + 3g_{\text{q2D}} n - \mu) A_q^- &= \epsilon_q A_q^+ \end{aligned} \quad (3.9)$$

for the eigenenergies ϵ_q and the eigenfunctions $A_q^\pm(r)$ of the elementary excitations. By adding/subtracting the two equations above by parts, one finds the standard form of the Bogoliubov eigen-energy equations (see for example Ref. [135]) with the density and phase amplitudes of the excitations,

$$A_q^\pm = u_q \pm v_q, \quad (3.10)$$

being related with the Bogoliubov amplitudes u_q, v_q (see Eq. (2.62)).

³From now on, we omit subscripts for the 2D quantities, while using an explicit label for the corresponding three-dimensional quantities when necessary.

$n = \langle \hat{n}(r) \rangle$, one can recover a Bogoliubov spectrum of excitations (see Box 3.1) even in the absence of a BEC⁴, rendering superfluidity possible. By applying the Bogoliubov theory in the 2D gas, we can reach two important conclusions: density fluctuations are suppressed and phase fluctuations destroy long-range order. We discuss these two results in the following Sec. 3.2.1.

3.2.1 Implications of the Bogoliubov analysis

Suppression of density fluctuations and the quasi-condensate

The long-wavelength Bogoliubov excitations are phonons with amplitudes $u_q, v_q \approx 1/\sqrt{2q\xi} \gg 1$ (Sec. 2.3.3). Their density A_q^- and phase A_q^+ components (see Box 3.1) are given by $A_q^\pm = u_q \pm v_q$. By combining these relations, one finds that $A_q^+ \gg A_q^- \approx 0$ for the case of phonons, and therefore density fluctuations become unimportant at large scales ($> \xi$). The suppression of density fluctuations has significant consequences for the behaviour of the 2D gas, as we describe below. Since in an ideal gas there are no phonon excitations, one can easily attribute this reduction to interactions.

This suppression, expressed also as $\langle \delta \hat{n}^2 \rangle < n^2$ with $\langle \delta \hat{n}^2 \rangle = \langle \delta \hat{n}(r=0) \delta \hat{n}(0) \rangle$, results⁵ in a second-order correlation $g_2(0) < 2$ and thus in a deviation from the expected behaviour $g_2(0) = 2$ of a Bose gas in the absence of a BEC owing to the bunching of bosons. In fact, for very low temperatures $g_2(0) \rightarrow 1$ and the gas resembles a BEC where the density fluctuations can be totally neglected. The regime where a ‘local BEC’ exists⁶ is called the quasi-condensate regime; one can straightforwardly define a quasi-condensate density n_{qc} with $n_{\text{qc}}^2 = [2 - g_2(0)]n^2$. In analogy to a BEC, the quasi-condensate can be characterised by a classical field

$$\psi_0(r) = \sqrt{n_{\text{qc}}} e^{j\theta(r)}, \quad (3.11)$$

with a spatially-dependent phase $\theta(r)$ and identical local properties a genuine BEC would manifest: a quasi-condensate should show the same reduction of the three-body recombination rate and the same density profile as a true BEC.

With such a classical field describing the properties of the low-temperature gas, the Hamiltonian of Eq. (3.5) is approximated by a classical Hamiltonian, analog to Eq. (2.59), of the form

$$H = \frac{\hbar^2}{2m} n_{\text{qc}} \int (\nabla \theta(r))^2 d^2r \quad (3.12)$$

up to an additive constant $gn_{\text{qc}}^2 \int d^2r/2$. In the following we further make the heuristic substitution $n_{\text{qc}} \rightarrow n_{\text{s}0}$, with $n_{\text{s}0}$ the superfluid density of the 2D gas as if only Bogoliubov excitations were

⁴A formal justification of the applicability of Bogoliubov theory to 2D was shown in Ref. [146].

⁵Directly from the definition of the density-density correlation function in Sec. 2.3.1 and after neglecting the shot-noise contribution, one finds $\langle \delta \hat{n}^2 \rangle / n^2 = g_2(0) - 1$.

⁶The identification of the quasi-condensate as a true BEC requires a test on the existence of long-range order, and the answer to that is negative, as we discuss below.

present. This substitution is qualitatively justified if one identifies the Hamiltonian in Eq. (3.12) as the kinetic energy of a superfluid through the superfluid velocity $v_s = \hbar \nabla \theta / m$.

Absence of long-range order

The other important consequence from Bogoliubov theory is the destruction of long-range order through fluctuations in the phase field of the excitations. The investigation of long-range order requires the analysis of the first order correlation function $g_1(r)$ at $r \rightarrow \infty$ (Sec. 2.3.2). The use of the classical field of Eq. (3.11) gives $g_1(r) \approx \langle e^{j[\theta(r) - \theta(0)]} \rangle$. Starting from this expression, one finds an algebraic decay of the correlations (see Box 3.2),

$$g_1(r) \approx (r/\xi)^{-1/D_{s0}} \quad (3.13)$$

for $r > \xi$, where we introduced the dimensionless superfluid phase-space density of the gas, $D_{s0} = n_{s0} \lambda^2 = 2\pi \hbar^2 n_{s0} / m k_B T$. This result shows that for $T = 0$ a BEC does indeed exist with $n_0 = n_{qc} \approx n$ since $D_{s0} = 2\pi \hbar^2 n_{s0} / m k_B T \rightarrow \infty$. For any finite T , however, $g_1(r \rightarrow \infty) = 0$ and long-range order is destroyed. This result, first derived in Ref. [147], is in agreement with the Mermin-Wagner-Hohenberg theorem [65, 66].

Using Eq. (3.13) we can define some characteristic size l_b of the Bogoliubov phase fluctuations as $\langle [\theta(l_b) - \theta(0)]^2 \rangle \sim 1$, resulting in $l_b \sim \xi \exp\{D_{s0}/2\}$ [144]. For temperatures of interest, one finds $l_b \gg \xi$ and thus the existence of block of size l_b^2 characterised by true BEC.

3.2.2 The Berezinskii-Kosterlitz-Thouless phase transition

Long-wavelength Bogoliubov phase fluctuations destroy long-range order in 2D, but they do not suffice to explain the superfluid to normal-gas phase transition, indicated also by the change of $g_1(r)$ from decaying algebraically at low temperatures (Eq. (3.13)) to exponentially at higher temperatures. To describe the transition, one needs to take into account the excitation of quantised vortices, non-linear excitations on top of which small-amplitude Bogoliubov phase fluctuations still exist. Vortices can be seen as stationary solutions in the GP equation; it is the classical field directly associated with the suppression of density fluctuations (the quasi-condensate) that provides the platform for the excitation of vortices.

A single vortex is characterised by a point of phase singularity (defect) at which the density of the gas must vanish and around which the phase varies by $2\pi\nu$ with an integer vorticity ν . The size of a vortex is of the order of the healing length ξ ; for larger distances the effect of a vortex in the density of the gas is negligible, justifying the suppression of density fluctuations even in the presence

Box 3.2: Destruction of long-range order

Starting from $g_1(r) \approx \langle e^{j[\theta(r) - \theta(0)]} \rangle$, it is common to use a cumulant expansion^a for $g_1(r)$ which allows to express it as

$$g_1(r) \approx e^{-\frac{1}{2} \langle [\theta(r) - \theta(0)]^2 \rangle}. \quad (3.14)$$

The quantity $\langle [\theta(r) - \theta(0)]^2 \rangle$ can be calculated within the long-wavelength limit of the Bogoliubov formalism, and using Eq. (3.8) we get

$$\langle [\theta(r) - \theta(0)]^2 \rangle = \frac{1}{2n_{s0}} \sum_{\epsilon_q < \mu} \frac{\epsilon_q}{\epsilon_q^0} [2N^0(\epsilon_q) + 1] [1 - \cos(qr)]. \quad (3.15)$$

With the low-temperature approximation $2N^0(\epsilon_q) + 1 \approx 2k_B T / \epsilon_q$ and looking for the asymptotic behaviour for $qr \rightarrow \infty$ after converting the sum into an integral, one finds

$$\langle [\theta(r) - \theta(0)]^2 \rangle \approx \frac{mk_B T}{\hbar^2 \pi n_{s0}} \ln(r/\xi), \quad (3.16)$$

the length-scale of ξ entering due to the cut-off μ in the summation. Combining Eqs. (3.14) and (3.16), we find the final result of Eq. (3.13) stated in the main text.

^aFor the random variable $X = j[\theta(r) - \theta(0)]$ one may write $\langle e^X \rangle = \exp(\sum_i \kappa_i / i!)$ with κ_i the cumulants of X . The first-order $\kappa_1 = \langle X \rangle$ has to be zero in our case and the second-order $\kappa_2 = (\langle X^2 \rangle - \langle X \rangle^2) / 2$ leads to the result mentioned in the main text. The higher orders can be neglected for $r \rightarrow \infty$; more details can be found in Ref. [147].

of vortices. On the contrary, the abrupt change⁷ in the phase introduced by a vortex plays a substantial role in the coherence of the gas, even if the probability of exciting vortices of considerable energy is much smaller than smooth Bogoliubov excitations.

Below, we first present a simplistic argument based on the thermodynamics of the vortices that however captures the main properties of the BKT transition: a topological transition from a superfluid to a normal gas with a discontinuity in the superfluid density at the critical point emerging due to the proliferation of free vortices in the 2D gas. To estimate the superfluid density for temperatures close to the critical T_c , however, we need to go beyond that simplistic model and consider the more systematic analysis first conducted by Kosterlitz: the renormalisation-group approach. Together with the properties of scale invariance of the quasi 2D gas and of the universality close to the transition, we finally discuss the predicted superfluid density close to the transition.

The superfluid to normal-gas BKT transition

The essentials of the BKT phase transition can be revealed by considering the simplest case of a transition between a state with no vortices and a state with a single vortex, as depicted in Fig. 3.1(a) and (b), respectively. The two configurations with a different net vorticity, $\nu = 0$ and $\nu = 1$, respectively, are said to be topologically distinct: smooth deformation⁸ of the phase field in one configuration to generate the second leads to inevitable discontinuities at the boundaries of the

⁷For any two points along a line passing through the singularity but in opposite sides with respect to the latter there is a phase difference of $\nu\pi$, no matter how close these two points lie.

⁸i.e. by keeping the field spatially continuous during this process.

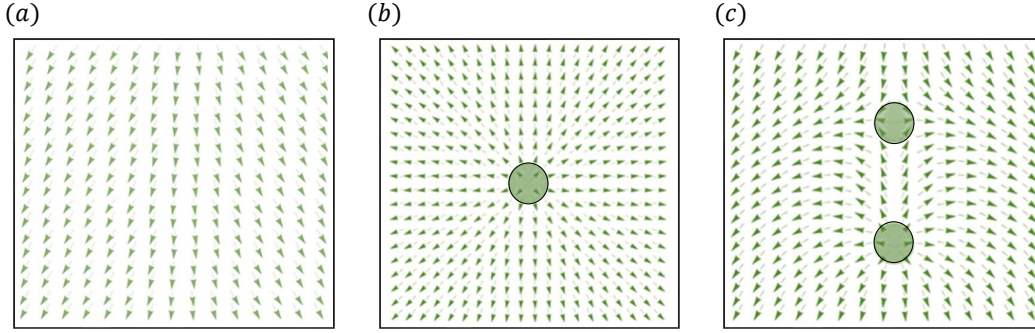


Figure 3.1: A pictorial representation of the phase of a classical field; the arrows at any point visually represent the phase field in the plane. In (a) only large-scale Bogoliubov excitations with a total vorticity $\nu = 0$ constitute the phase field, corresponding to low T . In (b) a single vortex with net vorticity $\nu = 1$ is shown. A vortex changes the long-distance behaviour of the phase inducing a distinct topology. Two bound vortices as in (c), on the other hand, restore the topology of (a) as one can see by comparing the phase field at the edges of these two cases.

system; there is a large energy gap and a large energy cost between such states making them robust against each other. Vorticity then becomes a topological invariant for the gas and the transition between states of different vorticity is called a topological phase transition.

A qualitative argument of why this topological transition is connected with superfluidity is as follows: Assume some superfluid move in a vortex-free configuration, say along x , with a velocity $v_s = \frac{\hbar}{m} \frac{\Delta\theta}{L}$, where $\Delta\theta$ the phase difference in a length L as imposed by some external conditions. When the vortex is present, this phase is modified as $\Delta\theta \rightarrow \Delta\theta - \pi$ resulting in a reduced superfluid velocity and if $\Delta\theta < \pi$ in the destruction of superfluidity.

Based on Fig. 3.1(a) and (b), one observes that the effect of a vortex in the phase remains strong even far from its core. One can estimate the additional energy of the single-vortex state compared to the vortex-free case as⁹ $E_v = k_B T (D_{s0}/2) \ln(R/\xi)$. The vortex of an area $\sim \xi^2$ can be anywhere in the plane of an area $\sim R^2$ and thus it carries an entropy $S_v = \ln(R/\xi)^2$. The free energy $F_v = E_v - k_B T S_v$ associated with the vortex, or expressed now as $F_v = (D_{s0} - 4)(k_B T/2) \ln(R/\xi)$, quantifies the favourability of a vortex excitation. For $D_{s0} > 4$, one gets $F_v > 0$ and the vortex remains energetically unfavourable; on the contrary, when $F_v < 0$ the vortex-state is excited and the quasi-long range order together with the superfluidity are diminished. The critical point is thus related with $F_v = 0$, or equivalently with

$$D_{s0} = 4, \quad (3.17)$$

and since $D_{s0} = 0$ in the normal-gas phase, this transition is characterised by a universal jump in

⁹When discussing about vortices, it is typical to assume circularly symmetric systems of some large radius R , instead of a box system we discussed up to now. This will not modify the physical arguments since we consider $R \rightarrow \infty$ for the thermodynamic limit. In this case, the energy of the vortex is found from Eq. (3.12) as $E_v = \frac{\hbar^2}{2m} n_{s0} \int (\nabla\theta)^2 d^2r$ with $\nabla\theta = i_\theta/r$ (i_θ being the unit vector along the θ direction). Substituting, we find $E_v = \frac{\hbar^2}{2m} n_{s0} \int_\xi^R \frac{2\pi r dr}{r^2}$ and finally the result in the main text.

the superfluid density¹⁰.

In a more realistic situation, it is the existence of a reservoir of free vortices that eventually forces superfluid velocity to go to zero. In the same more realistic scenario, it is not the vortex-free state as in Fig. 3.2 (a) which serves as the background platform, but rather a situation like in Fig. 3.2 (c): a state of bound-pairs of vortices with opposite winding. The net vorticity in (c) is $\nu = 0$, so this case remains topologically equivalent to the vortex-free state depicted in (a). This equivalence becomes apparent by checking the long-distance field from the vortex-pair, with similar boundaries. This observation intuitively justifies the claim that the reduction of the superfluid velocity by such a pair remains negligible compared to the single-vortex situation.

Renormalisation-group and the superfluid density

To obtain more quantitative results beyond the superfluid-density jump, we present the key results from a renormalisation-group analysis, without going into details that lie beyond the scope of this thesis. The starting point of such an analysis is the classical Hamiltonian of Eq. (3.12), which remains still (approximately) valid despite the presence of vortices, after the substitution $\theta(r) \rightarrow \theta_B(r) + \sum_i \nu_i \Theta(r, r_i)$. Here $\theta_B(r)$ corresponds to the Bogoliubov phase fluctuations and the sum-term takes into account the random distribution of vortices, each characterised by a central position r_i and a vorticity ν_i . Using this Hamiltonian, Kosterlitz found that the superfluid density D_s of the gas satisfies

$$D_s^{-1} = D_{s0}^{-1} + 2\pi^2 \mathcal{Y}_0^2 \int_{\xi}^{\infty} \frac{dr}{\xi} \left(\frac{r}{\xi}\right)^{3-D_{s0}} \quad (3.18)$$

with \mathcal{Y}_0 the fugacity of the vortices in the system. Eq. (3.18) can be seen as a modification of the Bogoliubov-predicted bare superfluid density D_{s0} due to the existence of vortices (second term).

The above Eq. (3.18) does not directly provide the superfluid density D_s in the gas, since it depends on the unknown Bogoliubov component D_{s0} and the fugacity of the vortices. The renormalisation-group approach shows how D_s can be extracted through an equivalent but simpler system after integrating out all short length scales r (equivalently we define l such that $\xi < r < \xi' = \xi e^l$) and transferring the effect of the vortices at these small scales into the phonon contribution D_{s0} . With this integration out, pairs of vortices of relative distance r_0 with $\xi < r_0 < \xi e^l$ are eliminated from the new Hamiltonian since their phase fluctuations become negligible at lengths $> \xi e^l$. This is not the case for single vortices whose effect on fluctuations remains significant at large distances. By keeping only the largest scales of the system, one constructs an equivalent gas with (as in Fig. 3.1(b)) or without (as in Fig. 3.1(a)) single vortices.

In a more technical language, one can split the integral of Eq. (3.18) into two parts $\int_{\xi}^{\infty} = \int_{\xi}^{\xi e^l} + \int_{\xi e^l}^{\infty}$, and embed the first part in D_{s0}^{-1} . A scale-dependent Bogoliubov superfluid density $\mathcal{D}_s(l)$

¹⁰In the following we keep discussing the dimensionless superfluid (and total) phase-space density; for simplicity we refer to them directly as densities and appreciate this will not cause any confusion.

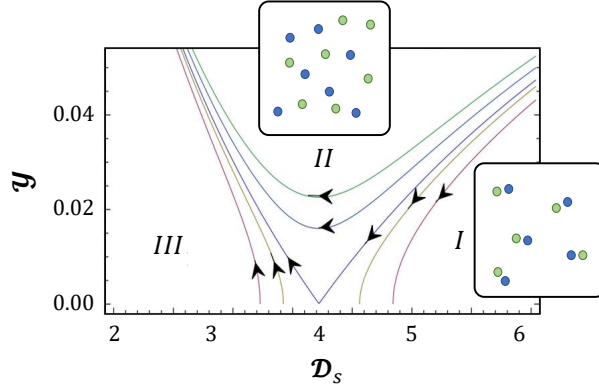


Figure 3.2: The BKT flows: Any point in the plane corresponds to an initial condition for the renormalisation equations of Eq. (3.20); physically this initial point represents the system's experimentally unmeasurable bare superfluid density of the Bogoliubov excitations and concentration of vortices when all scales $> \xi$ are considered. The line passing through that specific point gives the relevant solution of the renormalisation equations for the various integrated scales l ; different lines represent solutions with different initial conditions. The arrow in each line points towards increasing l . The physically relevant superfluid density for any initial point is identified as the corresponding solution for $l \rightarrow \infty$. The plane is separated into three regions. For initial points belonging to region I, the corresponding $\mathcal{Y}(l \rightarrow \infty) = 0$ and $\mathcal{D}_s(l \rightarrow \infty) \neq 0$; the gas is in its superfluid state. For points belonging to regions II or III, one gets $\mathcal{D}_s(l \rightarrow \infty) = 0$; the gas is in its normal state. The critical point corresponds to the separatrix (purple line) between regions I and II with a universal $\mathcal{D}_s(l \rightarrow \infty) = 4$. The separatrix between regions II and III does not have any physical significance. Physically, the difference between the two distinct situations is explained in the two cartoons with the (un)binding of vortex pairs.

is then obtained with $\mathcal{D}_s(l)^{-1} = D_{s0}^{-1} + 2\pi^2 \mathcal{Y}_0^2 \int_{\xi}^{\xi e^l} \frac{dr}{\xi} \left(\frac{r}{\xi}\right)^{3-D_{s0}}$, such that the full superfluid density is written as

$$D_s^{-1} = \mathcal{D}_s(l)^{-1} + 2\pi^2 \mathcal{Y}(l)^2 \int_{\xi^l}^{\infty} \frac{dr}{\xi^l} \left(\frac{r}{\xi^l}\right)^{3-D_s(l)} \quad (3.19)$$

with an also rescaled fugacity $\mathcal{Y}(l) = e^{(4-D_{s0})l/2} \mathcal{Y}_0$ [148]. The superfluid density of the gas can then be straightforwardly extracted as $D_s = \mathcal{D}_s(l \rightarrow \infty)$ - since the remaining integral in Eq. (3.19) vanishes - if the behaviour of $\mathcal{D}_s(l)$ is known. To that end, one considers an infinitesimal change in the scale dl in the defining relations for $\mathcal{D}_s(l)$ and $\mathcal{Y}(l)$ to obtain Kosterlitz's equations

$$\begin{aligned} \frac{d\mathcal{D}_s(l)}{dl} &= -2\pi^2 \mathcal{Y}^2(l) \mathcal{D}_s^2(l), \\ \frac{d\mathcal{Y}(l)}{dl} &= [4 - \mathcal{D}_s(l)] \mathcal{Y}(l)/2. \end{aligned} \quad (3.20)$$

which express the change in the effective Bogoliubov superfluid density and fugacity of the gas when one integrates out an infinitesimal amount of size.

In the following, we discuss an analytic result for the superfluid density based on the above renormalisation equations and the prescription $D_s = \mathcal{D}_s(l \rightarrow \infty)$ for temperatures close to the transition point for the quasi-2D atomic Bose gas. Before that, we briefly discuss the general behaviour of the numerical solutions of Eqs. (3.20) as depicted in Fig. 3.3. In this plot, any point in the $\mathcal{D}_s - \mathcal{Y}$ plane represents a potential bare $\{D_{s0}, \mathcal{Y}_0\}$ and the line passing through that point connects it with its cor-

responding $\{\mathcal{D}_s(l), \mathcal{Y}(l)\}$ for various l . The arrows on the lines indicate the direction of increasing l . One can identify two physically distinct (sets of) regions. Region I results in a finite $\mathcal{D}_s(l \rightarrow \infty)$ and a zero $\mathcal{Y}(l \rightarrow \infty)$, and thus it describes the low temperature regime characterised by tightly-bound pairs of vortices and by a finite superfluid density. Regions II and III give a zero superfluid density and a large density of vortices as $l \rightarrow \infty$, corresponding to the high temperature phase of the 2D Bose gas with a proliferation of free vortices. In between regions I and II, the separatrix (purple line) determines the critical point of the BKT transition, from which one regains the critical condition of Eq. (3.17), now with the experimentally-relevant renormalised superfluid density, and the jump in the superfluid density.

The superfluid density in an atomic gas: Close to the BKT transition (critical fluctuation regime), from the superfluid side, a quasi-2D Bose gas behaves in a scale-invariant and universal way. We already introduced the concept of scale invariance due to the density-independent and dimensionless \tilde{g} ; dimensionless quantities, like the superfluid density D_s , depend only on the quantity $x = \mu/k_B T$ for a fixed \tilde{g} . The notion of universality, on the other hand, stems from the fact that the microscopic details of the transition mechanism become irrelevant as the transition point is approached, and is a general feature of phase transitions. By combining these two properties, the superfluid density D_s then is expected to show a universal behaviour for different \tilde{g} and depend only on the rescaled quantity $X = (x - x_c)/\tilde{g}$, with $x_c = \mu_c/k_B T$ the value of x at the critical point.

Using the recursion relations of Eq. (3.20) together with the scale-invariance and universality properties of the atomic gas, the superfluid density satisfies

$$4/D_s(X) + \ln[D_s(X)] = \kappa(X) + \ln(4), \quad (3.21)$$

with κ a scale-independent quantity and where we introduced the $\ln(4)$ -term such that Eq. (3.21) is consistent with the results in Ref. [115] (see discussion below). A sketch of the derivation of Eq. (3.21) is given in Box. 3.3.

The extraction of D_s from Eq. (3.21) requires the knowledge of the quantity $\kappa(X)$. A simple analytic treatment for κ is not available, and thus Prokofev and Svistunov [115] proceeded to a numerical study; using classical Monte-Carlo simulation on a lattice that belongs to the same universality class as the 2D Bose gas, they found to a very good approximation that $\kappa(X) = 1 + \kappa'X$ with $\kappa' = 0.61 \pm 0.01$. Eq. (3.21) provides D_s for various temperatures, as long as the relation between X and T/T_c is known. We will discuss the latter in the following section.

Box 3.3: The superfluid density from the BKT recursion relations

The first step to extract $D_s = \mathcal{D}_s(l \rightarrow \infty)$ from the renormalisation-group relations of Eq. (3.20) is to eliminate the role of the fugacity $\mathcal{Y}(l)$. To that end, we note that the second recursive equation yields $d\mathcal{Y}^2/dl = 2\mathcal{Y}[d\mathcal{Y}/dl] = \mathcal{Y}^2(4 - D_s)$ and thus by combining with the other equation, we get

$$d\mathcal{Y}^2 = \frac{\mathcal{D}_s - 4}{2\pi^2 \mathcal{D}_s^2} d\mathcal{D}_s. \quad (3.22)$$

or

$$2\pi^2 \mathcal{Y}^2 = \ln(\mathcal{D}_s) + 4/\mathcal{D}_s - C. \quad (3.23)$$

The constant of integration C in our nomenclature is associated with the parameter κ of the main text as $C = \kappa + \ln(4)$ and depends only on X through the universality and scale invariance of the gas.

Substituting Eq. (3.23) in the first equation of Eq. (3.20) we finally get

$$\frac{d\mathcal{D}_s}{\mathcal{D}_s^2 [\ln(\mathcal{D}_s) - C] + 4\mathcal{D}_s} = -dl. \quad (3.24)$$

By integrating Eq. (3.24) for any fixed X :

$$\int_{\mathcal{D}_s(l_1)}^{\mathcal{D}_s(l_2)} \frac{d\mathcal{D}'_s}{\mathcal{D}'_s^2 [\ln(\mathcal{D}'_s) - C] + 4\mathcal{D}'_s} = l_1 - l_2, \quad (3.25)$$

from which for $l = l_2 - l_1 \rightarrow \infty$, the denominator of the l.h.s. must vanish, to find Eq. (3.21) in the main text.

3.2.3 The equation of state for the atomic two-dimensional Bose gas

The BKT theory sets the framework for understanding the behaviour of the superfluid density $D_s = n_s \lambda^2$, including its universal jump at the critical temperature T_c , but it does not provide any link with the total (phase-space) density $D = n \lambda^2$ of the gas. Due to its experimental accessibility and its connection to the thermodynamics of the gas, D is an important quantity that has been widely studied, both theoretically and experimentally. Through D , the critical point can be experimentally identified (since D_s is much harder to measure) and a connection between the universal parameter X and the temperature T/T_c of the gas is provided, i.e. $T/T_c = D_c/D(X)$, with D_c the density at the critical point. Unlike D_s , the total density does not manifest a universal behaviour at the critical point, but shows a \tilde{g} -dependence. Also unlike D_s , the total density retains a smooth behaviour at the critical point; the infinite-order BKT transition provides no discontinuity in any thermodynamic quantity.

In this section, we describe the behaviour of D with T/T_c , a relation that constitutes an equation of state (EoS) for the quasi-2D gas. The EoS, together with the dimensionless phase-space pressure $\mathcal{P} = \lambda^2 p/k_B T$, with p the pressure, provides the means for the extraction of all the thermodynamic quantities of the gas. The EoS will be proven invaluable to us, both for the experimental thermometry of the 2D gas and for the deduction of the superfluid density.

Different theories for D can appropriately describe different regions of $x = \mu/k_B T$ or equivalently different temperatures of the gas. In Fig. 3.3 we give an overview of the various regimes of the

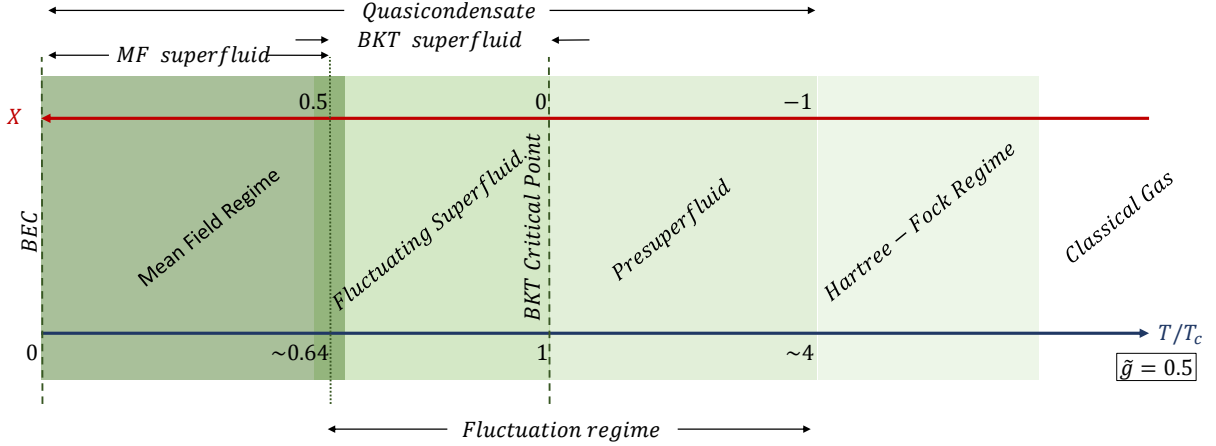


Figure 3.3: The various temperature regimes of the scale invariant 2D Bose gas versus the universal X and versus temperature (rescaled for the specific $\tilde{g} = 0.5$). The fluctuation region of the BKT transition is characterised by $-1 \lesssim X \lesssim 0.5$. The analytic treatment of Ref. [115] for the EoS is derived in the crossover $X \approx 0.5$ between the fluctuation and the mean-field regimes from the superfluid side but it remains valid in the whole superfluid region. For the superfluid density, two distinct predictions exist; the mean-field prediction, valid for $X \gtrsim 0.5$ and the BKT prediction for $0 \lesssim X \lesssim 0.5$.

quasi-2D gas, expressed both through the universal parameter X and through the temperature T/T_c as scaled for the specific case of an intermediate $\tilde{g} = 0.5$. In Fig. 3.4 we plot the predictions of these various theories for (a) D and (b) \mathcal{P} for the same case of $\tilde{g} = 0.5$, together with the Monte Carlo results [115] rescaled to the same \tilde{g} . It is worth noting here that scale invariance remains valid for all values of T/T_c , from a pure superfluid to a purely thermal cloud, validating a description with respect to x . We now give a brief description of these various regions for the 2D gas, starting from high temperatures (low X). After that, we summarise the final extracted EoS based on the different theoretical and numerical approaches together with the corresponding superfluid-density from the renormalisation-group results.

Classical regime: In the limit of very high temperatures (always having in mind restrictions related to 2D-ness), a classical-gas study yields $D_{\text{class}} = e^x$, while the pressure, generally connected with the density as $D = d\mathcal{P}/dx$, becomes also $\mathcal{P}_{\text{class}} = e^x$ since $\mathcal{P}_{\text{class}}(x \rightarrow -\infty) \rightarrow 0$.

Hartree-Fock regime: When quantum degeneracy comes into play, the ideal 2D Bose gas behaves as $D_{\text{ideal}} = -\ln(1 - e^x) \equiv G_1(e^x)$ [149] and $\mathcal{P}_{\text{ideal}} = G_2(e^x)$, where $G_i(z) = \sum_{k=1}^{\infty} \frac{z^k}{k^i}$ are the Polylogarithmic functions of order i . Taking further into account mean-field interactions and assuming a fully density-fluctuating ($g_2(0) = 2$) gas, one can replace $\mu \rightarrow \mu - 2g_{\text{q2D}}n$ to get the Hartree-Fock (HF) model for the phase-space density

$$D_{\text{HF}} = -\ln\left(1 - e^{x - \tilde{g}D_{\text{HF}}/\pi}\right), \quad (3.26)$$

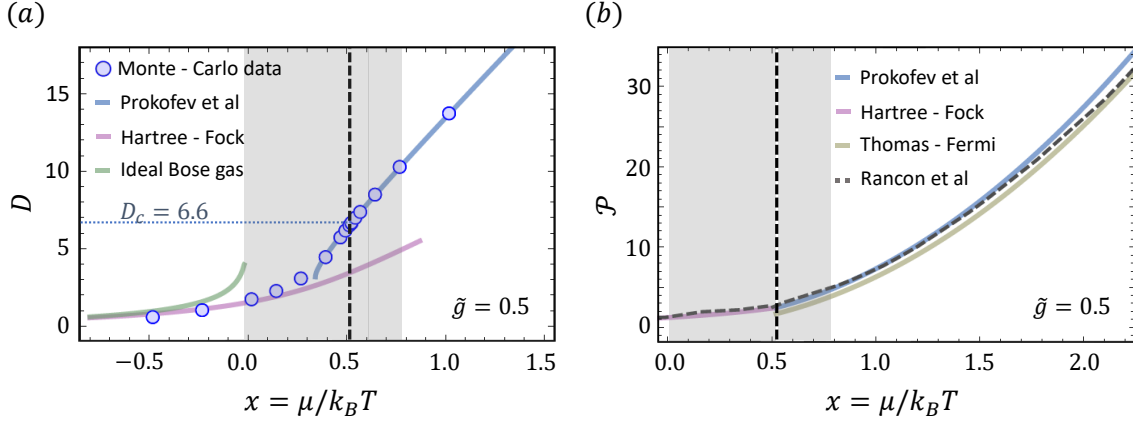


Figure 3.4: (a) The dimensionless phase-space density of the low- T 2D Bose gas with $\tilde{g} = 0.5$. The shaded region denotes the fluctuation regime, which corresponds to the temperature range $0.64 \lesssim T/T_c \lesssim 4$. The vertical straight line represents the BKT critical point. Below T_c , the analytic approximation of Ref. [115], agrees well with Monte Carlo (MC) simulations. The Hartree-Fock prediction seems to be valid only in the absence of the quasi-condensate, beyond the fluctuation region. (b) Predictions for the phase-space pressure \mathcal{P} for the same \tilde{g} . The extraction of \mathcal{P} by integrating the ‘Prokofev function’ requires some unknown constant of integration. We pick to match the extracted \mathcal{P} with the corresponding value of the Hartree - Fock (HF) theory at the critical point, in agreement with experimental results [38, 39] and the numerical investigation by Rancon et al [150]. By plotting the latter, we see how the behaviour of \mathcal{P} changes from being in agreement with the HF theory to agreeing with the mean field TF theory when decreasing the temperature. Based on this, we can estimate that the TF theory works pretty well for $T/T_c < 0.25$.

which can be self-consistently calculated. The pressure can be also numerically extracted by integrating the resulting density with $\mathcal{P}_{\text{HF}}(x \rightarrow -\infty) \rightarrow 0$. The HF model remains a good description for the gas only in the absence of the quasi-condensate, due to the assumed form of the mean field (no suppressed density fluctuations).

Pre-superfluid regime: The appearance of the quasi-condensate forces the gas to enter its pre-superfluid regime and provides a classical field that serves as a background for vortices to emerge. The pre-superfluid behaviour typically appears at $x \approx 0$, or equivalently $X \approx -1$ (see Eq. (3.28)) which corresponds to $T(X)/T_c \sim 4$ (with a weak \tilde{g} -dependence), a result that is in agreement with experimental studies [74, 75, 151]. The pre-superfluid phase of the gas terminates at the BKT critical point with the pairing of the vortices and the emergence of superfluidity. A precise analytical prediction in this region for D is lacking, and one relies on numerical Monte-Carlo simulations. For the pressure \mathcal{P} , on the other hand, experimental studies seem to agree with the Hartree-Fock prediction down to the critical point [38].

The critical point: The critical point can be qualitatively approached with a simple analytical argument that starts by expressing the total density as $n = n_{\text{qc}} + \tilde{n}$, with $\tilde{n} \approx \int_{q_\xi}^{q_T} N^0(\epsilon_q) d^2q / (2\pi)^2$ the non-quasi-condensed component. The integral is restricted between the inverse healing length $q_\xi \sim \sqrt{\tilde{g}n}$ and an arbitrary cut-off of the order the thermal momentum, $q_T \sim \sqrt{mk_B T / \hbar^2}$. With

$\epsilon_q = \epsilon_q^0 \equiv \hbar^2 q^2 / (2m)$, one gets $\tilde{n} \sim \frac{mk_{\text{B}}T}{2\pi\hbar^2} \ln(q_T^2/q_\xi^2)$ and subsequently using the fact that at the critical point it is $n_{\text{qc}} \sim n_s(T_c^-) = \frac{4mk_{\text{B}}T}{2\pi\hbar^2}$ and $n \sim n_{\text{qc}}$ (and thus $q_\xi \sim \sqrt{\tilde{g}mk_{\text{B}}T/\hbar^2}$), we find the general scaling of the critical density $n_c \sim \frac{mk_{\text{B}}T}{2\pi\hbar^2} (4 + \ln(1/\tilde{g}))$. By inserting an unknown constant ξ_n to take into account the various inaccuracies, we write

$$D_c \equiv \frac{2\pi\hbar^2 n_c}{mk_{\text{B}}T} = \ln\left(\frac{\xi_n}{\tilde{g}}\right). \quad (3.27)$$

This scaling verifies once again that the BKT transition is driven by interactions since $D_c \rightarrow \infty$ for $\tilde{g} \rightarrow 0$. The constant ξ_n cannot be properly extracted from an analytical treatment. In Ref. [152] it was numerically deduced to be $\xi_n = 380 \pm 3$ for a very-weakly interacting gas, by using a classical Monte Carlo (MC) simulation. In a similar way, the critical normalised chemical potential is found to be

$$x_c = \frac{\tilde{g}}{\pi} \ln(\xi_\mu/\tilde{g}), \quad (3.28)$$

with $\xi_\mu = 13.2 \pm 0.4$.

Fluctuation regime on the superfluid side: In the presence of the superfluid, close to the BKT transition the total density gains additionally the universal character of the critical fluctuation regime, expressed as

$$D(X) - D_c = 2\pi M(X) \quad (3.29)$$

with $M(X)$ denoting the universal scaling with X . A characteristic of the 2D system is the existence of a broad critical-fluctuation regime. Because of that, the universal behaviour becomes dominant and captures almost the whole range of interest of X values studied within this thesis. From the superfluid side, the fluctuation realm extends up to $X \approx 0.5$ or equivalently $T(X)/T_c \sim 0.65 - 0.70$, as numerically investigated in [115].

A density-fluctuation-suppressed mean-field regime: At even lower temperatures ($X > 0.5$), a simple mean field approach is restored. Here, however density fluctuations are suppressed, i.e. one replaces $\mu \rightarrow \mu - g_{\text{q2D}}n$ [115]. Further, in the limit of zero temperature (Thomas-Fermi regime), the phase-space density becomes $D_{\text{TF}} = 2\pi x/\tilde{g}$ and the pressure $\mathcal{P}_{\text{TF}} = \pi x^2/\tilde{g}$.

The region around the boundary $X \approx 0.5$ is expected to satisfy the properties of both universality (as in the fluctuating regime) and the predictions of the low-temperature mean field. By investigating this boundary and combining these two different predictions, the authors of Ref. [115] derived an analytic approximation for $M(X)$. After the extrapolation to smaller $X > 0$ and the comparison with Monte Carlo (MC) simulations, they somewhat surprisingly concluded that the resulting analytical $M(X)$ remains a good description down to the critical point ($X = 0$). This analytical result is also plotted in Fig. 3.4 and compared with the MC simulations. Based on these remarks, in Fig. 3.5 we plot

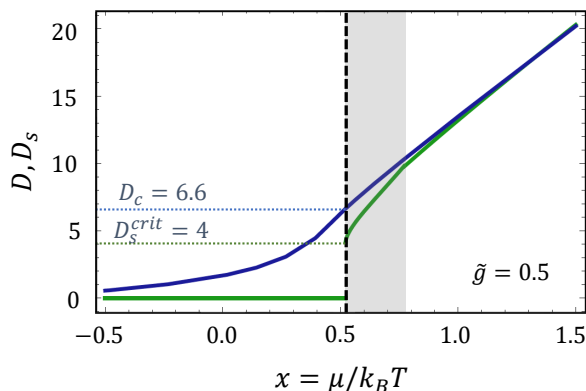


Figure 3.5: The superfluid density (green) for $\tilde{g} = 0.5$ as found separately at low temperatures ($x > 0.77$) and temperatures close to the BKT transition ($0.52 < x < 0.77$). Together we plot the total density, as a combination of analytic function of Ref. [115] in the superfluid region and an interpolation of the MC data for the pre-superfluid regime. The shaded region indicates the fluctuation regime from the superfluid side.

the overall prediction of $D(x)$ that we will use in the rest of this thesis (blue line), as a combination of the ‘Prokofev prediction’ at high x in the superfluid regime and an interpolation of the MC data and the Hartree-Fock prediction for $x < x_c$. This behaviour of D has been experimentally verified for various \tilde{g} [38, 153], including the ones for stronger interactions [39].

In the same Fig. 3.5, we finally show the prediction for the superfluid density (green line), the experimental extraction of which is the main topic of this thesis. Close to the critical point (shaded region), in the fluctuating regime, D_s is provided by Eq. (3.21) and the renormalisation-group treatment. For higher x (lower temperatures) where the gas enters the mean-field regime, this prediction strongly deviates, giving the unphysical result $D_s > D$; a mean-field prediction [115] is assumed instead, extracted from assuming only Bogoliubov excitations in Landau’s prescription for the normal component (see Eq. (2.40)). The merging of the two theories at the crossover between the fluctuation and the mean field regimes at $X = 0.5$ (or $x = 0.78$ for the case of $\tilde{g} = 0.5$ as in Fig. 3.5) gives the also unphysical kink in the D_s prediction.

Finally, as we mentioned in the beginning of this section, the combination of the (phase-space) density and pressure¹¹ is adequate for the extraction of all the thermodynamic quantities. Concentrating only on the relevant quantities for this work, one gets [154]

$$s = 2\mathcal{P}/D - x, \quad c_v = 2\mathcal{P}/D - D/(dD/dx), \quad \gamma = \frac{2\mathcal{P}(dD/dx)}{D^2}. \quad (3.30)$$

These thermodynamic quantities and the superfluid density will be important parameters for the sound propagation described by the two-fluid model of the atomic BKT superfluid, which will be

¹¹With a known $M(X)$ one can also extract the pressure of the gas in the fluctuation region. The only complication is the determination of the constant of the integration. We choose to satisfy $\mathcal{P}(x = x_c) = \mathcal{P}_{\text{HF}}(x = x_c)$, a condition that is very close to the theoretical prediction of a nonperturbative renormalisation-group approach [150] and has been verified experimentally both for weak [38] and stronger [39] interactions.

discussed in the next chapters.

3.3 Real gases: finite-size-system modifications

In ultracold atoms, the experimentally relevant samples of a few tens of microns in size will inevitably manifest finite-size effects and a modified behaviour compared to the gas studied previously in its thermodynamic limit. In this section we describe the expected deviations from the thermodynamic-limit behaviour as a background for discussing our results in chapter 5. Specifically, we are concerned with the effect of the quantisation of the excitation-mode energies in the gas that challenges the validity of a hydrodynamic description for the superfluid, and with the conversion of the BKT transition into a finite-width crossover. Before we go into more details for the finite-size-induced modifications, we note another possible source of deviations from the BKT theory: the dynamic probing of a real gas at finite frequencies and the introduced effects from the dynamics of (both bound pairs and free) vortices. The dynamic BKT theory [155, 156] that incorporated such effects was first presented to explain the behaviour of sound propagation in 2D helium [72] and recently [157] was adjusted to the language of ultracold gases. However, it is not yet clear if this mechanism is relevant for experiments in ultracold gases.

Questioning hydrodynamic conditions

The first direct consequence of a finite-sized system is the discretisation of its phononic spectrum of low-lying excitations, stemming from the need to satisfy the imposed boundary conditions. In two dimensions, the allowed wavevectors can be decomposed into two independent wavenumbers along the x and y direction. In each direction the allowed wavenumbers are $q = i\pi/L$ with $L = \{L_x, L_y\}$ the corresponding extent of the box and i a positive integer.

The phonon-energy discretisation has a detrimental effect in the ability of a typical atomic system to be hydrodynamic and will be an issue of discussion for our experimental results. To see that, we have to test the hydrodynamic condition of Eq. (2.1) for the lowest-lying excited mode of wavenumber $q = \pi/L$ and frequency ω . We find helpful to express Eq. (2.1) in an equivalent form as $\mathcal{K} \equiv \gamma_{\text{el}}/\omega \gg 1$. Using the elastic collision rate $\gamma_{\text{el}} = n_{3\text{D}}\sigma\bar{v}$, as introduced in Eq. (2.45), with a 3D density $n_{3\text{D}} \approx n/\ell_z$ and a velocity $\bar{v} \approx \hbar/(m\ell_z)$ coming from the confinement along z , we can estimate a lower bound for the ‘hydrodynamicity’ quantity \mathcal{K} as

$$\mathcal{K} \approx \frac{1}{\omega} \frac{\hbar n \tilde{g}^2}{2m}, \quad (3.31)$$

where we also used a cross-section $\sigma = 4\pi a^2$, assuming that for the range of interest the existence of a quasi-condensate has already totally reduced the fluctuations. An estimation for \mathcal{K} for the typical realisations of 2D atomic gases can be obtained if one substitutes $\omega \rightarrow \omega_{\text{B}} = c_{\text{B}}(\pi/L)$, with ω_{B} the

Bogoliubov frequency of the lowest mode to find

$$\mathcal{K}_B \approx \frac{\tilde{g}^{3/2} n^{1/2} L}{2\pi}. \quad (3.32)$$

In the weakly-interacting regime ($\tilde{g} \sim 0.1$), $\mathcal{K}_B \lesssim 1$ for typical gases ($L \sim 50\mu\text{m}$ and $n \sim 50\mu\text{m}^{-2}$); the hydrodynamic regime is difficult to be achieved.

Turning BKT transition into a crossover

The slow algebraic decay of correlations in the presence of a superfluid results in an extensive coherence for distances comparable to the system size L and thus in the appearance of a significant condensed fraction in the gas below T_c . At the critical point, one typically expects $g_1(L) \sim (L/\xi)^{-1/4} \approx 0.2 - 0.3$ for relevant \tilde{g} and L . Above T_c , with an exponential decay of correlations, $g_1(r) \sim e^{-r/l_c}$ with l_c the correlation length, a BEC would emerge roughly when $l_c \gtrsim L$ or equivalently at the critical phase-space density $D_{\text{BEC}} \approx \ln(4\pi L^2/\lambda^2)$, which is always larger than the BKT critical D_c for our experiments; a BEC does not appear without superfluidity.

However, the unavoidable termination of the renormalisation process at a scale $l = \ln(L/\xi)$, set by the system size, is already responsible for the modification of the BKT predictions. Due to the diverging behaviour of l_c as one approaches the BKT transition from above [149], i.e.

$$l_c = \lambda \exp\left(\frac{\sqrt{a_l T_c}}{\sqrt{T - T_c}}\right) \quad (3.33)$$

with a_l a constant of order unity¹², the modified effects will mainly appear in the region close to the transition. The net result is the conversion of the BKT transition into a crossover where the universal jump of D_s is rounded out into a steep yet continuous drop to zero.

A complete analytical study of the crossover-modifications is difficult; here we present some qualitative signatures of BKT in a finite system based on order-of-magnitude arguments and numerical simulations. Based on them, we identify a crossover region lying roughly between two characteristic temperatures T_1 and T_2 where the deviations from the infinite-system behaviour become most pronounced [159]. The boundary T_1 is characterised by $g_1(r) \propto r^{-1/4}$, similar to the behaviour at the critical point of the infinite system. The boundary T_2 is characterised as the lowest temperature at which $D_s = 0$. It is worth noting that based on the results of Ref. [159], the whole intermediate regime $T_1 < T < T_2$ still manifests an algebraic decay of $g_1(r)$ but with an exponent smaller than $-1/4$, a behaviour that is not allowed in the thermodynamic-limit. A third characteristic temperature T^* inside the crossover region, which often serves as the effective critical temperature for the finite-sized BKT transition, is identified as the one for which $D_s = 4$.

These three characteristic temperatures do not necessarily coincide with T_c , the critical temper-

¹²In Kosterlitz' theory of Ref. [158] it is assigned with the value $a_l \approx 2.25$.

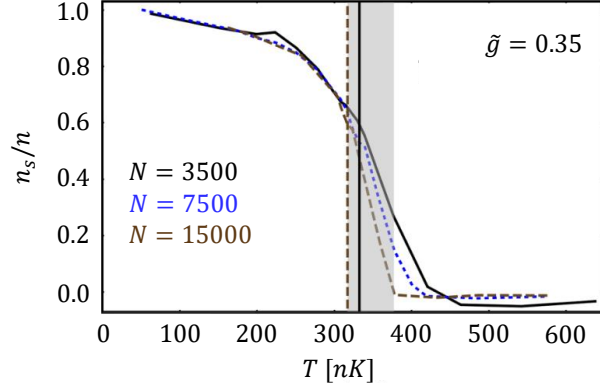


Figure 3.6: Finite-size effects in the superfluid fraction. A typical crossover region (shaded area) characterised by the edge temperatures T_1 and T_2 (see text) for a specific \tilde{g} and three different N for fixed n . The vertical straight line represents the ‘infinite-system’ T_c . The figure is reproduced from [159].

ature of the infinite system; the exact relative location of T_c inside the crossover region depends on L . Since T_2 is the highest temperature for which modifications are visible, one can approach the difference between T_c and T_2 from Eq. (3.33) with $l_c = L$ as

$$\frac{T_2 - T_c}{T_c} \approx \frac{a_l}{[\ln(L/\lambda)]^2}. \quad (3.34)$$

For the typical experimental values discussed above and for $a_l \sim 2$, we get a value $T_2 \sim 1.1T_c$. On the other hand, the definition of T_1 does not allow some simple analytic treatment to estimate its relation with T_c . However, numerical results [159–162] suggest that $T_c - T_1 \ll T_2 - T_c$, indicating that the superfluid region is not affected to the same degree by the departure from the thermodynamic limit. Finally T^* is shifted towards higher temperatures with decreasing L , linked with T_c as [163, 164]

$$T^*(L) - T_c \approx (T_2 - T_c)/4 \quad (3.35)$$

which gives a relative increase of $\sim 2\%$ for the previously used typical experimental values.

A brief summary: In this chapter we presented the main properties of a 2D ultracold-gas system, characterised by its scale-invariance that stems from the intrinsic three-dimensional character of the interatomic interactions. The description of the low-temperature region of this system requires to consider two types of excitations: smooth Bogoliubov phonons and quantised vortices. The latter are supported by the appearance of a quasi-condensate and are the essential elements for the description of a superfluid to normal-gas transition at a critical T_c ; the proper description is achieved through the BKT theory and the pairing of vortices below T_c that allows an algebraic decay of correlations in the system and thus superfluidity. A systematic renormalisation-group treatment for the 2D gas provides a prediction for the superfluid density for the various temperatures which includes the characteristic discontinuity at T_c . This discontinuity, however, is expected to smear out in real experiments owing

to the finite size of the system; the experimental relevance of this conversion to a crossover of finite width should depend on various parameters, like the interaction strength and the size of the system. Moreover, together with the superfluid density, we presented the equation of state for this 2D atomic gas from which all the thermodynamic quantities can be extracted. The superfluid density and thermodynamic quantities are the main inputs to Landau's two-fluid model for a prediction of the speeds of first and second sound that we make use of in chapter 5. The two-fluid model is built from general arguments and thus expected to be valid also in a 2D gas as long as a hydrodynamic description remains valid. Again, the finite size of the gas has an effect on the relevance of this model due to the quantisation of the excitation-mode energies in the system.

4

The realisation of a two-dimensional box trap

“If the word doesn’t exist, invent it; but first be sure it doesn’t exist.”

— Charles Baudelaire

In this chapter we detail the experimental realisation of a 2D homogeneous ultracold atomic ^{39}K gas that provides the means for our studies of BKT superfluidity (Chapter 5). The resulting apparatus is the final outcome of merging a previously existing ultracold-atom setup with a series of modifications and extensive additions. In a sense, and although the original machine was built almost ten years ago [165, 166], the new version to be described can be considered as the second generation of a 2D setup, while the first generation used a harmonically trapped 2D gas of both ^{39}K and ^{87}Rb atoms [167].

4.1 Setting the stage and initial steps

By comparing the available bosonic ^{39}K and ^{87}Rb , the former offers a significant advantage, vital for our work: it permits the tuning of interatomic interactions through easily accessible and broad Feshbach resonances¹ (see Sec. 2.3.1); we thus choose to concentrate on ^{39}K . The experimentally simplest method to realise a uniform 2D gas, as we discuss in detail in Sec. 4.3, consists in properly box-shaping and squeezing an already prepared harmonically-trapped BEC.

Typically the production of such a BEC, with a critical temperature of the order of hundreds of nK, is the result of two successive general cooling techniques, laser and evaporative cooling. Nonetheless, ^{39}K remains a relatively difficult species to cool down: on one hand, its unresolved manifold of the excited $P_{3/2}$ hyperfine states (see also Fig. 4.2 below) precludes a clean cycling transition for laser cooling and restricts the minimum attainable temperatures to relatively high values of the order of several hundreds of μK ; on the other hand, its small and negative background

¹We work with a ^{39}K -resonance at $B_0 = 402.7\text{G}$ with a width $\Delta_0 = 50\text{G}$, whereas the most promising resonance for Rubidium has a width around 0.2G [168].

scattering length (for example $a_{\text{bg}} = -29a_0$ [128] in its absolute ground hyperfine state; here a_0 is the Bohr radius) leads to a slow thermalisation rate (rendering evaporation inefficient) and eventually to an unstable collapsing BEC. The slow rate and the stability of the BEC can be modified again with the use of magnetic Feshbach resonances if atoms are trapped in an optical rather than a magnetic conservative potential. Optical confinement, however, has a limited trapping volume and trapping potential depths typically on the order of tens or hundreds of μK and thus it requires an efficient pre-cooling of the cloud to be trapped².

Fig. 4.1 gives an overview of our production steps of a BEC and subsequently of a 2D uniform gas. We classify the steps into two groups following the two-chamber composition of our vacuum system. The two chambers are connected with a narrow tube that allows differential pumping. The first (‘laser-cooling’) chamber is kept at a pressure of the order of 10^{-9}mbar , high enough for a fast trapping of atoms directly from its background vapor, where the atoms are laser-cooled. After that, the atoms are transported to the second chamber using an inhomogeneous magnetic confinement which moves along a mechanical track. In the second chamber, the ‘science cell’, at a pressure of around 10^{-12}mbar that provides a large lifetime for the atom cloud³, the BEC and the final 2D gas are produced.

The experimental apparatus around the first chamber remains essentially the same as described in the previous Ph.D. theses [165–167] of the group. Contrary, the setup surrounding the science cell is new and it will be discussed in depth in this chapter. The single most crucial part of this setup pertains to light shaping techniques for the construction of the used optical traps. Optical trapping exploits the dipole force exerted from light (of frequency ω) on the atoms; it is a conservative force which can equivalently be seen as the effect of the ac-Stark shift. The resulting trapping potential takes the form⁴ [169]

$$U_{\text{dip}}(r) = \frac{-3\pi c^2}{2\omega_0^3} \left(\frac{\Gamma}{\omega_0 - \omega} + \frac{\Gamma}{\omega_0 + \omega} \right) I(r). \quad (4.1)$$

In the above, ω_0 is the resonance frequency of an atomic transition, $1/\Gamma$ the excited-state lifetime and c the speed of light. It is this simple relation between the intensity $I(r)$ of the trapping beam and the potential $U_{\text{dip}}(r)$ that allows the sculpting of potentials of arbitrary geometries by shaping laser beam profiles. For red-detuned light ($\omega_0 - \omega > 0$), trapping occurs at intensity maxima, whereas blue detuning of light ($\omega_0 - \omega < 0$) serves for confinement in regions where light is absent. In order

²The previous version of the apparatus circumvented these difficulties with the addition of an intermediate step of sympathetic cooling for ^{39}K through its thermalisation with the easy to be evaporatively cooled ^{87}Rb in a deep magnetic trap. Due to the small intra-species scattering length $a_{\text{K-Rb}} = 36a_0$, the total experimental cycle for reaching degeneracy was around two minutes. To improve this timescale, we substituted sympathetic cooling with a stage of gray molasses (see below) on ^{39}K . This simplified substantially the apparatus and all the components that supported the cooling and trapping of ^{87}Rb are now removed from the setup. The newly attained cycle-time for degeneracy is of the order of 20s.

³Measured lifetime of ~ 150 s.

⁴In this chapter, we choose to use symbols widely accepted in the literature, like the polar coordinates ρ and ϕ , the speed of light c and the light frequency ω . Although the same symbols are used differently in the rest of this thesis, we appreciate that there will be no confusion to the reader.

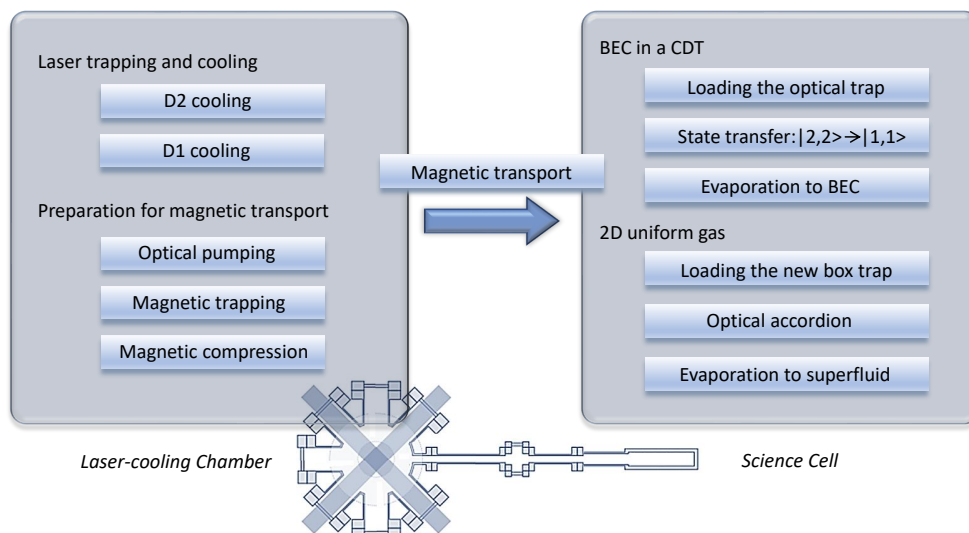


Figure 4.1: Overview of the ‘technical’ steps followed until the production of a degenerate 2D uniform gas of ^{39}K atoms. We split the steps into two large categories, according to the corresponding chamber of our apparatus in which they take place. These steps are described (briefly or in detail) throughout the current chapter.

to minimize the scattering rate between photons and atoms

$$\Gamma_{\text{sc}} = \frac{3\pi c^2}{2\hbar\omega_0^3} \left(\frac{\omega}{\omega_0}\right)^3 \left(\frac{\Gamma}{\omega_0 - \omega} + \frac{\Gamma}{\omega_0 + \omega}\right)^2 I(r), \quad (4.2)$$

that comes from the scattering force and leads to heating, we are restricted to work with far-detuned light and high-power laser beams.

Before we go into details of the apparatus around the science cell, we first give a brief description of the initial stages in the laser-cooling chamber, concentrating on the new aspects that have been introduced in this latest version of our ultracold-atom machine.

Before the magnetic transport

Typically, laser cooling is achieved in two steps, an initial cooling in a magneto-optical trap (MOT) followed by further successive cooling in optical molasses. Two essential components are required for the implementation of laser cooling in the MOT: a six-beam configuration of pairs of $\sigma^+ - \sigma^-$ circularly-polarised light along three perpendicular directions, and a quadrupole magnetic field $B = B'(x/2, y/2, -z)$ with gradient B' , centered at the intersection of the six beams. Each of the six optical beams normally requires two different frequencies, the ‘cooling’ and the ‘repump’ to sustain the addressed cooling transition. For details of the principles of these cooling techniques see for example Ref. [165].

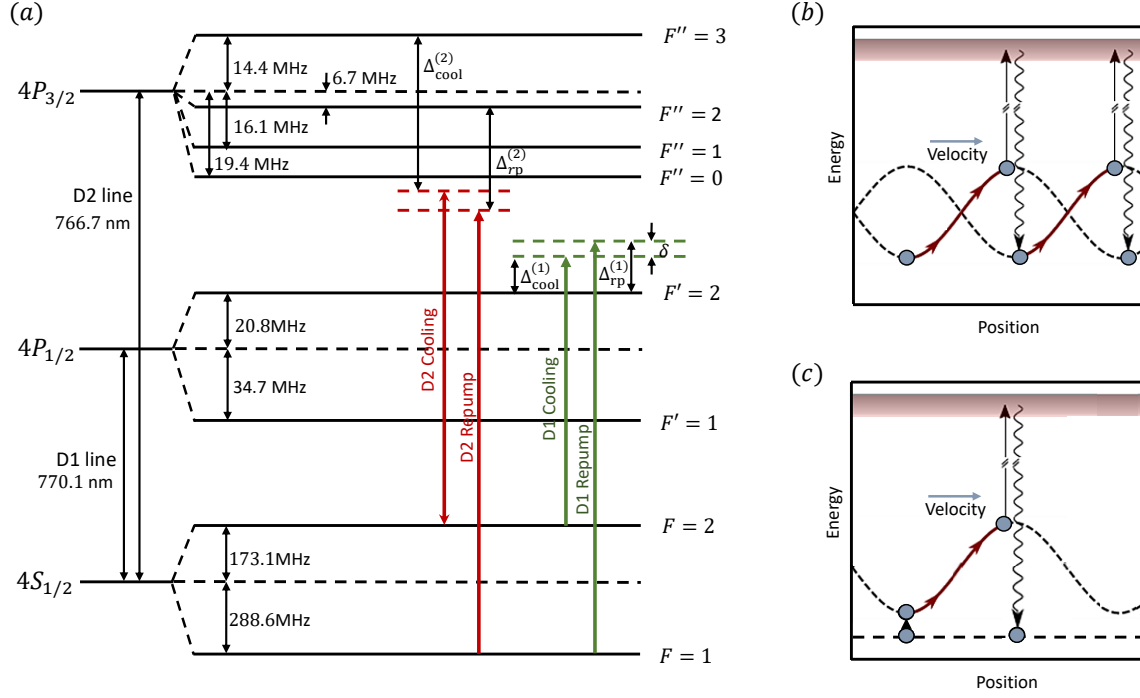


Figure 4.2: (a) The hyperfine splitting of the low-lying states for ^{39}K . The $4P_{3/2}$ fine state is not experimentally well-resolved since the whole manifold is only 5.4 linewidths. The lines in red illustrate the frequencies used for the initial D2 cooling, while the green lines are used for the successive D1 cooling, as described in the text. (b) Sisyphus cooling exploited in the optical molasses: polarisation gradients create a spatially varying light shift, different for the various sub-states of the ground state. The optical pumping of the atoms from potential ‘hills’ to ‘valleys’ for properly detuned light results in the final cooling of the gas since energy is taken away with the larger-energy emitted photons compared to the absorbed ones. (c) When the Sisyphus effect is combined with dark ground states with a departure rate dependent on the atomic velocity, a gray molasses scheme is formed providing much lower temperatures.

Cooling on the D2 line.

In Fig. 4.2(a) the hyperfine structure of the three lowest fine-structure states of ^{39}K is depicted. In the absence of a strong magnetic field, the total angular momentum and its z -projection, F and m_F , are good quantum numbers for the description of the atomic hyperfine states. For a species with well-resolved hyperfine states in the $P_{3/2}$ manifold, the MOT step demands for the cooling and repump beams to be near-red detuned ($\sim -\Gamma$) from the cycling $F = 2 \rightarrow F'' = 3$ and the $F = 1 \rightarrow F'' = 2$ transitions of the D2 line, respectively. For ^{39}K , where the excited states are energetically overlapping within their linewidths, this strategy leads to heating from the other (blue-detuned) hyperfine states, and one has to detune the frequency of the cooling and repump beams to the red side of the entire hyperfine structure of the $P_{3/2}$ state [170, 171]. Such a large detuning offers a large capture velocity from the MOT (enabling to trap atoms directly from the vapour) when combined with large beam intensities, but it also leads to temperatures much larger than the Doppler limit ($145\mu\text{K}$ for ^{39}K).

Experimentally, we start the MOT stage with an intensity $I_{\text{cool}} \approx 10I_s$ per beam and a ratio

$I_{\text{cool}} : I_{\text{rp}} \approx 2 : 1$ for the cooling and repump components, while the optimised⁵ detunings are $\Delta_{\text{cool}}^{(2)} = -5.4\Gamma$ and $\Delta_{\text{rp}}^{(2)} = -7.0\Gamma$ (see Fig. 4.2(a) for their definition). Here $I_s = 1.75\text{mW}/\text{cm}^2$ is the saturation intensity for the cycling transition $F = 2 \rightarrow F'' = 3$ for ^{39}K and $\Gamma = 2\pi \times 6.0\text{MHz}$ the excited state linewidth. With a magnetic gradient $B' \approx 8\text{G}/\text{cm}$ along z , we load a few 10^9 atoms during the 7-second step. The temperature of the cloud is then around 1mK . To achieve a higher phase-space density [172], we subsequently decrease the beam intensities to $I_{\text{cool}} = 0.2I_s$ and $I_{\text{cool}} : I_{\text{rp}} \approx 20 : 1$, and reduce the detunings to $\Delta_{\text{cool}}^{(2)} = -3.6\Gamma$ and $\Delta_{\text{rp}}^{(2)} = -4.8\Gamma$, while simultaneously increasing the magnetic gradient to $14\text{G}/\text{cm}$. At the end of this 80ms-step we obtain a gas temperature of around $300\mu\text{K}$.

Cooling on the D1 line.

To reach temperatures below the Doppler limit, optical-molasses cooling is applied. In a conventional optical molasses, cooling relies on a Sisyphus-like behaviour of the moving atoms; polarisation gradients from the pairs of counter-propagating beams create periodically modulated Zeeman-energy sublevels of the ground state, between which the atoms are pumped, such that they lose kinetic energy (Fig. 4.2(b)). In its most common realisation on a well-resolved D2 line, low-intensity cooling and repump light, far red-detuned from the resolved $F = 2 \rightarrow F'' = 3$ and $F = 1 \rightarrow F'' = 2$ transitions, are applied. For ^{39}K this configuration does not allow considerable sub-Doppler forces. Alternative schemes on the D2 line have been implemented, like using low-intensity near-red-detuned light [173], or blue-detuned light in a $F \rightarrow F' = F$ transition [174, 175].

The latter case is an example of a cooling method known as ‘gray’ molasses. The resulting low temperatures and high densities can be attributed to the existence of dark ground sub-levels, states not coupled to the excited manifold through the applied light, the optical pumping to which leads to much reduced scattering of light. In its simplest scenario, a dark state is simply a Zeeman sub-state due to the polarisation of the applied light. For blue-detuned light, the rest ‘bright’ ground states get a positive light shift which varies in space due to polarisation gradients, compared to the spatially constant dark state, as illustrated in Fig. 4.2(c). Sisyphus cooling between the bright and the dark states then results in the final lowering of the temperature.

This situation becomes even more favorable when light in the D1 line is used instead [176, 177], i.e. blue detuned with respect to the $F = 2 \rightarrow F' = 2$ transition, and with the addition of a second ‘repump’ beam⁶ close to the resonance of the $F = 1 \rightarrow F' = 2$ transition (green lines in Fig. 4.2(a)). The enhancement is partially explained by the lack of a $F \rightarrow F' = F + 1$ transition, the close proximity of which would limit the overall cooling efficiency, as happens for the D2 line. But most importantly, the addition of the repump beam creates effectively a three-level ($F = 1$,

⁵All mentioned parameters emerged after an iterative experimental optimisation of the various laser-cooling steps having as a goal the maximisation of the atom-number loaded in the optical-dipole trap (see Fig. 4.1) of fixed trap-depth. In this way, not only the atom-number, but also the temperature is optimised, providing us the maximum initial phase-space density at the beginning of the processes in the science cell.

⁶These names are merely a convention for this cooling scheme.

$F = 2$ and $F' = 2$) Λ -system [178] and under the Raman condition ($\Delta_{\text{cool}}^{(1)} = \Delta_{\text{rp}}^{(1)}$ or $\delta = 0$) new dark states emerge as coherent superpositions of the $F = 1$ and $F = 2$ ground states. The additional Doppler detuning from the Raman condition (due to the different frequencies of the two laser beams) converts these dark states into ‘gray’ states and the optical departure of the atoms from them becomes velocity-selective. Therefore, the gray states provide, on one hand, more gray molasses cooling cycles (compared to the single-beam case) and, on the other hand, a preference for affecting predominantly the high-energy atoms. This further Raman cooling, of around a factor of 3, manifests a Fano-like profile with the detuning δ of a sub-natural linewidth on top of the background single-beam cooling of the $F = 2 \rightarrow F' = 2$ gray molasses scheme.

We implement gray molasses by adding on the six $\sigma^+ \text{-} \sigma^-$ polarised MOT-beam configuration two more frequencies of light locked on the D1 line, with an independent control in frequency and power. Optical molasses start with the turning off of the magnetic field of the MOT stage and interchanging the D2-laser beams with the D1 ones. We operate on the Raman condition with an overall detuning $\Delta_{\text{cool}}^{(1)} = \Delta_{\text{rp}}^{(1)} = 4.1\Gamma$, although this overall detuning seems rather insensitive. An initial large intensity for the two beams of $I_{\text{cool}} \approx 2.8I_s$ and $I_{\text{cool}} : I_{\text{rp}} \approx 3.5 : 1$ captures and cools essentially all the already trapped atoms for 2.6ms; the gradual ramping down of the intensities by a final factor of ~ 7 at the end of its 7ms duration provides a temperature of $9\mu\text{K}$.

Optical pumping and magnetic trapping.

After laser cooling, the atoms are transported to the ‘science’ cell with the help of a movable magnetic quadrupole field. Distributed among all the sub-levels of the ground state manifold after gray molasses, the atoms are first optically pumped to the magnetically trappable $|F = 2, m_F = 2\rangle$ state with the help of a weak guide field and a σ^+ circularly polarised pumping beam consisting of two frequencies. For the optical pumping, we use light on the D1 line; its ‘cooling’ component, resonant on the $F = 2 \rightarrow F' = 2$ transition illuminates the cloud for $900\mu\text{s}$ in the presence of the repump light that also minimises losses from atoms being transferred back in the $F = 1$ manifold during the pumping cycles.

The quadrupole magnetic field is then ramped up to its maximum available value of $B' = 160\text{G/cm}$ along its strong axis, trapping and compressing the atoms in the $|F = 2, m_F = 2\rangle$ state. The subsequent transport over a distance of 75cm takes place in a time interval of 2.5s. At the end of the transfer, the temperature of the cloud increases to roughly $130\mu\text{K}$, as a result of the adiabatic compression of the cloud during the magnetic trapping and possible non-adiabatic effects during the transport.

4.2 Production of a Bose-Einstein condensate

In the ‘science’ cell the atoms are transferred from the magnetic to an optical trap. There, they are evaporatively cooled to degeneracy after appropriately tuning the scattering length. Evaporation, the removal of the most energetic atoms by gradually decreasing the depth of the trap followed by the re-thermalisation of the remaining particles to a lower temperature, is typically characterised by the quantity $\gamma_{\text{ev}} = -d \ln D_{3\text{D}}/d \ln N$, expressing the efficiency of increasing the phase-space density $D_{3\text{D}}$ at the centre of the cloud after an atom has departed from the trap. In the most common successful scenario, γ_{ev} takes an almost constant in time value typically larger than 3.

Optical dipole trap

The experimentally simplest form of an optical trap consists of a single far-red-detuned Gaussian beam with the atoms trapped around its focal point. Such a beam propagating along some axis y' with a characteristic intensity $I(\rho', \phi', y') = \frac{2P}{\pi w^2(y')} \exp\left(-2\frac{\rho'^2}{w^2(y')}\right)$, with the corresponding polar coordinates $\{\rho', \phi'\}$ of the plane perpendicular to y' , is translated according to Eq. (4.1) into a Gaussian trapping potential of maximum trap-depth

$$U_{\text{odt}} = U_{\text{dip}}(r=0) = \frac{2P}{\pi w_0^2} \frac{3\pi c^2}{2\omega_0^3} \left(\frac{\Gamma}{\omega_0 - \omega} + \frac{\Gamma}{\omega_0 + \omega} \right). \quad (4.3)$$

In the above, P denotes the total power, $w(y') = w_0 \sqrt{1 + (y'/z_{\text{R}})^2}$ the waist with w_0 its minimum value, and $z_{\text{R}} = \pi w_0^2/\lambda_0$ the Rayleigh range of the trapping beam of wavelength λ_0 . Near the trapping minimum, one can expand this potential to get a harmonic-oscillator approximation

$$U_{\text{dip}}(\rho', \phi', y') \approx U_{\text{odt}} \left[1 - 2 \left(\frac{\rho'}{w_0} \right)^2 - \left(\frac{y'}{z_{\text{R}}} \right)^2 \right] \quad (4.4)$$

characterised by the angular frequencies $\omega_{\rho'} = (4U_{\text{odt}}/mw_0^2)^{1/2}$ and $\omega_{y'} = (2U_{\text{odt}}/mz_{\text{R}}^2)^{1/2} \ll \omega_{\rho'}$.

For such a single-beam configuration, the initial temperature of $\sim 130\mu\text{K}$ of the cloud requires a beam-waist w_{01} no larger than $\sim 30\mu\text{m}$ to get a trap-depth of the order of 1mK for our available laser of $\lambda_0 = 1064\text{nm}$ at a maximum available power $\sim 13\text{W}$ on the atoms. Following some rough estimations⁷, a condensate can be, in principle, successfully formed after evaporation in the trap if

⁷Concentrating on the beginning (end) of a hypothetical evaporation route, characterised by a phase-space density D_i (D_f) and an atom-number N_i (N_f), we can approach the overall efficiency parameter as

$$\gamma_{\text{ev}} = \frac{\ln(D_f/D_i)}{\ln(N_i/N_f)} = \frac{\ln D_f - \ln N_i - 3 \ln(\hbar\bar{\omega}_i) + 3 \ln(k_{\text{B}}T_i)}{\ln N_i - \ln N_f}. \quad (4.5)$$

where in the last step we used that the phase-space density in a harmonic trap is given by $D = N(\hbar\bar{\omega})^3/(k_{\text{B}}T)^3$ with $\bar{\omega}^3 = \omega_x\omega_y\omega_z$. With the requirement of $\gamma_{\text{ev}} \gtrsim 3$, the initial temperature $T_i \sim 130\mu\text{K}$, trapping frequency $\bar{\omega}_i \sim 6 \times 10^3 \text{s}^{-1}$ (coming directly from $w_0 \sim 30\mu\text{m}$ and $P \sim 13\text{W}$), the final $D_f \sim 1$ for condensation and a lower bound $N_f \sim 5 \times 10^5$, we obtain the required $N_i \gtrsim 10^7$. After realising our trap, we find that we can routinely create a BEC if initially $N \gtrsim 9$ million.

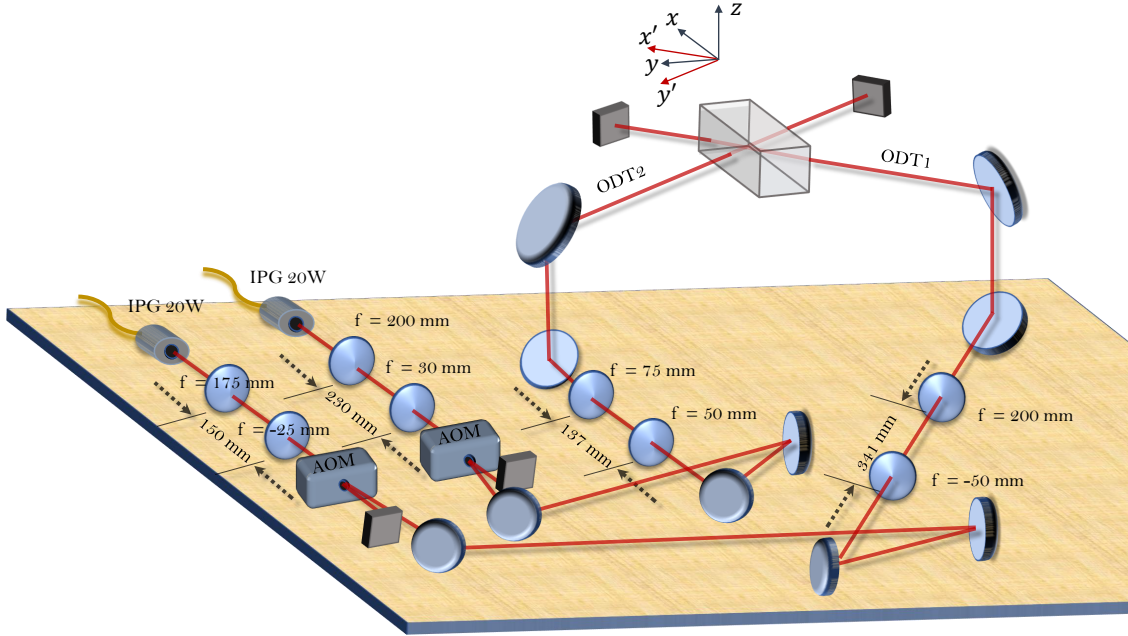


Figure 4.3: Overview of the CDT setup. Two 20W ytterbium fibre lasers (YLR-20-LP) operating at 1070nm and 1064nm provide the two ODT beams, respectively. The beams, both with an initial size of 2.5mm ($1/e^2$ -radius), are demagnified (~ 0.4 mm) so each passes through an acousto-optical modulator (AOM) in the most efficient way (90% and 75% of efficiency for the relevant order). The AOMs (operating RF frequency of 110MHz) are used for controlling the power on the atoms and are stabilised via PID feedback. Finally, a cage system of two lenses for each of the beams is responsible for focusing them on the position of the atoms. The choice of the focal lengths and the distances between them was done to get the desired waists, described in the main text, at a distance (45cm and 50cm respectively from the last lens of the cage) restricted by the experimental setup.

we initially confine at least around 10×10^6 atoms in this optical trap.

The full setup for our optical dipole trap is illustrated in Fig. 4.3. We superimpose the already-discussed ‘ODT1’ beam, with a second one (‘ODT2’ beam) to create a crossed dipole trap (‘CDT’). The two beams are separately prepared and focused on the position of the atoms intersecting at an angle of 90° with respect to each other and 45° to the long axis of the science cell (in Fig. 4.3 we define two useful reference systems xyz linked with the direction of the science cell and $x'y'z$ linked with the dipole traps), both propagating in the horizontal plane. An optimum loading and evaporation has been found for a large ODT2 waist w_{02} ($\sim 150\mu\text{m}$), since the relatively large trapping volume minimises atom losses from three-body collisions. With the chosen waist, ODT2 indeed does not play a role in the initial loading of the atoms, but it serves in the later stages of evaporation, where it provides an additional confinement along the weakly trapped axial direction x' of ODT1.

Fig. 4.4 shows the measured radial frequencies of ODT1 and ODT2 for various powers of the corresponding laser beam. By turning off one of the two, we observe a breathing mode oscillation of the cloud in the remaining trap. The measurements are conducted with $a \sim 0$ such that the extracted frequency of the breathing mode is double the characteristic frequency of the trap. The beam powers on the atoms are deduced from an average of the power measurements just before and

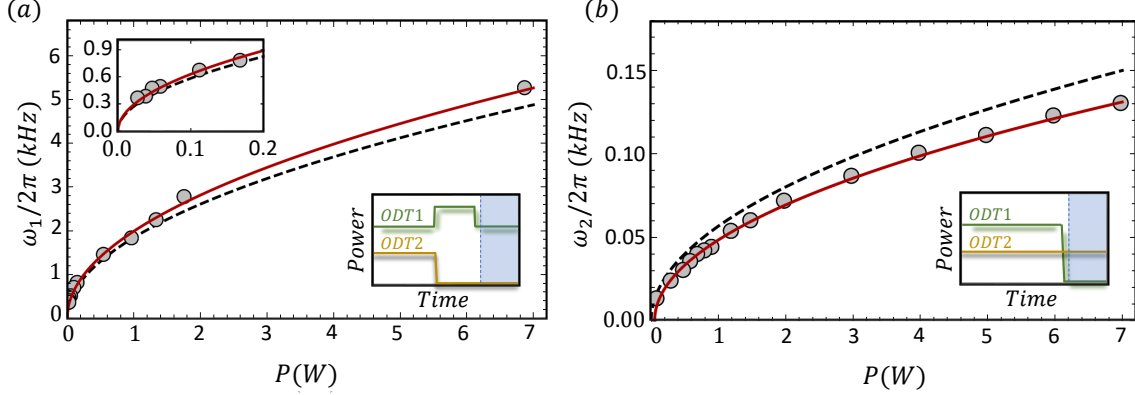


Figure 4.4: Measured trapping frequencies versus light power for (a) ODT1 and (b) ODT2 along z -direction. The low-right cartoons indicate the method used for measuring these frequencies: For each beam, the other one is turned off triggering breathing-mode oscillations in the remaining trap. For ODT1 measurements we found a better signal is we temporarily quench its power as well. The blue region is where oscillations are observed. Black dashed lines: expectation based on measured waist with the use of a camera. Red lines: a fit of the form $\omega/2\pi \propto \sqrt{P}$ on the data which gives a refined estimation for the beam waists. The larger expectation for ODT2 compared to the measured frequency can be explained, in most probable scenario, by a slight misalignment of the beam in its axial direction with respect to its focus.

after the science cell. Under the assumption of equal losses from both sides of the cell, we find a $\sim 15\%$ of decrease in power in each of the two surfaces of the cell in relatively good agreement with the expectation of $\sim 80\%$ transmittance through the entire science cell at a 45° -incidence [165]. The black dashed lines correspond to the expected behaviour of the frequencies with our best estimated value of the waists, $w_{01} = 27\mu\text{m}$ and $w_{02} = 154\mu\text{m}$, as measured with a camera (in the absence of the science-cell effects). The red line is a fit on the data which can be used to extract the final waists on the atoms, $w_{01} = 26\mu\text{m}$ and $w_{02} = 164\mu\text{m}$. The errors of these fits are negligible. With the knowledge of the powers and the waists of the two beams, we approach the total potential of our crossed-dipole trap close to its center by

$$U_{\text{CDT}}(x', y', z) \approx -(U_{01} + U_{02}) + \frac{2U_{01}}{w_{01}^2} x'^2 + \left(\frac{U_{01}\lambda_0}{\pi w_{01}^4} + \frac{2U_{02}}{w_{02}^2} \right) y'^2 + \left(\frac{2U_{01}}{w_{01}^2} + \frac{2U_{02}}{w_{02}^2} \right) z^2 \quad (4.6)$$

with the trap-depths U_{01} and U_{02} given by Eq. (4.3) for each beam separately.

BEC in the crossed dipole trap

Both ODT beams are already turned on while the atoms are transported to the science cell; ODT1 is at its maximum available power of around 13W on the atoms, and ODT2 at a value of 0.4W. At these powers, the lifetime of the atoms in the dipole trap is limited by the trapping light (one-body scattering with a rate $\Gamma_{\text{sc}} = \Gamma(U_{01} + U_{02})/\hbar(\omega_0 - \omega)$ [169]) to $\sim 3\text{s}$, so the whole loading stage should be as fast as possible before we initiate the evaporation process. We found an optimum waiting time of 2s for the loading, with both the magnetic and the optical trap on.

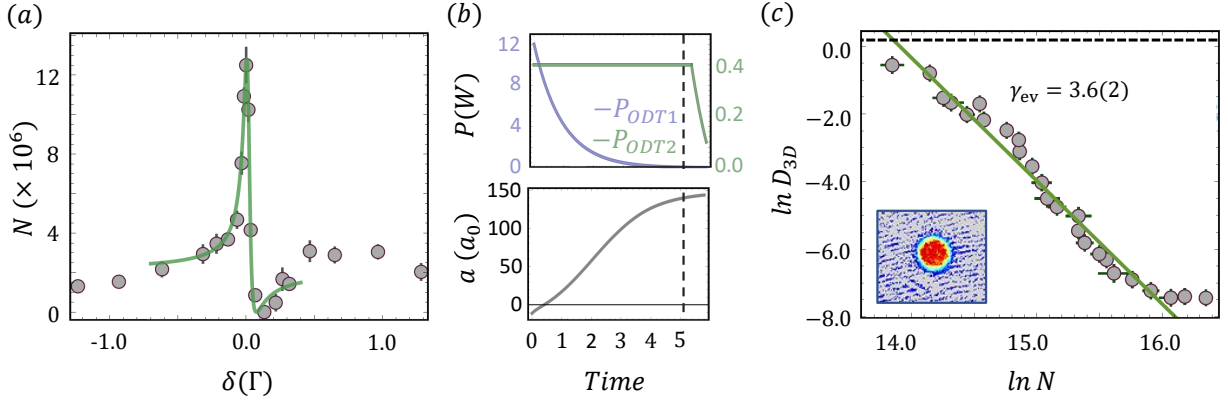


Figure 4.5: (a) The loading of the CDT: Number of atoms loaded in the dipole trap vs the Raman detuning in the stage of D1-gray molasses. The green line is a fit of the Fano-form $F(\gamma + \delta - \delta_0)^2/[(\delta - \delta_0)^2 + \gamma^2]$ to the data, with γ , δ_0 and F the fitting parameters. This gives a sub-natural width of $\sim 0.03\Gamma$. (b) Evaporative cooling: The evolution of the ODT powers (upper panel) and the scattering length (lower panel) in a total ramp of 5.8s. BEC appears after 5.2s, indicated by the vertical dashed line. ODT1 is ramped down from 12W exponentially with a time constant of 0.9s. ODT2 remains constant at 0.4W until before the end that the two trap-heights become equal, after which time ODT2 follows ODT1. (c) The central phase-space density $D_{3D} = N(\hbar\bar{\omega}/k_B T)^3$, with $\bar{\omega}$ the geometric average of the trapping frequencies, versus the atom number in the non-degenerate regime of the gas. The slope indicates the efficiency of evaporation and gives $\gamma_{ev} = 3.6(2)$. The black dashed line corresponds to the critical phase space density $D_{3D}^c \approx 1.20$ [120]. In the inset we show a typical density distribution of a final pure BEC after 20ms of free expansion. The distribution is well fitted with a parabolic profile, characteristic for the Thomas-Fermi description of a BEC.

With this scheme, a maximum of $12.5(7) \times 10^6$ of atoms (around 2.5% of the atoms transferred to the cell) are loaded into the optical trap, as shown in Fig. 4.5(a). This figure demonstrates the importance of gray-molasses cooling in achieving such loading numbers: we show the effect of the loaded atom number N on the detuning δ between the D1 cooling and repump beams from the Raman resonance. Since the dipole trap has a fixed trap-depth for the specific powers, the observed atom-number is a direct measure for the temperature of the ‘arriving’ cloud, which, as we already mentioned, follows a Fano-resonance behaviour with detuning. In this spirit, and together with fixed trapping frequencies (during loading), the loaded number of atoms in the dipole trap constitutes a simple tool for maximising the phase-space density of all the previous preparation stages.

The optically trapped atoms are in the $|F = 2, m_F = 2\rangle$ hyperfine state. In order to make use of the wide Feshbach resonance presented in Sec. 2.3.1 for evaporation, we transfer the atoms to the $|F = 1, m_F = 1\rangle$ ground state. We apply a Landau-Zener sweep of the Feshbach field in the presence of microwave radiation at 476.7MHz. The magnetic field is increased from 6.8G to 7.7G in 20ms, which is proven adiabatic enough for $\sim 98\%$ of the atoms to stay in the lower-energy dressed state corresponding to the $|1, 1\rangle$ state when the microwave field is turned off⁸.

We then ramp down the power of the CDT beams as in the upper panel of Fig. 4.5(b). For the dominant ODT1 we use an exponential ramp until the end, whereas for ODT2 we keep its power constant until the point that the two trap-depths U_{01} and U_{02} become equal; after this moment, ODT2

⁸Details about the antenna and the hardware used can again be found in Ref. [165, 166].

follows the behaviour of ODT1. To compensate the detrimental effect of three-body losses with the efficiency of evaporation, we simultaneously ramp up the scattering length, as shown in the lower panel of Fig. 4.5(b). In the end, the cloud has a scattering length of $147a_0$. During the whole duration of evaporation, the ratio of the total trap-depth over $k_B T$ remains around 7. To characterise the efficiency of evaporation we measure the approximately constant quantity $\gamma_{\text{ev}} = 3.6(2)$ in Fig. 4.5 (b). With this evaporation trajectory, a BEC is observed after 5.2s at a critical temperature of around 550nK for a total atom number of around 6.5×10^5 , with an uncertainty of $\sim 15\%$ in both quantities; their calibration is discussed in Sec. 4.8. Beyond the critical point, further evaporation leads to the purification of the BEC with an increasing condensed fraction. After 5.8s of evaporation we get an essentially pure BEC of 2×10^5 atoms, with a geometrically average frequency of $\bar{\omega}/2\pi = 51\text{Hz}$ and Thomas-Fermi radii $R_{x'} = 7.7\mu\text{m}$, $R_{y'} = 47.8\mu\text{m}$ and $R_z = 7.6\mu\text{m}$, in respective directions of the harmonic trap.

The reproducibility of the BEC, both in atom number and position, is important for the stability of the final uniform 2D gas. To that end, we need to discuss possible sources of instabilities. We first note that the CDT light and the RF power inevitably heat the controlling AOMs (see Fig. 4.3), creating lensing effects that systematically change the focus position between the initial and final steps of evaporation. The effect is much stronger for the high-power ODT1; there is a change of around $250\mu\text{m}$ in the position of the focus along the beam propagation between the beginning and the end of evaporation. We take care to place the ODT focus in such a way that the harmonic BEC occurs at the desired position of the final uniform cloud. In addition to that fast change of the focus within a single run, the BEC position slowly drifts in the course of time, mainly due to slow warming up of the CDT laser heads. The difference between a completely cold and a warm run is translated into a change of the BEC position by $20\mu\text{m}$ in the horizontal plane. Although this slow drift does not create significant differences in the final number of atoms in the BEC, it provably matters for the loading of the box trap, especially for small boxes. To avoid such undesired effects, the machine is routinely warmed up for 2 hours before collecting data.

With a BEC at hand, we proceed to describing our realisation of a two-dimensional (Sec. 4.3) and an in-plane box (Sec. 4.4) trap. We follow a similar approach for both confinements: we first present the various options available, we then set our requirements and finally, based on the optimum technique identified, we give a brief description of our setup and its characteristics. At the end of each section, we discuss important technical issues of the corresponding realisation.

4.3 The two-dimensional confinement

Background

By satisfying the relevant conditions of Eq. (3.1), two-dimensional atomic samples were first produced in 2001 in the group of W. Ketterle [179], where a cylindrical lens was used to focus a

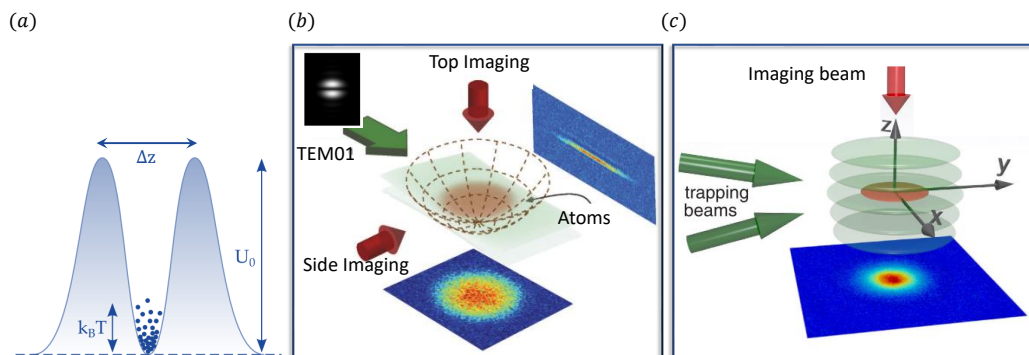


Figure 4.6: (a) The trapping potential of a height U_0 generated from two repulsive light sheets for the confinement of the atoms in two dimensions. (b) A real-life example (taken from [183]) of using a TEM_{01} laser mode to create the 2D potential, and (c) a real-life example (taken from [184]) of using a 1D optical lattice for the same reason.

red-detuned beam along one direction in order to create a highly anisotropic trap. Such light-sheet potentials have been commonly used since, although various other aspects have been exploited to give rise to alternative 2D confinements, like gravito-optical [180] or RF-dressed magnetic [181] traps. For purely optical methods, the latest implementations of 2D samples have concentrated on using blue-detuned repulsive light to limit losses and heating: the atoms get confined in a dark ‘sheet’ between two intensity maxima of the applied beam profile, as illustrated in Fig. 4.6(a), thus reducing the detrimental effect of spontaneous emission⁹.

Two types of techniques to shape this dark sheet have been widely used. As of first type, a Hermite-Gaussian TEM_{01} -like mode is shone on the atoms, see Fig. 4.6(b). Such a beam profile is holographically generated [185], with the use of a $0-\pi$ phase-plate to imprint a phase difference between the two halves (upper and lower) of a Gaussian beam; when imaged, the resulting beam produces a nearly TEM_{01} mode. The TEM_{01} -like technique is briefly characterised in Box 4.1. Alternatively, two coherent beams that interfere form a one-dimensional optical lattice, in the dark fringes of which atoms can be trapped. An example for the latter configuration is shown in Fig. 4.6(c), and Box 4.2 briefly discusses this technique.

To decide on a specific implementation for the 2D optical confinement of the atoms, we first set our requirements.

⁹Technical heating caused by laser intensity and beam-pointing fluctuations cannot be avoided with choosing a blue-detuned trap [182].

Box 4.1: TEM₀₁-like beam

The light intensity of the TEM₀₁ mode,

$$I_{01}(x, z) = \frac{2P}{\pi w_x w_z} \frac{(2z)^2}{w_z^2} \exp\left(-\frac{2x^2}{w_x^2}\right) \exp\left(-\frac{2z^2}{w_z^2}\right) \quad (4.7)$$

with P the total power and $w_{x,z}$ the beam waists, gives a maximum trap-depth

$$U_0 = \frac{4P}{\pi e w_x w_z} \frac{3\pi c^2}{2\omega_0^3} \left(\frac{\Gamma}{\omega_0 - \omega} + \frac{\Gamma}{\omega_0 + \omega} \right) \quad (4.8)$$

at $\{x, z\} = \{0, \pm w_z/\sqrt{2}\}$. Thus, the waist w_z is related to the distance Δz between the intensity maxima as $\Delta z = \sqrt{2}w_z$. Expanding around the minimum at $\{x = 0, z = 0\}$, the trapping frequency is

$$\nu_z = \frac{1}{\Delta z} \sqrt{\frac{[4 \exp(1)/\pi^2] U_0}{2m}} \approx \frac{1}{\Delta z} \sqrt{\frac{U_0}{2m}} \quad (4.9)$$

with an error less than 5%. When using a $0 - \pi$ phase-plate to approach the TEM₀₁ mode, close to the center of the beam the actual light intensity is a factor of π lower compared to I_{01} due much broader wings [185], with Eq. (4.9) remaining approximately still valid.

Box 4.2: One-dimensional optical lattice

The cleanest way of interference occurs when a cylindrical lens of focal length f focuses two similar (same power P , wavelength λ_0 , and waists w_x and w_z) and parallel beams of a relative distance d . Following the rules of Fresnel propagation, the intensity pattern at the focal point of the lens is

$$I_{1D}(x, z) = \frac{2Pw_z}{\lambda_0 f w_x} \left[1 + \cos\left(\frac{2\pi}{\Delta z} z\right) \right] \exp\left(-\frac{2x^2}{w_x^2}\right) \exp\left(-\frac{2z^2}{(\lambda_0 f / \pi w_z)^2}\right), \quad (4.10)$$

which corresponds to a simple small-beam interference pattern of periodicity $\Delta z = \lambda_0 f / d$ with an envelope of a focused Gaussian beam of waist $w'_z = \lambda_0 f / \pi w_z$. The tightest confinement occurs between the central ($z = 0$) and the adjacent ($z = \pm \Delta z$) intensity peaks of potential height

$$U_0(x = 0, z = \pm \Delta z) = \frac{4Pw_z}{\lambda_0 f w_x} \exp\left(-\frac{2\pi^2 w_z^2}{d^2}\right) \frac{3\pi c^2}{2\omega_0^3} \left(\frac{\Gamma}{\omega_0 - \omega} + \frac{\Gamma}{\omega_0 + \omega} \right). \quad (4.11)$$

Expanding around the minimum of the potential, the trapping frequency is found to be

$$\nu_z = \frac{1}{\Delta z} \sqrt{\frac{U_0}{2m}}. \quad (4.12)$$

Prerequisites and constraints

1. **Trapping frequency:** The first prerequisite is to satisfy the 2D conditions of Eq. (3.1) for the transverse trapping frequency $\nu_z = \omega_z / 2\pi$. For an estimation it is adequate to approximate μ_{3D} by the 3D Thomas-Fermi limit. For an in-plane box potential $\mu_{3D} = \left(\frac{3}{2^{5/2}} \omega_z g_{3D} m^{1/2} n \right)^{2/3}$ as extracted from the normalisation condition $N = \int n_{3D}(r) dr$ with $n_{3D}(r) = \frac{\mu_{3D} - \frac{1}{2} m \omega_z^2 z^2}{g_{3D}}$ and a Thomas-Fermi

radius $(2\mu_{3D}/m\omega_z^2)^{1/2}$ along z . In Fig. 4.7(a), we estimate the minimum frequency required for various densities and scattering lengths for the conditions $\hbar\omega_z > k_B T, \mu_{3D}$ to be simultaneously satisfied over a wide range of temperatures even above the critical BKT temperature T_c . We set a minimum request for $\nu_z \approx 5\text{kHz}$, which will be enough for surface densities smaller than roughly $20\mu\text{m}^{-2}$ even for the highest accessible interaction strengths.

2. Potential height: Second, we need a potential height U_0 that is large enough to allow the trapping of the atoms at a total power that is experimentally available. For the highest temperatures of interest ($\lesssim 300 - 400\text{nK}$), the minimum potential height of the 2D ‘blades’ has to be at least around $2 - 3\mu\text{K}$. On the other hand, and although in principle there should be no harm for larger U_0 , in practice this height sets also the scale for imperfections (see Fig. 4.13 below and the relevant discussion) in the dark center of the potential, and therefore we should keep it as low as possible.

3. Beam extent: Another issue relevant for our final goal of a uniform trap is related with the finite extent of the applied beam perpendicular to the transverse confinement. Due to the typical Gaussian profile of the beam (of waist W_x) in this horizontal direction, the maximum height of the potential $U_0(x) = U_0 \exp(-2x^2/W_x^2)$ leads to a spatially-dependent zero-point energy $\hbar\omega_z(x)/2 = \hbar\pi\nu_z \exp(-x^2/W_x^2)$ and thus, with a Taylor expansion, to an in-plane anti-trapping potential of frequency

$$\nu_x = \sqrt{\hbar\nu_z/(2\pi mW_x^2)}. \quad (4.13)$$

To determine a minimum acceptable size W_x for a given box size L_x , we have to compare the potential difference $\Delta U_x = m(2\pi\nu_x)^2(L_x/2)^2/2$ caused by this anti-trapping with the relevant energy scales (temperature and chemical potential) of the box. At the critical temperature, one gets

$$\frac{\Delta U_x}{k_B T_c} = \frac{m\nu_z L_x^2 \ln(\xi_n/\tilde{g})}{8\hbar W_x^2 n}. \quad (4.14)$$

We pick a desired minimum waist of around $170\mu\text{m}$ to guarantee that ΔU_x is at least an order of magnitude smaller than T_c in the relevant range of parameters (see Fig. 4.7(b)). Of course, for lower temperatures the ratio $\Delta U_x/k_B T$ becomes larger and at $T = 0$ the Thomas-Fermi result gives $\Delta U_x/\mu_{2D}$ to be $2\pi/\tilde{g} \ln(\xi_n/\tilde{g})$ times larger compared to $\Delta U_x/k_B T_c$.

The chosen trapping method

For a maximum height of $\sim 3\mu\text{K}$ and a minimum distance $\Delta z \sim 15\mu\text{m}$ between the two intensity maxima, slightly larger than the extent of the BEC to be loaded along this direction, we can estimate (using Eq. (4.9) or Eq. (4.12)) a resulting frequency of 1.2kHz , way below our target value of 5kHz . From the same relation(s), it becomes apparent that in order to increase the frequency without boosting U_0 one has to squeeze the 2D blades to a distance of around $3\mu\text{m}$. However, such a scenario

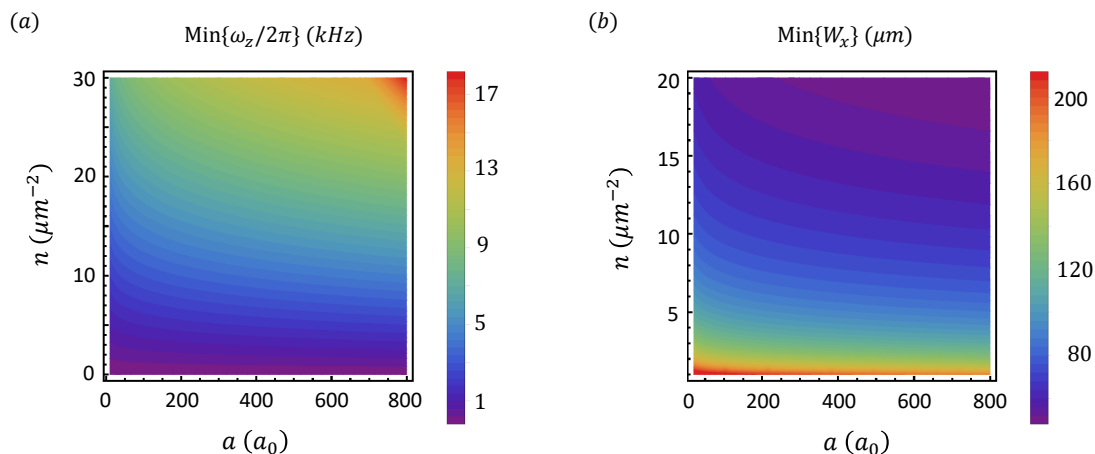


Figure 4.7: (a) Minimum transverse frequency $\nu_z = \omega_z/2\pi$ that satisfies $\hbar\omega_z > k_B T$ and $\hbar\omega_z > k_B \mu_{3D}$ for various densities and scattering lengths. We pick $T = 1.4T_c(n, a)$, so the gas remains strictly 2D even at temperatures above the BKT critical one. We note that it is the condition $\hbar\omega_z > k_B T$ that predominantly determines the minimum acceptable ν_z , apart from very large a . (b) Minimum extent (waist) in the x -direction of the 2D for $\Delta U_x/k_B T_c = 10\%$ for a typical box-size of $40\mu\text{m}$.

would lead to an abrupt decrease in the atom number loaded from the BEC or equivalently to a multiple-fringe loading in the case of a lattice. To avoid such a situation, we implement a technique often referred to as an optical accordion [186]: the atoms are first loaded in an initial configuration with a large Δz and then dynamically compressed by reducing the spacing of the two blades.

This (adiabatic) compression can be easily realised with the standing-wave technique. In its simplest form, two parallel beams at a distance d are focused by a cylindrical lens of focal length f ; the spacing $\Delta z = \lambda_0 f/d$ decreases with moving the two initial parallel beams further apart. Compared to the TEM₀₁-mode technique, the interference-method is also cleaner since it avoids corrugations originating from unavoidable imperfections of a manufactured phase-plate. These corrugations become even more detrimental for the case of a uniform in-plane trap since its typical extent is significantly larger than 2D gases in harmonic traps. On the other hand, the interference of two in-phase beams that results in an intensity maximum in the center of the lattice profile manifests two relative drawbacks: first, the position of the minimum of the potential changes together with a changing Δz , deteriorating the stability of the trap and making the beam alignment sensitive to it; second, the unavoidable intensity imbalance between two adjacent maxima leads to an overall reduced potential height at a waste of useful power.

In order to circumvent these inconveniences, we combine the two methods: a $0-\pi$ phase-plate imposes a π -phase difference between the two interfering beams (and thus a potential minimum always at the lattice center independently of Δz), whereas a finite distance between these two beams eliminates the effect of imperfections at the junction of the two surfaces of the phase-plate. The scheme of our setup is shown in Fig. 4.8. The trapping potential is produced from light at $\lambda_0 = 532\text{nm}$, far blue-detuned to keep the photon absorption rate negligible. For the interference of the

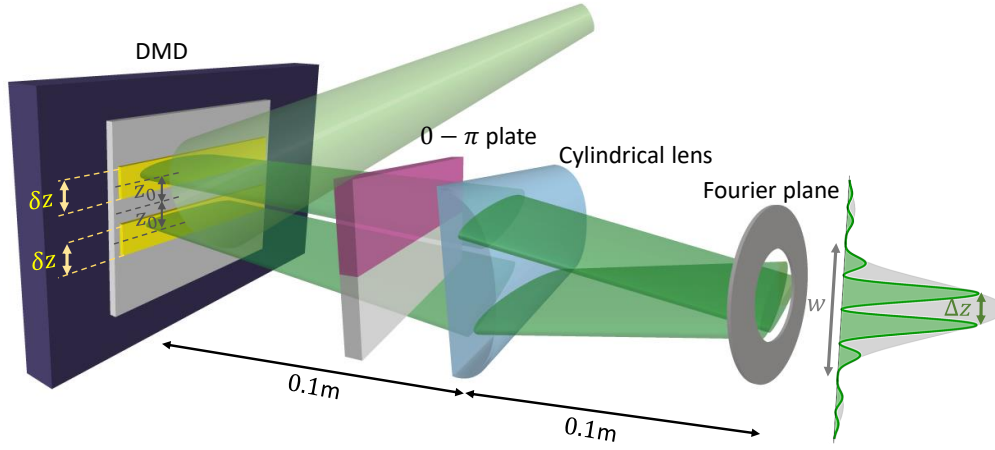


Figure 4.8: The main elements for the two-dimensional confinement. A single Gaussian beam is shaped by the chosen pattern on the digital-micromirror device (DMD) and then Fourier imaged with the use of a cylindrical lens with a focal length of 100mm. Putting a $0 - \pi$ phase plate in the route of the beam provides us with a zero-intensity beam in its symmetry center. The chosen displayed geometry on the DMD is a two-bar horizontal pattern, the dimensions δz and z_0 of which determine the final beam on the atoms as explained in the main text.

two beams we use a cylindrical lens with a focal length of 100mm. With this choice, the beam profile remains extended along the horizontal direction to satisfy the beam-extent requirement. For the shaping of these interfering beams, but also for the dynamic compression of the spacing Δz , we chose to exploit the capabilities of a digital micromirror device (DMD); it is a spatial light modulator that acts on the intensity of the incoming (Gaussian) beam with a large number (in our case 1024×768) of controllable micromirrors (of pitch $13.6\mu\text{m}$), switched to two possible positions ($\pm 12^\circ$ with respect to their diagonal axis). The mirrors that are in the $+12^\circ$ position are said to be ‘on’, reflecting the light to the phase-plate and eventually to the atomic plane, whereas the light in the rest of the mirrors is discarded.

More details about the operation, the control and the capabilities of the used DMD will be discussed in Sec. 4.5. Here it is enough to consider the DMD as a diffraction grating constructed by the micromirrors, with a filling factor of 92% that produces many diffraction copies of the Fourier transform of the displayed shape in the far field. All orders but one are then blocked and the remaining is shone on the atoms. The efficiency of the chosen order depends both on the incoming beam direction and the choice of the pattern on the DMD (‘off’ mirrors waste their power). The loss of power is in general considered the main disadvantage of using a DMD for potential shaping. However, as we discuss below, it is feasible to produce trapping heights of some μK with a total power of around 100mW on the atoms, a value achievable starting with an available 2W-laser.

Details of the final trap

The details of the optical-accordion process till the final 2D uniform gas will be presented in Sec. 4.7, after all the relevant components are introduced. Here we discuss the experimental choices made for this final gas to satisfy the three criteria we set before, namely a trapping frequency of at least 5kHz, a trapping height of about $2 - 3\mu\text{K}$ and a minimum possible anti-trapping along the x - and y -directions. This discussion also facilitates the quantitative characterisation of our setup that follows.

The degrees of freedom we can externally control are the size of the Gaussian beam incident on the DMD (characterised by the waists w_x and w_z), the projected pattern on the DMD, and the imaging of the resulting Fourier space distribution onto the atoms (demagnification). Starting from the latter, we picked a demagnification factor $M_{2\text{D}} \equiv w_x/W_x = 10$ so as to use a large fraction of the DMD active area (see Sec. 4.7) and to keep a simple telescopic system that avoids aberrations from small focal-length lenses.

Regarding the DMD geometry, we display a pattern of two rectangular horizontal bars as depicted in Fig. 4.8, to control the intensity profile on the atoms along z and avoid cutting part of the power of the initial beam along the horizontal x -direction. The two controlling parameters of this geometry then become the width δz of the bars and their distance z_0 from the center of the DMD (defined in Fig. 4.8). The intensity distribution in the Fourier plane, and thus rescaled on the atoms, from the rectangularly-masked Gaussian beam on the DMD has a rather complicated form¹⁰. To get some intuition, however, we discard the Gaussian dependence, i.e. we assume that $\delta z \ll w_z$, and find that the intensity profile on the Fourier plane is approximated by:

$$I(x, z) = I_{\max} \operatorname{sinc}^2 \left(\frac{\pi \delta z}{\lambda_0 f} z \right) \sin^2 \left(\frac{2\pi z_0}{\lambda_0 f} z \right) \exp \left(-\frac{2x^2}{w_x^2} \right) \quad (4.15)$$

with the normalisation constant $I_{\max} = \frac{2P\delta z}{f\lambda_0 w_x} \sqrt{\frac{2}{\pi}}$, where P is the total power of the light on the Fourier plane. In Fig. 4.9(a) we compare the approximation of Eq. (4.15) with numerical simulations based on Fraunhofer propagation [187] and find rather good agreement between the two with no appreciable difference in their respective potential heights. This analytical intensity profile offers the following characteristic quantities:

¹⁰The Fourier transform of a masked Gaussian field $E(z) = [\operatorname{rect}(\frac{z-z_0}{\delta z}) - \operatorname{rect}(\frac{z+z_0}{\delta z})] \exp(-\frac{z^2}{w_z^2})$, where $\operatorname{rect}(z)$ is the rectangular function of value 1 in the interval $\{-1/2, 1/2\}$ and zero otherwise, is

$$E(k) = jw_z \exp \left(\frac{k^2 w_z^2}{4} \right) \left[\operatorname{erfi} \left(\frac{k w_z^2 + 2j z_0 - j \delta z}{2w_z} \right) + \operatorname{erfi} \left(\frac{k w_z^2 - 2j z_0 + j \delta z}{2w_z} \right) - \operatorname{erfi} \left(\frac{k w_z^2 - 2j z_0 - j \delta z}{2w_z} \right) - \operatorname{erfi} \left(\frac{k w_z^2 + 2j z_0 + j \delta z}{2w_z} \right) \right]$$

where $\operatorname{erfi}(z) = -(2j/\sqrt{\pi}) \int_0^{jz} e^{-t^2} dt$ is the imaginary error function.

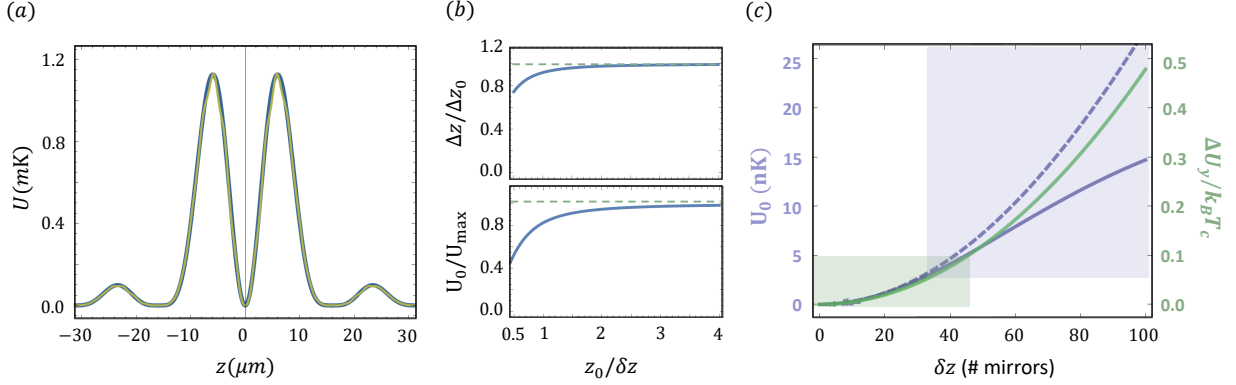


Figure 4.9: (a) Comparison between the numerically extracted potential profile along z using Fraunhofer theory of propagation (yellow) and the analytical approximation Eq. (4.15) (blue) for a situation with $\delta z = 50$ mirrors that validates our discussion in the main text. (b) Corrections for the actual spacing Δz and potential height U_0 due to a finite width δz of the bars-geometry in the DMD. Both are ‘universal’, depending only on the ratio $z_0/\delta z$. (c) The potential height U_0 (blue) and the potential difference (green) along y due to anti-trapping for a typical gas ($L = 40\mu\text{m}$, $n = 10\mu\text{m}^{-2}$, $\tilde{g} = 0.1$) for $z_0 = 50$ mirrors. The dashed line gives the height of the potential without the corrections in (b) showing that thick bars indeed reduce the achievable U_0 due to the sinc-envelope. The shaded regions indicate the acceptable δz for U_0 and ΔU_y based on the discussion in the main text. We pick to work with $\delta z = 50$ mirrors for our final configuration.

1. **The spacing Δz between the two intensity maxima:** From the sine-term of Eq. (4.15) alone, one can approximate Δz with $\Delta z_0 \equiv \lambda_0 f / 2z_0$. As expected from the reciprocal relation between real and Fourier space, it is the distance z_0 that controls the spacing between the intensity maxima on the atoms. For a desired distance of $2 - 3\mu\text{m}$ on the atoms (taking into account the demagnification M_{2D}) it requires a shift $z_0 \approx 0.8\text{mm}$ of the bars on the DMD (or around 60 micromirrors). We note that the non-physical situation with bar widths $\delta z > 2z_0$ can be incorporated to our studies after defining an effective $z_0^{\text{eff}} \rightarrow z_0/2 + \delta z/4$ and an effective $\delta z^{\text{eff}} \rightarrow 2z_0^{\text{eff}}$ for that case. Furthermore, a more careful treatment for Δz , including the effect of the sinc-dependence yields a suppression of the spacing that depends only on the ratio $z_0/\delta z$. The correction $\Delta z/\Delta z_0$ is plotted in the upper panel of Fig. 4.9(b) and allows a slightly smaller z_0 than 60 micromirrors to achieve the desired spacing. We eventually pick $z_0 = 50$ mirrors.

2. **The potential height U_0 :** With a given total power P on the atoms, the trapping potential $U(z) = U_{\text{max}} \text{sinc}^2\left(\frac{\pi\delta z}{\lambda f} z\right) \sin^2\left(\frac{2\pi z_0}{\lambda f} z\right)$ would give a height $U_{\text{max}} = I_{\text{max}} \frac{3\pi c^2}{2\omega^3} \left(\frac{\Gamma}{\omega_0 - \omega} + \frac{\Gamma}{\omega_0 + \omega}\right)$ for an infinitesimally small δz . The finite width of the bars, however, provides the additional sinc-envelope of a width¹¹ $w = 2\lambda_0 f / \delta z$ that suppresses the potential height to a value U_0 by a factor that depends only on the ratio $z_0/\delta z$; this dependence is depicted in the lower panel of Fig. 4.9(b). On the other hand, the maximum power on the atoms is not a constant but itself depends on δz , with larger bars picking a larger fraction of the total incoming to the DMD power P_{tot} . With simple calculations, we

¹¹ w is defined as the distance between the first two zeros of $I(z)$ around $z = 0$ (see Fig. 4.8).

can estimate the power on the atoms

$$P(z_0, \delta z) = \kappa_{2D} P_{\text{tot}} \left[\operatorname{erf} \left(\frac{\delta z - 2z_0}{\sqrt{2}w_z} \right) + \operatorname{erf} \left(\frac{\delta z + 2z_0}{\sqrt{2}w_z} \right) \right]. \quad (4.16)$$

Here $\kappa_{2D} \approx 0.18$ is an experimentally deduced coefficient (see also discussion below) that takes into account power losses from the DMD (diffraction efficiency of the selected order, filling factor of the grating etc) and the following optical elements (transmission from mirrors, the cell etc) and $\operatorname{erf}(x) = \frac{2}{\sqrt{\pi}} \int_0^x e^{-t^2} dt$. In Fig. 4.9(c) we show the resulting potential height U_0 (straight blue line) as a function of δz for $z_0 = 50$ mirrors and for our maximum incoming power. The blue shaded region roughly indicates the acceptable values of δz based on the requirement that $U_0 \gtrsim 2\mu\text{K}$.

3. The trapping frequency ν_z : A Taylor expansion of the potential $U(z)$ around its central minimum at $z = 0$ gives $\nu_z = \frac{1}{\Delta z_0} \sqrt{\frac{U_{\text{max}}}{2m}}$. One can show that the corrections $\Delta z/\Delta z_0$ and U_0/U_{max} cancel out for any ratio $z_0/\delta z$ (with an error less than 1%), and thus we can also approximate $\nu_z = \frac{1}{\Delta z} \sqrt{\frac{U_0}{2m}}$. This result is the same as in the general cases of Eq. (4.9) and Eq. (4.12) described above, validating our discussion for the desired Δz .

4. The anti-trapping frequencies ν_x and ν_y of the $x - y$ plane: We already expressed the requirement $W_x \approx 170\mu\text{m}$ along x . With the chosen M_{2D} we finally pick the size for the incoming beam to be $w_x = 1.7\text{mm}$. More elliptic profiles were tested but the need for a large width also along z forced a circular profile ($w_z = w_x$). For the desired $\nu_z = 5\text{kHz}$, the anti-trapping frequency along x is estimated to be $\nu_x \approx 6\text{Hz}$.

Along the propagation direction, a theoretical prediction requires a numerical treatment of the optical setup using Fraunhofer propagation theory. At any displacement Δy along our propagating laser beam with respect to the focal position, we extract the central frequency $\nu_z(\Delta y)$ of the numerically obtained intensity profile. We then attribute an effective Gaussian waist W_y by fitting the resulting $\nu_z(\Delta y)$ with a function $\propto \exp(-\Delta y^2/W_y^2)$. By repeating the same process for various δz (while keeping $z_0 = 50$ mirrors) we end up getting the (somehow surprising) result $W_y = \frac{1.05\lambda_0 f}{\delta z}$. We can now approach an anti-trapping frequency along y analogue to Eq. (4.13) as $\nu_y = \frac{\delta z}{\lambda_0 f} \sqrt{\hbar w_z / (2.1\pi m)}$ and conclude that thin bars minimise ν_y . In Fig. 4.9(c) we also show the prediction (green line) of the potential difference along y due to W_y in units of the critical temperature for a typical box of $L_y = 40\mu\text{m}$. The shaded region denotes roughly the acceptable δz with an arbitrary but reasonable cut-off $\Delta U_y/k_B T_c = 0.1$. A compromise for ν_y and U_0 leads us to pick $\delta z = 50$ mirrors and estimate an anti-trapping frequency $\nu_y \approx 14\text{ Hz}$.

Experimental setup and characterisation

Following our above described theoretical considerations, the full experimental setup related to the 2D confinement is shown in Fig. 4.10. The light, generated by a 2W green laser (*Laser Quantum*

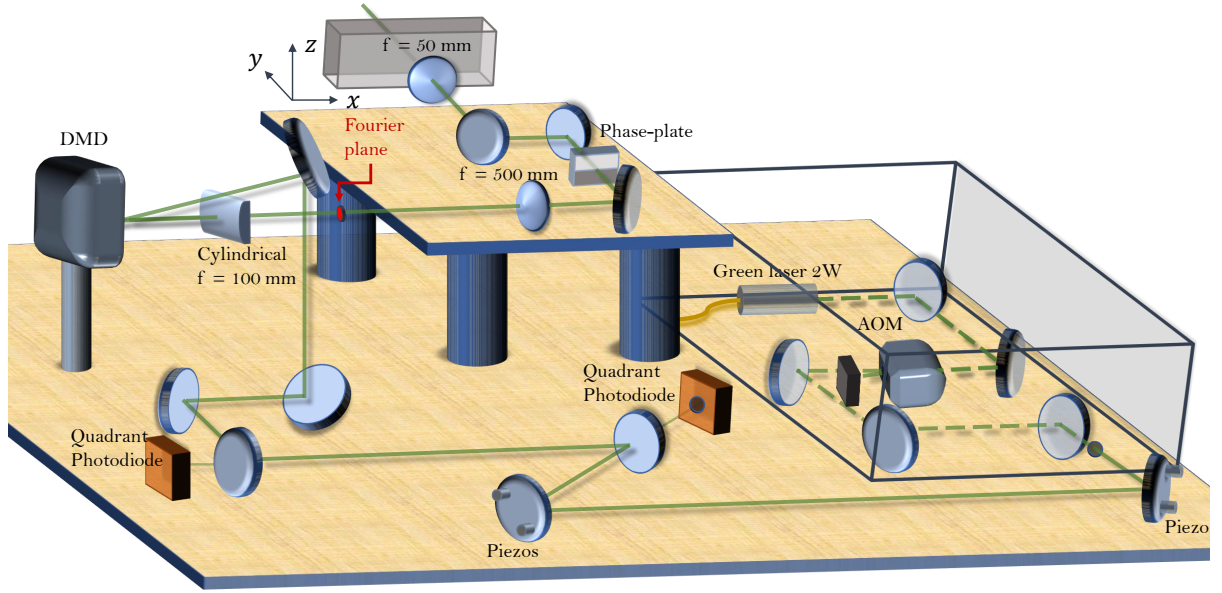


Figure 4.10: The full setup for the production of a 2D gas. The final apparatus follows the ideas set in Fig. 4.8. In the final implementation, the phase-plate is eventually placed after the Fourier plane for reasons of space limitation, after we experimentally checked that the quality of the blades is not deteriorised.

gem 532) passes through a high-power AOM (*AA Opto-electronic, MCQ 110-A3-VIS*) aligned for a maximum efficiency of 85% for the first diffracted order that allows the fast control of its power and then directed onto the DMD using a periscope to fulfil the blazing condition¹². At an angle of around 25° with respect to the diagonal of the ‘on’ mirrors, the overall efficiency of the selected 10th order of diffraction is $\sim 22\%$ when all the mirrors are at the ‘on’ position. The DMD is placed in one focal-length distance of a cylindrical lens. In the opposite focal point of the lens, an iris blocks the rest of the diffraction orders. This focal point is subsequently imaged on the atoms with two lenses of 500mm (*Thorlabs, AC254-500-A-ML*) and 50mm (aspheric, *Thorlabs, AL2550-A*) focal lengths. The $0-\pi$ phase-plate was obtained from the previous version of the 2D confinement of our machine [167].

We next verify that we can satisfy the initially imposed requirements. In Fig. 4.11 we show (i) two examples of the beam profile on the atoms as recorded with a camera together with (ii) the corresponding prediction (Fraunhofer numerics). In both cases we keep $\delta z = 50$ mirrors and increase the distance z_0 verifying that it compresses the space between the blades. Sub-figures (iii) show a cut of the intensity profiles along z in the central region of the beam giving very good agreement between theory and experiment.

¹²A blazing condition [188] (see also Ref. [189]) occurs when the direction of reflection from the individual mirrors coincides with the direction of an order of diffraction of the DMD, transferring in principle all the power into the specific order. The maximum diffraction efficiency of the used DMD is 65%.

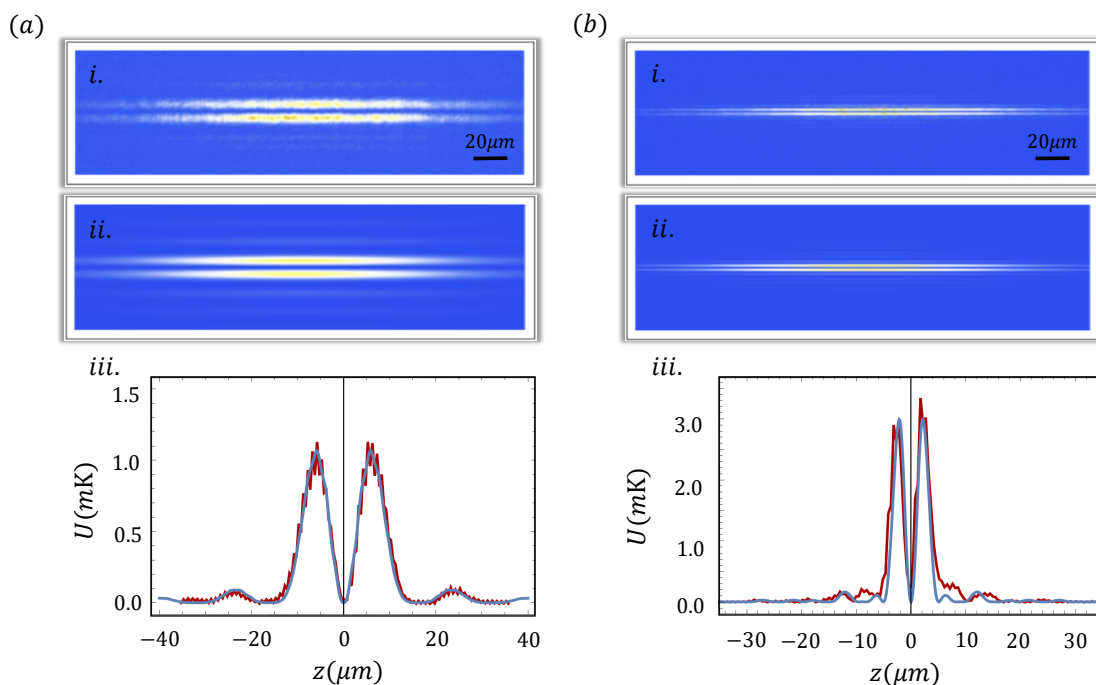


Figure 4.11: The experimentally extracted (i) and the numerically calculated using Fresnel theory (ii) intensity profiles on the atoms for two DMD patterns. In (a) we used $z_0 = 0$ and $\delta z = 50$ mirrors. In (b) we used the ‘optimum’ $z_0 = 50$ and $\delta z = 50$ mirrors for the satisfaction of our criteria. We also show (iii) a cut of the above profiles along z in the central region of the beams. Red lines correspond to the experimental images and blue lines to the theory at the same power.

Images of the beam profile can be straightforwardly used to extract the spacing and the height of the potential peaks. Fig. 4.12(a) presents the results for the spacing Δz as we keep a constant $\delta z = 50$ mirrors and scan the distance z_0 . In this process one can distinguish two different regimes, separated by the dashed vertical line in the plot. For $z_0 < 25$ mirrors the two bars partially overlap, mimicking the situation of a TEM_{10} -like mode. For $z_0 > 25$ mirrors one can see the Fourier profile as the interference of the two distinct bars.

Fig. 4.12(b) illustrates the potential maximum along z . Due to space limitations we were unable to extract the power on the atoms by averaging the measured power just before and after the ‘science’ cell. Alternatively, we estimated the loss in power from the relevant optics and the cell based on their specification data [166]. At small distances z_0 , the increase of U_0 with z_0 is a consequence of the increase of δz^{eff} . At larger distances, as the bars move further away from the center of the incoming beam, U_0 starts decreasing due to a smaller fraction of the total power.

Finally, in Fig. 4.12(c) we plot the resulting transverse frequency. The red points are the experimentally measured frequencies, as deduced by measuring the breathing mode after the perturbation of the 2D confinement in the same way as in Sec. 4.2 for the frequencies in the CDT. The gray points correspond to a fit of the camera-obtained potential profiles close to their minimum around $z = 0$. For distances larger than 50 mirrors we observe a reduction in the visibility of the interference profile,

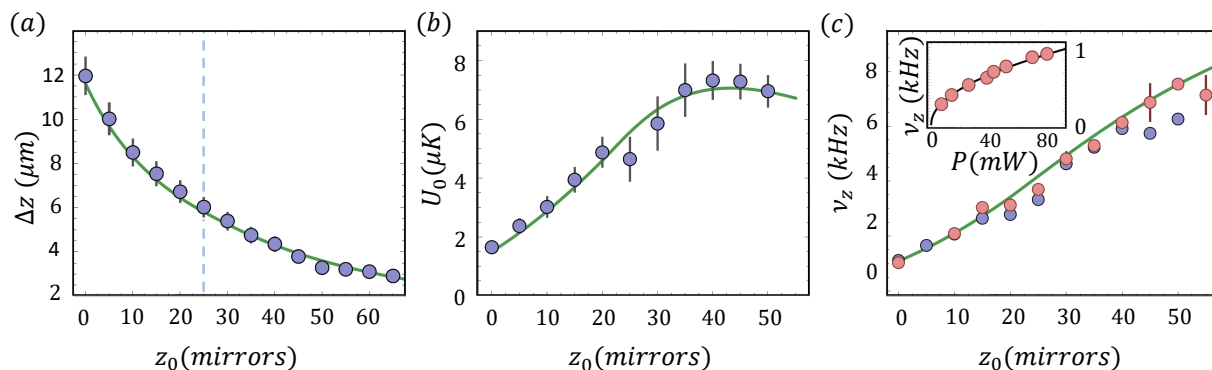


Figure 4.12: Characterisation of the quality of our 2D trap for $\delta z = 50$ mirrors and varying the distance z_0 . (a) The spacing between the two potential maxima as extracted from a camera. For $z_0 \leq 25$ mirrors, the two bars on the DMD can be equivalently be thought as a single larger centered bar. The green line indicates the theoretical predictions after taking into account the corrections described in Fig. 4.9. We are able to achieve a spacing down to $\sim 2.5\mu\text{m}$ after which no gain is observed; this saturation may be caused due to physical reasons (aberrations) or due to our detection resolution. (b) The corresponding potential height U_0 , as extracted from the camera and the measurement of the total power. The errorbars indicate the difference in height between the two peaks (standard deviation) whereas the point represents the mean height. The theoretical green line is the prediction taking into account the effects of the picked fraction of power from the incoming beam, the various sources of loss and the corrections due to the sinc-envelope (see main text). (c) The transverse frequency measured through the atoms (red points) and through the light (blue points). The theoretical curve is composed by the lines in (a) and (b) and the prediction $\nu_z = (1/\Delta z)\sqrt{(U_0/2m)}$. The fact that the measured frequency using the atoms exceeds the light measurement for higher distances z_0 indicates that the limitation in Δz we observe is mainly due to the detection resolution.

a result translated into lower fitted frequencies. The theoretical prediction (black line) is derived from combining the predictions in Δz and U_0 .

Before we shift our attention to the discussion of the new in-plane uniform confinement, we make two technical comments for our 2D setup:

Further technical considerations

Laser stability. The stability of the laser-beam position is crucial for the reliable operation of our experiments. Position instabilities of the incoming light beam are translated into potential-height imbalances of the two blades and decrease the interference contrast of the pattern derived from the DMD. The top panel of Fig. 4.13(a) shows the shift in time of the incoming beam position just before hitting the DMD; the reason of this shift is the slow heating of both the laser head and used AOM, but also shorter-timescale fluctuations (shot-to-shot) are significant. The predominant shift of almost 2.5mm in the z -direction is a serious limitation when compared with the total size of the DMD extent of 10mm and the incoming beam waist of 1.7mm.

To overcome this effect, we implement an automatic beam-walking technique. Two quadrant photodiodes (*Thorlabs, PDQ80A*) detect power imbalances between the four (horizontal and vertical) quarters of their area from the laser light that is partially transmitted through two back-polished mirrors ($\sim 1\%$ of the total beam power is transmitted), as seen in Fig. 4.10. The four voltage signals

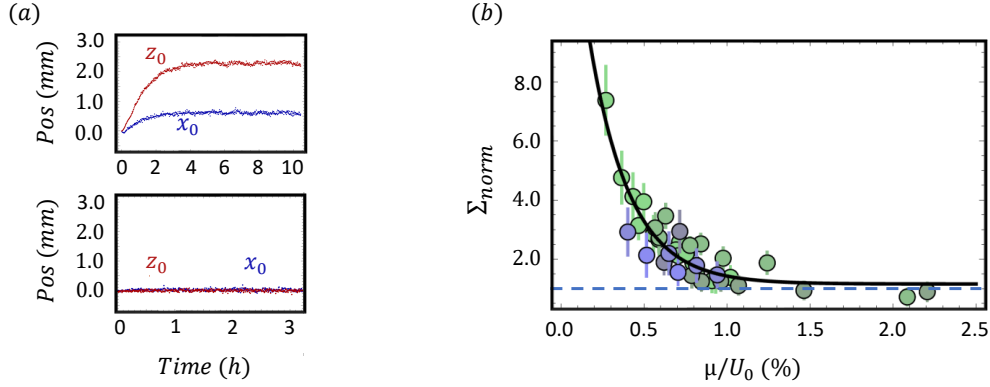


Figure 4.13: (a) The drift of the 2D laser beam on the DMD (upper panel) and its correction (lower panel) after the implementation of an automatic beam walking technique. (b) The deviation of the density profile from being homogeneous along the x direction of the observed imperfections (see main text). The parameter $\Sigma_{\text{norm}} = \sigma_{n,x}/\sigma_{n,y}$ quantifies this emergence of inhomogeneity. The data points correspond to $\Delta z = 6.8\mu\text{m}$ (blue) and $\Delta z = 3.2\mu\text{m}$ (green). The hue of the points indicate the used scattering length (lighter colors for $150a_0$ up to $800a_0$ for darker colors). The dashed line shows the expected behaviour for a truly uniform gas. The solid line is a heuristic exponential fit on the data.

(two directions per photodiode) are fed into an Arduino microcontroller board (*Arduino Nano*). The Arduino itself is connected with four piezo-electric actuators of a maximum travel of $30\mu\text{m}$ each, which have been inserted in the mounting of two mirrors for the control of their position. When the Arduino is triggered¹³, it starts scans on the length of the four piezos (in pairs in the x - and z -direction), in a way that it mimics the process of beam walking, until the signals in the quadratic photodiodes are totally balanced. The corrected position of the beam center on the DMD after a beam-walking scan is completed is depicted in the low panel of Fig. 4.13(a). There is no visible shift on the atoms after walking has finished.

Potential defects. The large potential heights that come together with the required large transverse frequencies lead to undesired and difficult-to-overcome imperfections in the 2D trapping light profile, affecting the atom density and hampering the production of a uniform gas. We found a ‘quasi-periodic’ modulation of the light intensity along the x direction (and in the nominally dark region of the 2D trap) as the most pronounced defect in our trap. This modulation with a ‘periodicity’ of the order of $15\mu\text{m}$ was tested to be irrelevant of the existence of the DMD or the phase-plate in our setup. Although its exact origin was not identified, the most plausible explanation relates it with imperfections of the collimated (along x) beam due to diffraction effects; an alternative explanation could link them with the interference of the trapping light with itself at the surfaces of the ‘science’ cell, or wavefront distortions on other optical elements. Similar defects seem to appear in other 2D atomic gas experiments, as revealed to us during various private communications.

To quantify the role of the defects, we test the homogeneity (see next section) of a very-low-

¹³During continuous running of the machine, the triggering occurs at the MOT stage of each experimental cycle and the beam walking is finished in a couple of seconds, before the green laser is shone into the atoms.

temperature 2D gas in a box as a function of its chemical potential and correlate it with the height U_0 of the 2D potential. Fig. 4.13(b) shows the results for various chemical potentials (by changing both the density and the scattering length of the gas) and various spacings Δz of the 2D confinement. We calculate the parameter Σ_{norm} , the relative standard deviation $\sigma_{n,x}$ of the surface density along slices in x normalised by its standard deviation $\sigma_{n,y}$ along y , i.e. $\Sigma_{\text{norm}} = \sigma_{n,x}/\sigma_{n,y}$. We can distinguish two different regimes. For large chemical potentials, no defects are visible in the density profile and $\Sigma_{\text{norm}} \approx 1$. For lower μ , the density profile along x deviates from being homogeneous and lines of lower and higher densities along y appear. The appearance of corrugations occurs at around $\mu/U_0 = 0.01$. In other words, we estimate imperfections on the beam at an energy scale of around 1% of the potential height U_0 , which we acknowledge as an additional lower bound for the studied gases' energy scales (chemical potential and temperature). Of course, this condition is easier to be satisfied for higher temperatures and larger interaction strengths.

4.4 The uniform in-plane confinement

In this section we describe our realisation of an in-plane box potential, which together with the two-dimensional confinement of the previous section constitute the essentials of our experimental platform.

Background

An optical blue-detuned uniform trap requires a hollow laser beam with a dark central region where the atoms are confined. The first techniques to implement such a beam profile followed the same holographic principles already discussed for a 2D trap; carefully chosen phase patterns to be imprinted on a Gaussian beam have been exploited to create hollow beams in the far-field. Among the various choices, static phase plates¹⁴ [190, 191], axicon lenses¹⁵ [87, 192] or more flexible and computer-controlled spatial light modulators (SLM), like the phase-only-controlling liquid crystal (LC) SLM [83] (that can mimic both phase-plates and lenses) have been experimentally used. However, the larger relevant length scales of the hollow beams compared to 2D traps have allowed additional techniques to be tested and successfully produce uniform potentials. One such technique utilizes a fast rotating laser beam to paint a time-averaged uniform disk-shaped potential on the atoms [193, 194]. This rotation is made by two orthogonal acousto-optical modulators that operate out-of-phase and is typically of the order of 10kHz. Another verified technique uses a mask in the path of the beam to sculpt its intensity profile, which is directly imaged on the atomic plane. Several experiments used static masks, lithographically manufactured, but recent developments have incorporated tunable

¹⁴A useful phase plate is that of a circular shape that imposes a π -phase difference between the inner and outer parts of a Gaussian beam. This configuration generates a Laguerre-Gaussian intensity profile in the far-field.

¹⁵An axicon lens, essentially a glass cone, can be regarded as a phase plate with radial phase gradient that creates a Bessel function in the near field, the Fourier transform of which is a circle.

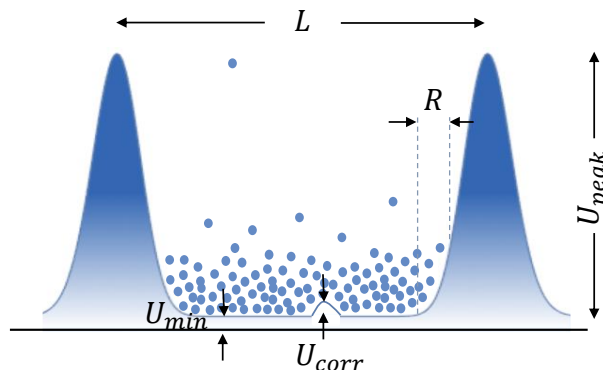


Figure 4.14: A typical potential for the realisation of a box trap. The characteristic quantities of this box denoted in the sketch are discussed in the main text.

intensity masks, like the DMD, that allow changeable shapes for the projected light [84, 85, 195].

Prerequisites and constraints

Fig. 4.14 shows a cartoon mimicking the typical potential resulting from these various methods that aim for a uniform trap. Such a potential is characterised by (1) an average background value U_{min} of its central region where atoms are to be trapped, (2) an effective size L of this region, (3) a potential height U_{peak} which serves for confining the atoms, (4) a finite potential slope that connects the uniform central region with the potential maximum, and (5) a typical height U_{corr} of inhomogeneities inside the central region. The last two properties constitute the limits of how uniform a certain realisation can become. We now discuss these characteristics in view of our requirements, as well as various physical and technical constraints.

1. **Central uniformity:** Ideally, one should aim for $U_{min} = 0$. A constant background light has no effect apart from adding to the heating and losses of atoms from the trap due to light absorption. In most realistic situations, however, some light in the central region will not be spatially homogeneous, leading to short range potential disorder. As in the case of the 2D confinement, one has to compare these variations with the energy scales (thermal and interaction) of the trapped cloud to determine if they play a detrimental role against homogeneity. For our realisation, we can set an upper limit in what is acceptable by keeping these potential corrugations smaller than the anti-trapping or the defect-related potential differences occurring from the 2D confinement.

2. **Potential height:** As in the case of the 2D trapping, we need to reach potential heights of $2\mu\text{K}$ in order to trap properly atoms at a temperature up to around 400nK. As we will show, we can use this height to evaporate the cloud in the new trap and control its temperature. A desired feature is to realise a potential height that is as uniform as possible along the confining walls for a systematic control of the temperature and evaporation.

3. **Box size:** The exact definition of the size of a trap of finite sharpness is not straightforward without referring to density distributions. This question will arise in next chapter and we will discuss it in more detail. For now we can assume that the slope of the edges is rather unimportant and define a trap size as the distance between the two potential maxima. When compared with the size of the harmonically-confined BEC in its elongated direction (without any additional compression), all the BEC atoms are trapped if the box size is larger than $\sim 60\mu\text{m}$; in reality, most atoms are confined for a size of at least $20\mu\text{m}$. In the other limit, technical issues, like the achievable potential height or the resulting 2D densities, restrict the box to relatively small values. Typically, we can ask for a proper trapping when the size is in the interval $20 - 80\mu\text{m}$.

4. **Slope of the edges:** The deviation from an ideal box with infinitely sharp edges is typically described with the leading power-law behaviour of the potential ($U \sim r^\beta$). The value of β is used also to quantify the departure from the traditional harmonic potentials ($\beta = 2$). Experimental large traps with β up to ~ 80 have been constructed. For our convenience, we also define a characteristic length R (see Fig. 4.14) over which the potential increases from its ‘minimum’ value to the relative energy scale of the system (temperature, chemical potential), relevant for the atoms. For $R \ll L$, one may call it a box trap. This claim becomes obvious if R is smaller than the healing length of the system, in which case the finite-slope potential would be essentially indiscernible from an ideal box.

The chosen trapping method

Having set our criteria, we proceed to deciding which technique to pursue for building a box trap. We first abandon the idea of painting an average potential, due to the close proximity of the maximum beam-rotating frequency with our transverse trapping frequency and the fear of extensive heating; our optimum options lie between a holographic ‘Fourier’ imaging or a direct imaging with the use of a DMD. At this point, there is enough experimental literature that allows us to make a safe choice based on our desires. For example, one can have a look at the PhD thesis of Alex Gaunt [196] of our group, where various phase patterns of the holographic method are compared, and those of Lauriane Chomaz [143] in Paris and Klaus Hueck [197] in Hamburg, where the direct and Fourier imaging techniques are contrasted in the context of 2D systems.

We choose to work with a DMD as an intensity mask and project directly its displayed image onto the atoms. The main advantage of this method is its intuitive simplicity and the ability it offers to shape arbitrary potentials with sharp edges; this is a key feature for the construction of a textbook-like rectangular box trap. A common disadvantage of a direct imaging technique is its limited depth of focus, making the hollow region of the intensity pattern we project really dark only for a very limited regime along its propagation axis. This could be a real constraint for 3D experiments, but not in our case of a transverse extent for the cloud of a few hundreds of nm; the depth of focus of our imaging pattern will be an order of magnitude larger than this size. A second obvious disadvantage is the highly inefficient way this technique treats the available power, especially by throwing away

the central part of the incoming beam to sculpt the dark trapping region. In what follows, we sketch our experimental choices to nevertheless make this method satisfy our requirements.

Details of the final trap

Our first choice pertains to the magnification between the DMD pattern and the atomic plane. We use a demagnification factor of $M_v = 68$ to realise box sizes up to $100\mu\text{m}$ using up to 70% of the DMD pixels. In order to have reasonably uniform potential walls, and also to be able to change the box size at will, the DMD is illuminated with a beam of waist $w_i = 7.2\text{mm}$ which occupies the whole area of the DMD. With this beam, the relative change (non-uniformity) of the potential along the walls for a typical square box of $40\mu\text{m}$ would be, in principle, no more than 7%, while the walls potential for a $80\mu\text{m}$ box will be 0.76 times smaller than that of a $20\mu\text{m}$ box.

Given the demagnification, we can estimate the required power for a potential height of around $2\mu\text{K}$. From the discussion above, it is sufficient to concentrate on the single case of a $40 \times 40\mu\text{m}^2$ box. If P_v is the total power of the incoming beam on the DMD then a single pixel¹⁶ (of size $s_{\text{px}} = 13.6\mu\text{m}$) on the DMD corresponds to an intensity of

$$I_{\text{walls}} \approx \kappa_v M_v^2 \frac{2P_v}{\pi w_i^2} \exp\left(-4 \frac{(100s_{\text{px}})^2}{w_i^2}\right) \approx 9.8 \times 10^6 P_v \quad [1/\text{m}^2] \quad (4.17)$$

on the atoms. Here, $\kappa_v \approx 0.29$ is again an experimentally extracted constant that accumulates the various losses of power of that pixel during the propagation, like the diffraction efficiency of the DMD, the absorption of the various optical elements and the cell. Using light at 532nm, as for the 2D confinement, one would require around 3.5W of initial power on the DMD. Instead, we use light at 760nm, much closer to the atomic transition; we can then achieve the goal of the same potential height ($2\mu\text{m}$) with 50 times less power (70mW). The increased light scattering rate from this choice is not capable of creating significant losses in the dark trapping region; with simple calculations, one gets a lifetime (solely because of the light) of 50s if $U_{\text{min}} \sim 0.05U_{\text{peak}}$ (for $U_{\text{peak}} \approx 2\mu\text{K}$), which is comparable to the lifetime due to background collisions of 150s in our science cell.

With light at 760nm, we can exploit the optical components already in place around the cell, especially the vertical imaging setup [165]; with the trapping beam counter-propagating to the imaging beam, the imaging objective acts as a diffraction-limited objective also for the DMD projection (with a demagnification of 5.2). The total setup, with the additional steps of demagnification, is illustrated in Fig. 4.15. For the production of the DMD-shaped beam, we use a CW Ti:Sapphire (TiSa) laser (*Coherent Ti:Sapphire MBR-110*) which is pumped by a 18W green laser (*Coherent Verdi V18*) to generate light at a tuneable wavelength over the range 700 – 795nm for our chosen birefringent filter. At 760nm, we get up to 1.2W of output power which, after passing through an

¹⁶The relevant pixel for the box of $40 \times 40\mu\text{m}^2$ occupies the position of index $\{100, 100\}$ with respect to the central pixel of the DMD.

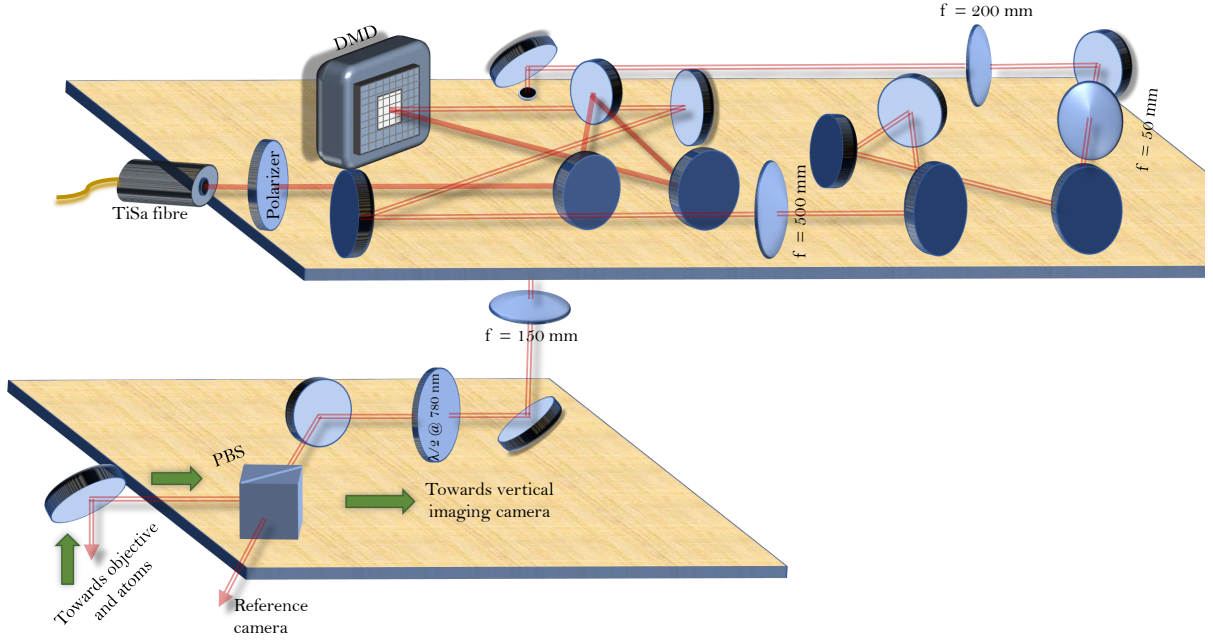


Figure 4.15: The full setup for the production of a uniform gas.

AOM (*AA Opto-electronics, MT80-A1,5-IR*) for an external fine-control of the final power, is subsequently fiber-coupled to reach our experimental table. There, the beam is masked by the projected pattern on the DMD and imaged to the atoms. Two initial steps of demagnification (500:50 and 200:150) are added before the final demagnification from the imaging objective to construct the total M_v .

Setup characterisation

The direct imaging of the DMD pattern on the atoms permits arbitrary geometries, limited only by the imaging resolution and other technical defects. We restrict our discussion to the simple but relevant case of box potentials. We create such potentials by switching on rectangular frames of DMD pixels. An example of the resulting light intensity that is projected on the atomic plane is depicted in the upper panel of Fig. 4.16(a) for the case of a square box of $L \approx 60\mu\text{m}$, and its corresponding potential in a slice along x in the lower panel of the same figure. Using this potential, we trap the atoms in the central region of the low light intensity. An example of the density distribution obtained with absorption imaging (Section 4.8) for the trapped gas is shown in Fig. 4.16(b). With images of the light and the atom density at hand, we attempt to characterise our uniform traps.

With a maximum stabilised power of around 100mW hitting the DMD, box potentials at a height up to $\sim 3\mu\text{K}$ can be realised. As expected, the maximum height of the potential has a slight dependence on the size of the projected box; the decrease of the achievable height for larger boxes of a few percent is irrelevant for the purposes of trapping gases at a temperature of some hundreds or even tens of nK.

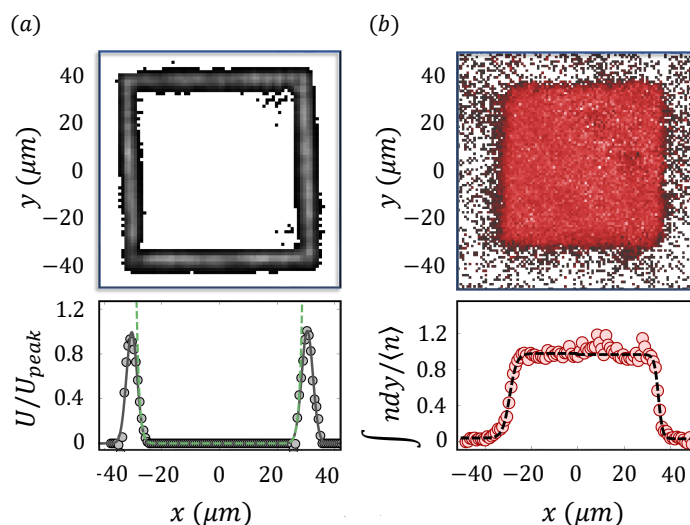


Figure 4.16: A typical example of (a) the trapping light for the in-plane confinement and (b) the resulting density profile. The lower panels show a normalised cut across x and the integrated density along y , respectively.

In the central dark region of the trap, the light intensity shows some ripples which depend on the box size. For the smallest boxes of around $20\mu\text{m}$, the average central intensity approaches the 3% of the potential barrier, whereas for larger boxes (above $40\mu\text{m}$) this background is suppressed to values below 1%. The standard deviation of the potential in the central region normalised to the potential barrier remains low at values about 0.5%. Its peak-to-peak deviations can reach up to 5% of the barrier, especially for smaller boxes. These corrugations seem larger than the defects originating from the 2D confinement. However, we note that the relevant heights for the box trap that we will work with are in the range of $100 - 500\text{nK}$, much lower than the corresponding heights from the 2D trap, making the latter the prevailing source for density inhomogeneities. Inspecting the density profile of the gas, we calculate a typical standard deviation of around 8% on the mean density, when 2D-light defects are well suppressed.

Together with the light profile in Fig. 4.16(a), we show (dashed line) a characteristic $U \sim r^\beta$ fit for the determination of the leading power-law β as a measure of the potential slope. The fit is restricted to values up to $0.7U_{\text{peak}}$ and the extracted β is plotted in the upper panel of Fig. 4.17(a) for various box sizes. The results show a clear deviation from the harmonic case even for the smallest boxes and are comparable to other recently built uniform experiments [196–198]. We also estimate the length R over which the potential increases from its mean central value to $0.2U_{\text{peak}}$, corresponding to a typical (but also relevant for our experiment - see Section 4.7) $\eta = U_{\text{peak}}/k_{\text{B}}T \approx 5$. A very similar parameter R_n is alternatively extracted from the atom-density profiles as shown (dashed line) in the lower panel of Fig. 4.16(b); we chose to fit the low-temperature density profiles with $n_0 \tanh(x/R_n)$, the same form as for a finite-sized perfectly-uniform BEC where $R_n \rightarrow \xi$. We find $R_n = 1.7(3)\mu\text{m}$, a value very similar to the best estimation we have for the system’s resolution.

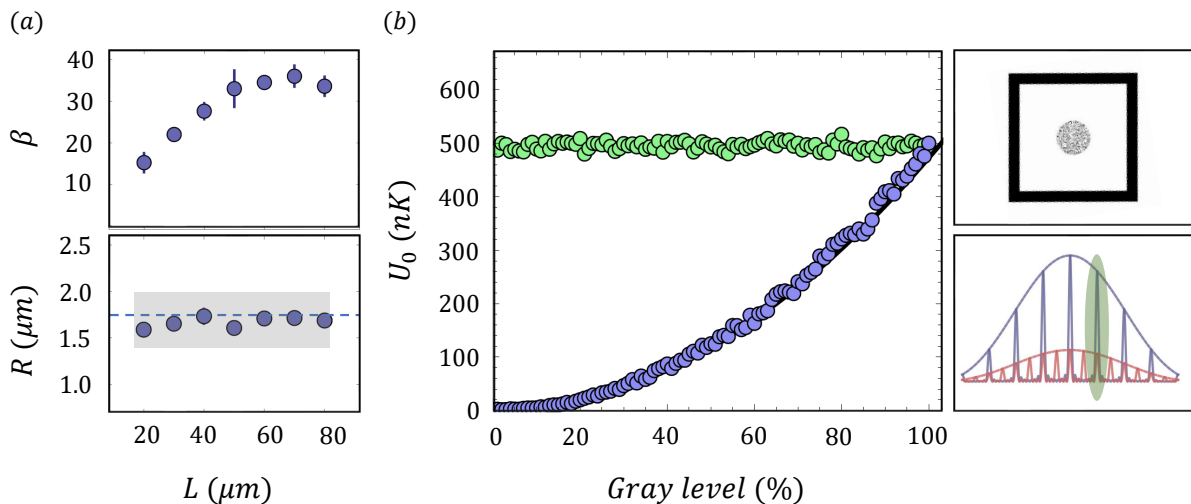


Figure 4.17: (a) Upper panel: The power-law exponent of the in-plane trapping potential as determined from the light images on the atomic plane. Lower panel: the characteristic length R for the slope of the edges. The data points are extracted from light images, whereas the shaded regime corresponds to the behaviour of the atom-density (see main text). The dashed line shows our best estimation for the system's resolution. (b) Potential height (blue points) versus gray-scaling level or equivalently the fraction of DMD mirrors that are turned on. In the specific testing geometry (shown in the upper side cartoon), the barrier remains to a level 100% and we change the fraction of mirrors in the central regime of the DMD. The green data-points correspond to the potential height of the barrier. The potential height follows a parabolic behaviour with the fraction of the mirrors that are turned on due to the parabolic change of the intensity peak of one diffraction order with the number of the slits. The black line in the main figure is a prediction for U_0 based on this parabolic dependence, the knowledge of the central area that is used for gray scaling, and the measured power when all the mirrors are turned on (no additional grating). The low-side cartoon illustrates the change of the efficiency of the selected order with the changing of the gray level based on Eq. (4.18). The blue line corresponds to a doubling of the number of mirrors compared to the red line. The total power is also doubled, but the intensity of the selected order is quadrupled.

Another comment we want to make is related with the choice of a framed wall for the potential barrier as in Fig. 4.16(a) and the blocking of the light in the outer part of the trap from reaching the atomic plane. This frame serves two purposes. On one hand, we found experimentally that allowing light in the outer part of the trap creates undesired effects in the central density profile, probably due to reflection effects. On the other hand, a very thin frame would lead to a reduced trap-depth. To see that, we first calculate the effective size of a single DMD mirror on the atomic plane to be $s_{\text{px}}/M_{\text{v}} = 0.2\mu\text{m}$. This size is well below the optical resolution ($1.7\mu\text{m}$) of the imaging of the DMD pattern. This means that around $(1.7/0.2)^2 \approx 72$ mirrors correspond to the same diffraction-limited spot on the atomic plane and keeping some of them off would result in the decrease of the total power in that spot. A width of at least 9 mirrors is then necessary for reaching the maximum available trap-depth.

Gray scaling: Although the projected DMD patterns are binary, the relatively low resolution compared to the DMD mirror-size on the atom plane permits a spatial gray-scaling of the resulting potential with, in our case, around 72 different gray levels. The intensity of a resolution-limited

spot on the atoms is then controlled by the turning on of a proper number of neighbor mirrors that are connected with that spot. We found that a simple ‘throwing-the-dice algorithm’ for turning on or off each mirror (with a probability of being on equal to the desired gray level) provides smoother monotonic behaviour of the light intensity compared to other, commonly used algorithms (like the Floyd-Steinberg error diffusion algorithm [199]). An example of our gray-scaling technique is illustrated in Fig. 4.17(b). In this example we use the central region of the atomic sample to test gray scaling, while keeping the trapping barrier at its maximum value (see upper cartoon in the side). The resulting potential height in the center for various chosen gray levels (blue points) together with the height of the barrier (green points) are shown in the main figure.

An initially surprising result is that the central potential height is not proportional to the fraction of the mirrors that are turned on and subsequently to the picked power, but there is rather a parabolic dependence. We interpret this behaviour as the result of the change of the efficiency of the projected order of diffraction with the gray level. A simple way to understand this effect is by considering the central gray-scaled pattern of the DMD as a separate external grating made from the combination of the ‘on’ and ‘off’ mirrors of that pattern. With a simple one-dimensional (along - say - x) model of diffraction, the intensity profile of this grating is

$$I = I_0 \frac{\sin^2(\pi N_s d_s x / \lambda_0 f)}{\sin^2(\pi d_s x / \lambda_0 f)} \text{sinc}^2(\pi w_s x / \lambda_0 f), \quad (4.18)$$

with N_s the number of the slits (‘on’ mirrors), d_s the distance between the slits, and w_s their width (mirror size). By increasing the gray level (number of mirrors that are ‘on’) by a factor F , the total power indeed changes by F ($I_0 \rightarrow FI_0$); at the same time, the effective number of the slits in the grating changes as $N_s \rightarrow FN_s$ and their average distance reduces as $d_s \rightarrow d_s/F$. This leads to a change of the intensity peak of any order (and thus of the potential on the atoms) by a factor F^2 as can be obtained from Eq. (4.18). This situation is depicted and described in the low-side cartoon of Fig. 4.17(b).

4.5 Integration of the DMDs into the experimental setup

In the previous sections we treated the DMDs almost as black boxes that mask the incoming beams with a desired shape for direct (box trap) or Fourier (2D trap) imaging. In this section we give some more details of their functionality from a more technical perspective and discuss their integration to our experimental apparatus.

A simplified block diagram of our DMD-controlling setup is shown in Fig. 4.18. The core of the hardware of this setup (the ‘chipset’) consists of the actual micromirror device, a digital controller and an internal memory board. Each micromirror on the chip is mounted on a 1-bit memory cell, the value of which sets the position of the mirror through electrostatic forces. Sequences of images can be loaded into the internal memory board and then one-by-one to the memory cells with a fashion

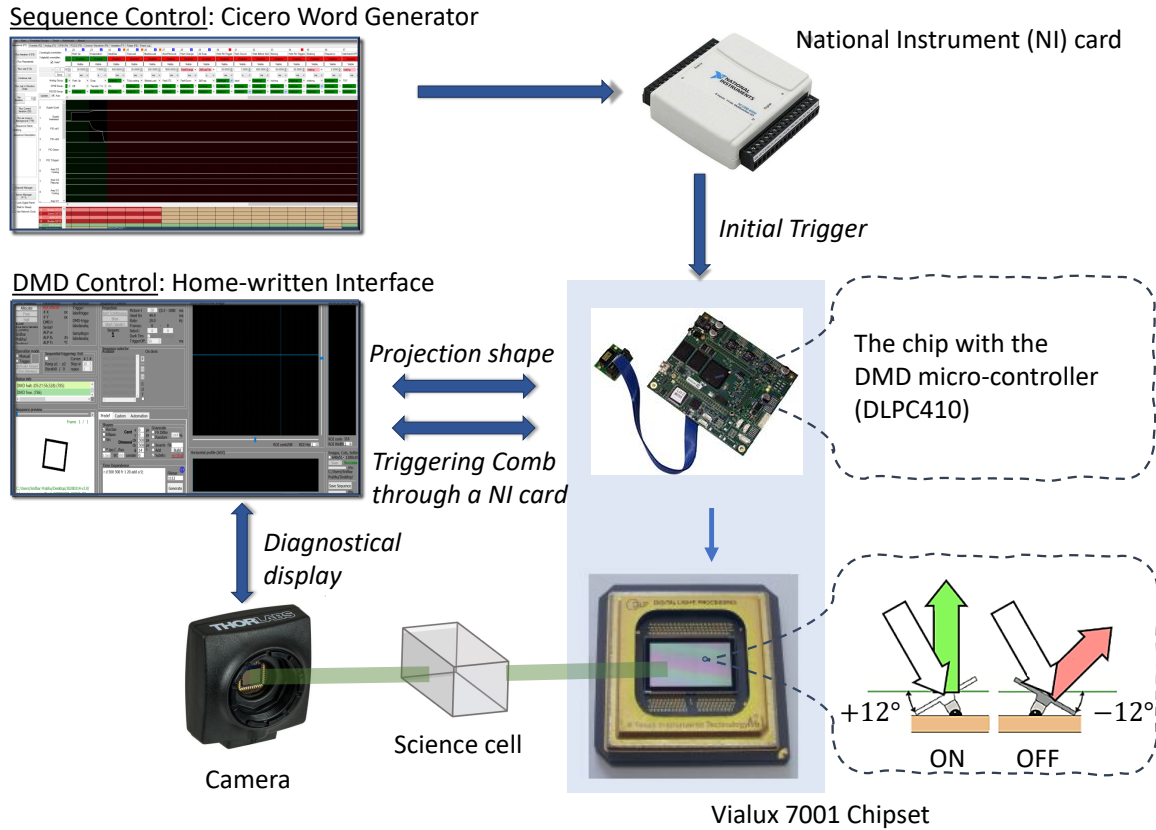


Figure 4.18: Simplified block diagram of the DMD-controlling setup.

controlled by the DMD controller. The refresh rate (or its inverse ‘picture’ time) of the frames in the sequence can be generally set either by an internal to the chipset clock or externally through a triggering comb of pulses.

We use the V7001-model from Vialux. The DMD display consists of 1024×768 mirrors of dimensions $13.6 \times 13.6 \mu\text{m}^2$. The chipset supports a wide range of optical wavelengths including 760nm and 532nm at a maximum efficiency¹⁷ of $\sim 68\%$. It allows storing $\sim 14 \times 10^3$ frames and offers a high refresh rate. For binary images the maximum rate of 23kHz permits a large spectrum of dynamic performances ranging from the slow adiabatic deformation of the corresponding light potential to almost instantaneous quenches for studies of out-of-equilibrium phenomena. Apart from binary frames, one can project images of a depth up to 8 bits (256 levels) of gray scaling by binary pulse modulation, i.e. the flickering of the mirrors for the corresponding fraction of time. However, this flickering rate, being comparable to the transverse trapping frequency, may cause heating and losses of atoms; to minimise such effects, we perform gray-scaled patterns, when necessary, only with the spatial method of sub-sampling as discussed in the previous section.

¹⁷Total reflected power when all mirrors are on compared to the incoming power.

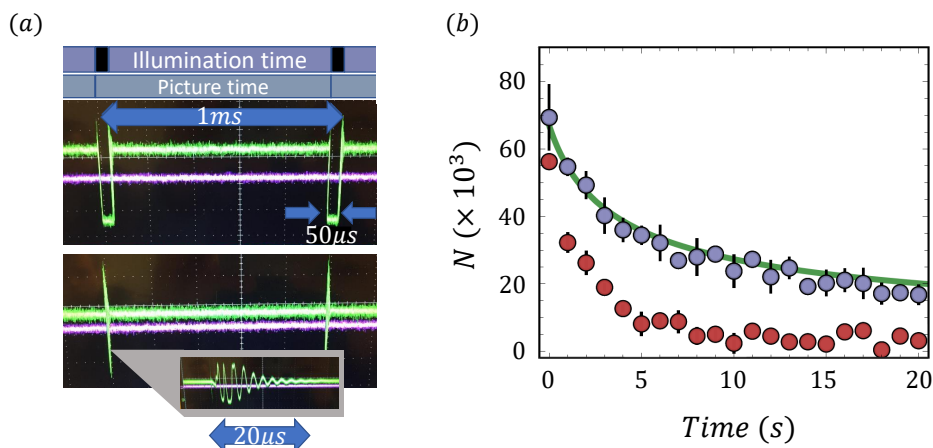


Figure 4.19: (a) Illumination on the atoms when DMD operated with (upper panel) or without (lower panel) a dark phase in the beginning of each picture time. (b) The corresponding evolution of the number of trapped atoms in a box of size $30\mu\text{m}$ and transverse frequency of 0.6kHz with (red points) and without (blue points) the dark phase. The green line indicates the expected evolution for a purely static potential due to three-body losses for the measured atom number in the beginning of the process. The agreement between theory and experiment for the lifetime in the uninterrupted mode is valid for all relevant transverse frequencies that we checked.

We control the DMD projection using a friendly C++ based interface-program developed by Julian Schmitt in our group that allows a simple generation of various DMD patterns. It communicates with the DMD controller allowing us to create and project frame patterns in a static, repeated (video-like) or triggered mode. It also communicates with a camera that displays the projected pattern on the atomic plane for diagnostic reasons. For externally triggering the DMD, and following our general strategy of controlling the experiment [165], we use a National Instrument digital output card (*PCIe 6341*). The card talks with both Cicero Word Generator [200] (our machine controlling software) and the DMD interface program. Through Cicero we can synchronize the triggering event with the rest of the experimental sequence with the use of a universal FPGA clock; the DMD interface program is responsible for sending triggering pulses, one pulse for each new frame, at a predetermined by us rate after the activation signal from Cicero has been received.

Static potentials with DMDs: The possibility to realise truly static projections on the atoms was one of our main concerns when deciding to implement trapping potentials using DMDs, due to the inherently dynamic nature of these SLMs: in order to protect the mechanical parts from being stuck or deformed, DMD manufacturers typically implement a refresh of the projected pattern at a period of a picture time, even for static projections. During this refresh, the mirrors enter a ‘dark’ phase where they are moved to a flat 0° position, before retaking their desired (on or off) place. This situation is visible in the upper panel of Fig. 4.19(a), where we show the light illuminated on the atoms from a static projection, as monitored by a photodiode. Fortunately, our DMD supports a (software-based) uninterrupted mode where the dark phase is basically suppressed. However, even in this case there is a residual ringing of the mirrors in the beginning of each picture time (lower

panel), for a duration of around $10\mu\text{m}$.

In order to check if this behaviour of the DMD poses a limitation to the trapped atom gas, we measure in Fig. 4.19(b) the number of atoms staying in a (2D and in-plane) static potential in the course of time in both the presence (red points) and the absence (blue points) of the dark phase. We observe a boost of the gas lifetime when the uninterrupted mode is applied. To quantify if the remaining ringing causes additional losses and heating, we also plot (green line) the expected behaviour of the number of atoms in the ideal case of a truly static trap, with losses occurring only due to three-body recombination events (Sec. 2.3.1). This result indicates no additional significant loss and heating due to the dynamic nature of the DMDs. However, we note that in case such detrimental effects become relevant in the future, one could implement a hardware-based suppression of the ringing by overriding the internal DMD hardware clock, as in Ref. [201].

4.6 Compensation of magnetic fields

Having characterised the newly-built 2D box trap in Sec. 4.3 and 4.4 and discussed its technical incorporation to the setup in Sec. 4.5, in the following we discuss an equally important requirement for generating truly uniform gases: the compensation of residual magnetic field inhomogeneities in the trapping region.

For ^{39}K atoms in the high-field seeking $|F = 1, m_F = 1\rangle$ ground state, magnetic field minima give rise to potential peaks. For the production of uniform gases, we need to minimize the in-plane spatial variation of the existing (desired or stray) fields in the vicinity of the atoms; effective field-gradients smaller than 10^{-3} G/cm are required in order for the potential variations to fall below 1nK within our boxes. In addition, we desire to cancel the effect of gravity which corresponds to a field gradient of 6.9 G/cm. This gradient, which gives a potential difference of $\sim 10\text{nK}$ in a length-scale of one transverse oscillator length $\ell_z \approx 200\text{nm}$, is not, in principle, crucial for the final 2D gas of a potential height $\sim 1\mu\text{K}$. However, on one hand, the preparation of such a cloud becomes more efficient when gravity is compensated, and, on the other hand, we need to maintain the ability for long 3D free expansions of the cloud.

In Fig. 4.20(a), we sketch the configuration of the coils surrounding our science cell. The exact dimensions, distances and number of windings for these coils are given in [165, 166]. Two parallel groups of coils (green) along z of radius R_{Fesh} in Helmholtz configuration generate the Feshbach field to control the atomic interactions and will be responsible for a relatively high bias field of 350 – 400G in the vicinity of the atoms. In an ideal Helmholtz configuration (with a distance $d_{\text{Fesh}} = R_{\text{Fesh}}$ between the two groups of coils), the resulting field has only a z -component and its magnitude B_0 is truly homogeneous in an extended region around the center of the coils. In that scenario, gravity (but also any stray in-plane gradient) can be cancelled out with the use of our transport coils (blue)

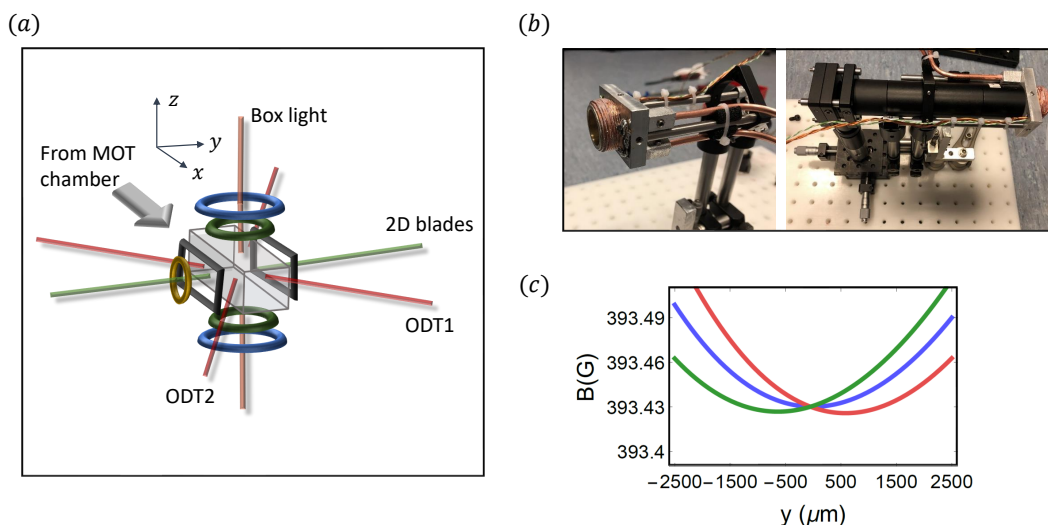


Figure 4.20: (a) Geometry of the coils for the production of the necessary fields and the compensation of stray fields. One can discern the transport quadrupole coils (blue), the Feshbach coils (green), the y -compensation bias coils (black) and the newly placed anti-Ioffe coil (yellow). (b) A picture of this new water-cooled coil before it was placed in the experiment. It is mounted together with the horizontal imaging objective. With the freedom to move along all three directions, we experimentally placed the coil in a way that it required acceptable currents in order to properly cancel the potential gradients on the atoms. (c) The magnitude of the magnetic field along y from the combination of the Feshbach, the quadrupole and the new anti-Ioffe coils. The large Feshbach bias along z transforms the field along y into a curvature. The current in the anti-Ioffe coil (7A, 9A and 11A for the red, blue and green curves respectively) mainly shifts the position of the field minimum. By considering the position $y = 0$ as the one where atoms lie, compensation occurs for the blue curve with an anti-trapping frequency of around 1Hz. The absolute value of the minimum field also changes with the anti-Ioffe current approximately by 0.1G/A, which is not shown here for plotting reasons.

which provide a quadrupole field with a gradient¹⁸ $B' = 0.8\text{G/cm/A}$ along the strong z axis. The magnitude of the Feshbach plus quadrupole field then is approximately

$$B = B_0 + B'z + \frac{1}{2} \frac{B'^2}{4B_0} \rho^2, \quad (4.19)$$

which simultaneously can compensate gravity (when $B' = 6.9\text{ G/cm}$) and suppress the quadrupole or other in-plane gradients due to the large value of B_0 .

However, in our experiment we noticed a surprisingly large (and Feshbach-dependent) ‘gradient’ of around $0.8(2)\text{G/cm}$ along y , impossible to be explained within Eq. (4.19), unless the atoms were displaced by about 0.2m along y with respect to the symmetry center $\{x_0, y_0, z_0\} = \{0, 0, 0\}$ of the coils. We attributed¹⁹ this push of the atoms to a squeezing of the Feshbach coils ($d_{\text{Fesh}} < R_{\text{Fesh}}$), facilitated by a small misalignment Δy between y_0 and the position of the atoms. In this more

¹⁸A perfect quadrupole generates a field $B_{\text{quad}} = \{-(B'/2)\rho, B'z\}$ in its radial ρ and axial z direction.

¹⁹After discarding other possibilities, like a tilt of Feshbach coils with respect to the vertical direction.

realistic scenario, we substitute the magnitude of the z -component²⁰

$$B_0 \rightarrow B_0 \left(1 - \underbrace{\frac{3}{4} \frac{d_{\text{Fesh}}^2 - R_{\text{Fesh}}^2}{(d_{\text{Fesh}}^2/4 + R_{\text{Fesh}}^2)^2}}_{A_{\text{F}}} \rho^2 \right) \quad (4.20)$$

in the first term of Eq. (4.19) to get a first order correction of the total field (assuming a large displacement only along y). The added in-plane curvature depends now linearly on B_0 and even small mismatches between d_{Fesh} and R_{Fesh} make it prevail, giving an enhanced local ‘gradient’ on the atoms. Using Eq. (4.20) (with the experimental $R_{\text{Fesh}} = 3.7\text{cm}$) in Eq. (4.19) and with an intrinsic squeezing of 0.5cm for the Feshbach coils by construction [166], we get a displacement $\Delta y \approx 1\text{mm}$ in order to reproduce the observed gradient.

Instead of aligning the atoms on the center of the fields, an attempt of which degraded our BEC production, we opted for better flexibility to shift the field’s center towards the position of the atoms. To that end, we added a new coil to the setup (the yellow coil in the sketch, properly pictured in Fig. 4.20(b)), consisting of three layers with eight circular windings of copper per layer of radius $R_{\text{A}} = 1.2\text{cm}$ and placed $D_{\text{A}} = 1.9\text{cm}$ away from the atoms along the y -direction. Mounted on a water-cooled hollow steel block, it permits the necessary currents I of around 10A without any considerable heating. This new coil resembles the configuration of an Ioffe coil, like the one used in previous versions of the machine, and since it is placed antidiometrically to that old coil, we adopted for it the figurative name ‘anti-Ioffe’ coil.

A simple model that captures our compensation method uses just the Feshbach and the anti-Ioffe coils. The latter generates at the distance D_{A} a bias field $B_{\text{A}} \approx (3 \times 8)\mu_0 I R_{\text{A}}^2 / 2(D_{\text{A}}^2 + R_{\text{A}}^2)^{3/2}$ and a quadrupole of gradient $a_{\text{A}} = B_{\text{A}} 3D_{\text{A}} / (D_{\text{A}}^2 + R_{\text{A}}^2)$ along y . In the above, $\mu_0 = 4\pi \times 10^{-7} \text{H/m}$ is the magnetic permeability of free space. The magnitude of the total field from these two coils close to the Feshbach center and along y (at $x = z = 0$) is written as

$$\begin{aligned} B(y) &= \left((B_{\text{A}} + a_{\text{A}}y)^2 + (B_0 - B_0 A_{\text{F}} y^2)^2 \right)^{1/2} \\ &\approx B_0 \left(1 - A_{\text{F}} y^2 \right) + \frac{1}{2} \frac{(B_{\text{A}} + a_{\text{A}}y)^2}{B_0}. \end{aligned} \quad (4.21)$$

which shows a parabolic behaviour with a minimum at $y_0 = -B_{\text{A}} a_{\text{A}} / (a_{\text{A}}^2 - 2A_{\text{F}} B_0^2)$. In the absence of the anti-Ioffe coil, Eq. (4.21) reduces to Eq (4.20) with a minimum at $y_0 = 0$; for a change of current from I by δI , the change of the minimum position is to an excellent degree linear with

$$\delta y_0 = \frac{4B_{\text{A}} a_{\text{A}} A_{\text{F}} B_0^2 / I}{(2A_{\text{F}} B_0^2 - a_{\text{A}}^2)^2} \delta I \quad (4.22)$$

²⁰See Appendix E of Ref. [165] for a detailed derivation of the magnetic field in a real Helmholtz configuration.

within the range of the parameters we use. With this simple model, one can estimate the shift of the field minimum by 10A on the anti-Ioffe coil (that is eventually used) to be around 0.6mm, quite close to the calculated shift of 1mm.

This parabolic behaviour is also found if we numerically estimate the field produced by the combination of all the coils taking into account all the details of our geometry; with this simulation we find very good quantitative agreement with the experimental choices of currents for the compensation of the fields. The resulting field is illustrated in Fig. 4.20(c), for three different values of the anti-Ioffe current. With increasing current, y_0 shifts towards negative y -values with the position of the coil being located at $y = -1.9$ cm. There is, in addition, a very weak dependence of the field minimum and the strength of the curvature on the anti-Ioffe current. However, using our simulations, we deduce that the resulting anti-trapping frequency from this curvature remains between 1Hz and 2Hz for all relevant cases. This frequency corresponds to a maximum of ~ 1 nK variation of the magnetic potential for the largest boxes of $100\mu\text{m}$ size when y_0 coincides with the atomic position, and becomes thus irrelevant for the homogeneity of our cloud.

Experimentally, we optimised empirically the currents of the transport and anti-Ioffe coils for each value of the Feshbach current by minimising the displacement of a freely expanding cloud in the presence of the same magnetic fields from both the vertical and horizontal imaging directions.

4.7 The procedure for producing a degenerate 2D uniform gas

Having introduced all the necessary components, here we describe the process we follow to create a 2D uniform gas from a harmonic BEC. In short, and as summarised in Fig. 4.21, the process consists of an initial step of transferring the atoms from the CDT to the box trap, a subsequent step of compressing the cloud for freezing out its transverse direction and a final step for the control of its density, temperature and interaction strength. These three steps are separately discussed in what follows.

Loading of the box trap. The loading of the 2D-box trap presupposes the alignment of the corresponding light potentials with the position of the prepared BEC. We align the box trap such that its sides lie along the x and y directions (see Fig. 4.3). In this way the elongated BEC points along the diagonal of the box, allowing a maximum number of trapped atoms. The alignment of the 2D blades was proven more tricky. Using the results of enhanced anti-trapping when not properly aligned, we now trivially determine the focus (y direction) and the position of the blades along x . The vertical alignment is completed by temporarily removing the phase-plate and achieving a split of the BEC into two equal parts from the resulting central intensity of the light. Due to the automatic control (walking) of the beam position, there is no need for any daily realignment of the blades.

With an aligned box trap, we proceed to the loading from an almost pure BEC or alternatively from a partially condensed cloud, depending on the desired final temperature. For the range of

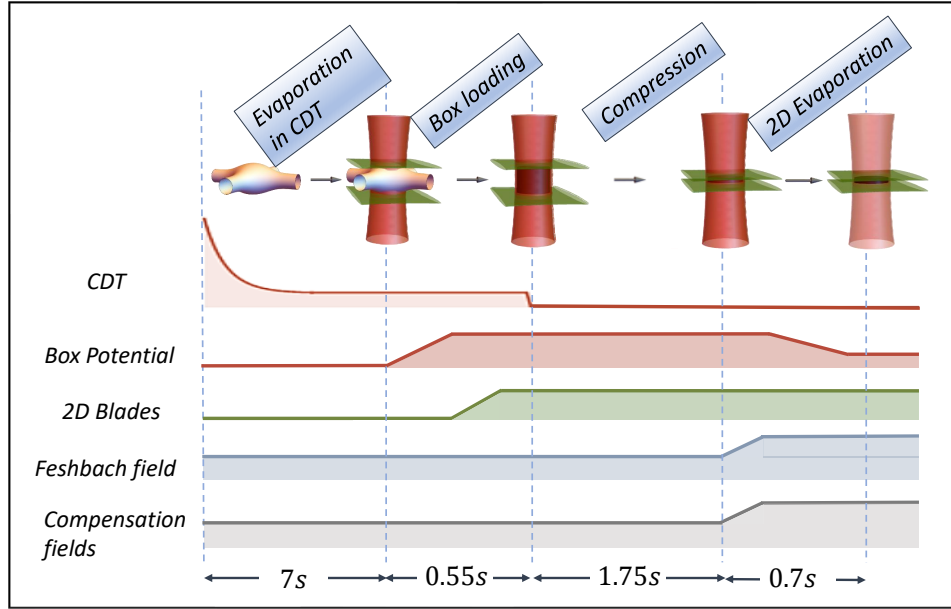


Figure 4.21: An overview of the steps used for the production of the 2D uniform gas as described in the main text. The lines of the various quantities represent power if they are related to light potentials or current if they are for magnetic fields.

temperatures we are interested in this thesis, we consider the case of a quasi-pure BEC. The loading starts by first ramping up linearly the power of the box potential in 250ms and subsequently the power of the 2D blades for another 250ms, while keeping the CDT powers at their previously constant values. A short waiting of 50ms in this combined trap is followed by the ramping down of the CDT. We keep the height of the box potential at around 600nK independently of the chosen box size to prevent the atoms from being evaporated from the trap.

To facilitate the loading of a large number of atoms, we may first shrink the BEC before the ramping up of the 2D-box potentials, either by ramping up the power of the CDT (recompression of the cloud) or by decreasing the scattering length. However, the versatility of our setup allows the trapping of most BEC atoms for a wide range of box sizes and spacings between the blades without any change in the BEC properties. In Fig. 4.22 we show the atom number loaded in the box trap for various choices of (a) box sizes and (b) blades spacing, when almost all the atoms are trapped along the transverse direction or the horizontal plane, respectively. The efficiency of loading is around 90% for $L \gtrsim 50\mu\text{m}$ in a qualitative agreement with the BEC size. For smaller boxes the loading efficiency decreases and we indeed achieve better loading by reducing a ; in the future, if higher atom numbers are required for even smaller boxes, one can exploit the dynamical capabilities of DMDs to realise a compression of the cloud also in the $x - y$ plane.

For the transverse confinement we use $\Delta z = 19\mu\text{m}$ to get practically all the BEC atoms in the

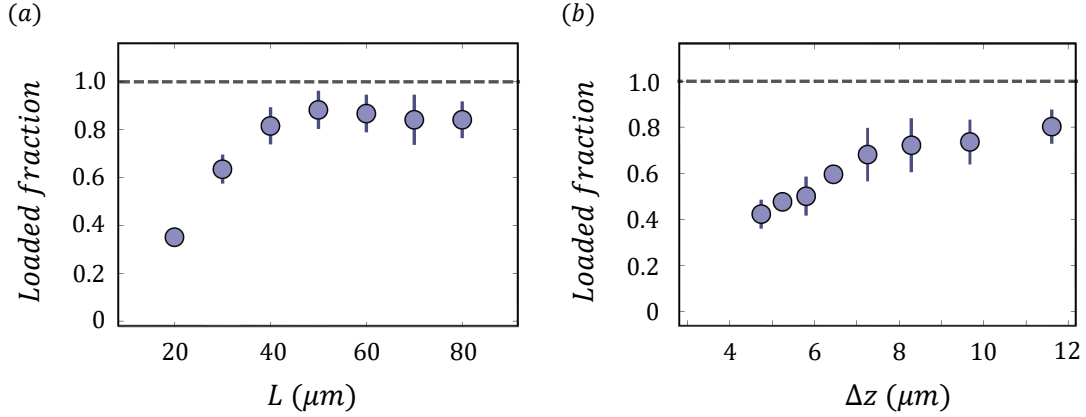


Figure 4.22: The loading efficiency of our 2D-box trap for various (a) box sizes and (b) blades spacings starting from a quasi-pure BEC with 1.8×10^5 atoms. In (a) we kept $a = 170a_0$ and $\Delta z = 19\mu\text{m}$, whereas in (b) it is $a = 20a_0$ and $L = 60\mu\text{m}$. Extrapolating for $\Delta z \approx 3\mu\text{m}$, the efficiency of loading the central minimum of the 1D lattice drops to around 20%, with the simultaneous loading of adjacent minima. We choose to load the 2D trap with $\Delta z = 19\mu\text{m}$, that traps essentially all the atoms in the central minimum of the 1D lattice.

main potential minimum during loading²¹ with a transverse frequency of 250Hz. For large box sizes, the temperature of the trapped cloud is around 30nK; for smaller boxes, we found an increased temperature of around 50nK, and we attribute it to heating effects from the interaction of the atoms with the box light. For the method to extract the temperature, we refer to Sec. 4.8. Although it is experimentally difficult to measure the temperature of the harmonic quasi-pure BEC, we note that the 3D phase-space density is expected to decrease²² by a factor of almost 3 during the loading from a 3D harmonic to a 1D harmonic + 2D uniform trap even in the absence of additional heating effects [202].

Adiabatic compression in the box trap. Following our discussion in Sec. 3.1 and 4.3, we aim to freeze out the atomic motion along the vertical direction with $\omega_z \approx 2\pi \times 5\text{kHz}$. For the initial trapping frequency $\omega_z \approx 2\pi \times 250\text{ Hz}$ during the loading, the condition $\hbar\omega_z > k_B T_c$ is satisfied only for a very small number of atoms ($N < 10^3$) for our typical box sizes (with a weak logarithmic dependence on \tilde{g}). In addition, in accordance with Eqs. (2.46) and (3.3), the interaction strength scales as $\tilde{g} \propto a\sqrt{\omega_z}$, whereas the three-body loss-rate constant scales²³ as $L_3^{(2D)} \propto a^4\omega_z$, and thus a larger transverse frequency makes it easier to get into strong interactions with slower losses as compared to increasing the scattering length.

As introduced in Sec. 4.3, we compress the loaded gas along z by dynamically decreasing the

²¹The chosen pattern consists of $z_0 = 0$ and $\delta z = 30$ mirrors, referring to the parameters as defined in Fig. 4.8.

²²The change in $D^{(3D)}$ when modifying adiabatically the power-law of the trapping potential follows $D_2^{(3D)}/D_1^{(3D)} = e^{\gamma_2 - \gamma_1}$, where $\gamma_i = 3/2 + \sum_{k=1}^3 1/s_k$ and s_k characterising the trapping potential $U \propto \sum_{k=1}^3 x_k^{s_k}$. In our case $\gamma_1 = 3$ and $\gamma_2 \approx 2$, giving $D_2^{(3D)}/D_1^{(3D)} \approx e^{-1}$.

²³Scattering is still considered three-dimensional, so we can still write $dn_{3D}/dt \sim -L_3 n_{3D}^3$. With $n \approx n_{3D} \ell_z$ we can write an effective 2D loss-rate with a constant $L_3^{(2D)} \approx L_3/\ell_z^2$ providing the scaling in the main text. For a more detailed treatment see the discussion in Sec. 4.8.

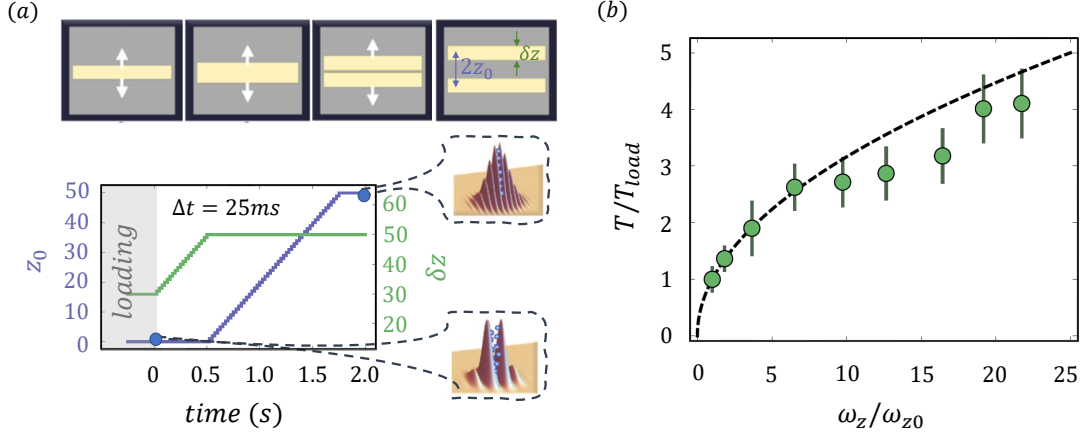


Figure 4.23: Optical accordion. (a) The top cartoons show the evolution of the DMD pattern. We remind the definitions of z_0 as the distance of the bars from the horizontal symmetry of the DMD and δz as the width of the bars. The main plot quantifies this evolution in terms of z_0 (blue) and δz (green). We picked a DMD picture time of 25ms to secure adiabatic conditions without considerable losses. The resulting spacing δz of the blades follows the route shown in Fig. 4.12. (b) The evolution of the temperature of the cloud during compression. The dashed line shows a square-root adiabatic prediction as explained in the main text.

periodicity Δz of the applied 1D lattice. Optical lattices with dynamically adjustable periodicity, often called optical accordions, have been suggested [203, 204] and implemented [205] before, and also for a 2D Bose gas [84]. Our main innovation was the implementation of an accordion based on a DMD. The details of the chosen route to compress the gas are described in Fig. 4.23(a) and can be split into two distinct stages. During the first stage, we keep $z_0 = 0$ while δz increases from 30 to 50 mirrors with a rate of 2 pixels/ Δt , where Δt is the pre-determined picture time of the refresh of the projected frames. In a second stage, the width of the two initially overlapping bars remains at $\delta z = 50$ mirrors, while they separate with the same rate of ± 2 pixels/ Δt (or 1 pixel of change in z_0 every Δt). In the end of the compression, we have the desired configuration (Sec. 4.3) of two separated bars with $z_0 = 50$ and $\delta z = 50$ mirrors; at this configuration and with the used power, we find a potential height a bit less than $3\mu\text{K}$ and a frequency of $5.5(1)$ kHz.

We can approximate the condition for an adiabatic compression as

$$\frac{d\omega_z(t)}{dt} \ll \omega_z^2(t). \quad (4.23)$$

By first neglecting digitalised effects related to the DMD, we reach the adiabatic condition $\Delta t \gg 1\text{ms}$ for our compression protocol²⁴. Strictly speaking, however, the derivative $d\omega_z/dt$ never satisfies the condition in Eq. (4.23) because of a δ -like time-dependence at the moments of the refresh of the DMD pattern. We plot in Fig. 4.23(b) the evolution of the measured temperature during the applied

²⁴According to the discussion in Section 4.3, the trapping frequency during compression evolves as $\omega_z(t) = 2\pi\sqrt{\frac{U_0}{2m}\frac{1}{\Delta z}} = Kz_0(t)$, with $K = \frac{4\pi}{\lambda_0 f}\sqrt{\frac{U_0}{2m}}$. The central position of each bar changes as $z_0(t) = z_{0i} + \frac{\Delta\delta z}{\Delta t}t$, where z_{0i} the position at the beginning of compression and $\Delta\delta z = 1$ pixel. By replacing $\omega_z(t)$ into Eq. (4.23), one finally gets $\Delta t \gg \frac{\Delta\delta z}{Kz_{0i}^2}$ or $\Delta t \gg 1\text{ms}$ for our effective $z_{0i} = 7.5$ mirrors and the relevant trapping heights.

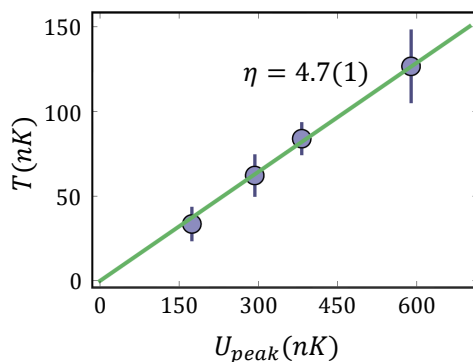


Figure 4.24: Temperature of the prepared 2D uniform gas for different in-plane potential heights U_{peak} for $L_x = 22\mu\text{m}$, $L_y = 36\mu\text{m}$ and $\tilde{g} = 0.64$. We generally find a slope $\eta = U_{\text{peak}}/k_{\text{B}}T \approx 4$ to 5 with a slight dependence on the box size. In the shown specific case, $\eta = 4.7(1)$.

compression. The picture time is chosen, as in all our future results, to be $\Delta t = 25\text{ms}$, giving a total compression time of 1.75s. For the specific measurement, we used a large square box of $70\mu\text{m}$ to start with the lowest temperature and a large in-plane potential height of $2\mu\text{K}$. In the same plot, we compare the results with the theoretical prediction $T \propto \sqrt{\omega_z}$ for the adiabatic compression of an ideal Bose gas²⁵ and find good agreement.

Control of the temperature and atom number. Unlike in the case of a large in-plane potential height as used for the results in Fig. 4.23(b), by restricting U_{peak} to lower values we notice that T saturates to a value that depends linearly on U_{peak} ; this is a balancing effect between the tendency to higher temperatures through compression and lower temperatures through evaporative cooling. We exploit this behaviour to control the temperature and atom number (through losses and evaporation) in the trap before commencing the main experiment. In more detail, the 1.75s-step of the compression occurs always at a height $U_{\text{peak}} \approx 600\text{nK}$. By the end of compression, we typically get a gas with $N \approx 80 \times 10^3$ at around 120nK. The Feshbach and compensation fields are ramped to their final experiment-dependent values after which a ‘2D evaporation’ process is applied, in which U_{peak} is linearly ramped to give the desired temperature. The total duration of this step is 0.7s with an additional holding time for the determination of N through three-body losses.

An example of controlling the temperature with U_{peak} is shown in Fig. 4.24 for a cloud of dimensions $L_x = 22\mu\text{m}$ and $L_y = 36\mu\text{m}$. In this case, we find $\eta = U_{\text{peak}}/k_{\text{B}}T = 4.7(1)$. We note that this number is not universal for our experiment, but slightly depends on the size of the cloud. We also note that after long holding times, we have noticed an additional cooling and a precise calibration

²⁵A simple way to obtain the dependence $T \propto \sqrt{\omega_z}$ for the ideal 2D uniform gas is through considering a transverse condensate [142, 143]; the atoms condense in the z -ground state when the 2D phase-space density, D , reaches approximately the value $D_c^{\text{trans}} \approx \frac{\pi^2}{6} \frac{k_{\text{B}}T}{\hbar\omega_z}$. Furthermore, D (being $\propto n/T$) decreases during adiabatic compression since n (the integrated density along z) remains constant, while T increases to satisfy an unchanged total 3D phase-space density. However, since the adiabatic compression of an ideal gas does not change the populations of the transverse states, the fraction D/D_c^{trans} should remain constant during compression; this condition, together with the relations $D_c^{\text{trans}} \propto T/\omega_z$ and $D \propto n/T$, give the desired dependence $T \propto \sqrt{\omega_z}$.

of temperature is required if comparing clouds at different times.

4.8 Imaging and calibration of density and temperature

So far we have taken for granted the various physical quantities (like the atom number and the temperature of the gas) that have appeared in our discussion throughout this chapter. Before continuing with next chapter, here we describe the techniques used for the probing of the prepared 2D gas and for the extraction of the relevant parameters. To that end, we have incorporated imaging from two different sides, bottom to top (vertical imaging) and along the x direction (horizontal imaging). Additionally, we are able to image the gas either with the strong Feshbach bias field turned off (low-field imaging) or on (high-field imaging). The latter becomes a crucial tool in obtaining the in-trap (*in-situ*) density distribution, since the turning off of the fields requires a significant amount of time (~ 5 ms). In Sec. 4.8.1 we concentrate on our implementation of high-field imaging along the vertical direction which is the one used for the experimental results discussed in this thesis.

For the probing we use absorption imaging. It consists of shining a pulse of resonant light on the atoms and collecting their shadow on a CCD (charged couple device) camera, as a result of cycles of absorption and isotropic re-emittance of the imaging photons. Standard absorption imaging exploits a closed transition; atoms cycle between two states and can be treated as a two-level system. For a resonant to the transition ($\Delta = 0$) and low-intensity ($I \ll I_{\text{sat}}$) imaging light of a given polarisation, the low density of the atoms can be deduced using the Beer-Lambert law. According to that, an imaging beam passing through an atom cloud of infinitesimal thickness dz along the z -direction is attenuated by $dI(z) = -n_{3\text{D}}\sigma_0 I(z)dz$, with σ_0 the resonant scattering cross-section. For a real cycling transition, $\sigma_0 = 3\lambda^2/2\pi$ which in our case is $2.83 \times 10^{-9}\text{cm}^2$. The integration over the line-of-sight for vertical imaging yields directly the 2D atom density in the trap

$$n = -\frac{1}{\sigma_0} \ln \left(\frac{I_{\text{fin}}}{I_{\text{init}}} \right) \quad (4.24)$$

with I_{fin} (I_{init}) the final (initial) beam intensity after (before) passing through the atoms. The quantity $\text{OD} = -\ln(I_{\text{fin}}/I_{\text{init}})$ is the corresponding optical density. Experimentally, the intensities I_{fin} and I_{init} are extracted from two consecutive images, with and without the presence of the atoms, respectively. A third image, with an intensity I_{bg} in the absence of the imaging light is typically taken, its intensity being subtracted from both I_{fin} and I_{init} in order to remove misleading effects of any stray light.

Deviations from the simple Beer-Lambert description are proven to be significant in many real situations, especially for a 2D cloud, when one of the above assumptions is violated. We describe the various sources of such deviations and the way we took care of them in Sec. 4.8.2.

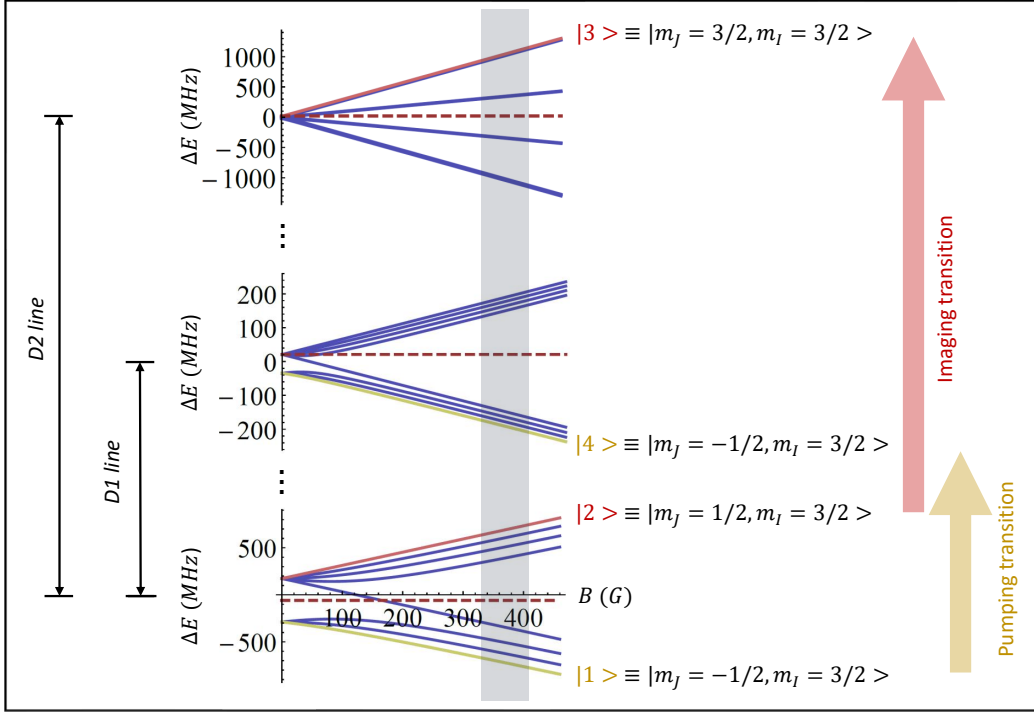


Figure 4.25: The splitting of the hyperfine states of the three lowest fine manifolds in the presence of a uniform magnetic field of magnitude B . The yellow state in the ground manifold is where our gas is prepared. The two red states are used for high field imaging. The yellow excited state of the D1 line is the intermediate state used for pumping the atoms before they get imaged. The shaded region corresponds to the working interval around the Feshbach resonance.

4.8.1 High-field imaging of the 2D plane

The eigenenergies of the characteristic Hamiltonian describing the hyperfine and Zeeman effects of the ^{39}K atoms in their three lowest fine states and in the presence of a magnetic bias [120] are shown in Fig. 4.25. At a low field the energy levels are described by the usual F and m_F quantum numbers. In the limit of very strong magnetic fields, the nuclear \vec{I} and electronic \vec{J} angular momenta of the atoms decouple and m_J and m_I become good quantum numbers. For the here relevant case of a moderately strong magnetic field between 350G and 400G, the Hamiltonian's eigenstates retain some small admixtures from different $|m_J, m_I\rangle$ states.

The 2D gas to be imaged has been prepared in the total ground state (yellow line in Fig. 4.25) denoted as $|1\rangle$, which is adiabatically connected to the low-field $|F = 1, m_F = 1\rangle$ and the high-field $|m_J = -1/2, m_I = 3/2\rangle$ state. It can be expressed as a superposition $|1\rangle = \alpha |m_J = -1/2, m_I = 3/2\rangle + \beta |m_J = 1/2, m_I = 1/2\rangle$ with β^2 between 2% and 2.5% (for $B = 400\text{G}$ and 350G , respectively). The non-zero β results in a depumping effect when the atoms are imaged in the almost cycling transition $|1\rangle \rightarrow |m_J = -3/2, m_I = 3/2\rangle$ of the D2 line [167]. To avoid this depumping, we choose to use the $|2\rangle = |m_J = 1/2, m_I = 3/2\rangle$ state of the ground manifold (adiabatically connected with the $|F = 2, m_F = 2\rangle$) which remains unmixed with the other $|m_J, m_I\rangle$ states. Starting from $|2\rangle$ we

image using the transition to $|3\rangle = |m_J = 3/2, m_I = 3/2\rangle$ of the D2 line by shining σ^+ resonant circularly polarised light (red lines in Fig. 4.25). The polarised light propagates along z in the opposite direction of the TiSa beam, while the Feshbach field serves as a quantisation axis.

We pump the atoms from $|1\rangle$ to $|2\rangle$ prior to imaging by shining a light beam linearly polarised with a polarisation parallel to the Feshbach field, and resonant with the $|1\rangle \rightarrow |4\rangle = |m_J = -1/2, m_I = 3/2\rangle$ transition of the $P_{1/2}$ fine manifold. The atoms that get excited to the state $|4\rangle$ decay spontaneously to either $|1\rangle$ or $|2\rangle$ (selection rules for the allowed dipole transitions dictate $\Delta m_J = 0, \pm 1$ and $\Delta m_I = 0$, the latter being a direct consequence of the unimportant magnetic component of the light). Since there is no resonant light to some excited state in the $|2\rangle$ state, the net result is a depopulation of $|1\rangle$ with the simultaneous population of $|2\rangle$.

The essentials of the imaging setup (objective and camera) were left untouched compared to the previous generations of this machine and are described in detail in [165]. In short, the objective is characterised by a numerical aperture $NA = 0.27$ which leads to a depth of field of about $5.0\mu\text{m}$ and a diffraction-limited resolution of $\sim 1.7\mu\text{m}$. The atom cloud is imaged onto the CCD camera (*Princeton Instruments, PIXIS 1024-BR*) with a magnification of 5.2. The corresponding pixel size in the atomic plane is $0.94\mu\text{m}$, as calibrated after the comparison with horizontal imaging and exploiting the effect of free fall of the atoms due to gravity.

The imaging beam is provided by the same laser used for cooling and trapping, locked in the D2 line. For $B = 350 - 400\text{G}$, the required additional $490 - 560\text{MHz}$ compared to the zero-field transition $F = 2 \rightarrow F'' = 3$ (as used for the already set low-field imaging technique) are supplied by the combination of using the D2-repump light (instead of the D2-cooling light, see Fig. 4.2) and an additional 100MHz-AOM . The optical pumping beam is taken as a small fraction of the D1 laser light with an extra 200MHz-AOM . Furthermore, these AOMs are used for the control of the imaging and pumping intensities, but also as a fast shutter allowing imaging exposure times τ_0 of some tens of μs . The three imaging pulses to obtain I_{init} , I_{fin} and I_{bg} are shone with a time difference of 600ms for the proper reading out of the camera; before each pulse the same sequence of events is repeated to minimize the difference of the external conditions between the three images. To minimise even further possible changing conditions in time, we externally correct the obtained intensity in the second image I_{init} by normalising its background counts to the first one, I_{fin} .

4.8.2 Calibration of density and temperature

With the help of vertical high-field imaging, as just presented, we are able to extract important experimental quantities of the imaged gas, like its density distribution and temperature, necessary for explaining the observations already discussed in this chapter, but also in the next one. Here we describe the techniques we apply for the determination of these two quantities, the density and the temperature of the gas.

Density

The validity of the Beer-Lambert (BL) law, $n = \text{OD}/\sigma_0$, for the deduction of the atom density is fundamentally limited to low light intensities and low atom densities. After introducing the dominant sources of modification from this law in a realistic experimental setting, we describe our method of extracting the surface density from the measured OD.

High-intensity effects: The finite intensity of the imaging beam and the subsequent saturation of the excited state results in a lower photon scattering rate and thus a reduced cross-section $\sigma(I)$. Within a two-level system, $\sigma(I) = \sigma_0 (1 + I/I_s + (2\Delta/\Gamma)^2)^{-1}$ [38], where we have additionally considered the effect of detuning Δ from the imaging resonance. The substitution $\sigma_0 \rightarrow \sigma(I)$ in the Beer-Lambert law with an effective intensity I , such that $I_{\text{fin}} = I_{\text{init}} - n\sigma(I)I$ yields

$$n\sigma_0 = -\ln\left(\frac{I_{\text{fin}}}{I_{\text{init}}}\right) + \frac{I_{\text{init}} - I_{\text{fin}}}{I_s}. \quad (4.25)$$

This correction shows that for considerable intensities, it is not only their ratio before and after the atomic plane that is important for extracting n , but that an absolute calibration of the recorded intensities is required.

High-density effects: High densities of the imaged sample cause the emergence of van der Waals interactions between the induced atomic dipoles by the imaging light or equivalently the multiple scattering of photons from adjacent atoms modifying the predictions of imaging a dilute sample. The effects from multiple scattering become more pronounced in a 2D gas. To see that, we first note that these modifications should depend on the proximity between the atoms; with an interparticle distance $n_{3\text{D}}^{-1/3}$, the corrections then should follow a scaling $n_{3\text{D}}k_0^{-3}$ where $k_0 = 2\pi/\lambda_0$ is the imaging wavenumber. This scaling can be expressed through the surface density as $nk_0^{-2}/(k_0\ell_z)$ showing that the strength of the modifications from the BL law depends on both the in-plane inter-particle distance and the optical thickness of the atomic sample. For a thick gas with $k_0\ell_z \gg 1$, as in the case of three dimensions, the modifications are suppressed even if $nk_0^{-2} \approx 1$. On the contrary, for a thin 2D gas multiple scattering leads to an appreciable reduction of the observed optical density compared to the ideal BL law for the true density. This reduction is also followed by a relatively small blue shift of the imaging resonance and the broadening of the absorption line [206].

Other sources of deviation: Apart from the reduction of the measured OD through its finite intensity, the imaging light introduces additional undesired modifications through a non-perfect polarisation. In our case, the large bias field prohibits transitions from $|2\rangle$ to the $|m_J = 1/2, m_I = 3/2\rangle$ and $|m_J = -1/2, m_I = 3/2\rangle$ states of the D2 line for any small π and σ^- components in the polarisation, respectively, since they are largely detuned from the light frequency. The gas then becomes

transparent for this fraction of the light with the ‘wrong’ polarisation. One could model this behaviour together with other relative effects, like an imperfect optical pumping to $|2\rangle$, with a heuristic substitution $I_{\text{init}} \rightarrow I_{\text{init}} + I_{\text{img}}$, $I_{\text{fin}} \rightarrow I_{\text{fin}} + I_{\text{img}}$, $I_s \rightarrow \alpha_{\text{img}} I_s$ and $\sigma_0 \rightarrow \beta_{\text{img}} \sigma_0$ in Eq. (4.25); the unknown I_{img} plays the role of the transparent part of the light and β_{img} the role of a total ‘fudge’ factor. The unknown parameters above can then be experimentally approximated, by requiring a prepared gas under the same conditions but imaged with different light intensity to physically have the same density distribution [38].

The motion of the atoms during imaging constitutes another possible source of deviation from the simple picture above. Absorption cycles transfer momentum $\hbar k_0$ to the atoms along the direction of the imaging propagation. The average force applied by the photons, $F = \gamma_{\text{img}} \hbar k_0$, with the scattering rate $\gamma_{\text{img}} = \frac{\Gamma}{2} \frac{I/I_s}{1+I/I_s+4\Delta^2/\Gamma^2}$ for the simplest case of a two-level system, leads mainly to two undesired effects. First, the corresponding average displacement $d_{\text{img}} = (F/m)\tau_0^2/2$ along z of the atoms during the imaging pulse of a duration τ_0 may bring them out of the focus of the imaging setup. Second, the average obtained velocity $v_{\text{img}} = (F/m)\tau_0$ Doppler-shifts the imaging resonance by $k_0 v_{\text{img}}$. Both effects depend on the imaging intensity through the average force.

Empirical corrections: To combine all the previous effects, if not more, in a simple theoretical model for the calculation of the density from the measured OD seems a daunting task. Alternatively, we use an empirical model extracted after imaging the same uniform gas for various atom densities and light intensities.

We first cancel pixelwise the effect of a variable intensity of the imaging beam by rescaling the measured OD according to the number of corresponding pixel counts C in the light image I_{init} . The main idea is illustrated in Fig. 4.26(a). Using the central part of a homogeneous cloud in the absence of density corrugations, the difference in the camera counts from shot to shot and from pixel to pixel within the same image is attributed to differences in the light intensity I . By changing the power of the imaging beam for the same atom density, we obtain the measured OD versus the number of counts, both normalised to an arbitrary reference $C_0 = 100$ counts (or equivalently $I/I_0 = C/C_0$) and the normalised $\text{OD}_0 = \text{OD}(C_0)$. We then repeat the same procedure for various atom densities (different reference values OD_0 for $C_0 = 100$ counts). We find that the normalised results OD_0/OD versus C/C_0 collapse to the same linear curve which we use as the rescaling function of OD to the reference C_0 . As a sanity test of this calibration, we estimate in Fig. 4.26(b) the total number of atoms in the testing box at a fixed density and for various imaging intensities before (red) and after (gray) applying the rescaling of the measured OD, and find that the corrected number of atoms is indeed independent of the used power of the imaging beam.

With a pixel-to-pixel intensity-corrected optical density, we then check the effect of n on OD_0 . We control the density by waiting a variable time in the trap prior to imaging for three-body collisions to remove a fraction of the atoms. The decrease of the 3D density follows Eq. (2.46) expressed in its local form as $dn_{3D}/dt = -L_3 \langle n_{3D}^2 \rangle n_{3D}$. With $n_{3D}(z) = n_{\text{co}} e^{-z^2/\ell_z^2}$ assuming that only the

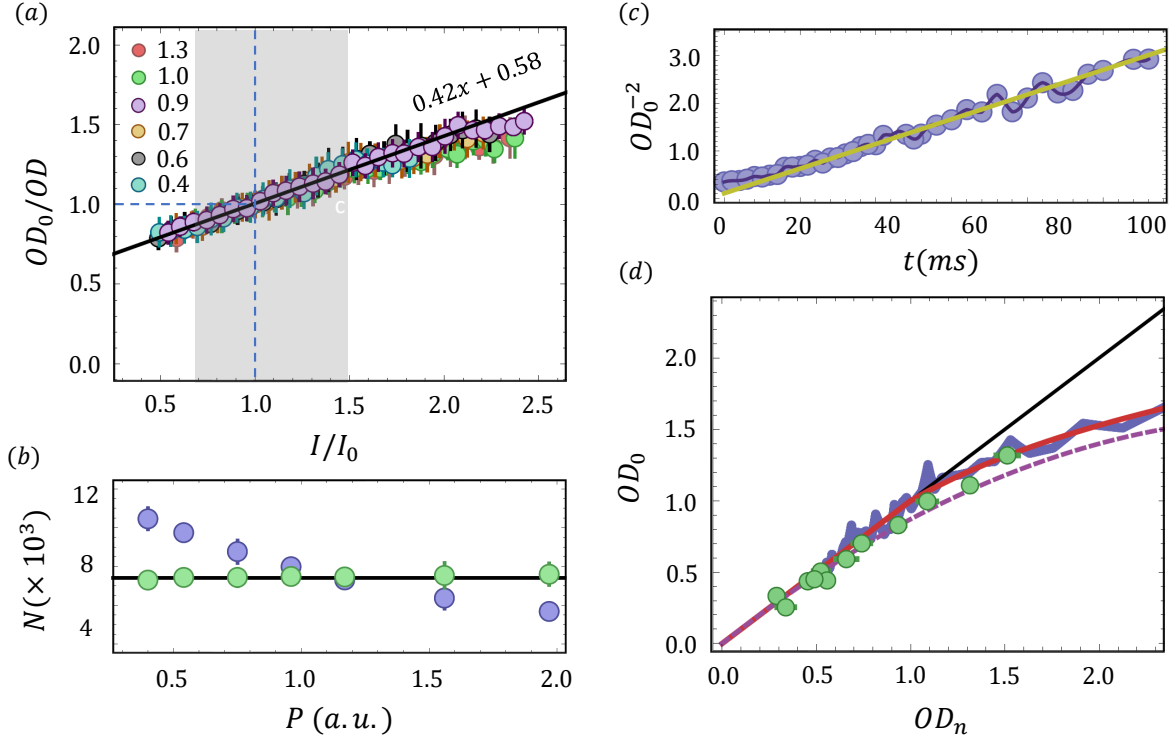


Figure 4.26: (a) Intensity corrections of the measured optical density OD for various atom densities (or equivalently various average normalised OD_0 in the range 0.4 to 1.3) as described in the main text. The arbitrary reference for this rescaling of $C_0 = 100$ counts (dashed line) corresponds to an average intensity $I_0 \approx 0.3I_s$. The black line is a linear fit of the collapsed OD s for the various densities. The gray area indicates the total range of variations (pixel-to-pixel and shot-to-shot) for our imaging process at a used average imaging intensity of $0.3I_s$. (b) The total atom number in a box for various imaging powers before (blue) and after (green) the intensity corrections based on the fitting function of the first panel. (c) The behaviour of the intensity-rescaled OD_0 for various waiting times in the trap in the presence of three-body losses. When plotted as OD_0^{-2} versus time, one expects a linear dependence (yellow fit of the data for large times). The deviation from this linear dependence is used for the extraction of a density-dependent correction as in (d). In this lower panel, the blue line is the actual corrections directly extracted from the data in (c). Red line: a fit on the data. Dashed purple line: a theoretical expectation based on [206]. Green points: OD measured from in-situ images versus after 25ms of free-expansion in which case the density effects are suppressed due to lower densities. In our imaging procedure we use an exposure time $\tau_0 = 30\mu s$ as a compromise between a good signal-to-noise ratio and negligible Doppler shifts for the used imaging intensities. This result does not contain the final density calibration with an intensity- and density-independent fudge factor S .

transverse ground state is occupied and $n_{co} = n/\ell_z\sqrt{\pi}$ the 3D density at the center of the transverse confinement, one writes equivalently for the surface density

$$dn/dt = -K_3n^3 \quad (4.26)$$

with $K_3 = L_3/(\ell_z^2\pi\sqrt{3})$. The real optical density OD_n after removing any possible density-effects from OD_0 should be $\propto n$ and thus one may also write that $dOD_n/dt = -(K_3S^2/\sigma_0^2)OD_n^3$. The constant S plays the role of a final intensity- and density-independent fudge factor and we discuss it

below. The differential equation for OD_n has the solution

$$OD_n^{-2}(t) = (2K_3S^2/\sigma_0^2)t + OD_n^{-2}(t=0). \quad (4.27)$$

We exploit the linear dependence on time of OD_n^{-2} to extract the density corrections in the optical density. In Fig. 4.26(c) we show the measured (after the applied intensity-corrections) OD_0^{-2} for various waiting times for the case of a transverse frequency $\nu_z = 5.5\text{kHz}$ at a scattering length $a = 636a_0$. The data points for $t > t_0$ are fitted with a linear line (yellow); we check that the fit does not depend on the choice of t_0 if it is larger than $\sim 7\text{ms}$. The yellow line physically represents the corrected OD_n even for high densities that OD_0 deviates from a linear behaviour. At any t one yields a measured OD_0 and a fitted OD_n . An interpolation of this result is shown (blue line) in Fig. 4.26(d). We found that a heuristic fit (red line) of the form $OD_0 = c \ln(aOD_n + b)$ works pretty well for OD values that deviate from the $OD_n = OD_0$ line; in our case $a = 3.97$, $b = -0.14$ and $c = 0.74$. The resulting fit is used for the density-corrections in the measured OD.

By assuming a linear behaviour between OD_n^{-2} and t we have neglected effects arising from the tight confinement along z in the scattering between the atoms. A more precise treatment, based on the discussion in Ref. [144], requires a correction in the collision rate K_3 by a factor η_{q2D}^6 , with $\eta_{\text{q2D}} = g_{\text{q2D}}(k)/(\hbar^2\tilde{g}/m)$ being directly related with the density-dependent component in the quasi-2D interaction strength of Eq. (3.4). For high densities this effect results in a downward bending of the OD_n^{-2} -versus- t line for small times and thus in the underestimation of the corresponding real ODs using our technique. In this thesis, however, we work in a low-density regime that this effect is expected to remain small; as a relative example, for a gas of $n = 3\mu\text{m}^{-2}$ and $\tilde{g} = 0.64$ (that we use in next chapter), the density-dependent corrections in the interaction strength are expected to be less than 2%.

To verify that the used correction is reasonable, we compare it with the results of a Monte Carlo simulation [206] that tests the effects of multiple scattering; the result of this simulation for $\ell_z k_0 = 2$ is plotted as the dashed purple line (for our experimental case $\ell_z k_0 = 1.8$). As another test of the validity of our correction function, in the same figure we also show (green points) the measured total atom number in the box when imaged in-situ (OD_0 -axis) and after some time of free expansion (OD_n -axis) where the cloud's density is reduced, both normalised to the in-situ measured OD. We note that for clouds with higher OD, beyond this simple calibration, we are following an alternative method of transferring part of the cloud in a controllable way in an invisible by the imaging light state; the density of the remaining atoms is then low enough rendering it valid to apply the above empirical corrections.

Having corrected for intensity fluctuations and multiple-scattering effects, the last step consists of relating the extracted OD_n with the absolute value of the 2D atom density n . The arbitrary choice of the finite-intensity reference C_0 hints that still $OD_n < n\sigma_0$. We already introduced the notion of a 'fudge factor' S that leads to $n = OD_n S/\sigma_0$. As a first approach to estimate S , we can assume that

this fudge stems only from the finite intensity of the imaging light. We can then use an extrapolation of the fit of Fig. 4.26(a) to find the additional correction if we had chosen $C_0 = 0$ counts ($I/I_0 \rightarrow 0$ in the plot). This process gives an average $S = 1.75$. This result is in a very good agreement with calibrating S based on three-body losses ($S \approx 1.77$) such that the experimentally deduced slope of the fit in Fig. 4.26(c) equates $2K_3 S^2 / \sigma_0^2$ from Eq. (4.27) or through the critical density for a harmonic 3D BEC ($S \approx 1.80$) as described in [167]. The last two more general procedures assess a systematic uncertainty of around 15% in the extracted density.

Temperature

Equation-of-state measurement: The scale-invariance of a 2D system has allowed a robust extraction of the temperature for both Fermi [87] and Bose [207] uniform gases when a single transverse state is occupied. Inspired by these previous experiments, we implement a variation of this equation-of-state temperature-measurement. The idea is by scanning the chemical potential μ at a constant temperature to measure the density $n(\mu) = \lambda^{-2} D(\mu/k_B T)$, from which we get the best estimation of T through the known universal function D (Sec. 3.2.3); at a given n then and with the knowledge of T , the chemical potential of the gas is also obtainable.

To scan μ we project a gray-scaled potential defect onto the center of the atom gas in addition to the surrounding in-plane box walls from the ‘vertical’ DMD, as in Fig. 4.17(b). The resulting potential on the atoms is shown in the inset of Fig. 4.27(b). The height of this potential dip, V_{dip} , is controlled with the level of gray-scaling, and takes values between zero and the trap-depth U_{peak} . In the central region of the applied dip, the atom density gets depleted from the bulk value n to n_{dip} . By taking care to keep the area of the dip small in order not to influence the rest of the gas, the whole cloud is in thermodynamic equilibrium at some T and using local density approximation the local chemical potential in the dip is $\mu_{\text{dip}} = \mu - V_{\text{dip}}$. The normalised density of the dip to its bulk value is

$$n_{\text{dip}}/n = D\left(\frac{\mu - V_{\text{dip}}}{k_B T}\right) / D\left(\frac{\mu}{k_B T}\right). \quad (4.28)$$

We fit the experimental results $\{V_{\text{dip}}, n_{\text{dip}}/n\}$ using the interpolated version of the universal function D (see the discussion in Fig. 3.5) with T and μ as the fitting parameters.

In Fig. 4.27(a) we show the measured n_{dip}/n for various V_{dip} and for two different temperatures at $\tilde{g} = 0.64$. In this example of a box of $L_x = 22\mu\text{m}$ and $L_y = 36\mu\text{m}$, the square dip area of $10\mu\text{m} \times 10\mu\text{m}$ corresponds to around 12% of the total area of the trap; however, we use only the central $3\mu\text{m} \times 3\mu\text{m}$ region of the dip to extract n_{dip} in order to avoid misleading effects from the tails of the density distribution on the dip. We note that no considerable change in the bulk density outside the dip is observed for the various V_{dip} . The green (blue) points correspond to a temperature below (above) the BKT critical temperature. We found $T = 58\text{nK}$ for the blue points and $T = 34\text{nK}$ for the green points at an expected $T_c = 40\text{nK}$.

The relative uncertainty of the temperature extraction from this fitting process is between 10%

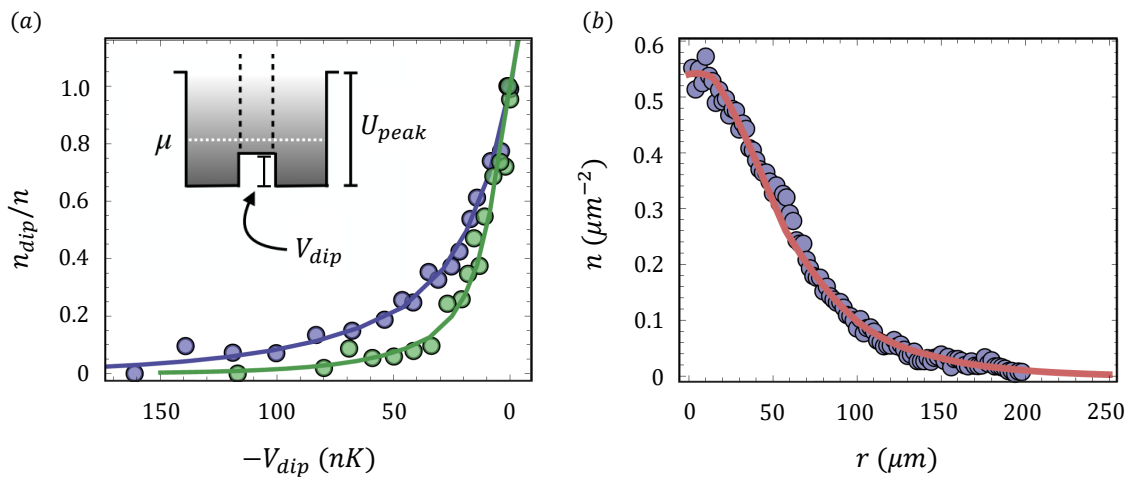


Figure 4.27: (a) Equation-of-state method for extracting the temperature of a 2D gas. The inset shows the concept behind this technique. A potential dip in the center of the trap of variable height V_{dip} depletes the central density n_{dip} which we show normalised to the bulk density n in the main plot. The behaviour of n_{dip} for various V_{dip} reveals the temperature and the chemical potential of the bulk gas. In these examples, we extract $T = 34\text{nK}$ (green) and 58nK (blue) for a box of $22 \times 38\mu\text{m}^2$ and $\tilde{g} = 0.64$. (b) An example of extracting the temperature using the time-of-flight (ToF) technique for a box of $70\mu\text{m}$ and $T = 68(9)\text{nK}$. The points correspond to the radially-averaged experimental density profile after $t = 25\text{ms}$ of ToF and the fit form is numerically extracted using the process described in the main text.

and 15% and is mainly related with the uncertainties in the dip-potential height and the resulting density of the dip. We note that this method of extracting temperatures may contain additional sources of systematic errors and one needs to validate it also with another type of measurement. One such source of possible errors stems from the (reasonable) assumption that temperature remains the same for all potential dips. Another source could be the one-body losses from the light of the dip; higher dips lead to faster losses and an underestimated n_{dip} that could modify the extracted temperature. For the potential heights we use ($U_{\text{peak}} \approx 200\text{nK}$), we find that these losses at a rate $\Gamma_{\text{loss}} = (\Gamma/\hbar(\omega - \omega_0))U_{\text{dip}}$ [169] are not important for our timescale of $\sim 2\text{s}$ even for the highest dips. They could lead to an underestimation of the extracted temperature by around 1% as we checked by correcting the density according to the predicted loss rate. In next chapter, we compare these results for the temperature with an independent measurement based on superfluidity.

Time-of-flight measurement: We have also attempted to extract the temperature using the more conventional technique of a time-of-flight (ToF) measurement. In this method one lets the cloud expand freely after turning off the interactions and depicts the expanded density distribution after some long time t as a rescaled version of the in-trap momentum distribution of the gas. This distribution is typically fitted with a model function with the temperature as the fitting parameter and the main question pertains to the deduction of a proper theoretical model for the fitting. Unlike in equation-of-state measurements, this technique is also valid for a semi-2D gas where additional transverse states may be occupied. Although assuming an ideal box potential simplifies the treat-

ment, we will discuss the implemented method from a more general perspective that allows various extensions like taking into account the proper power-law potential of the walls. We generally find temperatures that are slightly higher but consistent within their errors with the equation-of-state measurements. However, due to its less robust character (equation-of-state measurements are for example independent of the exact density fudge, unlike ToF measurements) and the need for additional assumptions (see below), the ToF technique is used only for fast and rough diagnostic estimations in our experiments. We note here that the results for the adiabatic compression of Fig. 4.23(b) are extracted using this method.

For the extraction of a meaningful temperature out of the ToF measurements without a rather involved analysis, we require that the gas do not include a quasi-condensate or a transverse condensate. In this case we are allowed to use a semi-classical approximation and a Hartree-Fock description for the density distribution of the gas (Sec. 3.2.3). For this requirement to be experimentally relevant, but also not restrictive, we use a microwave pulse to transfer most of the atoms to $|F = 1, m_F = 0\rangle$ state which is invisible by our high-field imaging; since the transferred atoms have very slow collision rates in $|F = 1, m_F = 0\rangle$ at relevant magnetic fields ($\sim 400\text{G}$), we make the essential assumption that the remaining atoms in $|F = 1, m_F = 1\rangle$ do not change their temperature.

In the general case of higher-energy z -states occupied, the total 2D density is a sum of the partial densities n_i in the i -th transverse level, i.e. $n(r, t) = \sum_{i=0}^{\infty} n_i(r, t)$. Due to ballistic conditions, the expanded density distribution in the i -th transverse state can be deduced after integrating the Bose-Einstein distribution over momentum p ,

$$n_i(r, t) = \int \frac{d^2p}{(2\pi\hbar)^2} g_0 \left(Z_i e^{-(p^2/2m)/k_B T} \right) \quad (4.29)$$

with the fugacity $Z_i = e^{\mu_i/k_B T}$, the partial chemical potential μ_i of the i -th state and the zeroth order polylogarithmic function $g_0(x) = 1/(x^{-1} + 1)$ as another way of expressing the Bose distribution function N^0 . From classical arguments, the momentum p connects the initial in-trap r' and the final after expansion r positions of the atoms as $p = m(r - r')/t$, and thus the expanded distribution takes the form

$$n_i(r, t) = \frac{m^2}{(2\pi\hbar)^2 t^2} \int_{L_x, L_y} \frac{d^2r'}{(2\pi\hbar)^2} g_0 \left(Z_i e^{-m(r-r')^2/(2t^2 k_B T)} \right). \quad (4.30)$$

To proceed further and be able to extract some model-function which can be used for fitting the experimental density distribution after ToF, we need to estimate the parameters Z_i . Within the Hartree-Fock theory, these fugacities are connected with the in-trap densities $n_i(r, t = 0)$ as

$$n_i(r, t = 0) = -\lambda^{-2} \ln(1 - Z_i). \quad (4.31)$$

The partial chemical potential, as a direct generalisation of Eq. (3.26) for many transverse states, is $\mu_i = \mu - V_i$ with $V_i = i\hbar\omega_z + 2 \sum_{k=0}^{\infty} g_{ik} n_k$ [208, 209] and the partial interaction strengths are given by

$g_{ik} = \frac{4\pi a \hbar^2}{m} \int dz |\phi_i(z)|^2 |\phi_k(z)|^2$ extracted from the overlap between the various z -eigenstates $\phi_i(z)$. In our analysis we use the ideal-gas z -eigenstates of a harmonic potential, the Hermite polynomials normalised to the oscillator length ℓ_z . Additionally, although we neglected it, V_i may contain a term describing the precise power-law of the trapping potential (see, for example, the process in Ref. [210]).

The Hartree-Fock equations of Eq. (4.31) are characterised by the parameters $x = \mu/k_B T$, $\zeta = \hbar\omega_z/k_B T$ and the scattering length a . For a given a , we numerically solve²⁶ Eq. (4.31) for the partial densities for various selected x and ζ . The theoretically estimated in-trap densities (or equivalently the Z_i 's) are then fed in Eq. (4.30) for the expanded density distribution. We interpolate the results for any arbitrary x and ζ and use this numerically extracted function as the fitting model for the radially-averaged experimental density distribution of the cloud after the expansion. An example of the experimental data and the fitting function is shown in Fig. 4.27(b) for the actual data during the optical accordion.

²⁶For efficiency reasons, we use only the first 4 lowest z levels and an estimator for the PSD of the next ones and check that the result is very similar to considering more levels.

5

First and second sound in a BKT superfluid

“I imagined I had discovered a new word. I rise up in bed and say, ”It is not in the language; I have discovered it. ’Kuboa.’ It has letters as a word has. By the benign God, Man you have discovered a word!... ’Kuboa’ ... a word of profound import.”

— Knut Hamsun, Hunger

This chapter describes the main experimental results of this thesis. By applying the hydrodynamic two-fluid model (Chapter 2) to the relevant case of a quasi-two-dimensional Bose gas (Chapter 3) we combine the previously verified predictions for the equation of state with the speeds of first and second sound, measured using our experimental platform (Chapter 4), to deduce the superfluid density and verify its universal jump at the BKT critical point.

The measurement of the first- and second-sound speeds is interesting in its own right; the hydrodynamic second sound has never been observed before in any two-dimensional quantum fluid, neither liquid helium nor ultracold gases. Probing sound in a 2D quantum gas can be a useful tool in the future for further systematic studies of the hydrodynamic modes and the extraction of transport quantities of this system.

We start this chapter (Sec. 5.1) with a brief overview of recent experiments on two-dimensional superfluidity and sketch the approach we follow to infer the superfluid density from first and second sound. In Sec. 5.2, we describe our experimental protocol that allows the observation of these hydrodynamic sound modes. In Sec. 5.3 we present our main results.

5.1 Setting the stage

Overview of the current state of the art on BKT superfluidity

The systematic investigation of 2D superfluidity dates back to the 1960s via studies of thin films of liquid helium [211–213]. The final link of superfluidity to the BKT mechanism in these systems was provided in 1978 with the extraction of the superfluid density n_s by Bishop and Reppy [72].

This result, based on the torsional oscillator technique that measures the decrease in the moment of inertia in the presence of a superfluid, as we described in Sec. 2.1, revealed also the characteristic jump in n_s at the critical point¹.

Two-dimensional ultracold gases, on the other hand, are a relatively new platform that have been studied experimentally for almost 20 years and many investigations have tested and supported the existence of BKT superfluidity. Among others, a critical velocity for frictionless flow has been measured for both Bose [77] and Fermi [81] 2D gases. The emergence of coherence [74, 75, 82, 184] at low temperatures has been observed and recently evidence for the algebraic decay of correlations [79, 214] below a critical temperature T_c has been reported. The measured critical T_c [39], (see also Refs. [80, 184, 215]) is in very good agreement with the BKT prediction for a wide range of interaction strengths. Even on a microscopic level, the observation of the proliferation of vortices above T_c [64, 73] and of bound vortex pairs below T_c [78], which disappear at even lower temperatures, confirmed the underlying mechanism of BKT superfluidity.

Despite this progress, the central quantity for a quantitative characterisation of superfluidity, the superfluid density n_s , has not yet been measured in 2D ultracold gases. Unlike in films of helium, the measurement of the angular momentum of the 2D gas and thus its moment of inertia from which n_s could be inferred is a difficult task. Also, unlike in a weakly-interacting 3D Bose gas, n_s does not coincide with an experimentally accessible condensate density. The quest for the superfluid density in 2D ultracold gases becomes especially intriguing for two main reasons: First, the ability to tune most parameters will allow the test of plausible theories under a wide range of experimental conditions, unavailable with liquid helium. Second, measuring the temperature-dependent n_s would provide a quantitative proof that the 2D Bose gas belongs to the universality class of systems described by the BKT theory.

Deduction of n_s in 2D ultracold gases: the idea

Superfluidity is a dynamical feature even if it is linked with the thermodynamic equilibrium of a fluid, and thus a deduction of the superfluid density requires the measurement of some transport quantity that directly depends on n_s ; the torsional oscillator measurement in liquid helium is such an example. In experiments with ultracold gases where one is mainly restricted to measure the density of the gas instead of rotational properties, the hydrodynamic second sound as described by Landau's two-fluid model is such a transport property with a direct link to n_s , as was first pointed out in Ref. [91].

Landau's model characterizes the dynamics of all superfluids in the collisional hydrodynamic regime, and thus is expected to be applicable also in 2D. From Eq. (2.18), which we repeat here in a more convenient dimensionless form, the first and second sound speeds in a uniform system

¹Although small corrections needed to be applied to take into account the dynamical nature of the measuring procedure.

normalised to Bogoliubov speed are

$$u_{1,2}^2 = \frac{u_{10}^2 + u_{20}^2 \pm \sqrt{(u_{10}^2 - u_{20}^2)^2 + \Delta_0^4}}{2} \quad (5.1)$$

with $u_{1,2} = c_{1,2}/c_B$, $u_{10,20} = c_{10,20}/c_B$ and $\Delta_0 = 4u_{10}^2 u_{20}^2 (\gamma - 1)/\gamma$; we remind that γ , being the ratio of isobaric to isochoric specific heat, characterises how compressible the gas is. The speeds of first and second sound depend on various thermodynamic quantities and the superfluid density. However, in two dimensions and for a given interaction strength \tilde{g} , the various dimensionless thermodynamic quantities and the superfluid phase-space density depend only on $x = \mu/k_B T$, or equivalently on T/T_c (see Sec. 3.3). It is then of no surprise that the normalised speeds of first and second sound also become universal through the combination of Eqs. (2.18) and (3.30):

$$u_{10}^2(x) = \frac{2\pi}{\tilde{g}D(x)} \frac{2\mathcal{P}(x)}{D(x)}, \quad u_{20}^2(x) = \Lambda(x) \frac{D_s(x)}{D(x) - D_s(x)}, \quad \gamma(x) = \frac{2\mathcal{P}(x)(dD/dx)}{D(x)^2} \quad (5.2)$$

Here, $\Lambda(x) = \frac{2\pi}{\tilde{g}D} \frac{(2\mathcal{P}/D-x)^2}{2\mathcal{P}/D-D/(dD/dx)}$ depends only on the dimensionless phase-space density D and pressure \mathcal{P} but not on the superfluid density.

Eqs. (5.1) and (5.2) show how the temperature-dependent superfluid density $n_s = D_s \lambda^{-2}$ can be deduced from u_{20} , and thus from measured $u_{1,2}$, as long as the thermodynamic functions D and \mathcal{P} are known. Additionally, one notices that a jump in n_s results in a discontinuity also in u_{20} . For the special case of an incompressible gas with $\gamma = 1$ (as it is approximately for liquid helium or a unitary Fermi gas), $u_1 = u_{10}$ and $u_2 = u_{20}$ and thus, one expects that the jump in n_s results in a discontinuity of the speed of second (and only second) sound. The finite compressibility ($\gamma > 1$) of Bose gases, however, leads to the mixing of u_{10} and u_{20} in u_1 and therefore to a discontinuity also in the speed of first sound (see also Fig. 5.1(a) later).

First and second sound in 2D experiments

Films of liquid helium, of a few-atomic-layer thickness d_{He} and created by adsorption on a bulk substrate, do not permit the excitation of first and second sound since the viscous normal component of the superfluid is pinned to the rough substrate². However, an alternative sound mode, the so-called third sound [216], can be excited, consisting of the propagation of the superfluid component on top of a static normal fluid, with a speed $\propto \sqrt{n_s/n}$.

Ultracold gases, on the other hand, are trapped inside smooth light or magnetic fields allowing, in principle, the excitation of first and second sound. However, unlike the situation in 3D gases, attempts to measure hydrodynamic sound modes in 2D have just recently been initiated [207], only after the

²The fluid has zero velocity relative to the substrate at their boundary (no-slip condition) even for atomically flat substrates. The finite viscous penetration depth $\sim \sqrt{2\eta/\omega\rho_n} \gg d_{\text{He}}$, that characterises the viscosity η , locks the normal component and prevents it from an in-phase (first sound) and out-of-phase (second sound) move with the superfluid component.

advent of box traps. A previous numerical solution of the two-fluid equations in the presence of a harmonic potential has been presented in Ref. [217]; the resulting in-phase and out-of-phase motion³ of fluctuations in temperature and pressure, analog to first and second sound, do not show a simple scaling with the superfluid fraction, nor a discontinuity at the critical point.

5.2 Probing first and second sound excitations

We saw above that the extraction of n_s requires the speeds of both first and second sound provided hydrodynamic conditions apply. In the following we first discuss the relevance of the hydrodynamic conditions for our 2D gas and the ability to couple both sounds with simple-to-probe density perturbations (Sec. 5.2.1). Then we describe the realised experimental protocol for measuring the speeds of the two sound modes (Sec. 5.2.2).

5.2.1 Density probes and the ability to observe first and second sound

Hydrodynamic conditions

The diluteness and the relatively weak intrinsic interactions of ultracold gases in combination with their finite size (see Sec. 3.3) make it difficult in most cases to satisfy the hydrodynamic condition of Eq. (2.1) even for the lowest-lying modes. A recent attempt in the group of J. Dalibard [207] to measure first and second sound using a ^{87}Rb gas with $\tilde{g} = 0.16$, $n \approx 50\mu\text{m}^{-2}$ and $L \approx 30\mu\text{m}$ revealed only one sound mode without a discontinuity at the BKT critical temperature. Those findings were attributed in Ref. [218, 219], and also by the authors of Ref. [207], to the deviation from hydrodynamic behaviour.

To quantify this, we estimate the expected 'hydrodynamicity' quantity $\mathcal{K} = \gamma_{\text{coll}}/\omega$ around the critical point in that experiment. Extracting \mathcal{K} is conceptually easier for normal gases above T_c with a collision rate proportional to the total density. In Sec. 3.3 we approximated \mathcal{K} by $\mathcal{K}_B \equiv \gamma_{\text{coll}}/\omega_B = \tilde{g}^{3/2}n^{1/2}L_y/(2\pi)$, with ω_B the Bogoliubov frequency, that reveals the important role played by interactions. More precisely, one can now write $\mathcal{K} = \mathcal{K}_B/u_1$. In Fig. 5.1(a) we show $u_{1,2}(T_c)$ as predicted from Eq. (5.1) and (5.2) using the thermodynamic quantities (Sec. 3.2.3), and the BKT superfluid density (Sec. 3.2.2). We use $u_1(T_c^+)$, just above the critical temperature to extract \mathcal{K} for various n and \tilde{g} ; the results for $L_y = 30\mu\text{m}$ are depicted in Fig. 5.1(b). The gas in Ref. [207] with the expected hydrodynamic $u_1(T_c)$ gives $\mathcal{K} \lesssim 1$, showing that this experiment was conducted in the crossover between the collisional and collisionless regimes.

In Fig. 5.1(b), we also show, as a realistic example, the line $\mathcal{K} = 4$ (green line). Due to the much stronger effect of \tilde{g} in \mathcal{K} , for $\mathcal{K} \gtrsim 4$ and with our available densities, we need a relatively high $\tilde{g} \gtrsim 0.4$. However, at these values of \tilde{g} , one is limited by atom-losses from three-body recombination events. In

³Apparently, the excitations are not plane waves anymore but can be decomposed into the normal modes characterising the symmetry of the trapping potential.

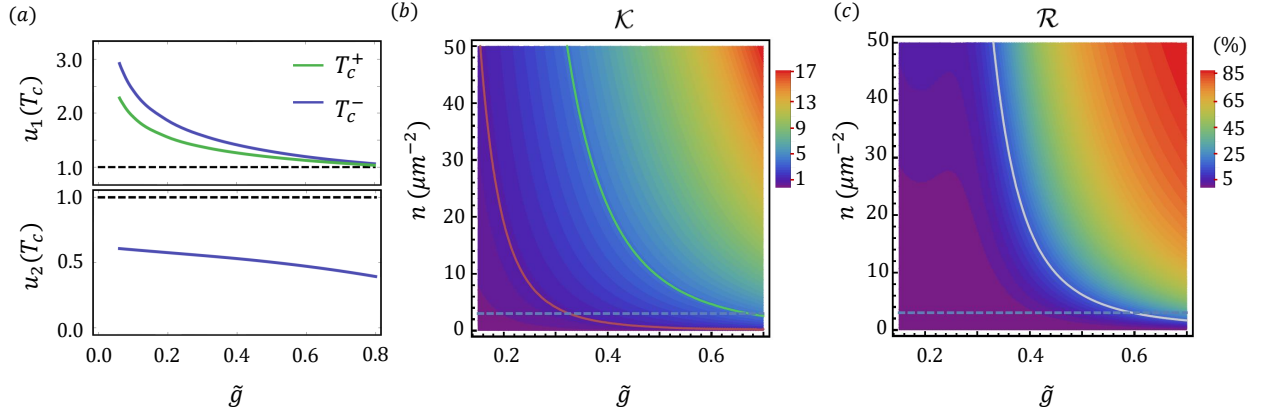


Figure 5.1: (a) Normalised first (upper panel) and second (lower panel) speed of sound just above (T_c^+) and below (T_c^-) the critical point. (b) The hydrodynamicity factor $\mathcal{K} = \gamma_{\text{coll}}/\omega$ for various densities n and interactions \tilde{g} for $L_y = 30\mu\text{m}$. Red (green) line corresponds to $\mathcal{K} = 1$ ($\mathcal{K} = 4$) and the dashed line to our choice of $n = 3\mu\text{m}^{-2}$. (c) Relative losses, $\mathcal{R} = [n(0) - n(t)]/n(0)$, during 4 Bogoliubov periods due to three-body collisions for various n and \tilde{g} , using the results of Ref. [123]. The white line corresponds to $\mathcal{R} = 15\%$.

Fig. 5.1(c) we quantify these losses as expected from their theoretical modeling (Sec. 2.3.1). The plot shows the relative decrease of the density $\mathcal{R} = [n(0) - n(t)]/n(0)$ for various \tilde{g} and initial $n = n(0)$ in a time duration of 4 Bogoliubov oscillations. The white line represents, as an example, the condition $\mathcal{R} = 15\%$.

For $T < T_c$, the above estimations for \mathcal{K} become less precise. Since the two-fluid model is based on thermodynamic equilibrium of both the superfluid and normal components, a simplistic attempt would consist of replacing $n \rightarrow n - n_s$ for the estimation of \mathcal{K} . In 2D, the expected $n_s/n \sim 0.6 - 0.7$ at T_c would decrease the predicted \mathcal{K} by around 3 times compared to a normal gas above T_c ; \mathcal{K} would be still above unity if one starts with proper hydrodynamic conditions. However, as pointed out in Ref. [220] for the 3D case of a BEC, if the gas is already collisional above T_c , it becomes even more hydrodynamic in the presence of a superfluid due to collisions between condensed and thermal atoms. This expectation becomes questionable at very low temperatures ($T/T_c \lesssim 0.5$) with only a few excitations constituting the normal component of the gas. We finally note that below T_c , the hydrodynamic requirement will be more difficult to be met for the first sound due to its higher frequency compared to second sound.

Density probes

Our ability to observe the in-situ density distribution of a 2D gas, without complications arising from integrating the third dimension or the expansion of the cloud, allows the use of the density response as a straightforward means to observe and analyse sound propagation. Historically, the common ways for studying sound excitations have been either through the free propagation of a localised density perturbation [207, 221, 222] or through energy-momentum spectroscopy (neutron or Bragg [223, 224] spectroscopy for liquid helium and ultracold gases, respectively). As discussed in

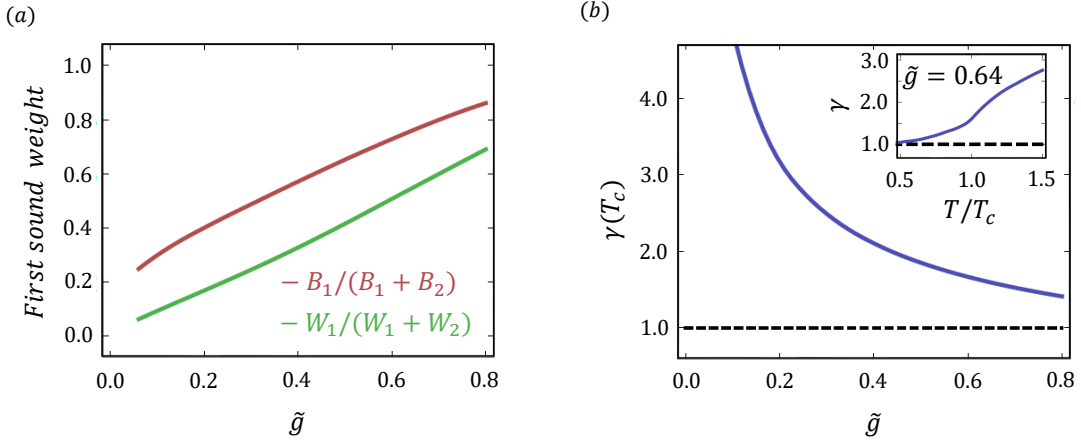


Figure 5.2: (a) The relative weight of the first-sound peak in $\text{Im}\chi(\omega)$ (red) and $S(\omega)$ (green) at the critical point as predicted by the dissipationless two-fluid model and using the classical-field equation of state and the BKT prediction for the superfluid density. (b) The ratio of compressibilities, γ for the same case as in (a). The inset shows γ versus T/T_c for the chosen $\tilde{g} = 0.64$.

Sec. 2.1.3, neutron scattering probes directly the dynamic structure factor, $S(\omega)$. The same quantity is probed through free propagation after a sudden kick of the gas; to see why, one can express the density response of Eq. (2.21) in the case of a sudden perturbation⁴ i.e $\delta U(\omega) \propto 1/j\omega$ as

$$\delta n(\omega) \propto \frac{\text{Im}\chi(\omega)}{\omega}, \quad (5.3)$$

revealing directly that $\delta n(\omega) \propto S(\omega)$ through the fluctuation-dissipation theorem of Eq. (2.29). In Bragg spectroscopy, on the other hand, the measurement of the transferred energy and momentum probes the absorptive part of the response function, $\text{Im}\chi(\omega)$ [110]. Of course, following the argument above for the free propagation, $\text{Im}\chi(\omega)$ is also obtained through the observation of density for a perturbation of the form $\delta U(\omega) \propto 1$; such a case can be mimicked by a monochromatically driven system: the ‘shaking’ of the gas at various frequencies Ω , one at the time, with $\delta U(\omega) \propto \delta(\omega - \Omega)$ allows the direct reconstruction of $\text{Im}\chi(\omega)$.

These two experimentally relevant quantities, $S(\omega)$ and $\text{Im}(\omega)$, should reveal the same excitation modes, first and second sound; the relative contribution of the two modes is, nevertheless, different: $S(\omega) \propto \text{Im}(\omega)/\omega$ suppresses (facilitates) the observation of first (second) sound as it suppresses the higher frequencies. To quantify this argument, we consider the dissipationless two-fluid model of Eq. (2.37). Within this model the relative weights of the two δ -peaks in the density response function $\chi(\omega)$, now expressed through the normalised speeds as $Z_1 = (u_1^2 - u_{20}^2)/(u_1^2 - u_2^2)$ and $Z_2 = (u_{20}^2 - u_2^2)/(u_1^2 - u_2^2)$, trivially satisfy the f sum rule $Z_1 + Z_2 = 1$. The corresponding weights $B_{1,2}$ in $\text{Im}\chi(\omega)$ are derived directly from Eq. (2.38) to be proportional to $Z_{1,2}/u_{1,2}$. In the same way, the weights $W_{1,2}$ in $S(\omega)$ become proportional to $B_{1,2}/u_{1,2} \propto Z_{1,2}/u_{1,2}^2$.

⁴The perturbation of a kick experiment can be modelled as a step function in time with its fourier transform $\propto 1/j\omega$.

One can now use Eqs. (5.1) and (5.2) for $u_{1,2}$ with the scale-invariant quantities described in Sec. 3.2 to predict the weights of first and second sound in both $\text{Im}\chi(\omega)$ and $S(\omega)$. In Fig. 5.2(a) we plot the resulting relative weight of first sound in $\text{Im}\chi(\omega)$ and $S(\omega)$ at T_c for different values of \tilde{g} . One notices that first sound is easier to be excited at higher \tilde{g} both in $\text{Im}\chi(\omega)$ and $S(\omega)$. This is the consequence of a decreased compressibility with increasing interactions⁵; $\gamma(T_c)$ versus \tilde{g} is plotted in Fig. 5.2(b). For an incompressible gas ($\gamma \rightarrow 1$), second sound is an entropy wave and thus density perturbations excite predominantly first sound. At such strong interactions, methods to probe $S(\omega)$ are advantageous for the observation of second sound. In the other limit ($\gamma \gg 1$) of weakly-interacting and highly compressible Bose gases, first (second) sound mainly corresponds to the excitation of the (normal) superfluid component; the relatively large superfluid fractions make second sound the prevailing mode in density perturbations. At these weak interactions, methods to probe $\text{Im}\chi(\omega)$ are advantageous for the observation of second sound.

5.2.2 Our experimental protocol for exciting first and second sound

For observing both hydrodynamic modes in density perturbations one thus needs to work with gases at intermediate interaction strengths around $\tilde{g} \approx 0.5$ and with low densities to avoid extensive losses. We implement a monochromatic driving technique which probes directly $\text{Im}\chi(\omega)$. This excitation method provides a straightforward analysis of the results, without complications from the coexistence of various frequencies in them at the same time. Also, probing $\text{Im}\chi(\omega)$ allows the deduction of the weights $Z_{1,2}$ in the f sum rule and the reconstruction of $S(\omega)$ with relatively small uncertainties. One has to be careful, though, to keep the applied driving force weak enough such that it does not modify the essentially uniform character of the system.

The uniform 2D gas is prepared as described in Sec. 4.7. We work with $\tilde{g} = 0.64(3)$, which corresponds to a scattering length⁶ of $a = 522(23)a_0$. For the final gas during the sound(s) propagation, the density n stays within 15% of its average value, $n = 3.0(5)\mu\text{m}^{-2}$, in the probed time-window (of a 100-ms duration). At these densities, the density-dependent correction of the 2D interaction strength (see Eq.(3.4)) remains low, around 2%; the assumption of \tilde{g} as the effective interaction strength is then well justified. The temperature is controlled by adjusting the in-plane potential height as described also in Sec. 4.7. With $\omega_z = 2\pi \times 5.5(1)\text{kHz}$, the gas is deep in the 2D regime, with both the interaction and thermal energy per particle below $0.3\hbar\omega_z$. We use two different box geometries $(L_x, L_y) = (21\ \mu\text{m}, 33\ \mu\text{m})$ and $(56\ \mu\text{m}, 23\ \mu\text{m})$ which also serves as a small confirmation test of scale invariance; for each data-set we take, we calibrate separately the size of the box as we describe later in Sec. 5.3.3.

⁵Although intuitive, a simple mathematical argument for that can be extracted from a low-temperature Thomas-Fermi gas; the compressibility $\kappa \propto \partial n / \partial \mu$ with $\mu \propto n\tilde{g}$ gives $\kappa \propto 1/\tilde{g}$.

⁶We calibrate a with an RF pulse that transfers the atoms in the $|m_J = -1/2, m_I = 1/2\rangle$ ground state; the obtained resonant frequency gives the magnitude of the field. With an already calibrated Feshbach resonance [129] the scattering length is straightforwardly extracted. The uncertainty in a and thus in \tilde{g} stems from a peak-to-peak oscillation of the magnetic field of 0.2G owing to the effect of the mains.

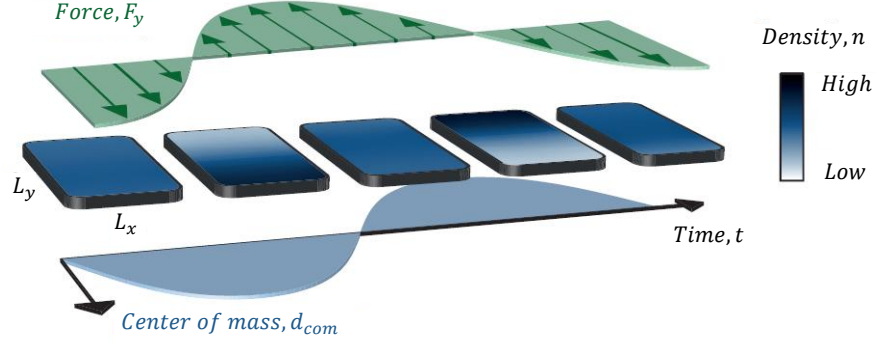


Figure 5.3: We apply an in-plane, spatially-uniform force $F_y(t) = F_0 \sin(\omega t)$, created by a magnetic field gradient to excite the longest-wavelength mode with wavenumber $q = \pi/L_y$ of first and second sound. The center of mass d_{com} of the cloud is consequently displaced and we use this oscillation to extract the resonances of first and second sound.

The driving potential $\delta U(r, t) = \delta U(r) \sin(\omega t)$ is realised using our ‘anti-Ioffe’ coil (Sec. 4.6). $\delta U(r)$ is linear in y , having no effect in the other directions, with a gradient linear in the applied current δI on top of the compensation of the magnetic fields⁷. The corresponding driving force $F_y = F_0 \sin(\omega t)$ is spatially uniform, and oscillates sinusoidally in time as shown in Fig. 5.3. We calibrate F_0 versus δI by allowing the gas to freely move in the plane under the effect of a fixed δI and fitting the center-of-mass displacement versus time with a constant-acceleration prediction. We find a linear acceleration F_0/m with the applied current and for most of our results we use $F_0/m \approx 0.074 \text{m/s}^2$ with a relative uncertainty of $\sim 5\%$.

By applying this force, the initially uniform distribution with density n is perturbed along y , and we decompose the resulting perturbation $\delta n(y, t)$ into the excitation modes of wavenumber $q_i = i\pi/L_y$, i.e.

$$\delta n(y, t)/n = \sum_{i=1}^{\infty} b_i(t) \sin(i\pi y/L_y). \quad (5.4)$$

Here, we set $y = 0$ at the center of the box (with $-L_y/2 \leq y \leq L_y/2$) and the sine basis is chosen such that at the edges of the box there are no density gradients (ignoring finite-size effects). We note that $b_i(t)$ contain the potential contributions from both first and second sound in the excitations of wavenumber q_i .

We experimentally extract $b_i(t)$ by calculating the overlap of the mode i with the (integrated along x) density distribution $n(y, t)$. A typical example of the density perturbation is illustrated in Fig. 5.4(a). In all the results described in this thesis, we find that only the b_1 -mode with $q = \pi/L_y$

⁷The main effect of the anti-Ioffe coil is to shift the position y_0 of the minimum in the parabolic field magnitude along y (see Sec. 4.6). When y_0 does not coincide with the position of the gas, the induced in-plane potential along y takes the form $U_B(y; I) = U_{B0} - \alpha_B [y - y_0(I)]^2$, as derived from Eq. (4.21), with U_{B0} and α_B values depending on the Feshbach field. For small changes of the current in the anti-Ioffe coil by δI the resulting difference in the potential varies in space as $\delta U(y) = 2\alpha_B \delta y_0 y$; $\delta U(y)$ is linear in y with a gradient linear in the displacement $\delta y_0 = y_0(I + \delta I) - y_0(I)$, and thus also linear in δI as directly deduced from Eq. (4.22).

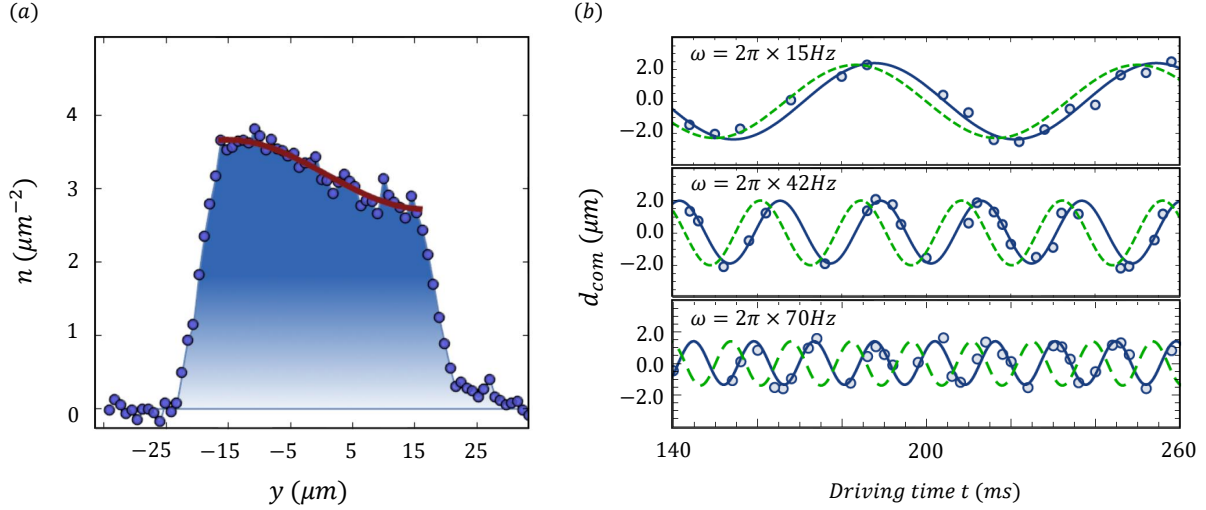


Figure 5.4: (a) An example of the density profile along y (integrated along x) from the application of a driving potential. The perturbation on top of the uniform density of the unperturbed gas shows the excitation of only the longest-wavelength mode with a wavenumber $q = \pi/L_y$. The red line is a fit on the density distribution using that mode. (b) Center-of-mass oscillations of the density distribution for three different driving frequencies for a box $(L_x, L_y) = (56 \mu\text{m}, 23 \mu\text{m})$. The blue lines show the single-frequency fit of Eq. (5.9), whereas the dashed green line represents the temporal behaviour of the driving force (in arbitrary units).

is excited. This behaviour is to be expected owing to the weakness (see also Sec. 5.3.6 later for a relevant discussion) and the symmetry of the applied driving potential. By decomposing the perturbing potential $\delta U(y, t) = -F_0 y \sin(\omega t)$ on the basis of the phonon modes as

$$\delta U(y, t) = \sum_{i=1}^{\infty} U_i \sin[(2i-1)\pi y/L_y] \sin(\omega t) \quad (5.5)$$

with $U_i = -4F_0 L_y / (2i-1)^2 \pi^2$, we find that $\delta U(y)$ contains predominantly the $q = \pi/L_y$ component and thus our perturbation excites the longest-wavelength phonon mode.

The observations above permit us to proceed to two simplifications. First, the potential perturbation can be well approximated by

$$\delta U(y, t) = U_1 \sin(\pi y/L_y) \sin(\omega t), \quad (5.6)$$

where we can also explicitly repeat that $U_1 = -4F_0 L_y / \pi^2$; second, the resulting density distribution can be expressed as

$$\delta n(y, t)/n = b_1(t) \sin(\pi y/L_y) \quad (5.7)$$

This perturbation displaces the center of mass of the cloud, $(1/L_y) \int dy y \delta n(y, t)/n$, by

$$d_{\text{com}}(t) = 2b_1(t)L_y/\pi^2 \quad (5.8)$$

with respect to the unperturbed $d_{\text{com}} = 0$ case. Eq. (5.8) between b_1 and d_{com} allows us to use the latter as the main observable in our analysis. Some typical examples of the observed center-of-mass oscillations are illustrated in Fig. 5.4(b) for various driving frequencies ω .

5.3 Data analysis and experimental results

Starting with the raw data of centre-of-mass oscillations at different drive frequencies and subsequently for various temperatures, we reconstruct the spectral absorptive response function, $\text{Im}\chi(\omega)$, in Sec. 5.3.1. We use the spectra first to verify the f sum rule (Sec. 5.3.2) and then to extract the speed (Sec. 5.3.3) and the damping (Sec. 5.3.4) of the two observed hydrodynamic sounds. Concentrating on the speeds, we infer the superfluid density (Sec. 5.3.5), as sketched in the previous Sec. 5.1. Finally, in Sec. 5.3.6 we discuss and justify assumptions that we adopted at various stages in this chapter and give some more details of our experimental results.

5.3.1 Excitation spectra

With the protocol described above, we repeat driving the cloud at various frequencies ω to extract the frequency-dependent centre-of-mass, $d_{\text{com}}(t; \omega)$. The cloud responds linearly and thus $d_{\text{com}}(t; \omega)$ oscillates with the driving frequency. Experimentally, after 150ms of driving we record the behaviour in a ~ 100 ms-time-window. Here the data are fitted well by assuming a steady-state oscillation. Our fit function

$$d_{\text{com}}(t; \omega) = R(\omega) \sin(\omega t) - A(\omega) \cos(\omega t) \quad (5.9)$$

gives the reactive $R(\omega)$ (in-phase with the driving force) and absorptive $A(\omega)$ (out-of-phase with the driving force) response of the cloud. As seen also in Fig. 5.4(b), at low driving frequencies the atoms oscillate in phase with the driving force giving $A(\omega = 0) = 0$, whereas for high frequencies the response has close to a π -phase difference with the phase of the driving force.

Starting from the measured $A(\omega)$, one can reconstruct the imaginary part of the response function, $\text{Im}\chi(\omega)$. By combining Eqs. (5.7) to (5.9), one gets the absorptive response $\delta n(\omega) = -n\pi^2 A(\omega)/2L_y$, and together with Eq. (5.6) for the driving potential, this yields

$$\text{Im}\chi(\omega) = \frac{\delta n(\omega)}{\delta U(\omega)} = -\frac{n\pi^4}{8L_y^2 F_0} A(\omega). \quad (5.10)$$

This connection clearly indicates that the measured $A(\omega)$ is the key to observing the propagation of both first and second sound. Being proportional to $\text{Im}\chi(\omega)$, it is expected to show two distinct peaks when $T < T_c$, following the two-fluid behaviour as represented by Eq. (2.38). Also, from its relation with $\text{Im}\chi(\omega)$, one can rewrite the f sum rule of Eq. (2.30) in terms of $A(\omega)$ as

$$f_{\text{sum}} \equiv \int_{-\infty}^{\infty} d\omega \omega \frac{\pi A(\omega)}{8F_0/m} = 1. \quad (5.11)$$

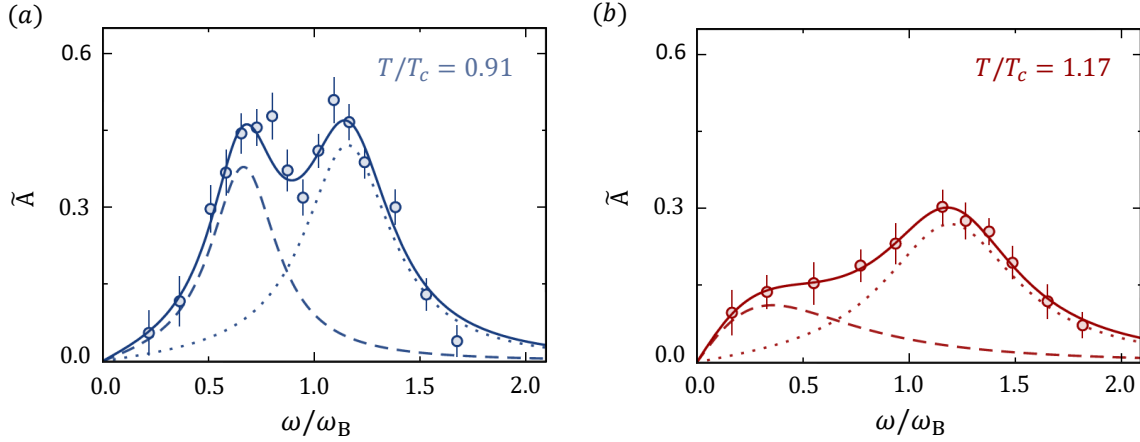


Figure 5.5: Two examples of the normalised response spectra $\tilde{A}(\omega)$ for (a) low ($0.91T_c$) and (b) high ($1.17T_c$) temperatures. In these examples $n \approx 3\mu\text{m}^2$, $L_y \approx 33\mu\text{m}$ and $F_0/m \approx 0.074\text{ms}^2$. Below T_c we observe two resonances corresponding to the first (dotted) and second (dashed) sound. Above T_c we instead observe just the first-sound resonance (dotted), while the second sound is replaced by a diffusive, overdamped mode (dashed).

We test experimentally this universal condition for $A(\omega)$ in next section. Eq. (5.11), or its rescaled form $f_{\text{sum}} \equiv \int_{-\infty}^{\infty} d\omega \omega \tilde{A}(\omega)/\omega_B^2 = 1$ with $\tilde{A}(\omega) = \omega_B^2 \pi A(\omega)/(8F_0/m)$, allows the direct comparison of various spectra at different temperatures when plotted versus ω/ω_B . Two such examples for two different temperatures are shown in Fig. 5.5.

Below some critical temperature (Fig. 5.5(a)), we indeed observe two resolved resonances corresponding to the first (higher- ω peak) and second (lower- ω peak) sound. Above this critical temperature (Fig. 5.5(b)), the lower- ω resonance disappears and we interpret this result as the conversion of second sound to the diffusive heat mode predicted by the one-fluid model (Sec. 2.1) that also couples to density perturbations owing to $\gamma > 1$. In order to determine this change in an unbiased way, we fit the experimental spectra with $A(\omega) = A_1(\omega) + A_2(\omega)$, where

$$A_{1,2}(\omega) = \frac{x_{1,2} \omega_{1,2}^2 \Gamma_{1,2} \omega}{(\omega^2 - \omega_{1,2}^2)^2 + (\omega \Gamma_{1,2})^2}. \quad (5.12)$$

In the above, the amplitudes $x_{1,2}$, resonance frequencies $\omega_{1,2}$, with $\omega_1 > \omega_2$, and damping rates $\Gamma_{1,2}$, are fit parameters. One can see Eq. (5.12) either as the direct result of taking the imaginary part of the dissipational model of Eq. (2.35) or, alternatively, as the extension of the dissipationless model of Eq. (2.38) after the inclusion of linear damping. We note that this form of the response corresponds to a simple model of two independent harmonic oscillators. Together with this fit, we also explicitly show in Fig. 5.5 the fitted contributions of the independent first (dotted) and second (dashed) sound modes.

In analogy to a harmonic oscillator, we define the quality factor of the sound modes as $Q_{1,2} = 2\omega_{1,2}/\Gamma_{1,2}$. We find that the first sound is always underdamped ($Q_1 > 1$). For the spectra at low temperatures (Fig. 5.5(a)), the fit gives that the second sound is also underdamped. For higher

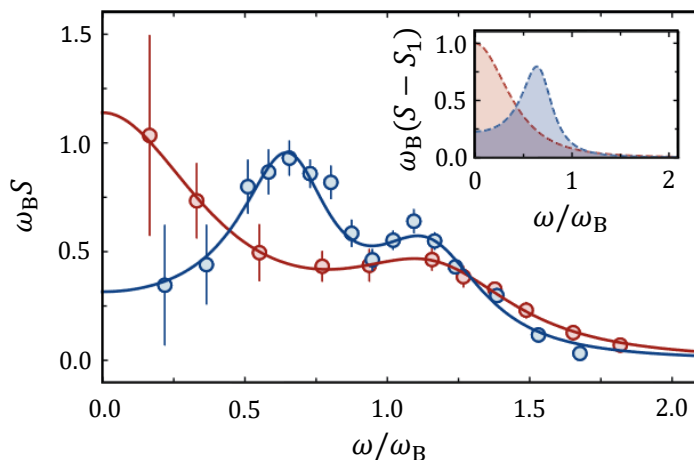


Figure 5.6: The corresponding dynamical structure factors $S(\omega)$ of the two spectra shown in Fig. 5.5 (in same colors). Here the diffusive mode of the high-temperature case has a maximum at $\omega = 0$, so its distinction from the second-sound resonance at low temperatures is clearer. The inset shows the fitted contributions to $S(\omega)$ from the second sound below T_c (blue) and the diffusive mode above T_c (red), omitting for clarity the first-sound contributions $S_1(\omega)$, which are similar at the two temperatures.

temperatures (Fig. 5.5(b)), the second term in the fit function gives that this mode is overdamped.

A more striking distinction between second sound and the diffusive mode can be gained by extracting the dynamic structure factor, linked with $\text{Im}\chi(\omega)$ and subsequently with $\tilde{A}(\omega)$ through the fluctuation-dissipation theorem of Eq. (2.29) as

$$S(\omega) = k_B T \tilde{A}(\omega) / (m c_B^2 \omega). \quad (5.13)$$

Indeed, unlike $\text{Im}\chi(\omega)$, which has to be zero at $\omega = 0$, $S(\omega)$ manifests a peak at zero frequency when the diffusive mode is present (see Eq. (2.34)). In Fig. 5.6 we calculate $S(\omega)$ for the two cases shown in Fig. 5.5; the inset highlights the difference between second sound ($\omega_2 > 0$) and the diffusive mode corresponding to $\omega_2 = 0$.

5.3.2 f sum rule and the critical temperature

We systematically measure $A(\omega)$ for different temperatures in the range from 23nK to 56nK. For a sanity test of the measured spectra $A(\omega)$, we check the validity of the f sum rule. In the top panel of Fig. 5.7 we calculate the value of the integral f_{sum} from Eq. (5.11) using the fit of the spectra (Eq. (5.12)) for the various temperatures. We find that the condition $f_{\text{sum}} = 1$ is well satisfied, and thus the observed modes ‘exhaust’ the f sum rule for the probed wavelength.

For the low-temperature spectra, where two resolved peaks are present, we further extract the values f_1 and f_2 , the contributions to f_{sum} from the $A_1(\omega)$ and $A_2(\omega)$ components in Eq. (5.12), respectively. The results for f_2 are plotted in the lower panel of Fig. 5.7 and show how f_2 decreases with increasing temperature. The experimentally extracted $f_{1,2}$ correspond to the theoretical weights

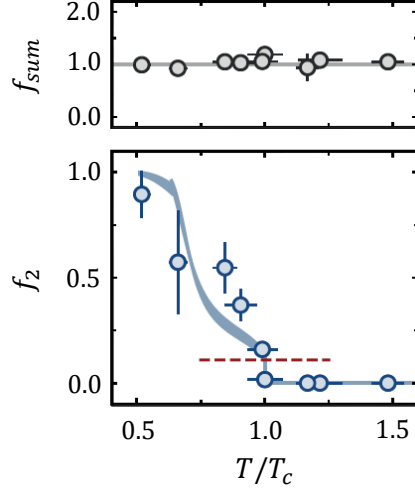


Figure 5.7: (a) The f sum rule is verified over a wide range of temperatures. (b) f_2 , the second-sound contribution to the constant f_{sum} , vanishes with increasing T and is used to experimentally identify T_c . The blue shading shows the theoretical prediction of the weight in the f sum, Z_2 , for an infinite dissipationless system. The thickness of the shaded area reflects the theoretical variations due to the uncertainty in \tilde{g} . The dashed line indicates the predicted discontinuity in Z_2 at T_c , which arises from the jump in the superfluid density. The obtained f_2 for the different measured spectra are plotted versus the rescaled T/T_c after the identification $T = T_c$ when $f_2 \rightarrow 0$. The errors in T/T_c come from the statistical uncertainty in the density n and do not include the systematic errors in the measured T or the systematic decrease in density due to atom losses, canceled by the process of determining T_c .

$Z_{1,2}$ in the f sum rule in the absence of dissipation, with $Z_1 + Z_2 = 1$. Currently, we are not aware of a general theoretical prediction on how the relative weights of the two sounds get modified in the presence of dissipation, if at all. However, the simple observation that the integrals

$$\int_{-\infty}^{\infty} \omega A_{1,2}(\omega) d\omega = x_{1,2} \omega_{1,2}^2 \pi, \quad (5.14)$$

directly related with the f sum rule, are independent of the damping rates $\Gamma_{1,2}$ hints that the weights of first and second sound are not significantly modified, at least as long as the fitting form of Eq. (5.12) remains applicable⁸ (i.e. in the presence of only linear damping).

From the observed behaviour of f_2 we identify a critical temperature for the (dis)appearance of second sound, as the lowest temperature at which $f_2 = 0$. By using the prediction for Z_2 for this identification, this temperature corresponds to T_c , the critical temperature of the 2D gas in the thermodynamic limit. In absolute numbers we find the inferred T_c to be 42nK (with a systematic uncertainty of 4nK), which is compatible with the BKT prediction $T_c = 2\pi\hbar^2 n / mk_B \ln(380/\tilde{g}) = 37(6)\text{nK}$ for our $n = 3.0(5)\mu\text{m}^{-2}$. In the language of finite systems the experimentally extracted critical temperature corresponds to T_2 (Sec. 3.3) and is expected to be around $\sim 5 - 10\%$ higher than the infinite-system critical temperature. However, within our systematic errors in temperature and density such a shift is not conclusive.

⁸We use this alternative method to extract the f sum weights as $f_{1,2} = \pi^2 x_{1,2} \omega_{1,2}^2 / (8F_0/m)$ for a double-check of the values shown in Fig. 5.7, obtained from a direct calculation of the integrals in Eq. (5.11).

In the limit $T \rightarrow 0$, the hydrodynamic two-fluid model for two-dimensional fluids predicts that the first and second sound speeds take the Bogoliubov-related values c_B and $c_B/\sqrt{2}$, respectively, with only the first sound coupling to density perturbations ($\gamma \rightarrow 1$ as $T \rightarrow 0$). On the other hand, for higher temperatures and for a \tilde{g} similar to ours, it is the second sound that mainly couples to density and extrapolates to the Bogoliubov speed of sound. One then expects at some relatively low temperature a hybridisation mechanism between the two sound modes at which the importance of the weights of first and second sound is inverted. Our measurements manifest an increasing importance of f_2 as temperature decreases down to $T/T_c \approx 0.5$, showing that if such a hybridisation mechanism exists, it should occur at even lower temperatures.

Above T_c , where the diffusive mode has replaced second sound, we can still define a weight for this heat mode in the f sum, f_{diff} , which together with f_1 they satisfy $f_{\text{sum}} = f_1 + f_{\text{diff}}$. We note that approximating the diffusive mode by a δ -function response at $\omega = 0$, as in the dissipationless one-fluid model of Eq. (2.34), gives $f_{\text{diff}} = 0$; in reality this mode has a non-zero contribution to the experimental f_{sum} coming from the low- ω behaviour. Because of this discrepancy, we instead estimate the ratio of weights $s_2/s_1 = \int [A_2(\omega)/\omega] d\omega / \int [A_1(\omega)/\omega] d\omega$ in $S(\omega)$, where s_2 represents the diffusive mode above T_c , and we compare the results with the theoretical prediction $s_2/s_1 \approx \gamma - 1$, as one can directly deduce from the same Eq. (2.34). For the three measured spectra above T_c , at a temperature $T/T_c = 1.17(4)$, $1.22(8)$, and $1.48(6)$ we find $s_2/s_1 = 1.1(5)$, $1.0(3)$ and $1.5(4)$, respectively, which are in good agreement with the corresponding predictions $\gamma - 1 = 1.1(1)$, $1.2(2)$ and $1.7(1)$. The uncertainty in the theoretical $\gamma - 1$ comes from the statistical uncertainty in T/T_c and we do not consider the systematic error in \tilde{g} (see relevant discussion in Sec. 5.3.6).

5.3.3 First and second sound speeds

We can now extract the speeds of first and second sound, $c_{1,2} = \omega_{1,2}/q$, through the fitted resonant frequencies $\omega_{1,2}$. Here, the wave number $q = \pi/L_y$ of the excitations requires the knowledge of the box-size L_y . Already from the cartoon in Fig. 4.14 it becomes apparent that a proper definition of the box-size is ambiguous due to the finite slope of the in-plane potential. We thus use the density profile of the corresponding uniform gas for a systematic determination of L_y . Specifically, we define L_y as the length of the region in which the density is above 90% of its value in the bulk. This choice is supported by the observation that with this definition of L_y it closely corresponds to the half-wavelength of the density oscillations in a driven system, i.e. the observed q , an example of which is depicted in Fig. 5.4(a). We discuss the uncertainty in extracting L_y together with other errors in Sec. 5.3.6.

In Fig. 5.8 we summarise our results for the temperature-dependent speeds of first (red) and second (blue) sound, normalised to the Bogoliubov sound c_B . Above T_c , the lower-frequency peak in $S(\omega)$ occurs at $\omega = 0$, i.e. $c_2 = 0$. In the same plot, we show the theoretical predictions of the normalised first and second sound for an infinite system, $u_{1,2}$, from Eqs. (5.1)-(5.2) and the

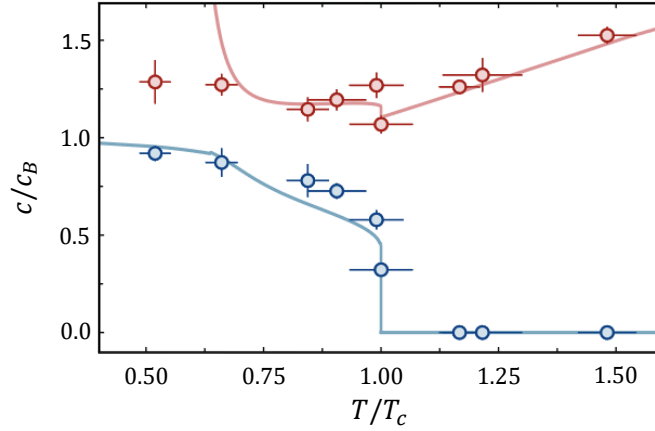


Figure 5.8: Normalised sound speeds, c_1/c_B (red) and c_2/c_B (blue), and the corresponding theoretical predictions $u_{1,2}$ of the infinite-system theory, based on identifying the temperature where second sound disappears as the critical temperature T_c in that theory. Owing to scale invariance in two dimensions, the predicted $u_{1,2}$ are functions of just T/T_c and \tilde{g} . Their discontinuities at T_c correspond to the infinite-system jump in superfluid density.

scale invariant predictions of Sec. 3.3, under the assumption that the theoretical critical temperature coincides with our defined T_c .

By comparing the measured normalised speeds with the infinite-system theory, we find a good overall agreement. Most importantly, the measurements reveal the abrupt decrease of the normalised speed of second sound at T_c in agreement with the expected discontinuity of ≈ 0.45 . The observation of c_2/c_B below this threshold, and similarly for f_2 in Fig. 5.7, is most likely a result of the finite-size modifications compared to the infinite-system theory. Due to the finite compressibility, the theory predicts also a smaller discontinuity in the speed of first sound (≈ 0.1), which is comparable to our errors and thus experimentally inconclusive. The agreement between theory and experiment is also in line with the scale invariance that governs the 2D gas, due to which the normalised first and second sound are expected to be independent of the actual box geometry (as long as hydrodynamic conditions are satisfied).

Failure of the theoretical prediction at low temperatures

At low temperatures, the theoretical prediction of first sound in Fig. 5.8 becomes unphysical. To understand why, we first note that $u_{1,2}$ depend on the predicted $D - D_s$ through u_{20} (see Eq. (5.2)). At low temperatures, u_{20} is extremely sensitive to this difference since $D \approx D_s$ and even small disagreements between the two independent theories (for D and D_s) can cause a substantial change in u_{20} . The divergence in u_{20} results in a subsequent divergence in u_1 . For an intuitive understanding of this, we consider the extreme case with $\gamma = 1$ (not so different from reality at these low temperatures). In Fig. 5.9(a) we show the calculated u_{10} and u_{20} as extracted from the theories for D and D_s versus $x = \mu/k_B T$. In this case with $\gamma = 1$, the sound speeds should coincide with u_{10} and u_{20} from the solutions of Eq. (5.1); first sound, u_1 , being the faster of the two then is identified as u_{10} for low

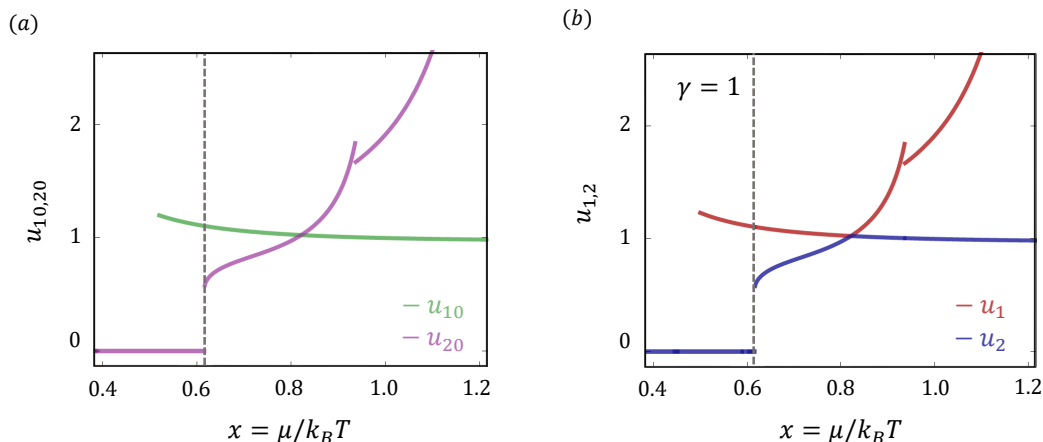


Figure 5.9: (a) The quantities u_{10} (green) and u_{20} (purple) for $\tilde{g} = 0.64$ as extracted using the scale-invariant thermodynamic quantities and the superfluid density prediction. (b) The subsequent normalised speeds, u_1 (red) and u_2 (blue) in the hypothetical scenario of $\gamma = 1$ for all values of x . The role of u_{10} and u_{20} is interchanged at $x \approx 0.8$ ($T/T_c \approx 0.75$) leading to the deviation of the speed of first sound at low temperatures. In reality, at low temperatures it is $\gamma \approx 1$ and the behaviour changes only quantitatively.

$x < 0.8$ (large $T \gtrsim 0.75T_c$) and as u_{20} for high $x > 0.8$ (low $T \lesssim 0.75T_c$). This is illustrated in Fig. 5.9(b). For a realistic γ close to unity, the situation is not qualitatively modified.

5.3.4 Dissipation of first and second sound

The obtained spectra also provide the damping rates $\Gamma_{1,2,T}$ for the two sound and the heat modes, which are linked to the corresponding sound and heat diffusivities through $D_{1,2,T} = \Gamma_{1,2,T}/q^2$ within the hydrodynamic theory [225]. For the heat mode, a proper extraction of the damping rate and subsequently the heat diffusivity requires refitting⁹ the spectra for $T > T_c$ with $A(\omega) = A_1(\omega) + A_T(\omega)$, where

$$A_T(\omega) = \frac{x_T \Gamma_T \omega}{\omega^2 + \Gamma_T^2}, \quad (5.15)$$

as deduced from Eq. (2.33). We concentrate on the diffusivity rather than the damping rates or the quality factor of these modes because the scale invariance of a 2D system hints that $D_{1,2,T}$ manifest a ‘universal’ behaviour and depend only on T/T_c for a given \tilde{g} [226], although this is not yet confirmed.

The results for $D_{1,2,T}$ in units of \hbar/m for the various temperatures below and above the transition point are shown in Fig. 5.10(a). The measured $D_{1,2,T}$ show a general insensitivity on T for the relevant range of temperatures and within the precision of our measurements, with values in the range $\sim (5-8)\hbar/m$. This behaviour may be connected with additional and dominating damping effects in our experiment, like a broadening by the loss-induced density drift during the measurements or by still imperfect hydrodynamic conditions, and more detailed studies on dissipation for a complete understanding of our measurements are needed. Despite the absence of a solid theoretical prediction¹⁰

⁹After this refit, we verified that the results presented before are not essentially modified.

¹⁰Such predictions within the hydrodynamic one- and two-fluid theories require the good knowledge of the shear

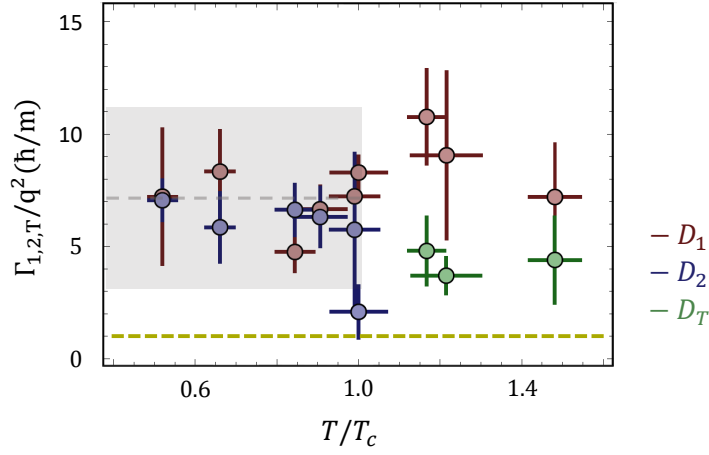


Figure 5.10: Measured diffusivity $D_{1,2,T} = \Gamma_{1,2,T}/q^2$ for the first (red) and second (blue) sound and the diffusive heat (green) modes. The yellow dashed line is the lowest expectable diffusivity in the limit that the free mean path becomes similar to the interparticle distances. The shaded regime corresponds to the measured first-sound diffusivity from Ref. [227] for the case of a Fermi gas (on its BEC side) for similar interaction strengths to ours and for low temperatures.

for $D_{1,2,T}$ in a 2D Bose gas to compare our results with, we briefly discuss simple expectations and comparisons with similar recent experiments with Fermi gases.

A crude first attempt is to apply the kinetic theory for a dilute gas, in which the diffusivity (of both sound and heat) is approximately $\bar{v}l_{\text{mfp}}$ (see for example [228]), with \bar{v} the mean velocity and l_{mfp} the mean free path of the atoms. Following the same process as for the collision rate in Eq. (3.31), we have $\bar{v} \approx \hbar/(m\ell_z)$ and $l_{\text{mfp}} \approx 1/(n_{3D}\sigma)$ with $\sigma \approx 4\pi a^2$ and $n_{3D} \approx n/\ell_z$, from which we finally get

$$D_{1,2,T} \sim \frac{\hbar/m}{4\pi a^2 n}. \quad (5.16)$$

This simple theory does not show a scale-invariant behaviour, as it includes a three-dimensional consideration of the atomic motion, and the resulting predictions are a few times higher than our measurements for the relevant densities. However, it directly shows how for strongly interacting gases, where $l_{\text{mfp}} \sim d_{\text{int}}$ and $\bar{v} \sim \hbar/(md_{\text{int}})$, with d_{int} the interparticle separation, the diffusivity reaches a minimum $\sim \hbar/m$. Although the exact prefactor is not known, in Fig. 5.10(a) we represent this quantum limit (dashed yellow line) as \hbar/m , motivated by the minimum of diffusivity that has been observed so far for both a 3D [226] and a 2D [227] unitary Fermi gas.

Specifically for 2D, in Ref. [227] the first-sound diffusivity was measured for different interaction strengths (adopting the language of the two-dimensional scattering length a_{2D}) and it was concluded that on the BEC side of the Fermi gas, i.e. $\ln(k_F a_{2D}) < 0$ with $k_F = (4\pi n)^{1/2}$, the limit $D_1 \sim \hbar/m$ is indeed reached in the strongly-interacting regime. Their measurements show furthermore that D_1

viscosity η and the thermal conductivity κ of the gas (see Eqs. (2.9), (2.10), and (2.36)), quantities that are still challenging both experimentally and theoretically.

increases for weaker interactions, $\ln k_{\text{F}}a_{2\text{D}} \lesssim -2$, to another plateau of $\sim (5-8)\hbar/m$. In our case¹¹ $\ln(k_{\text{F}}a_{2\text{D}}) \approx -8.5$, and our results indeed fall into this high-diffusivity plateau. In Fig. 5.10 the gray shaded region represents the measurements of Ref. [227] for the relevant for us interaction strength; the extent over our whole temperature region of a superfluid is indicative and does not correspond to the region of the original (low-temperature) measurements. As said in the beginning of this section, further studies are required to state whether this agreement is accidental or not.

5.3.5 Superfluid fraction and superfluid density

In Sec. 5.1 we argued how the measurement of the speeds of first and second sound could serve for the deduction of the superfluid density. In more detail, we saw that within the two-fluid model the sound speeds depend on both the thermodynamics of the gas and the superfluid density and thus with the knowledge of the former, the superfluid density can be inferred. Starting from Eq. (5.2) for u_{20} , one can express the superfluid fraction as

$$\frac{n_{\text{s}}}{n} = \frac{1}{1 + \Lambda(x)/u_{20}^2(x)}, \quad (5.17)$$

with $\Lambda(x)$ depending only on the scale-invariant and dimensionless thermodynamic phase-space density $D(x)$ and pressure $\mathcal{P}(x)$. The quantity u_{20} can be expressed through the first and second sound $u_{1,2}$ by inverting Eq. (5.1), yielding

$$u_{10,20} = \frac{\sqrt{u_1^2 + u_2^2 \pm \sqrt{u_1^4 + u_2^4 + 2u_1^2u_2^2(1 - 2\gamma)}}}{\sqrt{2}}, \quad (5.18)$$

where one has to be careful to correlate properly the two branches with the quantities u_{10} and u_{20} (see Fig. 5.9). We note that u_{20} depends also on $D(x)$ and $\mathcal{P}(x)$ through the coupling $\gamma(x)$.

We use the classical-field theoretical predictions of Ref. [115], as discussed in detail in Sec. 3.2.3 and plotted in Fig. 3.4, for the necessary thermodynamic $D(x)$ and $\mathcal{P}(x)$ entering the relations above. Although these predictions were theoretically derived for a weakly interacting 2D Bose gas, $D(x)$ and $\mathcal{P}(x)$ have been measured in the past [38, 39, 153] for a wider range of interaction strengths, including $\tilde{g} = 0.64$, with no evidence of deviation between theory and experiment. Using them and the measured first and second sound speeds, we show in Fig. 5.11(a) the calculated u_{20} from Eq. (5.18) together with its prediction. The disagreement between the theory and the measurement at low temperatures stems from the failing theory as we discussed before.

Combining u_{20} with the predicted $\Lambda(x)$, its behaviour for $\tilde{g} = 0.64$ being illustrated in Fig. 5.11(b), we extract the superfluid fraction, plotted in Fig. 5.11(c). Our results for n_{s}/n are compared in the

¹¹To connect our familiar language with the one using $a_{2\text{D}}$ as in Ref. [227], we use $\frac{4\pi\hbar^2}{m} \frac{1}{\ln(1/na_{2\text{D}}^2)} \approx \hbar^2\tilde{g}/m$ [144] to find $\ln(k_{\text{F}}a_{2\text{D}}) = \ln[(4\pi)^{1/2}e^{-2\pi/\tilde{g}}]$. For our $\tilde{g} = 0.64$, we get $\ln(k_{\text{F}}a_{2\text{D}}) = -8.5$. This correspondence hints the difficulty in reaching the quantum limit of diffusivity with a 2D Bose gas.

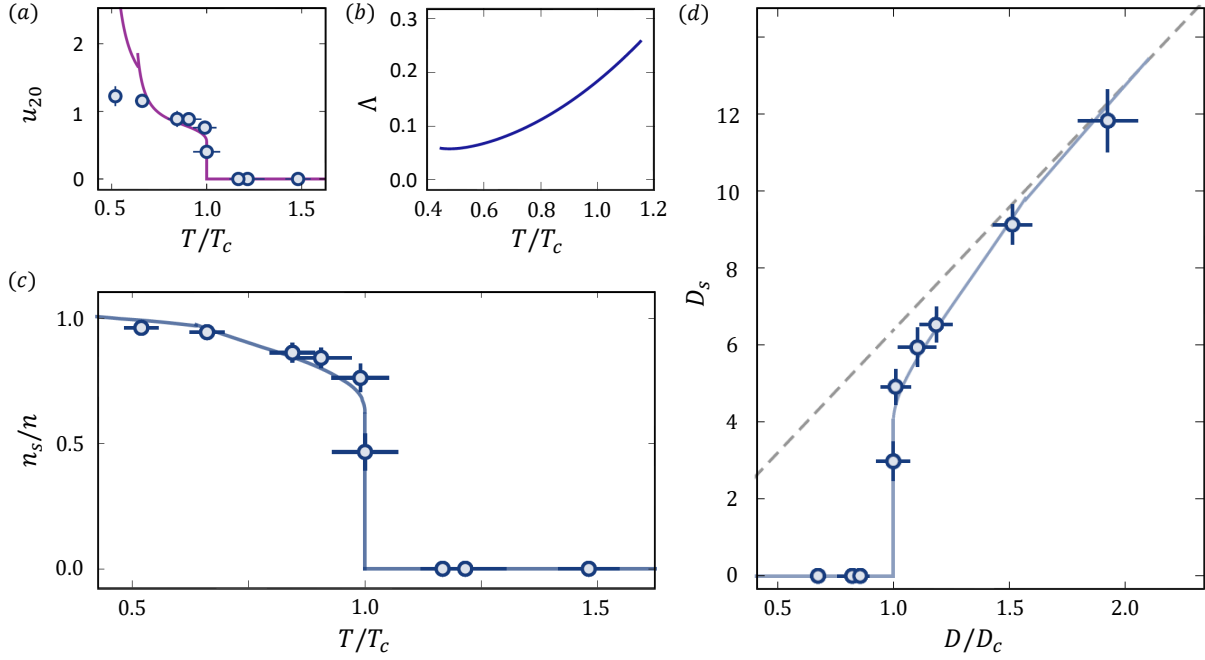


Figure 5.11: The extraction of the superfluid density step-by-step. (a) The deduced u_{20} from the measured speeds of first and second sound together with the infinite-system theoretical prediction. (b) The theoretical prediction for Λ that depends only on the thermodynamic D and \mathcal{P} , which have been previously verified. (c) The superfluid fraction, n_s/n , using the previous two results for u_{20} and Λ based on Eq. (5.17); the solid line shows the BKT prediction for the infinite system. (d) The superfluid phase-space density, D_s , deduced from the superfluid fraction and the total density. The solid line, the corresponding BKT theory, shows the universal jump of D_s from 0 to 4 at $D = D_c$. The dashed line corresponds to a 100% superfluid ($D_s = D$).

same plot with the corresponding prediction using the theoretical superfluid density (Sec. 3.2.2) and the theoretical equation of state (Sec. 3.2.3). The restoration of the agreement between theory and experiment at low temperatures is due to the small value of Λ there, physically implying an almost 100% superfluid fraction. As expected, the superfluid fraction manifests the same behaviour we found also in the speeds of sound, namely a sharp drop close to the critical temperature that resembles the jump in n_s .

This universal jump can be visualised if we further deduce the superfluid phase-space density as $D_s = (n_s/n)D_c/(T/T_c)$, with D_c the critical phase-space density of Eq. (3.27); we plot the resulting D_s versus $T_c/T = D/D_c$ in Fig. 5.11(d). The inferred D_s is again compared with the theory of the infinite system and is in good agreement with the expected discontinuity $4 \rightarrow 0$ at the critical point.

5.3.6 Further remarks

In the last part of this chapter we discuss and clarify various subtle aspects of the results discussed before.

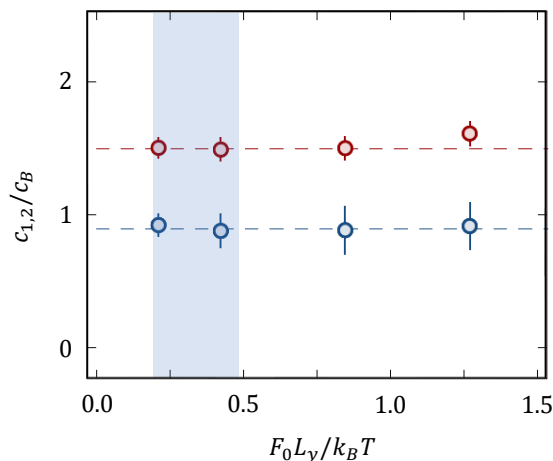


Figure 5.12: Speeds of first (red) and second (blue) sound, as extracted using various amplitudes F_0 of the driving force. For this test we used a gas at $T = 0.7T_c$ and $\tilde{g} = 0.4$. The dashed lines are guides to the eye, taken as the mean of the three points with the smallest driving amplitude.

Weakness of the perturbation

For the results to be quantitatively meaningful and comparable with theory, one has to verify that the presence of the driving potential does not alter the excitation spectra compared to those of the 2D uniform Bose gas. For that, we repeat our measurements for different amplitudes of the driving force and check the effect of F_0 on the first and second sound speeds.

In Fig. 5.12 we show the resulting normalised speeds for different edge-to-edge potential differences, $F_0 L_y$, normalised to $k_B T$ as the most relevant energy scale of the gas. The blue-shaded region represents the interval where the results that we presented in this chapter take place. With this check we verify that there is no essential change in the resonant frequencies in the range of driving forces we apply and our measurements properly describe those of a uniform gas.

Experimental uncertainties

Our experiments are subject to different sources of uncertainties, both statistical and systematic. However, in all the results we presented above, only uncertainties with a statistical character are included in the shown error bars. Their origin stems from the standard fitting errors of the raw centre-of-mass oscillations and of the subsequent absorptive spectra, and the statistical uncertainties in the density of the gas and the size of the container. Specifically, we consider shot-to-shot temporal variations in the average n and temporal and spatial variations in L_y along different x -values of the box. These errors are typically around $\sim 5\%$ in the density and below 3% in the size of the box. In addition to these statistical errors, various systematic uncertainties have to be kept in mind. Important systematic errors in density appear from the imperfect homogeneity of the gas ($\sim 10\%$) in its central region, the three-body losses during the driving ($\sim 15\%$), and finally the process of

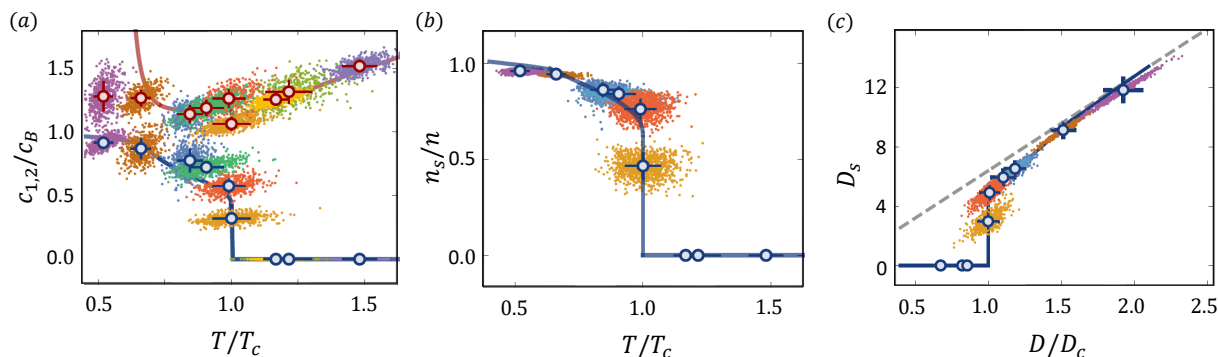


Figure 5.13: A ‘bootstrapping’-like method to estimate the uncertainties in (a) the speeds of first and second sound, (b) the superfluid fraction, and (c) the superfluid density. The resulting mean and one standard deviation are plotted on top of the random points, generated from a probability distribution that takes into account the uncertainties in the density, the box size and the fitted resonances in the driving frequency. The conversion from the speeds to the superfluid fraction requires the equation of state (or equivalently the quantity Λ); uncertainties of the latter stem only from the error in T/T_c in our approach.

absorption imaging ($\sim 15\%$). Systematic uncertainties on other relevant quantities also need to be mentioned, for example in the interaction strength \tilde{g} ($\sim 5\%$), in the amplitude F_0 of the driving force ($\sim 5\%$), or in the in-plane trap-depth ($\sim 10\%$) which ultimately determines the temperature of the gas.

Focusing on the statistical errors, we use a ‘bootstrapping’-like approach for the determination of the various uncertainties: For each measured absorptive spectrum at the nominal temperature T (we call that spectrum a ‘data-set’), we ‘randomly’ select values of T/T_c and $c_{1,2}/c_B$ and apply the analysis of Sec. 5.3.5 to obtain the corresponding c_{20} , Λ , n_s/n and finally D_s . By repeating this process a large number of times, we obtain a scatter of values for each of the above quantities, from which its uncertainty as one standard deviation is extracted.

The initial ‘randomly’ picked values of T/T_c and $c_{1,2}/c_B$, for the application of the above process, respect the statistics of our measured n and L_y , and the fitting results of the resonant frequencies $\omega_{1,2}$. Specifically, the samples of $T/T_c(n) = mk_B T \ln(380/\tilde{g})/(2\pi\hbar^2 n)$ and $c_B(n) = (\hbar/m)\sqrt{n\tilde{g}}$ depend on the density; for each repeat, we choose a value of n by sampling from a normal distribution originating from the measured mean and standard deviation of the density for the relevant data-set. In the same way, the samples of $c_{1,2} = \omega_{1,2}\pi/L_y$ are generated using the uncertainties in the box size L_y and the standard fit error on $\omega_{1,2}$. Within our experimental precision a correlation between the measured L_y and the obtained $\omega_{1,2}$ is a difficult task, and thus we resort to assuming that these two quantities are independent for the extraction of $c_{1,2}$; similarly, any n -dependence of $c_{1,2}$ is omitted.

The scatter plots for the normalised speeds of first and second sound, the superfluid fraction and the superfluid density are shown in Fig. 5.13. Together we show the extracted mean and one standard deviation of the corresponding quantities, already plotted in Figs. 5.8 and 5.11. From Fig. 5.13(a) one can see a correlation between $c_{1,2}/c_B$ and T/T_c , caused by the mutual density dependence of the two axes. A correlation between the two axes is even more visible in Fig. 5.13(c) where D_s is plotted

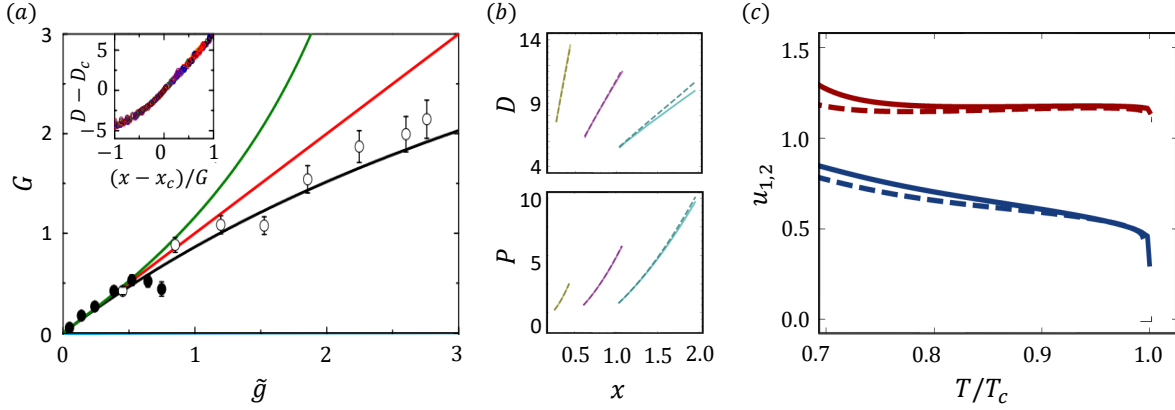


Figure 5.14: Testing the validity of the classical-field equation of state. (a) The optimal coupling constant G for various \tilde{g} and the universal function H (inset) that collapses all the equations of state; plot reproduced from Ref. [39]. (b) The phase-space density (top panel) and phase-space pressure (bottom panel) as derived from the classical-field theoretical results (straight lines) and extracted by rescaling the experimental universal function H (dashed lines) for three different interaction strengths, $\tilde{g} = 0.2$ (yellow), 0.64 (purple), and 1.5 (cyan) and for $x = \mu/k_B T$ that corresponds to T/T_c between 0.5 and 1.0. (c) The predicted speeds of first (red) and second (blue) sound using BKT prediction for the superfluid density and the classical-field equation of state (straight lines) or the rescaled version of the measured universal H (dashed lines).

versus D/D_c , since $D_s = (n_s/n)(D/D_c)D_c$. The shown error bars, also given in Figs. 5.8 and 5.11, represent the projection of the uncertainties on the plotted horizontal and vertical axes.

Error from considering the classical-field equation of state

The estimation for the superfluid fraction and superfluid density used not only the measured speeds of first and second sound but also the theoretical classical-field equation of state. It is thus important to justify that this treatment does not introduce significant errors. We argue based on the experimental results of Ref. [39].

In that work, the equation of state for the 2D Bose gas was experimentally measured for different interaction strengths \tilde{g} , ranging from the weak to the strong interaction regime, and the results overlap excellently after a rescaling

$$D - D_c(\tilde{g}) = H\left(\frac{x - x_c(\tilde{g})}{G(\tilde{g})}\right), \quad (5.19)$$

where again $x = \mu/k_B T$ and H is an experimentally obtained function (inset of Fig. 5.14(a), as reproduced from Ref. [39]). The quantity $G(\tilde{g})$ plays the role of a generalised coupling constant and is shown in the main panel of Fig. 5.14(a); for the weakly-interacting case $G = \tilde{g}$, whereas good general agreement with the experiment shows the behaviour $G = 2\pi\tilde{g}/(2\pi + \tilde{g})$ (black line in the plot). In the same work, the authors deduced the critical D_c and x_c and verified the classical field predictions of Eq. (3.27) and Eq. (3.28), respectively, for a wide range of interactions up to $\tilde{g} \sim 2$.

By rescaling back the universal function H to any specific \tilde{g} , we get the experimentally deduced

equation of state $D(x)$ that can be compared with the theoretical classical-field equation of state. The comparison is shown in the upper panel of Fig. 5.14(b), for three values of \tilde{g} , including our case (in purple) with $\tilde{g} = 0.64$ and $G = 0.58$; in this case the deviation is still negligible for the relevant range of temperatures. We further recreate the phase-space pressure $\mathcal{P}(x)$, shown in the lower panel of Fig. 5.14(b), and together with the rescaled D , we finally plot in Fig. 5.14(c) a comparison for the speeds of sound $u_{1,2}$ extracted from the classical-field prediction that we use in this thesis (straight lines) and the measured equation of state (dashed lines), showing minor differences in the range of interest for our results.

6

Conclusions and outlook

“This is the way the wor(l)d ends, not with a bang, but a whimper.”

— T. S. Eliot, *The Hollow Men*

In this thesis, we presented an experimental realisation of an interacting 2D uniform Bose gas of ^{39}K atoms, which we used as a platform to connect Landau’s two-fluid hydrodynamic model with the BKT theory for 2D superfluids. The tunability of interactions owing to a broad Feshbach resonance allowed us to work at a relatively strong interaction strength¹ with $\tilde{g} = 0.64(3)$, meeting the conditions for this connection. The gas homogeneity, on the other hand, provided suitable conditions to systematically probe the bulk properties of the gas. The main results of our studies can be summarised as follows:

1. In addition to the usual (first) sound of density excitations, present even in the absence of superfluidity, the second sound predicted within the two-fluid model is seen for the first time in any 2D fluid. Moreover, we observed the high-temperature continuation of second sound which appears as a diffusive heat mode.
2. The temperature-dependent speeds of first and second sound are in good agreement with a theoretical classical-field prediction for the infinite and scale-invariant 2D gas, when defining the critical temperature as the one at which second sound disappears.
3. The deduced superfluid density, a central quantity that had so far remained elusive in ultracold gases, shows agreement with the characteristic jump at the critical point, as described by the BKT theory.

Furthermore, we characterised the observed first and second sound modes by providing their damping rates and relative weights in their density response. These quantities are of great interest since they

¹But not so strong to modify the expected scale invariance of our system.

go beyond the predictions of the simple dissipationless two-fluid model; however, our results for these quantities have to be taken with a grain of salt and a more systematic investigation is required that excludes possible caveats arising from atom losses or imperfect hydrodynamic conditions.

Future studies for the behaviour of first and second sound in a 2D superfluid include:

1. The investigation of sound modes at even lower temperatures than explored in the present thesis, in order to test a possible hybridisation between the two sounds. Theory predicts that the hybridisation temperature increases with larger \tilde{g} [229]; however, it is not yet clear if at such low temperatures ($\sim 0.2 - 0.3T_c$), with only a small normal component in the gas, hydrodynamic conditions necessary for the excitation of first and second sound still remain valid.
2. A quantitative characterisation of finite size effects of our gas close to the BKT transition, which is expected to transform into a crossover. Recent numerical simulations [159, 230] estimate this crossover based on the behaviour of the superfluid fraction around T_c , a quantity that has now become experimentally accessible with the help of our technique. A careful study of the crossover will require, however, a more precise and independent determination of the temperature of the gas.
3. Connecting the hydrodynamic system where the two sound modes exist, as in our measurements, with the collisionless regime where a single sound without any discontinuity at T_c has been observed, as in the work of Ref. [207]. This will require repeating the experiment with smaller \tilde{g} .
4. The investigation of the dimensional crossover from 2D to 3D superfluidity by loosening the transverse confinement in the gas. It would be interesting to see how the critical temperature for the disappearance of second sound changes to meet the known limiting cases of a strict 2D BKT gas and the 3D BEC and if the sharp drop of second sound in the BKT superfluid could be distinguished from the smoother behaviour in a 3D gas.
5. The systematic study of dissipation of the two sound modes at various interaction strengths. It would be interesting to check if diffusivities as low as $\sim \hbar/m$, as observed in unitary Fermi gases [226, 227], can be measured also for the 2D Bose gas. The measurement of the sound diffusivities could lead to the extraction of transport quantities like the shear viscosity and the thermal conductivity of the gas.

Going beyond the sound investigation for the 2D Bose gas in thermodynamic equilibrium, our newly-built and versatile 2D uniform trap provides a broad range of experimental paths one could follow. An appealing perspective is the possibility to study non-equilibrium critical phenomena occurring at the BKT transition. The Kibble-Zurek (KZ) mechanism, for instance, that describes the critical dynamics of the emerging ‘order’ after a quench through a second-order transition [231],

has been theoretically revisited also for the infinite-order BKT case [232, 233]. Experimental access to the first-order correlation function would not only serve as a tool to explore the KZ mechanism, but it would also be an important result in its own right, providing the algebraic decay of the equilibrium correlations below T_c , a result that would reveal the superfluid jump from a different perspective, complementary to our studies.

Another direction would be the investigation of transport phenomena in a Bose² gas by constructing more complicated but convenient trapping geometries. An example would be the study of the thermo-mechanical effect, analog to the fountain effect in liquid helium, through the creation of two uniform gases (reservoirs) that are connected via a narrow channel. With the addition of disorder in the channel, by projecting for example an additional laser speckle pattern that mimics the role of the capillaries in helium, a ‘super-leak’ is formed in which temperature or chemical-potential differences between the two reservoirs lead to the transport of only the superfluid component through the channel [236, 237].

In general, our apparatus permits various studies in two dimensions, or even in one- or three-dimensions with some modifications, and the enthusiasm that I discern in the team allows me to look optimistically into the future of this machine. Until new progress is reported:



²Transport phenomena have been studied more in Fermi gases [82, 234, 235] owing to the similar character with the electrons in well-known mesoscopic systems, like a transistor.

Bibliography

- [1] A. Einstein. Quantentheorie des einatomigen idealen gases. *Sitz. K. Preuss. Akad. Wiss.* 1925, 3, 1925.
- [2] P. Kapitza. Viscosity of liquid helium below the λ -point. *Nature*, 141:74, 1938.
- [3] J. F. Allen and A. D. Misener. Flow of liquid helium II. *Nature*, 141:75, 1938.
- [4] G. B. Hess and W. M. Fairbank. Measurements of angular momentum in superfluid Helium. *Phys. Rev. Lett.*, 19:216–218, Jul 1967.
- [5] H. E. Hall and W. F. Vinen. The rotation of liquid Helium II: II. the theory of mutual friction in uniformly rotating Helium II. *Proceedings of the Royal Society of London. Series A. Mathematical and Physical Sciences*, 238(1213):215–234, 1956.
- [6] M. Zwierlein, J. R. Abo-Shaeer, A. Schirotzek, C. H. Schunck, and W. Ketterle. Vortices and superfluidity in a strongly interacting Fermi gas. *Nature*, 435(7045):1047–1051, 2005.
- [7] J. D. Reppy and D. Depatie. Persistent currents in superfluid Helium. *Phys. Rev. Lett.*, 12(8):187, 1964.
- [8] S. Beattie, S. Moulder, R. J. Fletcher, and Z. Hadzibabic. Persistent currents in spinor condensates. *Phys. Rev. Lett.*, 110:025301, 2013.
- [9] S. V. Pereverzev, A. Loshak, S. Backhaus, J.C. Davis, and R.E. Packard. Quantum oscillations between two weakly coupled reservoirs of superfluid ^3He . *Nature*, 388(6641):449–451, 1997.
- [10] S. Levy, E. Lahoud, I. Shomroni, and J. Steinhauer. The AC and DC josephson effects in a Bose–Einstein condensate. *Nature*, 449(7162):579–583, 2007.
- [11] D. D. Osheroff, R. C. Richardson, and D. M. Lee. Evidence for a new phase of solid ^3He . *Phys. Rev. Lett.*, 28:885–888, 1972.
- [12] J. Klaers, J. Schmitt, F. Vewinger, and M. Weitz. Bose–Einstein condensation of photons in an optical microcavity. *Nature*, 468(7323):545–548, 2010.

- [13] H. Deng, D. Press, S. Götzinger, G. S. Solomon, R. Hey, K. H. Ploog, and Y. Yamamoto. Quantum degenerate exciton-polaritons in thermal equilibrium. *Phys. Rev. Lett.*, 97:146402, 2006.
- [14] S. O. Demokritov, V. E. Demidov, O. Dzyapko, G. A. Melkov, A. A. Serga, B. Hillebrands, and A. N. Slavin. Bose–Einstein condensation of quasi-equilibrium magnons at room temperature under pumping. *Nature*, 443(7110):430–433, 2006.
- [15] M. H. Anderson, J. R. Ensher, M. R. Matthews, C. E. Wieman, and E. A. Cornell. Observation of Bose–Einstein condensation in a dilute atomic vapor. *Science*, 269:198, 1995.
- [16] K. B. Davis, M. O. Mewes, M. R. Andrews, N. J. van Druten, D. S. Durfee, D. M. Kurn, and W. Ketterle. Bose-Einstein condensation in a gas of sodium atoms. *Phys. Rev. Lett.*, 75:3969–3973, 1995.
- [17] D. G. Fried, T. C. Killian, L. Willmann, D. Landhuis, S. C. Moss, D. Kleppner, and T. J. Greytak. Bose–Einstein condensation of atomic hydrogen. *Phys. Rev. Lett.*, 81:3811, 1998.
- [18] C. C. Bradley, C. A. Sackett, J. J. Tollett, and R. G. Hulet. Evidence of Bose-Einstein condensation in an atomic gas with attractive interactions. *Phys. Rev. Lett.*, 75(9):1687, 1995.
- [19] B. DeMarco and D. D. Jin. Onset of Fermi degeneracy in a trapped atomic gas. *Science*, 285:1703, 1999.
- [20] S. L. Cornish, N. R. Claussen, J. L. Roberts, E. A. Cornell, and C. E. Wieman. Stable ^{85}Rb Bose–Einstein condensates with widely tunable interactions. *Phys. Rev. Lett.*, 85:1795, 2000.
- [21] A.G. Truscott, K.E. Strecker, W.I. McAlexander, G.P. Partridge, and R. G. Hulet. Observation of Fermi pressure in a gas of trapped atoms. *Science*, 291:2570, 2001.
- [22] G. Modugno, G. Ferrari, G. Roati, R. J. Brecha, A. Simoni, and M. Inguscio. Bose-Einstein condensation of Potassium atoms by sympathetic cooling. *Science*, 294(5545):1320–1322, 2001.
- [23] K. M. O’Hara, S. L. Hemmer, M. E. Gehm, S. R. Granade, and J. E. Thomas. Observation of a strongly interacting degenerate Fermi gas of atoms. *Science*, 298:2179, 2002.
- [24] T. Weber, J. Herbig, M. Mark, H. C. Nägerl, and R. Grimm. Bose-Einstein condensation of Cesium. *Science*, 299(5604):232–235, 2003.
- [25] G. Roati, M. Zaccanti, C. D’Errico, J. Catani, M. Modugno, A. Simoni, M. Inguscio, and G. Modugno. ^{39}K Bose–Einstein condensate with tunable interactions. *Phys. Rev. Lett.*, 99:010403, 2007.

- [26] S. Kraft, F. Vogt, O. Appel, F. Riehle, and U. Sterr. Bose-Einstein condensation of alkaline earth atoms: Ca 40. *Phys. Rev. Lett.*, 103(13):130401, 2009.
- [27] S. Stellmer, M. K. Tey, B. Huang, R. Grimm, and F. Schreck. Bose-Einstein condensation of strontium. *Phys. Rev. Lett.*, 103(20):200401, 2009.
- [28] M. De Escobar, P. G. Mickelson, M. Yan, B.J. DeSalvo, S. B. Nagel, and T. C. Killian. Bose-Einstein condensation of ^{84}Sr . *Phys. Rev. Lett.*, 103(20):200402, 2009.
- [29] B. J. DeSalvo, M. Yan, P. G. Mickelson, M. De Escobar, and T. C. Killian. Degenerate Fermi gas of ^{87}Sr . *Phys. Rev. Lett.*, 105(3):030402, 2010.
- [30] Y. Takasu, K. Maki, K. Komori, T. Takano, K. Honda, M. Kumakura, T. Yabuzaki, and Y. Takahashi. Spin-singlet Bose-Einstein condensation of two-electron atoms. *Phys. Rev. Lett.*, 91(4):040404, 2003.
- [31] M. Lu, N. Q. Burdick, S. H. Youn, and B. L. Lev. Strongly dipolar Bose-Einstein condensate of dysprosium. *Phys. Rev. Lett.*, 107(19):190401, 2011.
- [32] K. Aikawa, A. Frisch, M. Mark, S. Baier, A. Rietzler, R. Grimm, and F. Ferlaino. Bose-einstein condensation of erbium. *Phys. Rev. Lett.*, 108:210401, May 2012.
- [33] A. Griesmaier, J. Werner, S. Hensler, J. Stuhler, and T. Pfau. Bose-Einstein condensation of chromium. *Phys. Rev. Lett.*, 94:160401, 2005.
- [34] M. Greiner, C. A. Regal, and D. S. Jin. Emergence of a molecular Bose-Einstein condensate from a Fermi gas. *Nature*, 426(6966):537–540, 2003.
- [35] M. W. Zwierlein, C. A. Stan, C. H. Schunk, S. M. F. Raupach, S. Gupta, Z. Hadzibabic, and W. Ketterle. Observation of Bose-Einstein condensation of molecules. *Phys. Rev. Lett.*, 91:250401, 2003.
- [36] S. Jochim, M. Bartenstein, A. Altmeyer, G. Hendl, S. Riedl, C. Chin, J. Hecker-Denschlag, and R. Grimm. Bose-Einstein condensation of molecules. *Science*, 302:2101, 2003.
- [37] L. De Marco, G. Valtolina, K. Matsuda, W. G. Tobias, J. P. Covey, and J. Ye. A degenerate Fermi gas of polar molecules. *Science*, 363(6429):853–856, 2019.
- [38] T. Yefsah, R. Desbuquois, L. Chomaz, K. J. Günter, and J. Dalibard. Exploring the thermodynamics of a two-dimensional Bose gas. *Phys. Rev. Lett.*, 107:130401, Sep 2011.
- [39] L. C. Ha, C. L. Hung, X. Zhang, U. Eismann, S. K. Tung, and C. Chin. Strongly interacting two-dimensional Bose gases. *Phys. Rev. Lett.*, 110:145302, 2013.

- [40] S. Nascimbène, N. Navon, K. J. Jiang, F. Chevy, and C. Salomon. Exploring the thermodynamics of a universal Fermi gas. *Nature*, 463(7284):1057–1060, 2010.
- [41] N. Navon, S. Piatecki, K. Günter, B. Rem, T. C. Nguyen, F. Chevy, W. Krauth, and C. Salomon. Dynamics and Thermodynamics of the Low-Temperature Strongly Interacting Bose Gas. *Phys. Rev. Lett.*, 107:135301, 2011.
- [42] M. R. Matthews, B. P. Anderson, P. C. Haljan, D. S. Hall, C. E. Wieman, and E. A. Cornell. Vortices in a Bose-Einstein condensate. *Phys. Rev. Lett.*, 83:2498–2501, Sep 1999.
- [43] J. R. Abo-Shaeer, C. Raman, J. M. Vogels, and W. Ketterle. Observation of vortex lattices in Bose-Einstein condensates. *Science*, 292:476–479, 2001.
- [44] K. E. Strecker, G. B. Partridge, A. G. Truscott, and R. G. Hulet. Formation and propagation of matter-wave soliton trains. *Nature*, 417(6885):150–153, 2002.
- [45] L. Chomaz, R. M. W. van Bijnen, D. Petter, G. Faraoni, S. Baier, J. H. Becher, M. J. Mark, F. Waechtler, L. Santos, and F. Ferlaino. Observation of roton mode population in a dipolar quantum gas. *Nature physics*, 14(5):442–446, 2018.
- [46] R. Onofrio, C. Raman, J. M. Vogels, J. R. Abo-Shaeer, A. P. Chikkatur, and W. Ketterle. Observation of superfluid flow in a Bose-Einstein condensed gas. *Phys. Rev. Lett.*, 85:2228–2231, 2000.
- [47] M. Zwierlein, C. H. Schunck, A. Schirotzek, and W. Ketterle. Direct observation of the superfluid phase transition in ultracold Fermi gases. *nature*, 442(7098):54–58, 2006.
- [48] D. E. Miller, J. K. Chin, C. A. Stan, Y. Liu, W. Setiawan, C. Sanner, and W. Ketterle. Critical velocity for superfluid flow across the BEC-BCS crossover. *Phys. Rev. Lett.*, 99:070402, 2007.
- [49] M. Wenzel, F. Böttcher, J. N. Schmidt, M. Eisenmann, T. Langen, T. Pfau, and I. Ferrier-Barbut. Anisotropic superfluid behavior of a dipolar Bose-Einstein condensate. *Phys. Rev. Lett.*, 121(3):030401, 2018.
- [50] C. Chin, R. Grimm, P. Julienne, and E. Tiesinga. Feshbach resonances in ultracold gases. *Rev. Mod. Phys.*, 82(2):1225–1286, Apr 2010.
- [51] G. Roati, C. D’Errico, L. Fallani, M. Fattori, C. Fort, M. Zaccanti, G. Modugno, M. Modugno, and M. Inguscio. Anderson localization of a non-interacting Bose-Einstein condensate. *Nature*, 453:895, 2008.
- [52] M. Schreiber, S. S. Hodgman, P. Bordia, H. P. Lüschen, M. H. Fischer, R. Vosk, E. Altman, U. Schneider, and I. Bloch. Observation of many-body localization of interacting Fermions in a quasi-random optical lattice. *Science*, 349(6250):842–845, 2015.

- [53] D. White, T. Haase, D. Brown, M. Hoogerland, M. Najafabadi, J. Helm, C. Gies, D. Schumayer, and D. Hutchinson. Observation of two-dimensional Anderson localisation of ultracold atoms. *Nature Communications*, 11(1):1–8, 2020.
- [54] C. Meldgin, U. Ray, P. Russ, D. Chen, D. Ceperley, and B. DeMarco. Probing the Bose glass–superfluid transition using quantum quenches of disorder. *Nature Physics*, 12(7):646–649, 2016.
- [55] K. Baumann, C. Guerlin, F. Brennecke, and T. Esslinger. Dicke quantum phase transition with a superfluid gas in an optical cavity. *Nature*, 464(7293):1301–1306, 2010.
- [56] L. Tanzi, E. Lucioni, F. Famà, J. Catani, A. Fioretti, C. Gabbanini, R. N. Bisset, L. Santos, and G. Modugno. Observation of a dipolar quantum gas with metastable supersolid properties. *Phys. Rev. Lett.*, 122:130405, Apr 2019.
- [57] L. Chomaz, D. Petter, P. Ilzhöfer, G. Natale, A. Trautmann, C. Politi, G. Durastante, R. M. W. van Bijnen, A. Patscheider, M. Sohmen, M. J. Mark, and F. Ferlaino. Long-lived and transient supersolid behaviors in dipolar quantum gases. *Phys. Rev. X*, 9:021012, Apr 2019.
- [58] B. Paredes, A. Widera, V. Murg, O. Mandel, S. Fölling, I. Cirac, G. Shlyapnikov, T. Hänsch, and I. Bloch. Tonks–Girardeau gas of ultracold atoms in an optical lattice. *Nature*, 429(6989):277–281, 2004.
- [59] T. Kinoshita, T. Wenger, and D. S. Weiss. Observation of a one-dimensional Tonks–Girardeau gas. *Science*, 305:1125–1128, 2004.
- [60] M. Greiner, M. O. Mandel, T. Esslinger, T. Hänsch, and I. Bloch. Quantum phase transition from a superfluid to a Mott insulator in a gas of ultracold atoms. *Nature*, 415:39, 2002.
- [61] C. A. Regal, M. Greiner, and D. S. Jin. Observation of resonance condensation of fermionic atom pairs. *Phys. Rev. Lett.*, 92:040403, 2004.
- [62] M. W. Zwierlein, C. A. Stan, C. H. Schunck, S. M. F. Raupach, A. J. Kerman, and W. Ketterle. Condensation of pairs of Fermionic atoms near a Feshbach resonance. *Phys. Rev. Lett.*, 92:120403, 2004.
- [63] M. Bartenstein, A. Altmeyer, S. Riedl, S. Joachim, C. Chin, J. Hecker-Denschlag, and R. Grimm. Collective excitations of a degenerate gas at the BEC-BCS crossover. *Phys. Rev. Lett.*, 92:203201, 2004.
- [64] Z. Hadzibabic, P. Krüger, M. Cheneau, B. Battelier, and J. Dalibard. Berezinskii–Kosterlitz–Thouless crossover in a trapped atomic gas. *Nature*, 441:1118–1121, 2006.
- [65] P. C. Hohenberg. Existence of long-range order in one and two dimensions. *Phys. Rev.*, 158:383–386, 1967.

- [66] N. D. Mermin and H. Wagner. Absence of ferromagnetism or antiferromagnetism in one- or two-dimensional isotropic heisenberg models. *Phys. Rev. Lett.*, 17:1133–1136, 1966.
- [67] J M Kosterlitz and D J Thouless. Ordering, metastability and phase transitions in two-dimensional systems. *Journal of Physics C: Solid State Physics*, 6(7):1181–1203, apr 1973.
- [68] V. L. Berezinskii. Destruction of long-range order in one-dimensional and two-dimensional systems possessing a continuous symmetry group. ii. quantum systems. *Sov. Phys. JETP*, 34(3):610–616, 1972.
- [69] D. R. Nelson and J. M. Kosterlitz. Universal jump in the superfluid density of two-dimensional superfluids. *Phys. Rev. Lett.*, 39:1201–1205, Nov 1977.
- [70] I. Rudnick, R. S. Kagiwida, J. C. Fraser, and E. Guyon. Third sound in adsorbed superfluid films. *Phys. Rev. Lett.*, 20(9):430, 1968.
- [71] D. Bergman. Hydrodynamics and third sound in thin He II films. *Physical Review*, 188(1):370, 1969.
- [72] D. J. Bishop and J. D. Reppy. Study of the superfluid transition in two-dimensional ^4He films. *Phys. Rev. Lett.*, 40:1727–1730, 1978.
- [73] V. Schweikhard, S. Tung, and E. A. Cornell. Vortex proliferation in the Berezinskii-Kosterlitz-Thouless regime on a two-dimensional lattice of Bose-Einstein condensates. *Phys. Rev. Lett.*, 99:030401, 2007.
- [74] P. Cladé, C. Ryu, A. Ramanathan, K. Helmerson, and W. D. Phillips. Observation of a 2d bose gas: From thermal to quasicondensate to superfluid. *Phys. Rev. Lett.*, 102:170401, Apr 2009.
- [75] S. Tung, G. Lamporesi, D. Lobser, L. Xia, and E. A. Cornell. Observation of the presuperfluid regime in a two-dimensional Bose gas. *Phys. Rev. Lett.*, 105:230408, Dec 2010.
- [76] T. Plisson, B. Allard, M. Holzmann, G. Salomon, A. Aspect, P. Bouyer, and T. Bourdel. Coherence properties of a two-dimensional trapped bose gas around the superfluid transition. *Phys. Rev. A*, 84:061606, Dec 2011.
- [77] R. Desbuquois, L. Chomaz, T. Yefsah, J. Léonard, J. Beugnon, C. Weitenberg, and J. Dalibard. Superfluid behaviour of a two-dimensional Bose gas. *Nature Physics*, 8(9):645–648, 2012.
- [78] J. Choi, S. Seo, and Y. Shin. Observation of thermally activated vortex pairs in a quasi-2D Bose gas. *Phys. Rev. Lett.*, 110:175302, 2013.

- [79] P. A. Murthy, I. Boettcher, L. Bayha, M. Holzmann, D. Kedar, M. Neidig, M. G. Ries, A. N. Wenz, G. Zürn, and S. Jochim. Observation of the Berezinskii-Kosterlitz-Thouless phase transition in an ultracold Fermi gas. *Phys. Rev. Lett.*, 115:010401, 2015.
- [80] R. Fletcher, M. Robert-de-Saint-Vincent, J. Man, N. Navon, R. Smith, K. Viebahn, and Z. Hadzibabic. Connecting Berezinskii-Kosterlitz-Thouless and BEC phase transitions by tuning interactions in a trapped gas. *Phys. Rev. Lett.*, 114:255302, 2015.
- [81] L. Sobirey, N. Luick, M. Bohlen, H. Biss, H. Moritz, and T. Lompe. Observation of superfluidity in a strongly correlated two-dimensional Fermi gas. *Science*, 372(6544):844–846, 2021.
- [82] N. Luick, L. Sobirey, M. Bohlen, V. Singh, L. Mathey, T. Lompe, and H. Moritz. An ideal Josephson junction in an ultracold two-dimensional Fermi gas. *Science*, 369(6499):89–91, 2020.
- [83] A. L. Gaunt, T. F. Schmidutz, I. Gotlibovych, R. P. Smith, and Z. Hadzibabic. Bose–Einstein condensation of atoms in a uniform potential. *Phys. Rev. Lett.*, 110:200406, 2013.
- [84] J.L. Ville, T. Bienaimé, R. Saint-Jalm, L. Corman, M. Aidelsburger, L. Chomaz, K. Kleinlein, D. Perconte, S. Nascimbène, and J. Dalibard. Loading and compression of a single two-dimensional Bose gas in an optical accordion. *Phys. Rev. A*, 95(1):013632, 2017.
- [85] L. Clark, A. Gaj, L. Feng, and C. Chin. Collective emission of matter-wave jets from driven Bose–Einstein condensates. *Nature*, 551(7680):356–359, 2017.
- [86] Cheng-An Chen and Chen-Lung Hung. Observation of modulational instability and townes soliton formation in two-dimensional Bose gases. *arXiv:1907.12550*, 2019.
- [87] K. Hueck, N. Luick, L. Sobirey, J. Siegl, T. Lompe, and H. Moritz. Two-dimensional homogeneous Fermi gases. *Phys. Rev. Lett.*, 120:060402, 2018.
- [88] N. R. Cooper and Z. Hadzibabic. Measuring the superfluid fraction of an ultracold atomic gas. *Phys. Rev. Lett.*, 104(3):030401, 2010.
- [89] S. T. John, Z. Hadzibabic, and N. R. Cooper. Spectroscopic method to measure the superfluid fraction of an ultracold atomic gas. *Phys. Rev. A*, 83:023610, Feb 2011.
- [90] I. Carusotto and Y. Castin. Nonequilibrium and local detection of the normal fraction of a trapped two-dimensional Bose gas. *Phys. Rev. A*, 84:053637, 2011.
- [91] T. Ozawa and S. Stringari. Discontinuities in the first and second sound velocities at the Berezinskii-Kosterlitz-Thouless transition. *Phys. Rev. Lett.*, 112:025302, 2014.
- [92] R. Campbell, R. Smith, N. Tammuz, S. Beattie, S. Moulder, and Z. Hadzibabic. Efficient production of large ^{39}K Bose-Einstein condensates. *Phys. Rev. A*, 82:063611, 2010.

- [93] H. Fairbank and C. T. Lane. Rollin film rates in liquid helium. *Phys. Rev.*, 76:1209–1211, 1949.
- [94] J. F. Allen and H. Jones. New phenomena connected with heat flow in helium II. *Nature*, 141(3562):243–244, 1938.
- [95] A. Van Groenou, J. Poll, A. Delsing, and C. Gorter. The viscosity of the normal part of liquid helium II from heat conduction experiments. *Physica*, 22(6-12):905–910, 1956.
- [96] E Andronikashvili. A direct observation of 2 kinds of motion in Helium-II. *Zhurnal Eksperimentalnoi I Teoreticheskoi Fiziki*, 16(9):780–785, 1946.
- [97] L. Tisza. Transport phenomena in helium II. *Nature*, 141(3577):913–913, 1938.
- [98] L. Landau. Theory of the superfluidity of helium II. *Physical Review*, 60(4):356, 1941.
- [99] P. Chaikin, T. Lubensky, and T. Witten. *Principles of condensed matter physics*, volume 10. Cambridge university press Cambridge, 1995.
- [100] I. Khalatnikov. *An introduction to the theory of superfluidity*. CRC Press, 2018.
- [101] H. Hu, P. Zou, and X. Liu. Low-momentum dynamic structure factor of a strongly interacting Fermi gas at finite temperature: A two-fluid hydrodynamic description. *Phys. Rev. A*, 97:023615, 2018.
- [102] H. Callen. *Thermodynamics and an introduction to Thermostatistics*, 1998.
- [103] A. Griffin and E. Zaremba. First and second sound in a uniform Bose gas. *Phys. Rev. A*, 56:4839, 1997.
- [104] M. Plischke and B. Bergersen. *Equilibrium statistical physics*. World scientific, 1994.
- [105] L. Van Hove. Correlations in space and time and Born approximation scattering in systems of interacting particles. *Physical Review*, 95(1):249, 1954.
- [106] A. Woods and R. Cowley. Structure and excitations of liquid helium. *Reports on Progress in Physics*, 36(9):1135, 1973.
- [107] R. Kubo. The fluctuation-dissipation theorem. *Reports on progress in physics*, 29(1):255, 1966.
- [108] L. Kadanoff. *Quantum statistical mechanics*. Chap. 6. CRC Press, 2018.
- [109] P. C. Hohenberg and P. C. Martin. Microscopic theory of superfluid helium. *Ann. Phys.*, 34:291, 1965.

- [110] H. Hu, E. Taylor, X. Liu, S. Stringari, and A. Griffin. Second sound and the density response function in uniform superfluid atomic gases. *New Journal of Physics*, 12(4):043040, apr 2010.
- [111] I. Khalatnikov. Hydrodynamics of solutions of two superfluid liquids. *Sov. Phys. JETP*, 5:542, 1957.
- [112] D. T. Son. Vanishing bulk viscosities and conformal invariance of the unitary Fermi gas. *Phys. Rev. Lett.*, 98:020604, 2007.
- [113] J. Steinhauer, R. Ozeri, N. Katz, and N. Davidson. Excitation spectrum of a Bose–Einstein condensate. *Phys. Phys. Lett.*, 88(12):120407, 2002.
- [114] L. Pitaevskii and S. Stringari. *Bose-Einstein condensation and superfluidity*, volume 164. Oxford University Press, 2016.
- [115] N. Prokof'ev and B. Svistunov. Two-dimensional weakly interacting Bose gas in the fluctuation region. *Phys. Rev. A*, 66:043608, 2002.
- [116] E. Pollock and D. Ceperley. Path-integral computation of superfluid densities. *Phys. Rev. B*, 36(16):8343, 1987.
- [117] R. A. Cowley and A. D. B. Woods. Neutron scattering from liquid helium at high energies. *Phys. Rev. Lett.*, 21:787–789, Sep 1968.
- [118] I.V. Bogoyavlenskii, L.V. Karnatsevich, J.A. Kozlov, and A.V. Puchkov. Neutron scattering determination of condensate in liquid 4He. *Physica B: Condensed Matter*, 176(1-2):151–152, 1992.
- [119] A. Wyatt. Evidence for a Bose–Einstein condensate in liquid 4He from quantum evaporation. *Nature*, 391(6662):56–59, 1998.
- [120] C. Pethick and H. Smith. *Bose–Einstein condensation in dilute gases*. Cambridge university press, 2008.
- [121] C. Joachain. Quantum collision theory. 1975.
- [122] J. Dalibard. Collisional dynamics of ultra-cold atomic gases. In *Proceedings of the International School of Physics-Enrico Fermi*, volume 321, page 14, 1999.
- [123] M. Zaccanti, B. Deissler, C. D’Errico, M. Fattori, M. Jona-Lasinio, S. Müller, G. Roati, M. Inguscio, and G. Modugno. Observation of an Efimov spectrum in an atomic system. *Nat. Phys.*, 5(8):586–591, 2009.
- [124] P. Naidon and S. Endo. Efimov physics: a review. *Reports on Progress in Physics*, 80(5):056001, 2017.

- [125] R. Fletcher, R. Lopes, J. Man, N. Navon, R. Smith, M. Zwierlein, and Z. Hadzibabic. Two- and three-body contacts in the unitary Bose gas. *Science*, 355(6323):377–380, 2017.
- [126] J. Söding, D. Guéry-Odelin, P. Desbiolles, F. Chevy, H. Inamori, and J. Dalibard. Three-body decay of a Rubidium Bose–Einstein condensate. *Appl. Phys. B*, 69:257, 1999.
- [127] Y. Kagan, B. V. Svistunov, and G. V. Shlyapnikov. Effect of Bose condensation on inelastic processes in gases. *JETP Lett.*, 642:209, 1985.
- [128] C. d’Errico, M. Zaccanti, M. Fattori, G. Roati, M. Inguscio, G. Modugno, and A. Simoni. Feshbach resonances in ultracold 39K. *New Journal of physics*, 9(7):223, 2007.
- [129] R. J. Fletcher, J. Man, R. Lopes, P. Christodoulou, J. Schmitt, M. Sohmen, N. Navon, R. P. Smith, and Z. Hadzibabic. Elliptic flow in a strongly interacting normal Bose gas. *Phys. Rev. A*, 98:011601, Jul 2018.
- [130] N. Nygaard, B. I. Schneider, and P. Julienne. A two-channel R-matrix analysis of magnetic field induced Feshbach resonances. *Phys. Rev. A*, 73:042705, 2006.
- [131] K. Goral, T. Koehler, S. Gardiner, E. Tiesinga, and P. Julienne. Adiabatic association of ultracold molecules via magnetic-field tunable interactions. *Journal of Physics B: Atomic, Molecular and Optical Physics*, 37(17):3457, 2004.
- [132] C. Eigen, A. L. Gaunt, A. Suleymanzade, N. Navon, Z. Hadzibabic, and R. P. Smith. Observation of Weak Collapse in a Bose–Einstein Condensate. *Phys. Rev. X*, 6:041058, Dec 2016.
- [133] A. Griffin. *Excitations in a Bose-condensed liquid*. Number 4. Cambridge University Press, 1993.
- [134] O. Penrose and L. Onsager. Bose-Einstein condensation and liquid helium. *Physical Review*, 104(3):576, 1956.
- [135] R. Ozeri, N. Katz, J. Steinhauer, and N. Davidson. Colloquium: Bulk Bogoliubov excitations in a Bose-Einstein condensate. *Reviews of Modern Physics*, 77(1):187, 2005.
- [136] P. Nozières and D. Pines. *The theory of quantum liquids*. Westview Press, 1990.
- [137] P. B. Blakie, A. S. Bradley, M. J. Davis, R. J. Ballagh, and C. W. Gardiner. Dynamics and statistical mechanics of ultra-cold Bose gases using c-field techniques. *Adv. Phys.*, 57(5):363–455, 2008.
- [138] N. Proukakis and B. Jackson. Finite-temperature models of Bose–Einstein condensation. *Journal of Physics B: Atomic, Molecular and Optical Physics*, 41(20):203002, 2008.

- [139] M. Brewczyk, M. Gajda, and K. Rzażewski. Classical fields approximation for Bosons at nonzero temperatures. *Journal of Physics B: Atomic, Molecular and Optical Physics*, 40(2):R1, 2007.
- [140] E. Zaremba, T. Nikuni, and A. Griffin. Dynamics of trapped Bose gases at finite temperatures. *Journal of Low Temperature Physics*, 116(3):277–345, 1999.
- [141] Allan Griffin, Tetsuro Nikuni, and Eugene Zaremba. *Bose-condensed gases at finite temperatures*. Cambridge University Press, 2009.
- [142] L. Chomaz, L. Corman, T. Bienaimé, Rémi Desbuquois, C. Weitenberg, S. Nascimbene, J. Beugnon, and J. Dalibard. Emergence of coherence via transverse condensation in a uniform quasi-two-dimensional Bose gas. *Nature communications*, 6(1):1–10, 2015.
- [143] L. Chomaz. *Coherence and superfluidity of Bose gases in reduced dimensions: from harmonic traps to uniform fluids*. PhD thesis, Ecole normale supérieure-ENS PARIS, 2014.
- [144] D. S. Petrov, M. Holzmann, and G. V. Shlyapnikov. Bose-Einstein condensation in quasi-2d trapped gases. *Phys. Rev. Lett.*, 84:2551–2555, Mar 2000.
- [145] S. Shevchenko, D. Fil, and M. Mamalui. Existence of true bose-Einstein condensate in a 2d interacting gas in an anti-trap geometry. *Journal of low temperature physics*, 121(5):275–280, 2000.
- [146] C. Mora and Y. Castin. Extension of Bogoliubov theory to quasicondensates. *Phys. Rev. A*, 67:053615, 2003.
- [147] J. Kane and L. Kadanoff. Long-range order in superfluid Helium. *Physical Review*, 155(1):80, 1967.
- [148] AP Young. On the theory of the phase transition in the two-dimensional planar spin model. *Journal of Physics C: Solid State Physics*, 11(11):L453, 1978.
- [149] Z. Hadzibabic and J. Dalibard. Two-dimensional Bose fluids: An atomic physics perspective. *Riv. Nuovo Cimento*, 34(6):389–434, 2011.
- [150] A. Rançon and N. Dupuis. Universal thermodynamics of a two-dimensional Bose gas. *Phys. Rev. A*, 85:063607, Jun 2012.
- [151] AI Safonov, SA Vasilyev, IS Yasnikov, II Lukashevich, and S Jaakkola. Observation of quasi-condensate in two-dimensional atomic hydrogen. *Physical Review Letters*, 81(21):4545, 1998.
- [152] N. Prokof'ev, O. Ruebenacker, and B. Svistunov. Critical point of a weakly interacting two-dimensional Bose gas. *Phys. Rev. Lett.*, 87:270402, Dec 2001.

- [153] C. L. Hung, X. Zhang, N. Gemelke, and C. Chin. Observation of scale invariance and universality in two-dimensional Bose gases. *Nature*, 470:236, 2011.
- [154] M. Ota and S. Stringari. Second sound in a two-dimensional Bose gas: From the weakly to the strongly interacting regime. *Phys. Rev. A*, 97:033604, 2018.
- [155] V. Ambegaokar, B. Halperin, D. Nelson, and E. Siggia. Dissipation in two-dimensional superfluids. *Phys. Rev. Lett.*, 40(12):783, 1978.
- [156] V. Ambegaokar and S. Teitel. Dynamics of vortex pairs in superfluid films. *Phys. Rev. B*, 19(3):1667, 1979.
- [157] Z. Wu, S. Zhang, and H. Zhai. Dynamic Kosterlitz-Thouless theory for two-dimensional ultracold atomic gases. *Phys. Rev. A*, 102(4):043311, 2020.
- [158] J. Kosterlitz. The critical properties of the two-dimensional XY model. *Journal of Physics C: Solid State Physics*, 7(6):1046, 1974.
- [159] K. Gawryluk and M. Brewczyk. Signatures of a universal jump in the superfluid density of a two-dimensional Bose gas with a finite number of particles. *Phys. Rev. A*, 99:033615, 2019.
- [160] I. Maccari, L. Benfatto, and C. Castellani. The BKT universality class in the presence of correlated disorder. *Condensed Matter*, 3(1):8, 2018.
- [161] S. Pilati, S. Giorgini, and N. Prokof'ev. Critical temperature of interacting Bose gases in two and three dimensions. *Phys. Rev. Lett.*, 100:140405, Apr 2008.
- [162] L Benfatto, C Castellani, and Thierry Giamarchi. Broadening of the berezinskii-kosterlitz-thouless superconducting transition by inhomogeneity and finite-size effects. *Physical Review B*, 80(21):214506, 2009.
- [163] ST Bramwell and PCW Holdsworth. Magnetization and universal sub-critical behaviour in two-dimensional xy magnets. *Journal of Physics: Condensed Matter*, 5(4):L53, 1993.
- [164] S. T. Bramwell and P. C. W. Holdsworth. Magnetization: A characteristic of the Kosterlitz-Thouless-Berezinskii transition. *Phys. Rev. B*, 49(13):8811-8814, 1994.
- [165] N. Tammuz. *Thermodynamics of ultracold $^3\text{9K}$ atomic Bose gases with tuneable interactions*. PhD thesis, University of Cambridge, 2012.
- [166] R. Campbell. *Thermodynamic properties of a Bose gas with tuneable interactions*. PhD thesis, University of Cambridge, 2012.
- [167] R. Fletcher. *Bose-Einstein condensation and superfluidity in two dimensions*. PhD thesis, University of Cambridge, 2015.

- [168] A. Marte, T. Volz, J. Schuster, S. Dürr, G. Rempe, E. Van Kempen, and B. Verhaar. Feshbach resonances in Rubidium 87: Precision measurement and analysis. *Phys. Rev. Lett.*, 89(28):283202, 2002.
- [169] R. Grimm, M. Weidemüller, and Y. Ovchinnikov. Optical dipole traps for neutral atoms. *Advances in atomic, molecular, and optical physics*, 42:95–170, 2000.
- [170] R. Williamson and T. Walker. Magneto-optical trapping and ultracold collisions of potassium atoms. *JOSA B*, 12(8):1393–1397, 1995.
- [171] M. Santos, P. Nussenzeig, L. Marcassa, K. Helmerson, J. Flemming, S. Zilio, and V. Bagnato. Simultaneous trapping of two different atomic species in a vapor-cell magneto-optical trap. *Physical Review A*, 52(6):R4340, 1995.
- [172] C. Fort, A. Bambini, L. Cacciapuoti, F. Cataliotti, M. Prevedelli, G. Tino, and M. Inguscio. Cooling mechanisms in potassium magneto-optical traps. *The European Physical Journal D-Atomic, Molecular, Optical and Plasma Physics*, 3(2):113–118, 1998.
- [173] V. Gokhroo, G. Rajalakshmi, K. Easwaran, and C. Unnikrishnan. Sub-doppler deep-cooled bosonic and fermionic isotopes of potassium in a compact 2d–3d mot set-up. *Journal of Physics B: Atomic, Molecular and Optical Physics*, 44(11):115307, 2011.
- [174] A. Hemmerich, M. Weidemüller, T. Esslinger, C. Zimmermann, and T. Hänsch. Trapping atoms in a dark optical lattice. *Phys. Rev. Lett.*, 75:37–40, Jul 1995.
- [175] T. Esslinger, F. Sander, A. Hemmerich, T. Hänsch, H. Ritsch, and M. Weidemüller. Purely optical dark lattice. *Optics letters*, 21(13):991–993, 1996.
- [176] D. Rio Fernandes, F. Sievers, N. Kretzschmar, S. Wu, C. Salomon, and F. Chevy. Sub-doppler laser cooling of fermionic 40k atoms in three-dimensional gray optical molasses. *EPL (Europhysics Letters)*, 100(6):63001, 2012.
- [177] G. Salomon, L. Fouché, P. Wang, A. Aspect, P. Bouyer, and T. Bourdel. Gray-molasses cooling of 39k to a high phase-space density. *EPL (Europhysics Letters)*, 104(6):63002, 2014.
- [178] D. Nath, R. K. Easwaran, G. Rajalakshmi, and C. S. Unnikrishnan. Quantum-interference-enhanced deep sub-Doppler cooling of ^{39}K atoms in gray molasses. *Phys. Rev. A*, 88:053407, Nov 2013.
- [179] A. Görlitz, J. M. Vogels, A. E. Leanhardt, C. Raman, T. L. Gustavson, J. R. Abo-Shaeer, A. P. Chikkatur, S. Gupta, S. Inouye, T. Rosenband, and W. Ketterle. Realization of Bose-Einstein condensates in lower dimensions. *Phys. Rev. Lett.*, 87:130402, Sep 2001.

- [180] D. Rychtarik, B. Engeser, H.-C. Nägerl, and R. Grimm. Two-dimensional Bose-Einstein condensate in an optical surface trap. *Phys. Rev. Lett.*, 92:173003, Apr 2004.
- [181] K. Merloti, R. Dubessy, L. Longchambon, A. Perrin, P. Pottie, V. Lorent, and journal=New Journal of Physics volume=15 number=3 pages=033007 year=2013 publisher=IOP Publishing Perrin, H. A two-dimensional quantum gas in a magnetic trap.
- [182] T. A. Savard, K. M. O'Hara, and J. E. Thomas. Laser-noise-induced heating in far-off resonance optical traps. *Phys. Rev. A*, 56:R1095–R1098, Aug 1997.
- [183] P. Dyke, K. Fenech, T. Pepler, M. G. Lingham, S. Hoinka, W. Zhang, S.-G. Peng, B. Mulkerin, H. Hu, X.-J. Liu, and C. J. Vale. Criteria for two-dimensional kinematics in an interacting Fermi gas. *Phys. Rev. A*, 93:011603, Jan 2016.
- [184] M. G. Ries, A. N. Wenz, G. Zürn, L. Bayha, I. Boettcher, D. Kedar, P. A. Murthy, M. Neidig, T. Lompe, and S. Jochim. Observation of pair condensation in the quasi-2d BEC-BCS crossover. *Phys. Rev. Lett.*, 114:230401, Jun 2015.
- [185] NL Smith, WH Heathcote, G Hechenblaikner, E Nugent, and CJ Foot. Quasi-2d confinement of a bec in a combined optical and magnetic potential. *Journal of Physics B: Atomic, Molecular and Optical Physics*, 38(3):223, 2005.
- [186] S Al-Assam, RA Williams, and CJ Foot. Ultracold atoms in an optical lattice with dynamically variable periodicity. *Physical Review A*, 82(2):021604, 2010.
- [187] D. Voelz. Computational Fourier optics: a MATLAB tutorial. Society of Photo-Optical Instrumentation Engineers, 2011.
- [188] C. Palmer and E. Loewen. Diffraction grating handbook. 2005.
- [189] P. Zupancic. Dynamic holography and beamshaping using digital micromirror devices. *LMU München, Grainer Lab Harvard*, 242, 2013.
- [190] R. Ozeri, L. Khaykovich, and N. Davidson. Long spin relaxation times in a single-beam blue-detuned optical trap. *Phys. Rev. A*, 59:R1750–R1753, 1999.
- [191] T. Kuga, Y. Torii, N. Shiokawa, T. Hirano, Y. Shimizu, and H. Sasada. Novel optical trap of atoms with a doughnut beam. *Phys. Rev. Lett.*, 78:4713–4716, 1997.
- [192] B. Mukherjee, Z. Yan, P. Patel, Z. Hadzibabic, T. Yefsah, J. Struck, and M. Zwierlein. Homogeneous atomic Fermi gases. *Phys. Rev. Lett.*, 118:123401, 2017.
- [193] N. Friedman, L. Khaykovich, R. Ozeri, and N. Davidson. Compression of cold atoms to very high densities in a rotating-beam blue-detuned optical trap. *Phys. Rev. A*, 61:031403, 2000.

- [194] T. Bell, G. Gauthier, T. Neely, H. Rubinsztein-Dunlop, M. Davis, and M. Baker. Phase and micromotion of Bose-Einstein condensates in a time-averaged ring trap. *Phys. Rev. A*, 98:013604, 2018.
- [195] G. Gauthier, I. Lenton, N. Parry, M. Baker, M. Davis, H. Rubinsztein-Dunlop, and T. Neely. Direct imaging of a digital-micromirror device for configurable microscopic optical potentials. *Optica*, 3(10):1136–1143, 2016.
- [196] A. Gaunt. *Degenerate Bose gases: tuning interactions & geometry*. PhD thesis, University of Cambridge, 2015.
- [197] K. Hueck. *A Homogeneous, Two-dimensional Fermi Gas: Measurements in Position-and Momentum-space*. PhD thesis, 2017.
- [198] J.L. Ville. *Quantum gases in box potentials: Sound and light in bosonic Flatland*. PhD thesis, Université Paris sciences et lettres, 2018.
- [199] R. Floyd and L. Steinberg. An adaptive algorithm for spatial greyscale. In *Proceedings of the Society of Information Display*, volume 17, pages 75–77, 1976.
- [200] A. Keshet and W. Ketterle. A distributed, graphical user interface based, computer control system for atomic physics experiments. *Review of Scientific Instruments*, 84(1):015105, 2013.
- [201] K. Hueck, A. Mazurenko, N. Luick, T. Lompe, and H. Moritz. Suppression of kHz-frequency switching noise in digital micro-mirror devices. *Review of Scientific Instruments*, 88(1):016103, 2017.
- [202] P. Pinkse, A. Mosk, M. Weidemüller, M. Reynolds, T. Hijmans, and J. Walraven. Adiabatically changing the phase-space density of a trapped Bose gas. *Phys. Rev. Lett.*, 78:990, 1997.
- [203] T. Li, H. Kelkar, D. Medellin, and M. Raizen. Real-time control of the periodicity of a standing wave: an optical accordion. *Opt. Express*, 16(8):5465–5470, 2008.
- [204] R. Williams, J. Pillet, S. Al-Assam, B. Fletcher, M. Shotton, and C. Foot. Dynamic optical lattices: two-dimensional rotating and accordion lattices for ultracold atoms. *Opt. Express*, 16(21):16977–16983, 2008.
- [205] M. Miranda, A. Nakamoto, Y. Okuyama, A. Noguchi, M. Ueda, and M. Kozuma. All-optical transport and compression of ytterbium atoms into the surface of a solid immersion lens. *Phys. Rev. A*, 86:063615, 2012.
- [206] L. Chomaz, L. Corman, T. Yefsah, R. Desbuquois, and J. Dalibard. Absorption imaging of a quasi-two-dimensional gas: a multiple scattering analysis. *New Journal of Physics*, 14(5):055001, 2012.

- [207] J. L. Ville, R. Saint-Jalm, É. Le Cerf, M. Aidelsburger, S. Nascimbène, J. Dalibard, and J. Beugnon. Sound propagation in a uniform superfluid two-dimensional Bose gas. *Phys. Rev. Lett.*, 121:145301, Oct 2018.
- [208] R. Bisset, D. Baillie, and P. Blakie. Analysis of the Holzmamm–Chevallier–Krauth theory for the trapped quasi-two-dimensional Bose gas. *Phys. Rev. A*, 79(1):013602, 2009.
- [209] M. Holzmamm, M. Chevallier, and W. Krauth. Universal correlations and coherence in quasi-two-dimensional trapped Bose gases. *Phys. Rev. A*, 81(4):043622, 2010.
- [210] S. Tung. *Probing an interacting Bose gas in a quasi-two-dimensional trap*. PhD thesis, University of Colorado at Boulder, 2010.
- [211] C. Everitt, K. Atkins, and A. Denenstein. Detection of third sound in liquid helium films. *Phys. Rev. Lett.*, 8(4):161, 1962.
- [212] C. Everitt, K. Atkins, and A. Denenstein. Third sound in liquid helium films. *Physical Review*, 136(6A):A1494, 1964.
- [213] J. Rutledge, W. McMillan, J. Mochel, and T. Washburn. Third sound, two-dimensional hydrodynamics, and elementary excitations in very thin helium films. *Phys. Rev. B*, 18(5):2155, 1978.
- [214] R. Saint-Jalm. *Exploring two-dimensional physics with Bose gases in box potentials: phase ordering and dynamical symmetry*. PhD thesis, Université Paris Sciences et Lettres, 2019.
- [215] P. Krüger, Z. Hadzibabic, and J. Dalibard. Critical point of an interacting two-dimensional atomic Bose gas. *Phys. Rev. Lett.*, 99:040402, 2007.
- [216] K. Atkins. Third and fourth sound in liquid helium II. *Physical Review*, 113(4):962, 1959.
- [217] X. J. Liu and H. Hu. First and second sound in a two-dimensional harmonically trapped Bose gas across the Berezinskii–Kosterlitz–Thouless transition. *Annals of Physics*, 351:531–539, 2014.
- [218] M. Ota, F. Larcher, F. Dalfovo, L. Pitaevskii, N. Proukakis, and S. Stringari. Collisionless sound in a uniform two-dimensional Bose gas. *Phys. Rev. Lett.*, 121:145302, 2018.
- [219] A. Cappellaro, F. Toigo, and L. Salasnich. Collisionless dynamics in two-dimensional bosonic gases. *Phys. Rev. A*, 98:043605, Oct 2018.
- [220] R. Meppelink, S. B. Koller, and P. van der Straten. Sound propagation in a Bose-Einstein condensate at finite temperatures. *Phys. Rev. A*, 80:043605, Oct 2009.

- [221] M. Andrews, D. Kurn, H. Miesner, D. Durfee, C. Townsend, S. Inouye, and W. Ketterle. Propagation of sound in a Bose–Einstein condensate. *Phys. Rev. Lett.*, 79:553–556, 1997.
- [222] L. A. Sidorenkov, M. K. Tey, R. Grimm, Y. H. Hou, L. Pitaevskii, and S. Stringari. Second sound and the superfluid fraction in a Fermi gas with resonant interactions. *Nature*, 498(7452):78–81, 2013.
- [223] D. M. Stamper-Kurn, A. P. Chikkatur, A. Görlitz, S. Inouye, S. Gupta, D. E. Pritchard, and W. Ketterle. Excitation of phonons in a Bose–Einstein condensate by light scattering. *Phys. Rev. Lett.*, 83:2876, 1999.
- [224] J. M. Vogels, K. Xu, C. Raman, J. R. Abo-Shaeer, and W. Ketterle. Experimental observation of the Bogoliubov transformation for a Bose–Einstein condensed gas. *Phys. Rev. Lett.*, 88:060402, 2002.
- [225] K Tani. The damping constant of a collective mode in the hydrodynamic regime. *Journal of Physics C: Solid State Physics*, 3(2):L50, 1970.
- [226] P. Patel, Z. Yan, B. Mukherjee, R. Fletcher, J. Struck, and M. Zwierlein. Universal sound diffusion in a strongly interacting Fermi gas. *Science*, 370(6521):1222–1226, 2020.
- [227] M. Bohlen, L. Sobirey, N. Luick, H. Biss, T. Enss, T. Lompe, and H. Moritz. Sound propagation and quantum-limited damping in a two-dimensional Fermi gas. *Phys. Rev. Lett.*, 124:240403, 2020.
- [228] G. Yang, A. Migone, and K. Johnson. Relationship between thermal diffusivity and mean free path. *American Journal of Physics*, 62(4):370–372, 1994.
- [229] L. Verney, L. Pitaevskii, and S. Stringari. Hybridization of first and second sound in a weakly interacting Bose gas. *EPL (Europhysics Letters)*, 111(4):40005, 2015.
- [230] V. Singh and L. Mathey. Sound propagation in a two-dimensional Bose gas across the superfluid transition. *Phys. Rev. Research*, 2:023336, 2020.
- [231] J. Beugnon and N. Navon. Exploring the Kibble–Zurek mechanism with homogeneous Bose gases. *J. Phys. B: At. Mol. Opt. Phys.*, 50:022002, 2017.
- [232] A. Jelić and L. Cugliandolo. Quench dynamics of the 2D XY model. *Journal of Statistical Mechanics: Theory and Experiment*, 2011(02):P02032, 2011.
- [233] J. Dziarmaga and W. Zurek. Quench in the 1D Bose-Hubbard model: Topological defects and excitations from the Kosterlitz-Thouless phase transition dynamics. *Scientific reports*, 4(1):1–6, 2014.

- [234] D. Stadler, S. Krinner, J. Meineke, J. P. Brantut, and T. Esslinger. Observing the drop of resistance in the flow of a superfluid Fermi gas. *Nature*, 491(7426):736–739, 2012.
- [235] J. P. Brantut, J. Meineke, D. Stadler, S. Krinner, and T. Esslinger. Conduction of ultracold Fermions through a mesoscopic channel. *Science*, 337(6098):1069–1071, 2012.
- [236] D. J. Papoular, G. Ferrari, L. P. Pitaevskii, and S. Stringari. Increasing quantum degeneracy by heating a superfluid. *Phys. Rev. Lett.*, 109(8):084501, 2012.
- [237] T. Karpiuk, B. Gremaud, C. Miniatura, and M. Gajda. Superfluid fountain effect in a Bose-Einstein condensate. *Phys. Rev. A*, 86(3):033619, 2012.